

**SPECTRAL AND TIMING
PROPERTIES OF ACCRETION FLOWS
AROUND BLACK HOLES
FROM OBSERVATIONAL DATA**

**Thesis submitted for the degree of
Doctor of Philosophy (Science)
of the
Jadavpur University**

Anuj Nandi
Satyendranath Bose National Centre
for Basic Sciences
Block-JD, Sector-III, Salt Lake City
Kolkata 700098, INDIA

**SPECTRAL AND TIMING
PROPERTIES OF ACCRETION FLOWS
AROUND BLACK HOLES
FROM OBSERVATIONAL DATA**

**Thesis submitted for the degree of
Doctor of Philosophy (Science)
of the
Jadavpur University**

Anuj Nandi
Satyendranath Bose National Centre
for Basic Sciences
Block-JD, Sector-III, Salt Lake City
Kolkata 700098, INDIA

CERTIFICATE FROM THE SUPERVISOR

This is to certify that the thesis entitled “**Spectral and Timing properties of Accretion flows around Black Holes from Observational Data**”, submitted by **Mr. Anuj Nandi** who got his name registered on **25.05.2001** for the award of Ph.D.(Science) degree of Jadavpur University, absolutely based upon his own work under the supervision of **Professor Sandip K. Chakrabarti** and that neither this thesis nor any part of it has been submitted for any degree/diploma or any other academic award anywhere before .

Schambhat 9.3.2005

Prof. Sandip K. Chakrabarti

S. N. Bose National Centre for Basic Sciences,
Block-JD, Sector-III, Salt Lake, Kolkata, India.

Prof. Sandip K. Chakrabarti

, Professor

**S. N. Bose National Centre
FOR BASIC SCIENCES**

Block; Salt Lake, Calcutta-97

ABSTRACT

Astrophysical Black Holes (BHs) are very fascinating objects in nature. It is challenging to identify a black hole that may be present in a compact binary system or at the galactic center. Since black holes are by definition ‘black’, as light can’t escape from them, a ‘true’ identification of a black hole by observing the electromagnetic (EM) radiation is not possible. Therefore, the best way to ‘see’ or to identify a black hole is to study how matter behaves around these compact objects and what EM radiation it emits. The process of capture of matter by gravitating objects is called *accretion* and in steady state a disk-like structure is formed which is called an *accretion disk*. Highly collimated, relativistic matters are launched from the accretion disk in the form of continuous or discontinuous flows. These are called *Jets*. Since accretion disks and jets are common phenomena in many of the BH candidates, it is therefore important to observe the radiation that is coming out from these disk-jet systems, in different EM wave bands, i.e., from γ -rays to radio signals.

Among all the models which are present in the literature which deal with the structure and spectral properties of disk/jet systems, we find that the Two Component Advective Flow (TCAF) model is the most promising one to explain most of the X-ray features. In TCAF, the sub-Keplerian flow encounters a centrifugal barrier and forms a standing or oscillating shock. The post-shock region is termed as the CENBOL or CENTrifugal pressure supported BOundary Layer. Depending on the physical parameters, a shock may be oscillating in nature or it may even be absent. The oscillation of the shock may give rise to the temporal variability in the form of Quasi-Periodic Oscillations (QPOs) which are observed in many of the BH candidates. The CENBOL also acts like a virtual boundary layer of a black hole. It is the ‘power house’ of ‘hot’ electrons which intercepts soft Keplerian photons and reprocesses them to hard X-rays.

In the thesis, we present the observational results of spectral and timing properties of accretion flows around galactic black holes (GRS 1915+105 and SS 433).

In Chapter 1, we present a brief discussion about the compact objects, specially galactic black holes which may be present in X-ray binary system. We briefly present the X-ray astronomy missions which are the backbone of X-ray observations. We give an account on various models of accretion onto compact objects, starting from the Bondi accretion to TCAF paradigm and also give some order of magnitude calculation to show that accretion processes can explain the observed luminosities, temperatures etc. of the compact objects.

In Chapter 2, we present the data acquisition and analysis techniques in detail. We also discuss about the detector components of *RXTE* and *IXAE* X-ray telescopes. For spectral and timing analysis of X-ray data that are obtained with *RXTE*, we use the software HEASOFT consisting of FTOOLS and XSPEC packages, supported by NASA's HEASARC.

In Chapter 3, we analyze the X-ray data of the black hole (BH) candidate GRS 1915+105 which exhibits a rich variety of X-ray variabilities (light curves) (12 distinct classes) with QPOs ranging from ~ 0.001 Hz to ~ 67 Hz. In the light of the TCAF paradigm, we propose that five fundamental states of accretion/outflow configurations can explain most of the observed light curves. Theoretical understanding of the mass outflow from CENBOL has been verified by detailed spectral studies of X-ray data of GRS 1915+105. We also discuss about inner disk evacuation phenomenon (that causes huge radio flares) that is associated with X-ray dips (θ and β class) in X-ray light curves of GRS 1915+105.

In Chapter 4, we present results from Multi-wavelength campaign on September 2002 of SS 433 and find the photometric evidence of 'bullet-like' features in the system. We also carry out detailed spectral and timing analysis of *RXTE* data of SS 433 and find that the base of the jet is the major X-ray source, the identified iron lines in the spectrum satisfy the prediction of 'kinematic model' and the lack of both QPOs and Keplerian disk signature. All these properties can be well explained with the ideas that underlie in TCAF paradigm.

In Chapter 5, we studied the motion of magnetic flux tubes inside an accretion disk and find that the magnetic tension is the strongest force in a hot plasma (i.e., CENBOL) of proton temperature $\geq 10^{10}$ K. As a result, the magnetic flux tubes entering in this region collapse catastrophically, thereby occasionally evacuating the inner disk which causes huge radio flares. Matter is squeezed out of the disk in the form of jets. Such blobby jets may have been observed in SS 433, GRS 1915+105 etc. We estimate the mass of the ejecta which agrees with observations. We also discuss some other plausible mechanisms to produce 'bullet-like' ejections in SS 433.

In Chapter 6, we draw our conclusions.

ACKNOWLEDGMENTS

With great pleasure, I express my sincerest gratitude to my supervisor Professor Sandip K. Chakrabarti for his inspiring guidance, constant support and immense patience throughout the years of my Ph. D. period. I am grateful to him for setting ambitious goals and helping me find my own way to achieve them.

It is my pleasure to thank all the academic and non-academic staff of the S. N. Bose National Centre for Basic Sciences (SNBNCBS) for their enthusiastic support during my studies here. I thank Prof. S. Dattagupta, Director, SNBNCBS for giving me the opportunity to work here. My sincerest greetings goes to Prof. A. R. Rao of Tata Institute of Fundamental Research (TIFR), Mumbai, for helping me with his expertise in X-ray astronomy data analysis and related things. I am thankful to Dr. Tomaso Belloni of INAF, Mirate, Italy and Dr. Paolo Goldoni of CEA Saclay, France for their kind collaboration and fruitful discussions. I am also thankful to Dr. Santosh Vadawale and Dr. Sivkumar G. Manickam for their kind collaboration during their Ph. D. period. I would like to acknowledge the organizer of 4th Microquasar workshop for giving me the opportunity to attend the conference at Corsica. I would also like to acknowledge Abdus Salam International Centre for Theoretical Physics, Trieste, Italy, for giving me opportunity to participate in the Summer School on Astroparticle Physics in summer 2002. I would also acknowledge the Centre for Space Physics (CSP), Kolkata for providing a broad platform of 'astronomy & astrophysics', where I had spent many many sessions, attending seminars and delivering lectures.

My heartiest thanks goes to my friends and colleagues in SNBNCBS, with whom I have shared my stay in S. N. Bose. In this regard, I don't like to mention anybody's name, as because the 'unforgettable' moments that I have shared with them, I would like to keep in my memory forever. But I must mention the name of Dr. Indranil Chattopadhyay and Dr. Subhradip Ghosh, with whom I have shared moments of various shades.

I should thank all my colleagues, past and present, in the astrophysics group of S. N. Bose. Specially I would like to mention the name of Mr. Santabrata Das (Santa) whose friendly behavior, fruitful suggestions and strong help drove me to carry out my work. Among the others, I must mention the name of Mr. Samir Mandal, Mr. Kinsuk Acharyaa and Mr. Sabyasachi Pal of Centre for Space Physics, with whom

I had fruitful discussions on various aspects of astronomy and astrophysics.

Last but not the least I would like to acknowledge 'myself', without whose un-failing inner motivation this work could not have been completed.

PUBLICATIONS IN REFEREED JOURNALS

1. *Classification of light curves of the BH candidate GRS1915+105*, by Anuj Nandi, Sivkumar G. Manickam and Sandip K. Chakrabarti, in *Ind. J. Physics*, **74B(5)**, 331 (2000).
2. *On the source of quasi-periodic oscillations of the black hole candidate GRS1915+105: some new observations and their interpretations*, by Anuj Nandi Sivkumar G. Manickam, A. R. Rao and Sandip K. Chakrabarti, in *Mon. Not. Royal Astro. Society*, **324**, 267 (2001).
3. *Fundamental states of accretion/jet configuration and BH candidate GRS1915+105*, by Sandip K. Chakrabarti and Anuj Nandi, in *Ind. J. Physics*, **75B(1)**, 1 (2001).
4. *Observational evidence for mass ejection during soft X-ray dips in GRS1915+105*, by S. V. Vadawale, A. R. Rao, A. Nandi and S. K. Chakrabarti, in *Astron. Astrophys.*, **370**, 17L (2001).
5. *Computation of Outflow Rates from Accretion Disks Around Black Holes*, by Santabrata Das, Indranil Chattopadhyay, Anuj Nandi and Sandip K. Chakrabarti, in *Astron. Astrophys.*, **379**, 683 (2001).
6. *Ejection of inner accretion disk in GRS1915+105: The magnetic rubber-band effect*, by A. Nandi, S. K. Chakrabarti, S. V. Vadawale and A. R. Rao, in *Astron. Astrophys.*, **380**, 245 (2001).
7. *On the Ejection Mechanism of Bullets in SS 433*, by Sandip K. Chakrabarti, P. Goldoni, Paul J. Witt, A. Nandi and S. Das, in *ApJ*, **576**, 45L (2002).
8. *Spectral Signature of Mass Loss from (and Mass Gain by) an Accretion Disk around a Black Hole*, by Sandip K. Chakrabarti, Anuj Nandi, S. G. Manickam, S. Mandal and A. R. Rao, in *ApJ*, **579**, 21L (2002).
9. *Possible Photometric Evidence of Ejection of Bullet-like Features in the Relativistic Jet Sources SS 433*, by Sandip K. Chakrabarti, S.

- Pal, Anuj Nandi, B. G. Anandarao and Soumen Mondal, in *ApJ*, **595**, 45L (2003).
10. ***Evidence of Class Transitions in GRS 1915+105 from IXAE Data***, by Sandip K. Chakrabarti, Anuj Nandi, Asit Choudhury and Utpal Chatterjee, in *ApJ*, **607**, 406 (2004).
 11. ***X-ray Observation of SS 433 with RXTE***, by A. Nandi, Sandip K. Chakrabarti, Tomaso Belloni and P. Goldoni, in *MNRAS*, (in press) (2005).
 12. ***Class Transitions and Two Component Accretion Flow in GRS 1915+105***, by Sandip K. Chakrabarti, Anuj Nandi, A. K. Chatterjee, K.Choudhury, U.Chatterjee, in *Astron. Astrophys.*, **431**, 825 (2005).
 13. ***SS 433: Results of a Recent Multi-wavelength Campaign***, by Sandip K. Chakrabarti, B.G. Anandarao, S. Pal, Soumen Mondal, A. Nandi, A. Bhattacharyya, Samir Mandal, Ram Sagar, J. C. Pandey, A. Pati, S.K. Saha, in *MNRAS*, (submitted) (2005).

Contents

1	INTRODUCTION	1
1.1	Compact objects: What are they?	3
1.1.1	X-ray binaries	5
1.1.2	Mass function	7
1.2	X-ray Astronomy Missions	9
1.3	Radiative Processes in BH Astrophysics	13
1.3.1	Thermal emission	13
1.3.2	Non-thermal emission	16
1.4	Accretion Process	18
1.4.1	General considerations	18
1.4.2	Temperature of compact X-ray binaries	20
1.5	Structure of the accreting material	21
1.5.1	Gas dynamics	21
1.5.2	Steady, spherically symmetric accretion: Bondi Flow	23
1.5.3	Disk accretion: Keplerian/sub-Keplerian Flow	24
1.5.4	Advective accretion disk: Two Component Advective Flow (TCAF)	26
2	DATA ACQUISITION AND ANALYSIS	30
2.1	Data acquisition	30
2.1.1	All-Sky Monitor (ASM)	31
2.1.2	Proportional Counter Array (PCA)	31
2.1.3	High Energy X-ray Timing Experiment (HEXTE)	33
2.1.4	Data mode and Screening Criteria	33
2.2	Analysis	34
2.2.1	Timing Analysis	34
2.2.2	Spectral Analysis	37
2.3	Indian X-ray Astronomy Experiment (IXAE)	39
2.4	Observations in Infrared and Radio bands	40

3	GRS 1915+105: A FASCINATING ASTROPHYSICAL SOURCE	41
3.1	GRS 1915+105: A Galactic Microquasar	41
3.2	X-ray variabilities in GRS 1915+105	44
3.2.1	Classification of X-ray variabilities of GRS 1915+105	44
3.2.2	Advective flow paradigm and GRS 1915+105	49
3.2.3	Splitting of Peaks in Intermediate Class and related timing properties	53
3.3	Evidence of Class transitions in IXAE data	59
3.4	Spectral variabilities in GRS 1915+105	62
3.4.1	Spectral signature of Outflows from CENBOL: A theoretical study	63
3.4.2	Evidence for winds/outflows in the spectra of GRS 1915+105	65
3.4.3	Inner disk disappearance in GRS 1915+105: Spectral study .	69
4	SS 433: ENIGMA OF THE PAST CENTURY	73
4.1	The Black Hole Candidate SS 433	73
4.2	Photometric evidence of ejection of ‘bullet-like’ features	82
4.2.1	Results on short time-scale variabilities	84
4.2.2	X-ray and radio flares in support of the bullet-like features . .	85
4.3	X-ray observation of SS 433 with <i>RXTE</i>	87
4.3.1	Temporal features of SS 433 in different phases	89
4.3.2	Spectral fits of <i>RXTE</i> observation of SS 433	93
4.4	X-ray Flares in SS 433?	100
5	OUTFLOWS AND JETS IN MICROQUASARS	102
5.1	Outflows and Jets in Black Holes	102
5.2	The magnetized TCAF model for matter ejection	103
5.2.1	Basic assumptions	103
5.2.2	Governing equation of motion of the flux tubes	104
5.2.3	Estimation of the ejected mass from the inner accretion disk of GRS 1915+105	109
5.3	Ejection mechanism of bullets in SS 433	111

5.3.1	Cooling of the base of the jet by Comptonisation and separation of blobs	113
5.3.2	Resonance oscillation of accretion shocks in the presence of bremsstrahlung cooling	114
5.3.3	Nonsteady and nonlinear shock oscillation	114
5.3.4	Magnetic rubber-band effect	116
6	CONCLUSIONS AND DISCUSSIONS	118

List of Figures

- 1.1 Artists' conception of X-ray binary system which includes a black hole with its companion star from where matter is stripped off and transferred via Roche lobe overflow into an accretion disk around the hole. A torus of material is shown spiraling onto the black hole. This torus is the hot inner region of the accretion disk, wherefrom most of the X-rays are produced (courtesy: NASA). 6
- 1.2 Schematic representation of a X-ray binary system. Left one (a) shows the binary system (in centre of mass frame) with the components of the donor (normal star of mass M_d) and the compact object (black hole of mass M_c). Right-sided figure (b) represents the general position of the binary system in the plain of the sky. 8
- 1.3 The discovery observation (i.e., first discovery of extrasolar X-ray source), obtained by Aerobee rocket carrying Geiger counters which detected large X-ray flux near 195 degree azimuth in the direction of the constellation Scorpius (From Giacconi et al. 1962). 11
- 1.4 Schematic diagram of an unmagnetized TCAF model with all its components. The entire flow is a combination of Keplerian and sub-Keplerian flow. Compact object is surrounded by CENBOL, which is the power house of 'hot' electrons and hard X-rays are produced form it. Jets/Outflows are also originated form the CENBOL. 28

- 2.1 All Sky Monitor (ASM) light curves of X-ray novae GRO J1655-40. Figure shows that the source has undergone two major outbursts since its discovery in 1994 July. This double-peaked (broad) profile is quite unlike compare to other BH candidates. During first peak in 1996, the source exhibited strong flaring activity with non-thermal emission. In 1997 (second peak), the source spectrum was soft in nature and thermal except at the end of the outburst where the spectrum was hard. After 1997, the source goes beyond the detection level of ASM. 32
- 2.2 A typical X-ray light curves of a black hole candidate GRS 1915+105. The light curve is binned at 1 sec time resolution. Flux variation (photon counts/sec) is highly quasi-periodic in nature. 36
- 2.3 Power Density Spectra (PDS) which are generated for the same light curve (Fig. 2.2) of GRS 1915+105. The left-sided PDS shows the low frequency QPO (~ 0.02 Hz) along with the ‘broad power peak’ around ~ 0.2 Hz, whereas right-sided PDS is drawn to show the high frequency QPO (~ 7 Hz). 36
- 3.1 X-ray variabilities of GRS 1915+105 are classified in 12 classes (model-independent way) and their color-color diagram (HR1 \sim HR2) shows three basic states (A, B and C) with observed transitions. This figure is adopted from Belloni et al. (2000). 45
- 3.2 All possible light curves of the black hole candidate GRS 1915+105 (left panel). Along X-axis is time in seconds and along Y-axis is photon counts/sec (rate) in units of 10^3 . In right panel, ‘softness ratio’ A/C vs B/C is plotted for all the 12 classes shown in left panel. A, B and C are photon counts within intervals (0-3) keV, (3-17) keV and (17-60) keV respectively. Panel 1 belongs to Class-H, Panels (10-12) belong to Class-S, Panels (8-9) belong to Class-SS and the rest (Panels 2-7) belong to Class-I (see, text for details in section §3.2.1). 48
- 3.3 Schematic diagram of five possible fundamental modes of accretion -wind configuration. GRS 1915+105 stays most of the time in state HW, and moves CC and EA to form various classes of X-ray light curves. In parenthesis, we mark A, B and C to identify conjectured States of Belloni et al. (2000). The State H and State S represent canonical hard and soft states (see, text for details in section §3.2.2). The last Figure (f) shows variation the of the ratio of outflow to inflow rates as a function of compression ratio (R) (Chakrabarti, 1999). 51

- 3.4 Subdivisions of a quasi-repetitive structure of the light curve of Oct. 15th 1996 (ν class). Relatively hard radiations are emitted in the region marked Off (PDS shows strong QPO) with relatively lower count rates. There are typically two major peaks, P1 followed by P2. 55
- 3.5 Four panels showing light curves of a part of the observation on Oct. 15th 1996 (ν class) at different channels (energies are marked). Note that ratio of photon counts in P1 and P2 tends to become unity at higher energies. 56
- 3.6 Four panels showing light curves of a part of the observation on June 22nd, 1997 (ρ class) at different channels (energies are marked). . . . 56
- 3.7 Power Density Spectra (PDS) of three regions (left-sided) marked in Fig. 3.4 of the ν class. Several data segments have been added to improve statistics. Right-sided PDS shows three regions (marked as Fig. 3.4) of ρ class (Fig. 3.6). Note the absence of QPOs in P2 in both PDS. 57
- 3.8 A part of the light curve from the κ class is shown. Upper four panels are from *RXTE* and the lower two panels are from *IXAE* data. A small arrow indicates a ρ type burst. Presence of mini- ρ bursts within a κ class (in On states) indicates that ρ may be the *fundamental* type of all burst. 57
- 3.9 A part of the light curve from the so-called κ class is shown. In On⁺⁺ state, two dotted boxes are drawn and below the PDS of each box is plotted. Note the presence of QPO in lower box, which are nothing but mini-off states corresponding to mini- ρ bursts. 58
- 3.10 2 – 18 keV light curves as observed by *IXAE* (upper panel) and mean photon spectral index s_ϕ (lower panel) in 1st, 3rd and 5th orbits of June 22nd, 1997. GRS 1915+105 was (a) in the κ class, (b) in an unknown class and (c) went to the ρ class on that day. Lower panels show how s_ϕ distinctly change. Specifically it is noisy during transition. 61

- 3.11 Class transition as seen from *IXAE* and *RXTE* observations on the 8th of June, 1999 in two successive orbits (marked). *RXTE* photon counts are divided by 50 and shifted upward by 200 cts/sec for comparison. In (a), there was no significant variation in light curve or spectral index. GRS 1915+105 was in a class similar to χ but the counts were a factor of 10-20 times higher. There is a gap of 44 min. in the two *RXTE* data presented in (a) and (b). In (b), the source is distinctly in θ class. *RXTE* data is less noisy than the *IXAE* data because of higher counts. It was binned in 2 – 6 keV and 6 – 15 keV before computing s_ϕ in order that comparison with *IXAE* could be made (for details, see Chakrabarti et al. 2005). 61
- 3.12 Cartoon diagrams of the accretion disk near a black hole that includes a boundary layer (surface of the CENBOL). Panel (a) shows the ‘Off’ state where the outflow material fills up the region to the sonic point R_c . Panel (b) shows cases with prominent ‘On’ states where the material in the subsonic region cools and falls back on the CENBOL and takes time to drain. 64
- 3.13 Typical nature of calculated spectra (uncorrected for absorption) for Off and On states (*solid curves*) and low/hard and high/soft states (*dotted curves*). In the Off state, the spectrum appears to be softened with respect to low/hard state, and in On state, the spectrum appears to be hardened with respect to high/soft state. As a result, the pivoting point shifts toward higher energy. 65
- 3.14 Unfolded *RXTE*/PCA spectra of GRS 1915+105 obtained during the low/hard and high/soft states compared with Off and On states spectra during the irregular bursts observed on (a) 1997 June 18, (b) 1997 July 10. The histogram shows the fitted model. During the Off/On transitions, the pivoting occurs at a higher energy. 66
- 3.15 Same as Fig. 3.14, except that the observation ID of the On/Off and low states are chosen close to 1997 October 31 when IR/Radio flares were observed (Dhawan et al. 2000). The spectral slope variations are also seen on this days. 68

- 3.16 The simultaneous observation of GRS 1915+105 in Radio, infrared and X-rays on 1997 September 9. The X-ray light curve belongs to β class of Belloni et al. (2000). The infrared flare starts during the recovery from the hard X-ray dips, when a sharp, isolated X-ray spike is observed. These observations also show that there is anti-correlation between the hard X-rays and Radio emissions, suggesting that during huge radio flares, the inner part of the accretion disk is evacuated in the form of jets. This Figure is adopted from Mirabel & Rodriguez (1999) (MR99). 70
- 3.17 X-ray light curve (θ class) (top panel) and hardness ratio (HR1: 6–15 keV/2 – 6 keV) (bottom panel) of GRS 1915+105 obtained on 1999 June 8 using *RXTE*/PCA. The region chosen for proving the assertion of inner disk disappearance are shown in top panel, separated by dotted lines (see, Vadawale et al. 2001). The bottom panel shows that the hard X-rays are strongly reduced during the ‘soft dips’ in the light curve. 71
- 4.1 Upper panel shows Very Large Array (VLA) continuum mosaic of W50 at 1.5 GHz (Dubner et al. 1998). The radio counterpart of SS 433 is the bright unresolved source at the centre of the image. The lateral E-W extension of the SNR over $\sim 1^\circ$ (~ 50 pc) is caused by the injection of the relativistic jets from SS 433. The lower figure shows the optical spectrum of SS 433 obtained on 1979 March 20 with the Lick Observatory 3 m Shane reflector (Margon et al. 1979). The principle emission features are identified along with the blue and red shifted lines in the system. 74
- 4.2 A compilation of optical spectra of SS 433 obtained with a 5 month period from Lick Observatory. The principle $H\alpha$ line is fixed. The periodic motion, in opposite directions, of the blue and red moving lines is clear. 76
- 4.3 VLA maps of SS 433 produced over a 4 month period showing the growth of the radio lobes as predicted by the *corkscrew* motion of the precessing relativistic jets in the kinematic model (Hjellming & Johnston, 1981a; 1981b). 78

- 4.4 Schematic representation of kinematic model of SS 433 (see, section §4.1 for different notations). Figure shows the almost narrow beam (one-sided jet in the direction of OP) emanating along the rotation axis of an accretion disk which precesses with an angular velocity ω (jets precess with 164 day period). 81
- 4.5 The variation of Doppler shifts (z) with the precessional phase (ψ). Red and blue curves correspond to Doppler shifted values of the moving emission lines that are originated from the receding (red jet) and approaching (blue jet) jets respectively. The average velocity of the moving lines is about $12000 \text{ km sec}^{-1}$ which is almost constant and it is marked as dashed line ($z=0.034$). 82
- 4.6 Multi-wavelength observation of short time variability in SS 433 by radio (top), IR (middle) and X-ray (bottom) on 2002 September 27. The observations were made at the *GMRT*, Pune, at 1.28 GHz (radio), 1.2 m Mt. Abu infrared telescope at *J*, *H* and *K'* bands and with the *RXTE* satellite (2 – 20 keV), respectively. 83
- 4.7 Observations in Fig. 4.6 are plotted around the mean taken in each spell of observation. Considerable variations at a time scale of a few minutes are observed. (for details, see Chakrabarti et al. 2003). . . . 83
- 4.8 Differential photometry of SS 433 with respect to the two brightest standard stars (std1 and std2) in the same frame of object is plotted. Different curves are marked on the top right corner in each panel. The error bar for each individual differential measurement is also shown. Differential flux variation of SS 433 is above the 2σ level in comparison with that of standards. 86
- 4.9 Individual flares in very short timescales are caught. (a) A radio flare lasting 2.5 minutes (observed on 2002 September 29) and (b) an X-ray flare (observed on 2002 September 27) lasting for about 3.5 minutes. Each bin size is 16 sec. 86

- 4.10 The picture above is a soft X-ray image of the SNR W50/SS 433 system taken with the *ROSAT* X-ray observatory. SS 433, the compact object is seen as the black object at the center of the image along with the two prominent X-ray jets that are oppositely directed from the central object. The material in the jet on the left is speeding towards the Earth, while the jet on the right is directed away from the Earth. Image also shows the large scale diffuse X-ray emission produced by the supernova remnant (SNR), which surrounds the compact object, SS 433 (Courtesy: NASA). 88
- 4.11 X-ray light curves (background subtracted) extracted from **Standard-2** data of SS 433 for observations G, H, I, K and L (marked). Along X-axis is time (in seconds) and along Y-axis is photon counts/sec (rate). Short time-scale variabilities are observed (see, panel K and L). 91
- 4.12 Unfolded X-ray spectrum of SS 433 with different model components on (a) Obs. G on 27th September 2002, (b) Obs. I on 2nd of October 2003 (inferior conjunction) and (c) Obs. K on 13th of March 2004 (superior conjunction). While in (a), the precession/orbital phases were generic (see Table 4.1), in (b), the phases were very close to zero when the companion blocked the central object and in (c), the precession phase is close to zero but the orbital phase is close to 0.5. The model components are: thermal bremsstrahlung (solid histogram) and two Fe lines (dashed and long dash-dotted curves). In lower panels, residuals have also been shown. 95
- 4.13 Two parameter confidence region of the broad FeXXVI (a) line energy vs. Gaussian width and (b) line flux vs. Gaussian width from spectral fitting to the *RXTE*/PCA data of Obs. C. Contours correspond to 68%, 90% and 99% confidence. 97
- 4.14 Two parameter confidence region of the broad FeXXVI (a) line energy vs. Gaussian width and (b) line flux vs. Gaussian width from spectral fitting to the *RXTE*/PCA data of Obs. C. Contours correspond to 68%, 90% and 99% confidence. 97

- 4.15 Observed Doppler shifts (y-axis) of (a) FeXXVI and (b) FeXXV lines from the approaching (solid curve) and receding (dotted curve) jets super-imposed on the prediction from the ‘kinematic model’ with standard parameters (see, §4.1) as a function of the precessional phase ψ . Also shown in short-dashed and long-dashed curves the shifts obtained by respectively reducing and enhancing the jet velocity by ten percent. The horizontal curves represent intrinsic red-shifts for the corresponding jet velocities. See §4.3.2 for detailed criteria used in line-identifications. All the observations were plotted against the same precessional phase for clarity of the plot of the lines. 99
- 4.16 (a) ASM counts/s of SS 433 since 1996 till Oct. 26th, 2004. For clarity, we plotted only those points when the count over the background rate is positive. We superpose (with a shift of 2/sec along y-axis) the mean light-curve when folded around 368 days to show the periodic nature of a strong flare which repeats after every 368 days interval (This could be an artefact of the ASM observation). (b) Average ASM light curve obtained by folding around 368 days showing the presence of the strong flare. 100
- 5.1 A cartoon diagram of the accretion disk near a black hole which includes a shock (r_s), a sub-Keplerian and a Keplerian disk with a boundary at r_{tr} . Stochastic magnetic fields are sheared and amplified as they leave a Keplerian disk. In a hot, sub-Keplerian flow, these toroidal flux tubes catastrophically collapse squirting matter along the axis, and thereby evacuating the disk and producing outflows/jets. Dashed curves show typical trajectories (see, CD94 for details). . . . 105

- 5.2 Schematic representation of the bullet separations in SS 433 are shown. (a) The base of the jet is cooled down by soft photons from a Keplerian disk and it is detached when it becomes supersonic. (b) Resonance oscillation of the sub-Keplerian region due to the near matching of the infall time with the cooling time produces discrete ejecta during the phase when centrifugal barrier contracts. (c) Nonsteady motion of the centrifugal barrier due to the inability of the flow to find a steady shock solution. (d) Magnetic tension from toroidal flux tubes (shown as shaded narrow tori) causes them to collapse catastrophically in a hot ambient medium in rapid succession, which evacuates the centrifugal barrier. The recurrence time of (a) is the viscous timescale in the inner part of the disk, ~ 10 sec; (b-c) is ~ 50 sec; and (d) is random and dictated by the enhanced magnetic activity. 115

Chapter 1

INTRODUCTION

“You see but you do not observe.....

*It is a capital mistake to theorize
before one has data”*

–Sir Arthur Conan Doyle,
Scandal in Bohemia

As a science, *astronomy* which etymologically means “measurement of stars” (from greek), has a long history. It involves the observation of celestial objects along with the motions of planets, stars etc. and their luminosities, brightness, colors etc. It also includes the observation of strange and exotic objects and events, such as pulsating stars, variable X-ray sources, supernovae, compact objects (e.g. white dwarfs, neutron stars, black holes), Gamma Ray Bursts (GRBs), Active Galactic Nuclei (AGNs), Quasars and the universe as a whole.

Astrophysics, on the other hand is a very young science. And it is the discipline that seeks to explain all sorts of observational phenomena observed by the astronomers in physical terms. Thus *astrophysics* is a means of using physical laws learned in the earth-laboratory to study the celestial objects/phenomena in cosmology and to extract the new physics if it is there.

But, now-a-days there is no such distinct difference between *astronomy* and *astrophysics* and it almost becomes a single word “Astronomy & Astrophysics” which can be phrased as “.....*search for physical causes of observational phenomena*”. Rapid advances in this particular subject over the past several decades have been made possible because of advances in our understanding of fundamental physics and improvement in the equipments like telescopes (ground based as well as space-

borne), remote sensing systems, computers etc., we use to study the cosmos. With the advent of modern technology and space-age, the space-borne telescopes i.e., satellites are capable of seeing the objects in γ -rays, X-rays, Ultraviolet (UV) and Infrared (IR) radiations and thus focus has been intensified to understand the physical processes which are going on around or inside the objects. Also the sophisticated ground-based telescopes are used as an effective tool for capturing the optical and radio signals which are coming out from the same source.

The goal of the thesis is to study the spectral and timing properties, mostly in X-rays, of accretion flows around black holes. This has been investigated by analyzing the observational data from the space-borne X-ray telescopes. Depending on the telescope's detectors characteristics, we analyze data in different modes to understand different physical mechanisms which are going on around the compact objects. In this context, we have used the observational data from NASA's *Rossini X-ray Timing Explorer (RXTE)* mission and India's *Indian X-ray Astronomy Experiment (IXAE)* payload on-board IRS-P3. Apart from the X-ray scan of the compact objects, we have also presented the infrared and radio observational results using Mt. Abu's *Infrared Telescope* and NCRA's *Giant Metrewave Radio Telescope (GMRT)* to find out correlations between different wave bands. We have also carried out some theoretical work to understand the observed phenomena: mass outflow, inner disk evacuation (i.e., jet formation), bullet like ejections etc. that are associated with accretion disk around the compact objects. In this work, we have mainly focused on the galactic black hole candidates GRS 1915+105 and SS 433.

In this introductory Chapter, we first discuss about compact objects (white dwarfs, neutron stars and black holes) and their distinguishing features from theoretical point of view as well as from observational point of view. In §1.2, we present a brief report of the X-ray astronomy missions. Since 1949 to the present era how it develops and strengthen our views about the X-ray observation of compact objects, are discussed in detail. In §1.3, we write different radiative processes and knowledge of these processes are essential to explain most of the observed X-ray features. In §1.4, we present the general overview of accretion processes and discuss its implication to calculate luminosity, temperature, mass of the compact objects etc. Finally, we discuss about the development of accretion processes around the compact objects, specially around the black holes.

1.1 Compact objects: What are they?

Compact objects (stars) - *white dwarfs*, *neutron stars* and *black holes* - are the end products of stellar evolution. The process of evolution of a star ends with fueling out of most of its nuclear energy and the formation of the three distinct species of compact objects basically depends on the nature of the progenitor star, particularly star's mass.

The simplest evolution is the end point of a low mass star of mass $M \leq 7M_{\odot}$ to become one kind of compact object is *white dwarf*, in which the internal pressure support is provided by the electron degeneracy pressure. A typical white dwarf is half as massive as the Sun, yet only slightly bigger than the Earth. This makes a white dwarf very compact and they have average density in the range of $10^5 - 10^6$ gm cm⁻³ in which electron gas is completely degenerate except in outer layers whose total thickness is very small compared to the radius of the star itself. The higher the mass of the star, the smaller is the size. There is an upper limit of the mass of a white dwarf, the *Chandrasekhar limit* (about 1.44 times the mass of the Sun), after which the pressure of the electrons is no longer able to balance gravity, and the star continues to contract, eventually forming a *neutron star*. White dwarf stars are extremely hot ($\sim 10^6$ K), therefore the radiation emitted from the inner surface of the stars should be in the range of EUV to soft X-rays radiations. In 1862, the American optician Alvan Graham Clark discovered a less intense companion of the brightest star Sirius. Later, this companion was identified to be a white dwarf, called Sirius B and it is the binary counterpart of the brightest star Sirius A. Calculation suggests that Sirius B has a mass of about $1.05 \pm 0.03M_{\odot}$, a low luminosity of about $3 \times 10^{-3}L_{\odot}$ and high surface temperature of about 29,500 K which confirm the true compact nature of Sirius B. As the astronomy missions were carried out, many many white dwarfs have been detected in our own galaxy as a source of soft X-rays and EUV radiations which enables the physicist to study the structure and composition of the thin layers of these stars and also the internal nature of the core to some extent.

The possible end point of stellar evolution of a massive star of mass $M \geq 7M_{\odot}$ is a *neutron star*. It can be formed in a Type II supernova explosion as the remnant of the gravitational collapse of the massive star core. In the neutron star case, internal pressure support is provided by neutron degeneracy pressure. Neutron stars are very compact indeed, having masses of about mass of the sun and radii of about 10 km, which yield a density of its core material of the order of 10^{14} gm cm⁻³. It has also an upper mass limit, known as the *Tollman-Oppenheimer-Volkoff limit*

(about 3 times the mass of the Sun). Once this limit is reached by accreting more mass onto a neutron star, no further equilibrium is possible. The internal pressure (i.e., neutron degeneracy pressure) is insufficient to counterbalance the gravity and a catastrophic gravitational collapse sets in, further increasing the gravity on a time scale of milliseconds. The escape velocity at the surface, which was already $1/3$ of the speed of light for a neutron star, quickly reaches the velocity of light (c). A stage is reached wherefrom nothing, neither matter nor light, can escape and thus a *black hole* is formed.

Neutron stars are found in nature in two ways. In the first, the source is known as radio pulsars, which are rotating, magnetized neutron stars. These are observed to emit very intense pulses of radio emission once per rotation period (period lies between minute to milliseconds). In the second case, the neutron stars are found in binary X-ray sources, in which X-rays are produced by matter falling from companion onto the neutron star, a process known as *accretion*. In 1967, the first neutron star as a *pulsar* was discovered by Anthony Hewish and his co-workers, notably, Miss Jocelyn Bell Burnell at Cambridge, England. The Hewish group found strong radio pulses occurring at a regular rate, once in every 1.337 sec, which is coming from a particular direction and later the source is denoted as PSR 1919+21. To date, the total detected pulsars are more than 500. Recently pulsars have also been detected in other galaxies (LMC, SMC) which are sister galaxies of our own Milky way.

Another class of neutron stars with strong magnetic field of around $\sim 10^{15}$ Gauss has been discovered in the recent past years. Such highly magnetized neutron stars are called *magnetars*.

The third and the final possibility of forming a compact object with maximum compactness is a *black hole*. Black hole is such a compact object that the attractive force of gravity becomes so strong that no physical force can prevent collapse to a physical singularity and electromagnetic radiation cannot escape from it.

There are several other ways to form a black hole. Modern astrophysics considers four types of black holes in the universe: a) Galactic Black Holes (GBHs) of stellar masses ($3M_{\odot} \leq M_{BH} \leq 20M_{\odot}$), which were born when massive stars fueled out its nuclear energy or a neutron star crosses its upper mass limit and undergoes a supernova explosion, b) Supermassive Black Holes (SMBHs), with masses ranges from $\sim 10^6 M_{\odot} - 10^9 M_{\odot}$ at the centre of galaxies, c) Intermediate Mass Black Holes (IMBHs), with masses ranges from $\sim 10^2 M_{\odot} - 10^5 M_{\odot}$, which are classified as a new class of black holes due to their ultra-luminous X-ray activity and d) Primordial Black Holes (PBHs) which might appear from the large-scale inhomogeneities at

the very beginning of expansion of the Universe. Their masses can be arbitrary, but primordial black holes with $M_{BH} \leq 10^{15}$ gm will have radiated away their mass by the quantum process, known as the *Hawking radiation*, in a time $t \leq 10^{10}$ years (\sim age of the Universe). Only primordial black holes with mass $M_{BH} \geq 10^{15}$ gm could exist in the contemporary Universe. For detailed and deep discussion on compact objects, one could go through the excellent book written by Shapiro & Teukolsky (1983).

As this thesis work is based on timing and spectral properties of galactic black holes, i.e., first category black holes, I will discuss here a little more about the GBHs. These GBHs are mostly found in X-ray binary systems.

1.1.1 X-ray binaries

More than 50% of all the stars in our vicinity belong to binary systems. X-ray binaries are a class of binary system that are basically very luminous in X-rays. The X-rays are produced by infalling matter which releases immense gravitational potential energy, from one component (a relatively normal star) to the other component which is basically a compact object (a white dwarf, neutron star, or black hole). Figure (1.1) displays an artist's conception of X-ray binary system which includes a compact object (black hole) with its companion star from where matter is stripped off and transferred via Roche lobe overflow into an accretion disk around the hole. X-ray binaries were discovered by rocket flights in 1960s. Depending on the evolution process of the normal stars, X-ray binaries can be subdivided in two basic categories: Low Mass X-ray Binary (LMXB) and High Mass X-ray Binary (HMXB). On the other hand, both of these two categories can be termed as 'microquasars' (named after quasars, as these objects have some common features with quasars but all the physical properties associated with these system are simply the scale down version of quasars) if these X-ray binaries have the relativistic jets. My thesis work is based on the studies of two X-ray binaries (GRS 1915+105 and SS 433) which are well known 'microquasars'.

a) Low Mass X-ray Binary (LMXB):

Low Mass X-ray Binaries (LMXB) are binary stars where one of the components (primary one) is a black hole or a neutron star. The other component (donor) is filling its Roche lobe and therefore transfers mass to the compact object. The donor is less massive than the compact object (black hole), and usually on the main sequence having mass of about $1 M_{\odot}$. A typical LMXB emits almost all of its radiation in X-rays which is originated from the accretion disk around the compact



Figure 1.1: Artists' conception of X-ray binary system which includes a black hole with its companion star from where matter is stripped off and transferred via Roche lobe overflow into an accretion disk around the hole. A torus of material is shown spiraling onto the black hole. This torus is the hot inner region of the accretion disk, wherefrom most of the X-rays are produced (courtesy: NASA).

objects. Therefore, these objects are very bright in X-rays but are rather faint optically. GRS 1915+105 is a well studied LMXB system having a low mass donor ($1.2 M_{\odot}$) with a black hole of mass $14 \pm 4 M_{\odot}$.

b) **High Mass X-ray Binary (HMXB):**

In High Mass X-ray Binary (HMXB) system, one of the components is a neutron star or a black hole and other one (donor) is a massive star, usually a Be star or an evolved type, supergiant star. The donor mass ($\sim 10 M_{\odot}$) of HMXB system is much higher compared to LMXB. A fraction of the stellar wind from the donor is captured by the compact object (black hole), and produces X-rays as it falls onto the compact object. In HMXB, the massive star dominates the emission of optical light and therefore easy to detect. One of the most famous HMXB is Cygnus X-1 (often abbreviated to Cyg X-1) which was the first stellar-mass black hole discovered (Giacconi et al. 1962). The binary counterpart of Cyg X-1 is a variable optical star (HDE 226868) of magnitude 8.9. This binary system consists of high mass donor (O9-B0 supergiant) of mass $20 - 30 M_{\odot}$ with a compact object of mass $6 - 10 M_{\odot}$ (!). SS 433 is another prototype of HMXB system, the physical parameters of which are discussed in Chapter 4.

Now, we will briefly discuss the ‘mass function’ and its implication to know the nature of the compact objects.

1.1.2 Mass function

Determination of stellar masses in X-ray binaries and thus the ‘mass function’ absolutely depends on the knowledge of the fundamental law i.e., *Kepler’s harmonic law* which is stated as “the squares of the sidereal periods (p) of the planets are proportional to the cubes of the semi-major axes (mean radii) of their orbits” and algebraically it can be written as,

$$p^2 = \frac{4\pi^2 a^3}{G(M + m)}. \quad (1.1)$$

Let us consider a X-ray binary system of a normal star (observable in optical) and a compact object (observable in X-rays). The radial velocity studies can easily be applied to this binary system to measure the ‘actual observed’ velocities of both the normal star and the compact object. A schematic representation of the binary system is shown in Figure (1.2). Figure (1.2a) shows two components of the binary system along with their centre of mass at C (here, M_d and M_c denoted as the masses of donor and compact object respectively), whereas Figure (1.2b) represents

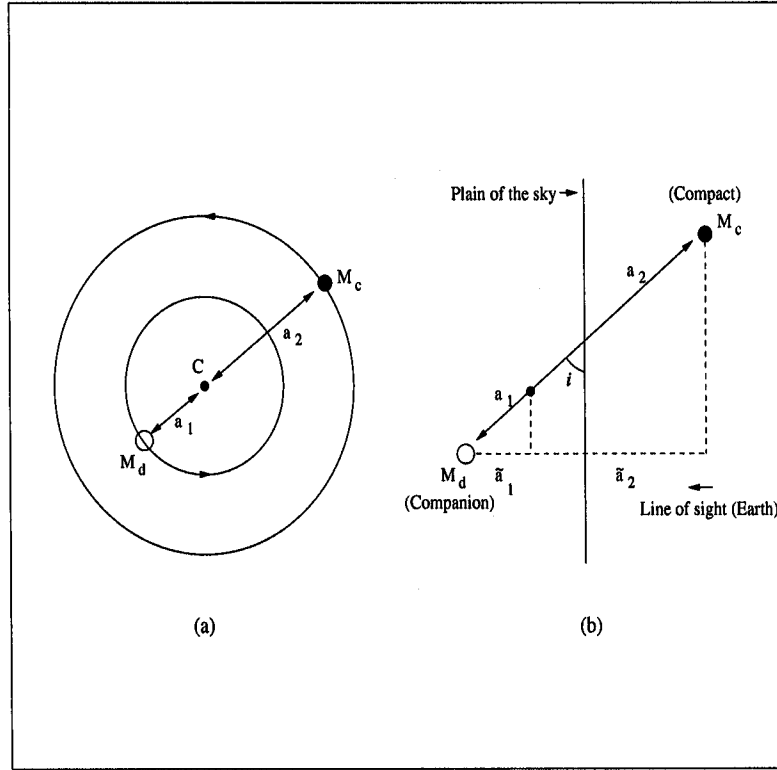


Figure 1.2: Schematic representation of a X-ray binary system. Left one (a) shows the binary system (in centre of mass frame) with the components of the donor (normal star of mass M_d) and the compact object (black hole of mass M_c). Right-sided figure (b) represents the general position of the binary system in the plain of the sky.

the general position of the binary system in the plane of the sky with respect to the line of sight. Now, referring to the Figure (1.2ab) and assuming a circular orbit (small eccentricity, $e < 1$) at an inclination i to the plane of the sky (defined as being perpendicular to the line of sight), the Kepler's harmonic law for this binary system gives,

$$p^2 = \frac{4\pi^2 \tilde{a}^3}{G(M_d + M_c) \sin^3 i}, \quad (1.2)$$

and in the centre of mass frame, we can write,

$$a_1 M_d = a_2 M_c, \quad (1.3)$$

where $a = a_1 + a_2$ is the separation between the normal star and compact object, $\tilde{a} = \tilde{a}_1 + \tilde{a}_2$ is the projection of separation of the same in the line of sight plane, such that $\tilde{a}_1 = a_1 \sin i$ and $\tilde{a}_2 = a_2 \sin i$. So, from the observational point of view, we actually observe these two quantities ($a_1 \sin i$ and $a_2 \sin i$) through measuring the so called K velocities of the optical star and compact object, as

$$K_d = 2\pi a_1 \sin i / p \text{ and } K_c = 2\pi a_2 \sin i / p.$$

Now, it is possible to calculate the mass ratio $q(M_d/M_c)$, but without any information of the value of inclination angle (i), we cannot calculate individual masses. So, in case of a single-line spectroscopic X-ray binary, we can only introduce a quantity (i.e., dependent on both of the system masses and inclination angle) that is the ‘mass function’ $f(M_d, M_c)$ by,

$$\begin{aligned} (M_d + M_c)p^2 &= \frac{4\pi^2 a^3}{G} = \frac{4\pi^2}{G} a_2^3 (1 + a_1/a_2)^3 \\ &= \frac{4\pi^2}{G} a_2^3 (1 + M_c/M_d)^3 \\ &= \frac{4\pi^2 \tilde{a}_2^3 (M_d + M_c)^3}{G \sin^3 i M_d^3}, \end{aligned} \quad (1.4)$$

$$\text{or, } f(M_d, M_c) = \frac{M_d^3 \sin^3 i}{(M_d + M_c)^2} = \frac{4\pi^2}{G} \left(\frac{\tilde{a}_2^3}{p^2} \right). \quad (1.5)$$

After some algebraic calculations, we can write

$$f(M_d, M_c) = \frac{M_d \sin^3 i}{(1 + M_c/M_d)^2} = \frac{p K_c^3}{2\pi G}, \quad (1.6)$$

which depends purely on the readily observable quantities: orbital period (p) and radial velocity (K_c). The ‘mass function’ is useful only for statistical studies or when an estimate of the mass of at least one component of the system already exists by some indirect means. For instance, if either M_c or $\sin i$ is unknown, the ‘mass function’ sets a lower limit for M_d , since the left-hand side is always less than M_d . Substituting the lower limit of M_d in Equation (1.6), one could obtain an lower limit for the compact object mass (M_c) and thus confirms the nature of the compact object.

1.2 X-ray Astronomy Missions

X-ray astronomy is an observational branch of ‘Astronomy & Astrophysics’, which deals with the study of X-ray emission from the celestial objects. The importance

of X-ray astronomy mission lies in the fact that the X-ray observations of celestial objects can not be carried out from the ground-based facilities because of photoelectric absorption of X-rays by the atoms and molecules of the Earth's atmosphere. As the X-ray sky is transparent to the observers (telescopes) at very high altitudes, the observation should be conducted above the Earth's atmosphere. The first on-board experiment with the sounding rocket V2 which enabled significant research, was carried out after the Second World War in 1949. With this experiment, the Naval Research Laboratory (NRL), USA, under the direction of Herbert Friedman, for the first time, was able to reveal that the Sun is a powerful source of X-ray radiations (Friedman et al. 1951). This important discovery actually caused many scientists to lose interest for searching non-solar X-ray sources. This was because the Sun appears as a bright source solely due to its proximity to the Earth and at the same time, it is also pointed out that the instrumentation available in those era would have had to be 10^5 times more sensitive to detect any non-solar objects (stars) which are nearest to the Earth. It took almost one decade for the development of rocket technology and improvement of sensitivity of the instruments, such that one could find the evidence of X-rays from the non-solar cosmic sources. In 1962, Giacconi and his team first discovered the X-ray source outside the solar system (Giacconi et al. 1962). The Observation was carried out with an Aerobee rocket carrying a payload consisting of three large area Geiger counters which detected large X-ray flux near 195 degree azimuth in the direction of the constellation Scorpius (see, Fig. 1.3). This source subsequently became known as Sco X-1.

After this great discovery, the potential of X-ray astronomy was revealed and the major discoveries made during 1962-1968 include: i) the detection of a diffuse background of X-rays, ii) the optical identification of Sco X-1, iii) the identification of Crab nebula, iv) the X-ray detection of the galaxy M87 in the virgo cluster and v) the detection of a ~ 20 min flare from Sco X-1. Cyg X-1, the first black hole candidate was also discovered in these early attempts in 1962 (Giacconi et al. 1962).

The first Earth-orbiting satellite entirely devoted to the study of cosmic X-ray sources was the UHURU satellite launched in 1970 (Giacconi et al. 1971). The major three discoveries with the UHURU satellite gave penetrating insight into the underlying nature of many galactic and extra-galactic X-ray sources. First, two eclipsing X-ray pulsars with Doppler-shifting periods, Her X-1 and Cen X-1 demonstrated the existence of a class of binary X-ray sources consisting of a normal star and a spinning, magnetized neutron star. The spin (typical period about 1 sec) of the magnetized neutron star results in the observed pulsing X-rays. This manifestation of neutron stars, closely following the identification of radio pulsars, revealed

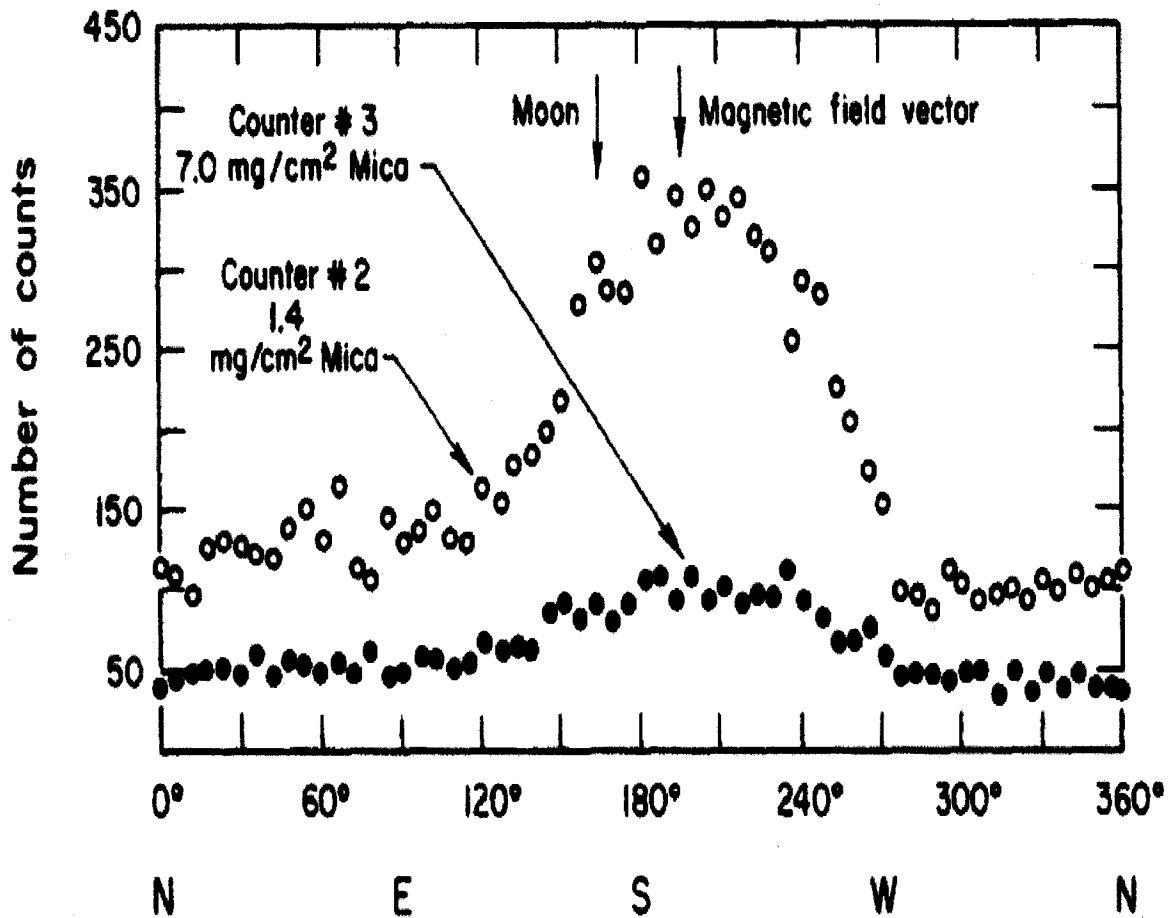


Figure 1.3: The discovery observation (i.e., first discovery of extrasolar X-ray source), obtained by Aerobee rocket carrying Geiger counters which detected large X-ray flux near 195 degree azimuth in the direction of the constellation Scorpius (From Giacconi et al. 1962).

a whole new domain of binary system evolution. The second discovery, of diffuse X-ray emission from several cluster of galaxies, suggested the presence of a dilute hot gas interspersed among the galaxies. Third, the detection of rapid aperiodic temporal variability of the intensity of Cyg X-1 led to the rocket and ground-based observations that identified the optical counterpart. Measurement of its optical mass function suggested that the source was a X-ray binary system containing a stellar mass black hole. UHURU also demonstrated that X-ray variability was a common phenomenon among the X-ray sources. These discoveries with other studies by UHURU brought X-ray astronomy solidly into the mainstream of astronomy.

After this, NASA took the challenge and planned for launching of series of very large scientific payloads called *High Energy Astronomy Observatories (HEAO)*. In this series, HEAO-2 spacecraft, named as Einstein X-ray Observatory (EXO), launched in 1978, which carried an X-ray imaging telescope, marked the second major success in the development of X-ray astronomy. Due to the imaging capability and the high sensitivity of the telescope, it is made possible to resolve the supernova remnants in a shell-like structure with compact objects sitting in the core and to detect X-ray emission from the most distant sources like quasars, high red-shift galaxies, cluster of galaxies, as well as faint X-ray sources located in the remote parts of our galaxy. (Most importantly, for the first time, a large number of guest observers used this X-ray Observatory).

The 1980s era of X-ray astronomy mission was considered to be the international collaborative and/or guest observing facilities program. During this period, the program was carried forward with the British *Ariel-6*, European *EXOSAT*, Japanese *Hakucho*, *Tenma* and *Ginga* and Soviet *Kvant* missions. Time variability studies of X-ray flux found to be very much important and specially *EXOSAT* was used extensively to exploit the discovery of quasi-periodic oscillations (QPOs) in the radiation from GX5-1 (van der Klis et al. 1985).

Another major development in X-ray astronomy occurred with the launch of the *ROSAT* Observatory which carried two independent focusing systems, a large X-ray telescope (XRT) and a smaller extreme ultraviolet (EUV) telescope. This mission first completed the X-ray scan of the sky in soft X-ray band (0.1 – 2.4 keV) and detected about 150,000 X-ray sources which included galactic as well as extra-galactic sources.

Another successful era of X-ray astronomy began just after the launch of *Rossi X-ray Timing Explorer (RXTE)* in December 30, 1995, which is still in working phase. The study of time variability phenomenon received a major boost from

RXTE mission due to its unique time resolution ($1 \mu\text{s}$) capability. Discovery of kHz quasi-periodic oscillations (QPOs) from low mass X-ray binaries, high frequency quasi-periodic oscillations (HFQPO) from galactic black holes and the spectral study in wide energy range ($2 - 200 \text{ keV}$) of many X-ray sources (e.g., black holes, neutron stars, X-ray pulsars, extra-galactic objects etc.) have reshaped our understandings of what goes on in the most violent and bizarre regions of the Universe. Prior to the *RXTE* launch, the Japanese *ASCA* Observatory which was launched in 1993, was the first X-ray astronomy mission to combine imaging capability with a broad pass band (up to 10 keV), good spectral resolution ($E/\Delta E \sim 30$) and a large effective area. Due to these unique characteristics, *ASCA* has enabled to discover an asymmetric feature of 6.4 keV iron fluorescence line from the Seyfert galaxy MCG-6-30-15, which is assumed to be the first compelling evidence for the existence of massive accreting black holes at the centre of the AGN. Apart from the *ASCA* observatory, the superior spectral resolution and sensitivity of the *XMM-Newton* Observatory of the European Space Agency (ESA) and spectacular X-ray imaging capability of *Chandra* X-ray Observatory, both of which were launched at the end of the last millennium, have already contributed to the advancement and understandings of high energy astrophysical processes in X-ray sources.

1.3 Radiative Processes in BH Astrophysics

All the celestial bodies in the Universe emit radiations which cover the entire electromagnetic spectrum that ranges from radio to γ -rays. The production of radiation in different wave-bands, basically depends on the nature of the medium and the physical processes associated with the system. In black holes astrophysics, the radiation is mostly dominated in the X-ray wavelengths. The emission mechanism of X-rays can be subdivided into two categories: thermal emission and non-thermal emission (Rybicki & Lightman, 1979). Below we will discuss these emission mechanisms for the production of X-ray radiations.

1.3.1 Thermal emission

The thermal emission mechanism can be subdivided in the following categories:

a) Blackbody radiation:

Blackbody radiation is generated from a medium which is both in complete thermodynamic equilibrium (i.e., the photons have equilibrium energy distributions

corresponding to the same temperature) and optically thick. These two conditions ensure that the populations of all excited states in the system is given by Boltzmann relation and the medium is a perfect absorber (i.e., a black body), which leads to a principle of complete balance – the rates of all upward and downward processes balance individually. Thus, the result of these conditions is that the emitted radiation from the medium is Planckian. Therefore, the Planck spectrum for the blackbody emission is given by,

$$B_\nu = 2h\nu^3 c^{-2} (\exp(h\nu - kT) - 1)^{-1},$$

where h is the Planck's constant. In reality, it is observed that most of GBHs emit blackbody radiation as a continuous energy spectrum which is emitted from the hot ($\sim kT$), optically thick plasmas (i.e., from the accretion disk).

b) Thermal Bremsstrahlung:

The acceleration of a charge particle in the Coulomb field of another charge causes to emit radiation which is called bremsstrahlung or free-free emission. The radiation from a highly ionized medium which is in local thermodynamic equilibrium (particles have Maxwell-Boltzmann velocity distribution) and is optically thin (so radiation field is not in equilibrium), has a characteristic shape of continuous spectrum that is determined only by the temperature. This particular type of bremsstrahlung process is known as the thermal bremsstrahlung.

The thermal bremsstrahlung spectrum falls off exponentially at higher energies and is characterized by the temperature, T . The intensity, I of the radiation at energy, E , is given by,

$$I(E, T) = Ag(E, T) Z^2 n_e n_i T^{-1/2} \exp(-h\nu/kT),$$

where A is constant, g is the 'Gaunt factor', a slowly varying function with value increasing as E decreases. It is to be noticed that the intensity is proportional to the square of the positive ions, Z , and the product of the electron density, n_e and the positive ion density, n_i . The X-ray continuum of the X-ray jets in GBHs are dominated by this process.

c) Line emission:

In a hot gas ($\sim 10^7$ K), X-ray line emission is also an important source of radiation. The elements heavier than hydrogen are not completely ionized except at high temperatures. When a fast electron strikes an ion with bound electrons, it often transfers energy to that ion, causing a transition to a higher energy level. After a short while, the excited ion decays rapidly to the ground state by radiating photons

of energy characteristics of the spacing of energy levels through which the excited electron passes. This radiation appears as spectral lines with energies determined by the radiating ion species (material present in the hot gas).

So, for example, in a 'He-like' ions, the so-called resonance line is produced when an electron jumps from $1s2p\ ^1P_1$ level to the $1s^2\ ^1S_0$ level. This emission mechanism is somehow complex whereas the emission of $H\alpha$ line is rather simple, which requires an electron to jump from $n = 3$ to $n = 2$ (n is the principle quantum number). Both these types of emission features are observed in the X-ray spectra of SS 433.

Most of the cases, it is found that the radiation from thermal gas is a blend of the thermal bremsstrahlung and the line radiation (from different ion species). Line emission appears predominantly in plasmas that have temperature of less than 5×10^7 K. Above this temperature, almost all the ions are stripped off their bound electrons that causes them to radiate the energy as an X-ray continuum. Thus observing the X-ray spectra, the shape of the continuum and the presence of lines can identify the origin as a hot gas of plasma. The temperature of the gas can be calculated from the particular lines present and from the shape of the high energy end of the bremsstrahlung continuum. The strength and energies of the lines also reveal the elemental composition of the hot gas.

d) Thermal Comptonisation:

Comptonisation (i.e., Compton scattering), a simple radiative process, occurs when a photon encounters with an electron. If the electron is stationary and the photon has an energy $E \ll m_e c^2 = 512$ keV, then the fractional wavelength increase is $\delta\lambda/\lambda = \varepsilon$ (when the scattering angle is 90°), where $\varepsilon = E/m_e c^2$. In the classical limit, as $\varepsilon \rightarrow 0$, the scattering is known as the Thomson scattering, where the electron oscillates in the electric field of the wave, radiating the scattered wave as it does so. The scattering cross-section is $\sigma_t = 8\pi r_0^2/3$, where r_0 is the classical radius of the electron. But, if the photon energy is such that $\varepsilon \geq 1$ (i.e., in the relativistic limit), the scattering cross-section is given by the Klein-Nishina formula, from which the relativistic limit for $\sigma_r = \pi r_0^2 (\ln 2\varepsilon + 1)/\varepsilon$ is obtained showing that the cross-section decreases at high energies.

On the other hand, if, instead of being stationary, the electron is in motion with a Lorentz factor γ , we have to go to its rest frame and calculate the photon energy $\varepsilon' = \gamma\varepsilon$ in that frame. Generally in Compton scattering, the photon energy is decreased (wavelength increased) and this energy is given to the electron, though the amount is small in the classical limit. The inverse process known as inverse Compton scattering, where the electron may have considerable thermal energy, which is

reduced and the photon gains energy. This has a great importance in astrophysics.

If the electron gas has a temperature T_e then the average energy transfer per scattering is $\Delta\varepsilon/\varepsilon = (4kT_e - \varepsilon)/m_e c^2$, showing that at high temperature, the photons gain energy from the electrons, whilst at low temperature it is the other way around. In any case, the fractional energy gain is very small, so that many scatterings are needed for a significant effect, leading to diffusion of the energies in phase space. Hence the emitted spectrum depends on the factor $y = \tau_{es} \Delta\varepsilon/\varepsilon$, where τ_{es} is the electron scattering optical depth.

If y is very large, the equivalent of the Planck formula for a non-scattering medium is the Wien equation, which has the asymptotic form $I_\nu \propto \nu^3 \exp(-\varepsilon/kT_e)$. It is observed that the high energy spectrum (≥ 10 keV) of the GBHs is power law like, which is purely characteristic of the Comptonisation process.

1.3.2 Non-thermal emission

The term ‘non-thermal’ emission generally refers to the radiation from particles whose distribution is not Maxwellian. Non-thermal emission are very important in any environment where there are high energy particles.

a) Cyclotron radiation:

It is already discussed that accelerating a charge particle will cause it to emit radiation. If an electron gas of hot plasma is permeated by a magnetic field, the electrons will be forced to gyrate about the field lines, and the radiation that is emitted as a result of this acceleration is known as the Cyclotron radiation when conditions are non-relativistic. The radiation is emitted at the gyrofrequency which is proportional to the magnetic field strength, B , and is given by $\omega_g = eB/m_e$. The radiation emitted is linearly polarized when viewed perpendicular to the direction of the field lines, and circularly polarized when the field is viewed end-on. In this particular type of emission process, unless the field strength (B) is large, the acceleration is not particularly large, nor is the intensity which depends on the square of the acceleration. In some X-ray binaries such as Her X-1 provide an impressive example where B can be order of 10^{12} Gauss, so that ν_g corresponds to hard X-rays at 10-30 keV.

b) Synchrotron radiation:

Synchrotron radiation is similar to that of Cyclotron radiation except that the electrons are relativistic ($v \sim c$) in nature. Hence, the frequency spectrum is much more complex and could be extended to many times the gyrofrequency. The fre-

quency of rotation, or gyrofrequency, in case of Synchrotron radiation, is given by $\omega_s = eB/\gamma m_e c$. As a result, the radiation produced is tightly beamed in a narrow angle about the forward direction of motion, by an amount determined by the Lorentz factor, $\gamma = (1 - v^2/c^2)^{-1/2}$. Hence in each rotation, a flash of light like a lighthouse is observed with a duration $\delta t \approx 1/(\gamma^3 \omega_s \sin \alpha)$, where α is the pitch angle. If we take the Fourier transform of the flash waveform, it will be extended to frequencies $1/\delta t \approx (\gamma^3 \omega_s \sin \alpha)$, which if γ is large, can be far above the gyrofrequency (ω_s). As with Cyclotron radiation, Synchrotron emission is also highly polarized. However, because of the effects of the relativistic beaming, circular polarization is suppressed and the polarization is primarily linear.

In this process, power radiated by mono-energetic electrons is given by,

$$P = \frac{4}{3} \sigma_t c \beta^2 \gamma^2 U_B,$$

where $\sigma_t (= 8\pi r_0^2/3)$ is the Thomson cross section, $\beta (= v/c)$ is the velocity of the electron, and $U_B (= B^2/8\pi)$ is the magnetic energy density. The energy spectrum of synchrotron radiation results from the superposition of the individual electron spectra, and the energy spectrum of the electrons can be approximated as power law distribution, i.e., $N(E) \propto E^{-p}$. Therefore, the resulting synchrotron emission spectrum will be also power law like, with an spectral index $s = (p - 1)/2$.

The Synchrotron process is important in many astrophysical contexts, including the emission from extragalactic radio sources, radio and optical emission from Crab Nebula as well as radio emission from relativistic jets and the emission of high energy X-rays from accretion disk in microquasars.

c) Non-thermal Comptonisation:

So far, we have discussed Comptonisation process in thermal plasma. However, with the presence of non-thermal electrons in the plasma, the process of Comptonisation will be modified with respect to the thermal case.

In case of thermal distribution, there is a roll over of the spectrum around 400 keV, whereas the effect of non-thermal electrons on Comptonisation will produce a high-energy tail that is above the thermal cut-off. The high-energy tail is simply the characteristic of the superposition of the individual electron spectra of non-thermal electrons which have optical depth (τ_{es}) $\ll 1$. Therefore, the spectral shape depends on the the energy index p of the power-law distribution of the electrons, and the resultant spectrum is power-law like, with an spectral index $s = (p - 1)/2$.

Second, the seed-photon flux (compared to the thermal case) will be much higher, so the luminosity in the thermal Comptonisation spectrum will increase correspond-

ingly. The high energy tails (beyond 400 keV) in the X-ray spectrum of black holes are modeled as power law distribution of non-thermal electrons that are present in the hot plasmas.

1.4 Accretion Process

In the context of accretion processes, it is very important to know what fraction of gravitational potential energy (i.e., released via accretion process) is converted into radiation and how efficient is the process compared to other mechanisms (e.g., nuclear reaction). On the other hand, observing the luminosity (isotropic radiation) one could easily measure the maximum allowed mass of a star and the temperature of the compact X-ray binaries etc. Here, we will discuss all these things.

1.4.1 General considerations

The process by which matter is captured by the gravitating objects is called *accretion* and the rate (in units of gm/sec) at which matter is accreted is known as *accretion rate*. Energy release via the accretion process is calculated in the following way:

Let us consider a star of mass M and radius R , and an element of gas of mass Δm in free fall from infinity. As the element of mass falls onto the star it gains kinetic energy (as it loses potential energy), i.e.,

$$\frac{1}{2}\Delta m v_{ff}^2 = \frac{GM}{r}\Delta m. \quad (1.7)$$

Now, if $r = R$, Δm hits the surface of the star, and it has to dissipate the excess kinetic energy, which will produce radiation. The rate at which energy is radiated away is given by,

$$\begin{aligned} L &= \frac{1}{2}\dot{m}v_{ff}^2 = \frac{GM\dot{m}}{R} = \frac{1}{2}\frac{(2GM/c^2)}{R}\dot{m}c^2 \\ &= \frac{1}{2}\left(\frac{r_g}{R}\right)\dot{m}c^2 = \eta\dot{m}c^2, \end{aligned} \quad (1.8)$$

where $r_g = 2GM/c^2$ is the Schwarzschild radius of the star and η is a parameter known as *efficiency* which is the measure of fractional change of gravitational energy into radiation. Again, η can be written as,

$$\eta = \frac{1}{2}\left(\frac{r_g}{R}\right) = \frac{G}{c^2}\left(\frac{M}{R}\right), \quad (1.9)$$

where M/R is the measure of the compactness of the star.

So far, we have talked about ‘normal’ stars, and written down the expression of efficiency factor η . This expression is quite well applicable to the compact objects and the calculated values are as follows,

- a) White Dwarf ($M \sim M_\odot$; $R \sim 5 \times 10^3$ km): $\eta \simeq 3 \times 10^{-4}$
- b) Neutron Star ($M \sim M_\odot$; $R \sim 14$ km): $\eta \simeq 0.1$
- c) Black Hole ($R = r_g = 2GM/c^2$): $\eta = 0.5$

Here, one important thing to note that the black hole has no hard surface, and accreted matter could disappear beyond the horizon, yielding no radiation at all. But, the radiation that we expect from the black hole environment (outside the horizon) that is basically coming out from the accretion disk around the hole.

Now in case of nuclear reactions, the mass difference between the end and initial products is transformed into energy. The most effective reaction is $4H^1 \rightarrow He^4$, which releases,

$$L_{nuc} = \frac{\Delta E_{nuc}}{\Delta t} \simeq 7 \times 10^{-3} \dot{m} c^2, \quad (1.10)$$

and the corresponding efficiency factor is $\sim 7 \times 10^{-3}$.

So, it is clear that the energy release (radiation) in accretion process is much more efficient (in accretion process up to 10% of rest mass turns into radiation, whereas in nuclear reaction it is less than 0.7%) than the nuclear reactions. But, one can see from Equation (1.8) that the luminosity (L) is directly proportional to \dot{m} . Naturally, a question will arise, which can be stated as, *can luminosity (L) increase arbitrarily as \dot{m} increases?* The answer to this question is: no! Because, radiation pressure stops accretion (\dot{m}) and lesser fuel means lesser luminosity (L), and accordingly, a characteristic luminosity, known as *Eddington luminosity* (L_{Edd}), at which no accretion is possible, can be defined by equating the inward gravitational pull (GMm_p/r^2) on protons with the outward radiative force ($L\sigma_t/4\pi r^2 c$) exerted on electrons due to the momentum deposition by photons. Therefore, the *Eddington luminosity* can be expressed as,

$$L_{Edd} = \frac{4\pi GMm_p c}{\sigma_t} \simeq 1.265 \times 10^{38} \left(\frac{M_{BH}}{M_\odot} \right) \text{ ergs sec}^{-1}, \quad (1.11)$$

where m_p is the mass of the proton, σ_t is the Thomson scattering cross-section, M is the mass of the gravitating object, M_{BH} is the mass of a black hole and M_\odot is the solar mass. The corresponding mass accretion rate is called the *Eddington accretion*

rate and is given by,

$$\dot{M}_{Edd} \simeq 1.44 \times 10^{17} \left(\frac{M_{BH}}{M_{\odot}} \right) \text{ gm sec}^{-1}. \quad (1.12)$$

Another important estimation, in this context is the variability time scale. The shortest time scale of variation of physical quantities close to a black hole horizon is,

$$t_g = r_g/c \sim 1 \times 10^{-5} \left(\frac{M_{BH}}{M_{\odot}} \right) \text{ sec}, \quad (1.13)$$

where $r_g (= 2GM/c^2)$ is the Schwarzschild radius and it can be scaled in terms of mass of the black hole as, $1r_g = 2GM_{BH}/c^2 = 3 \times 10^5 \left(\frac{M_{BH}}{M_{\odot}} \right) \text{ cm}$.

In observational astronomy, the *Eddington luminosity* and the corresponding accretion rate are treated as yardsticks to measure many physical properties of the stars as well as the compact X-ray binary system. In the next section, we will discuss briefly the importance of the above mentioned 'yardstick'.

Now, from the idea of definition of *Eddington luminosity*, we can write down the luminosity of the star, as

$$L \leq L_{Edd} = \frac{4\pi G m_p c}{\sigma_t} M, \quad (1.14)$$

where M and L are the mass and luminosity of a main sequence star.

On the other hand, using the Mass-luminosity relation and the above equation, one could calculate the maximum allowed mass of main sequence star. The maximum allowed mass is found to be $M \lesssim 100M_{\odot}$.

1.4.2 Temperature of compact X-ray binaries

In compact X-ray binaries, the conversion of potential energy of accreted matter into thermal energy, acts as major sources of X-ray radiation. The observed luminosity (L_{acc}) which is lower than the Eddington luminosity, carries the characteristic of the typical temperature profile of the X-ray binaries. Let us assume an object of radius R that emits a blackbody spectrum at a luminosity L_{acc} has a temperature T_{bb} . From the Stefan-Boltzman law, we can write,

$$T_{bb} = \left(\frac{L_{acc}}{4\pi R^2 \sigma} \right)^{1/4}, \quad (1.15)$$

where σ is the Stefan-Boltzman constant.

Now, if all potential energy of the accreted matter would turn entirely into radiation, the material would reach a temperature, T_{th} , which is known to be the thermal temperature of the hot plasma. For each pair H^+ and e^- , the potential energy is $G(m_p + m_e)M/R \approx GMm_p/R$, and the thermal energy is $2 \times 3kT/2$ ($3kT/2$ per particle). Hence, the thermal temperature is written as,

$$T_{th} = \frac{GMm_p}{3kR}. \quad (1.16)$$

Here, we can think of two extreme situations:

(a) Accretion flow is optically thick. Radiation (i.e., photon) reaches thermal equilibrium before it escapes from the medium, so emitted spectrum is blackbody and hence $T_{rad} \approx T_{bb}$,

(b) Accretion flow is optically thin. Radiation escapes the flow immediately (may be after one scattering) after it is produced, and hence $T_{rad} \approx T_{th}$.

In general, the actual temperature will be in between the two, i.e. $T_{bb} \lesssim T_{rad} \lesssim T_{th}$. Typical temperature values for galactic black holes are, $kT_{th} \approx 100$ MeV and $kT_{bb} \approx 1$ keV, which means that in accretion process the radiation emitted are mostly in X-rays. Similarly, in case of AGNs (for mass $M \sim 10^8 M_\odot$), the observed temperature is around $kT_{bb} \approx 20$ eV.

1.5 Structure of the accreting material

It is quite clear from the previous section that the accretion process is a very important one to explain the high luminosities observed in X-ray binaries and AGNs. Here, we will discuss about the real accretion process along with the development of accretion disk models, from Bondi flow to TCAF paradigm. Before going to talk about the different disk models, it is important to write down the basic equations which govern the flow dynamics.

1.5.1 Gas dynamics

Accreting material is (mostly) in gaseous form. Particles in the gas interact via Coulomb forces. On average a particle will travel a distance, λ , which is known as the mean-free path, before it interacts with another particle.

Provided we are interested in the macroscopic properties of the gas where system length (L) is far greater than the the mean-free path (λ) ($L \gg \lambda$), we can treat the

gas as fluid, and use the hydrodynamic equations. In this context, we can write down the three basic Equations which govern the fluid flow,

Conservation of mass:

$$\frac{dm}{dt} = 0 \iff \frac{d(\rho\Delta V)}{dt} = 0,$$

$$\text{or } \frac{\partial\rho}{\partial t} + \nabla(\rho.\mathbf{v}) = \mathbf{0}, \quad (1.17)$$

where ρ is the density of the fluid, \mathbf{v} is its velocity and ΔV is an arbitrary element of volume.

The gas will be characterized by the fluid variables $\rho(\mathbf{r}, t)$, $\mathbf{v}(\mathbf{r}, t)$ and $P(\mathbf{r}, t)$ (or $T(\mathbf{r}, t)$) and chemical compositions. As the flow variables depend both upon the position and time, the arbitrary gas element should possess a temperature, T and a density, ρ , and hence each element will produce a pressure, P . The flow variables will follow the *Perfect gas law* which is given by,

$$P = \rho kT / \mu m_{\text{H}}, \quad (1.18)$$

where μ is the mean molecular weight of the gas. For neutral H, $\mu = 1$ and for fully ionized H, $\mu = 1/2$.

Equation of motion (Euler equation):

$$\rho \frac{\partial\mathbf{v}}{\partial t} + \rho\mathbf{v}.\nabla\mathbf{v} = -\nabla P + \mathbf{f}, \quad (1.19)$$

where two terms in the left-hand side simply represent the transfer of momentum ($\rho \frac{d\mathbf{v}}{dt}$) which is due to the pressure gradient of the fluid flow and the external force (\mathbf{f}) fields acting on the fluid particles.

Energy conservation:

$$\frac{\partial}{\partial t} \left(\frac{1}{2}\rho v^2 + \rho\epsilon \right) + \nabla \left[\left(\frac{1}{2}\rho v^2 + \rho\epsilon + P \right) \mathbf{v} \right] = \mathbf{f}.\mathbf{v} - \nabla.\mathbf{F}_{\text{rad}} - \nabla.\mathbf{q}, \quad (1.20)$$

where ϵ is the internal energy of the gas element per unit mass ($\rho\epsilon$ is the internal energy per unit volume), $\frac{1}{2}\rho v^2$ is the kinetic energy per unit volume, $-\nabla.\mathbf{F}_{\text{rad}}$ accounts for the energy gain/lose due to emission/absorption of radiation by the gas element per unit volume, $-\nabla.\mathbf{q}$ accounts for the energy gained/lost by the element due to heat conduction.

In general, to calculate \mathbf{F}_{rad} one needs to solve one extra equation for the specific intensity of the radiation field, known as the *transport equation* (Rybicki & Lightman, 1979).

1.5.2 Steady, spherically symmetric accretion: Bondi Flow

Let us assume a compact object of mass M_c , accretes matter from a large gas cloud. The object is at rest with respect to the cloud. The matter flow is spherically symmetric, and adiabatic in nature, i.e., there is no exchange of energy with the outside world (gas cloud). The steady behavior of spherically accreting matter which has no angular momentum, was first studied by Bondi (1952). A detailed description of this particular type of flow has been given in *Theory of Transonic Astrophysical Flows* (Chakrabarti, 1990). In case of Bondi flow, the mass accretion rate is given by,

$$\dot{M} = 4\pi r^2 \rho v, \quad (1.21)$$

which is constant throughout the flow (solution of Equation (1.17)). As matter accretes radially towards compact objects, the density (ρ) and velocity (v) will go up simultaneously. But, in case of a Bondi flow on a Schwarzschild black hole, the matter velocity reaches the velocity of light (c) at the horizon with density close to zero as most of the matter drained through the horizon. On the other-hand, the flow at infinity where the matter is almost at rest, is characterized by the velocity v_∞ and density ρ_∞ . Apart from this two boundary conditions, the maximum attainable sound speed in a flow is $c/\sqrt{3}$. Thus the black hole accretion is transonic in nature, and the flow velocity becomes equal to the velocity of sound at a particular distance r , away from the compact object. The distance is called as sonic radius (r_s) at which the flow changes from subsonic to supersonic. The corresponding sound speed at sonic radius is a_s . Integrating the Euler's equation (Equation (1.19)) for adiabatic flow and applying the boundary conditions, we can write down the relation between the $a_s(r_s)$, the sound speed at r_s and $a_s(\infty)$, the ambient speed of sound at rest (far away from the object), which is given by,

$$a_s(r_s) = a_s(\infty) \left(\frac{2}{5 - 3\gamma} \right)^{1/2}, \quad (1.22)$$

where γ is the adiabatic index. The corresponding mass accretion rate, in terms of $\rho(\infty)$ and $a_s(\infty)$, is given by,

$$\dot{M} \approx 1.4 \times 10^{44} \left(\frac{M}{M_\odot} \right)^2 \left[\frac{\rho(\infty)}{10^{-24}} \right] \left[\frac{a_s(\infty)}{10 \text{ km/s}} \right]^{-3} \text{ gmsec}^{-1}. \quad (1.23)$$

This mass accretion rate would produce a luminosity of $\sim 10^{31} \text{ erg sec}^{-1}$ ($\sim 1\%$ of solar luminosity), so mass accretion from the interstellar medium is observationally not so important.

1.5.3 Disk accretion: Keplerian/sub-Keplerian Flow

Shakura-Sunyaev disk:

The first accretion disk flow model was proposed by Shakura (1972), but the complete work on the model was published in a subsequent article by Shakura & Sunyaev (1973) and the disk is generally known as the *Shakura-Sunyaev disk* (SS disk) or the *Standard disk*. At the same time a relativistic version of the model was put forward by Novikov & Thorne (1973). In this disk model, it is assumed that the accreted matter forms a geometrically thin disk in which matter rotates in Keplerian orbits and that the inflow velocity is much smaller than the free-fall velocity. The viscous torque ($t_{r\phi}$) acting on different layers of accreting matter, which is responsible for transporting the angular momentum outwards and thus making the accretion possible in this model was assumed to be proportional to the total vertically averaged pressure of the gas in the disk, p_{total} , i.e.,

$$t_{r\phi} = \alpha_{\text{ss}} p_{\text{total}}, \quad (1.24)$$

where $\alpha_{\text{ss}} < 1$ is the so called viscosity parameter. The larger value of α_{ss} , the more is the efficient transport of angular momentum outwards, which leads to higher radial velocity (at a constant \dot{M}) of the flow and lower the surface density (Σ) of the disk.

In general, the rate at which mass is deposited onto the accretion disk via mass loss from the companion (secondary star), will change depending on the companion's nuclear time scale, t_{nuc} (the time scale over which the radius of the secondary changes, and the star fills its Roche lobe). Now, it is obvious that $t_{\text{nuc}} > t_{\text{vis}}$ (the viscous time scale), which means that in general disk will be in steady state.

For the steady-state disk, the viscous dissipation (i.e., the flux which is radiated away from the disk) per unit disk face area at a radius R can be written as,

$$F(R) = \frac{3GM\dot{M}}{8\pi R^3} \left[1 - \left(\frac{R_{\star}}{R} \right)^{1/2} \right], \quad (1.25)$$

and the corresponding luminosity produced by the disk in between R_1 and R_2 is given by,

$$L(R_1, R_2) = 2 \int F(R) 2\pi R dR, \quad (1.26)$$

which yields,

$$L(R_1, R_2) = \frac{3GM\dot{M}}{2} \left[\frac{1}{R_1} \left[1 - \frac{2}{3} \left(\frac{R_{\star}}{R_1} \right)^{1/2} \right] - \frac{1}{R_2} \left[1 - \frac{2}{3} \left(\frac{R_{\star}}{R_2} \right)^{1/2} \right] \right]. \quad (1.27)$$

Now putting $R_1 = R_*$ (the radius of the central star or the Schwarzschild radius) and $R_2 = \infty$ the total luminosity which is radiated away from the accretion disk is given by,

$$L_{\text{disk}} = \frac{GM\dot{M}}{2R_*} = \frac{1}{2}L_{\text{acc}}. \quad (1.28)$$

So, half of the gravitational energy is radiated away from the accretion disc.

Since the Shakura-Sunyaev disk is optically thick, each element of the disk face radiates as a blackbody spectrum with temperature $T(R)$ given by equating the dissipation rate to the blackbody flux, and hence the local effective temperature is given by,

$$T(R) = \left[\frac{3GM\dot{M}}{8\pi R^3\sigma} \left(1 - \left(\frac{R_*}{R} \right)^{1/2} \right) \right]^{1/4}, \quad (1.29)$$

where σ is the Stefan-Boltzmann's constant. In most of the X-ray binaries the blackbody spectrum peaks at energies ~ 1 keV, while for AGNs at ~ 10 eV. Thus, though the Shakura-Sunyaev disk model is valid for the accretion rates found in most of these objects, it is unable to explain the observed emission features of accreting black holes at energies higher than 10 keV.

Also at low accretion rates the gas pressure dominates throughout the accretion disk, and thus making the disk stable in nature. However, when the accretion rate increases, the radiation pressure starts to dominate over the gas pressure and the inner region (close to the black hole) of the *Standard disk* becomes thermally unstable. This happens typically for accretion rates $\dot{M} \geq 10^{-2}\dot{M}_{\text{Edd}}$. We will discuss these major issues in the following sections.

Slim accretion disk:

With the increase of accretion rate, the optical depth to absorption, τ , in the disk also increases. In this situation, the emitted photon (radiation) has to travel until it escapes from the disk. The travel time is roughly proportional to τ^2 and close to the Eddington accretion rate the photon escape time exceeds the time scale of advection (Jaroszyński, Abramowicz & Paczyński, 1980). Therefore, a fraction of the radiation that is produced in the disk is *advected* through the black hole event horizon. Accretion flows where the advection occurs are termed as ADAFs i.e. Advection Dominated Accretion Flows.

Abramowicz et al. (1988) showed that as a result of advection a new branch of equilibrium solutions for stationary disk is possible at moderately super-Eddington accretion rates. The flow is optically thick and the pressure is dominated by radiation. However, because of advection, the flow now becomes stable. Unlike the

Standard disk, the disk - so called 'slim disk' - is now geometrically thick, with the disk height comparable to the radial distance. Since the disk is neither geometrically thin nor Keplerian the gas flow in the disk may be substantially sub-Keplerian in nature, with higher inflow velocity.

In case of slim disk, the radiation spectrum is more difficult to calculate than in the case of *Standard disk* (optically thick disks at low accretion rates). Depending on the viscosity parameter (α_{ss}) values, the nature of the spectrum changes and for higher α_{ss} (> 0.3) the spectrum becomes harder than the blackbody spectrum (Beloborodov, 1998). But this disk model again failed to explain the observed features at high energies of the order of 100 keV.

In late 80's and early 90's, it was a challenge to explain the new findings and discoveries which were associated with the black hole binaries. Actually, the advancement of space-borne (satellite) and ground based (radio antennas) instruments have triggered the challenge. The X-ray spectrum observed in the black hole candidates were quite complex. In low energy range (< 10 keV), the spectrum was modeled as a blackbody spectra but at high energies (few 100 keV) spectrum was power-law like and the slope changes from time to time. The *Standard disk* and the *slim-disk* both were unable to reproduce the hard spectra extending upto 100 keV and beyond. For that, the presence of hot ($T_e \sim 10^9\text{K}$), optically thin plasma is required. At the same time, X-ray variabilities observed in GBHs are quasi-periodic in nature and their Fourier decomposition shows a very prominent peak in the power density spectrum (PDS). This feature is known as the quasi-periodic oscillation (QPO) which is observed in most of the galactic black hole candidates. Also from the radio observations it was found that the jets and outflows that are observed in GBHs are coming out from vicinity of the hole. To explain all the above features, one should look for a complete accretion disk model instead of several many models, each perhaps suitable for a specific purpose, i.e., to explain a specific observation.

1.5.4 Advective accretion disk: Two Component Advective Flow (TCAF)

In early 90's, Chakrabarti and his collaborators (Chakrabarti, 1990; Chakrabarti & Molteni, 1993; Chakrabarti & Titarchuk, 1995; hereafter referred to as CT95; Chakrabarti, 1996a; 1996b; Molteni, Sponholz & Chakrabarti, 1996; hereafter referred to as MSC96) for the first time presented a global and complete accretion disk solution incorporating all the physical processes while solving the most general flow equations. The aim was to achieve a single paradigm so that all sorts of

observational features could be explained within a single framework. A schematic representation of an advective accretion disk is shown in Figure (1.4).

An advective accretion disk is the one which advects, or carry ‘something’, namely, mass, entropy, energy etc. Since this fundamentally means that radial velocity must be present, therefore in advective disk there should be finite radial velocity which may even reach the velocity of light on the horizon. Therefore, before entering into a black hole, matter had to be supersonic (i.e., Mach number, $M = v/a > 1$, where v and a are radial velocities and sound speed respectively), and thus, had to pass through at least one sonic point ($M = 1$), and as a sub-Keplerian flow (i.e., a flow with angular momentum $\lambda < \lambda_K$, the Keplerian angular momentum). This makes the infall time $t_{in} < t_{vis} \sim t_{ff}/\alpha_{ss}$, where, t_{vis} , t_{ff} and α_{ss} are the viscous timescale, free-fall time scale and the viscosity parameter of Shakura and Sunyaev (1973) respectively. This makes $\lambda \sim$ constant close to a black hole. Since the centrifugal force $\lambda \sim 1/r^3$ grows much faster compared to the gravitational force $\sim 1/r^2$, for a large region of the parameter space (Chakrabarti, 1990), a stable solution can have a standing shock wave before entering into a black hole, thereby creating a ‘boundary layer’. Depending on the physical parameters, a shock may be oscillating in nature or it may even be absent. The oscillations of the shock may give rise to the temporal variability in the form of QPOs which are observed in many of the BH candidates. In this ‘boundary layer’, the flow kinetic energy is converted into the thermal energy forming a hot Compton cloud which can inverse-Comptonize the soft photons into hard photons and produce outflows and winds (Chakrabarti, 1999). This boundary layer is called the CENtrifugal pressure supported Boundary Layer (or, CENBOL).

Basically, CENBOL forms when specific energy is positive - a cool, Keplerian disk cannot have a CENBOL. A cool Keplerian disk remains on the equatorial plane, while a hot sub-Keplerian flow of positive energy stay away from the plane. There are several models in the literature (see, Chen, Abramowicz & Lasota, 1997; Esin et al. 1998; Zdziarski, 2001; Malzac, Beloborodov & Poutanen, 2001) which uses Keplerian disk at the outer boundary. These models are unable to explain observations, unless other components, such as Compton clouds, magnetized corona etc. (origins of which are unspecified) are also invoked. Because both the hard X-rays and the major parts of the outflows/jets are expected to be produced at the CENBOL, it plays a crucial role in astrophysical description of galactic and extra-galactic black holes.

Two Component Advective Flow (TCAF) (Fig. 1.4) is a combination of two types of flows: Keplerian component which is accreted in long, viscous time scale

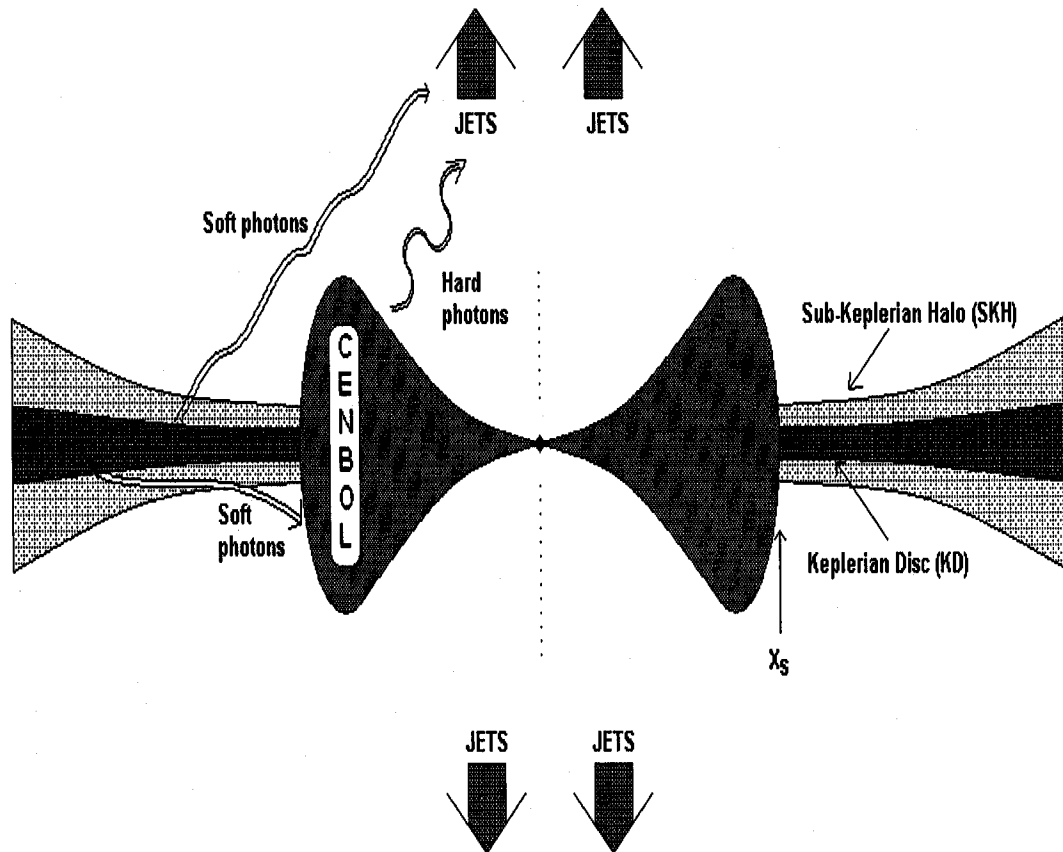


Figure 1.4: Schematic diagram of an unmagnetized TCAF model with all its components. The entire flow is a combination of Keplerian and sub-Keplerian flow. Compact object is surrounded by CENBOL, which is the power house of 'hot' electrons and hard X-rays are produced from it. Jets/Outflows are also originated from the CENBOL.

and the initially sub-Keplerian component, which plunges in the short, free-fall time scale. The TCAF solution is the combination of solutions with high and low angular momentum at the outer boundary with a standing shock at around few tens of r_g (if shock conditions are satisfied, here $r_g = 2GM/c^2$ is the Schwarzschild radius). Recently, Smith, Heindl, Markwardt & Swank (2001) and Smith, Heindl & Swank (2002) provided conclusive evidence that the accretion flow comprises of the two components, one is Keplerian and the other one is sub-Keplerian. They showed that for wind accretors (such as Cyg X-1, LMC X-1, LMC X-3 etc.), Keplerian disk is small and thus the power law index follows the photon flux. For those (such as 1E1740.7-2942, GRS 1758-258) accreting from Roche-lobe overflow the derivative of the flux is correlated with the power law index with a lag of tens of days. This is interpreted as the viscous time scale of the large Keplerian disk. No other model in the literature is capable of explaining such a behavior. We will discuss the other importance and predictions of TCAF solutions to explain observational facts and results that are presented in the respective Chapters of this thesis.

Chapter 2

DATA ACQUISITION AND ANALYSIS

2.1 Data acquisition

Most of the work described in this thesis is based on the use of data obtained with the *Rossi X-ray Timing Explorer (RXTE)* satellite and the *Indian X-ray Astronomy Experiment (IXAE)* payload on IRS-P3 satellite. *RXTE*, launched in December 1995, is a NASA's astronomy satellite designed to study the brightest X-ray sources in the sky. These include the most luminous sources in our own Galaxy (i.e., X-ray binaries), AGNs, quasars and ULXs (recently discovered) that are the most luminous sources known in the Universe. Major advantage of *RXTE* over previous X-ray instruments is due to its unparalleled detector characteristics. Detectors have the unique capability of tagging the X-ray events with microsecond accuracy over the broad energy range 2 – 200 keV which enables *RXTE* to probe temperatures, magnetic fields and other fundamental physical properties close to the observed sources (mostly compact objects) as well as the geometry of the systems, nature and characteristics of the compact object itself (e.g., masses, spin periods and size of the neutron stars etc.). There are three main instruments on-board the *RXTE* satellite: the Proportional Counter Array (PCA) (Jahoda et al. 1996), the High Energy X-Ray Timing Experiment (HEXTE) (Rothschild et al. 1998), and the All-Sky Monitor (ASM) (Levine et al. 1996).

The satellite orbits the earth at an altitude of 580 km with an inclination of about 23° and a period of about 100 mins. Therefore, it passes through the South Atlantic anomaly (SAA) region in 6 of the 14 – 15 daily orbits. During such a passage, lasting typically for 10 – 20 mins, then the instruments are put in safe mode to protect them against the highly charged particle flux. Furthermore, unless sources are located near one of the poles of the orbit they will be occulted for typically 30 mins by the earth once in a complete orbital period of 100 mins.

2.1.1 All-Sky Monitor (ASM)

The All-Sky Monitor (ASM) on-board the *RXTE* operates in 1.5 – 12 keV energy range and monitors around the sky scanning 80% of each satellite orbit. The ASM consists of three wide-angle Scanning Shadow Cameras (SSCs), each of which contains a position-sensitive proportional counter (PSPC) (total collecting area of 90 cm²) that views the sky through a coded mask. The X-ray intensity and direction measurements are derived from the displacements and strengths of the shadow patterns cast by the X-ray sources with the camera's field of view (FOV). Each camera has FOV of 6° × 90° FWHM and detection sensitivity up to 30 mCrab (1 Crab = 75.5 SSC cts/sec). The X-ray events detected by ASM are normally processed on-board by two ASM Event Analyzers (EAs) in the Experiment Data System (EDS) before insertion into the telemetry stream. Typically, a source is observed 5 – 10 times a day, and the full coverage is obtained in a series of 90 sec stationary exposures known as 'dwells'. The ASM also provides the unequally sampled data in one-day average from a number (typically 5 – 10) of individual ASM dwells. ASM has proved to be a unique instrument on-board *RXTE* due to its fascinating first-results or quick look capability, such as detection of a new transient in the sky, state change of known sources and quasi-periodic or highly flux variations in a longer time scale etc. Figure (2.1) shows the ASM light curve of an X-ray novae GRO J1655-40. The source has undergone two major outbursts since its discovery in 1994 July. The first peak in 1996 shows strong flaring with intense non-thermal emission (VH state), whereas the spectrum of 1997 was soft and thermal except for the hard spectrum in nature mostly at the end of outburst (Sobczak et al. 1999). After 1997, the source goes beyond the detection level of ASM and it becomes a 'dead' source and almost there is no 'signature of life' in ASM till now. On the other-way, the ASM light curve of GRS 1915+105 is very complex (see, http://xte.mit.edu/ASM_lc.html) and variable in short time scale (~ days) whereas SS 433 shows a quasi-periodicity of 184 days (!!) in the ASM light curve (see, Figure 4.16). Furthermore, the ASM public archive containing the continuous light curves of more than 400 X-ray sources.

2.1.2 Proportional Counter Array (PCA)

The Proportional Counter Array (PCA) is comprised of five co-aligned detectors, called proportional counter units (PCUs) with a total collecting area of 6500 cm². The PCA is effective over the energy range 2 – 60 keV with 18% energy resolution at 6 keV. PCA detectors have the features of high throughput (12,800 counts sec⁻¹ for

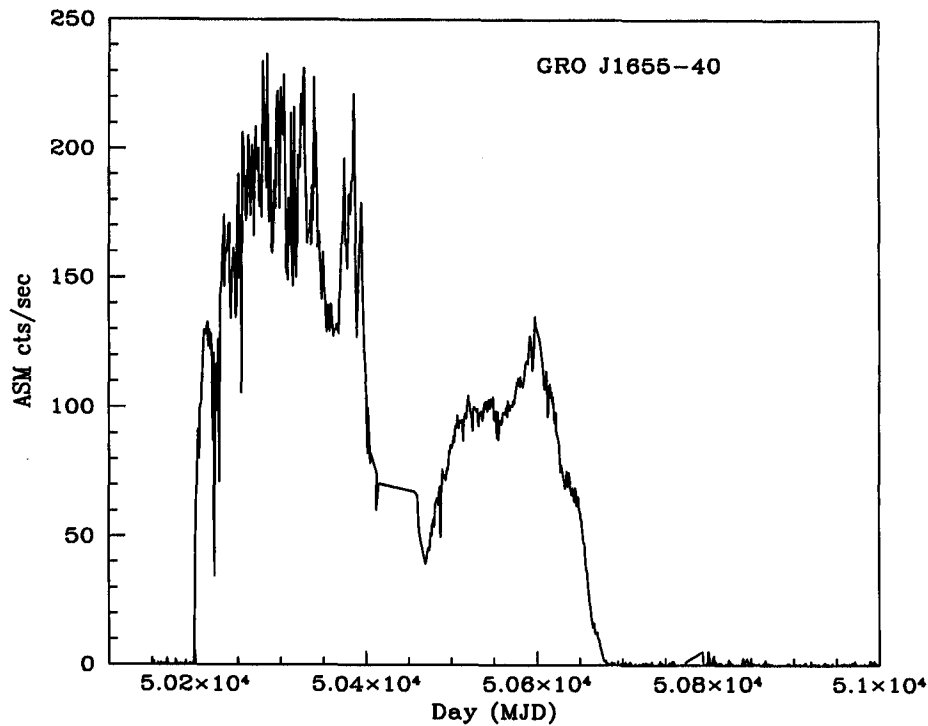


Figure 2.1: All Sky Monitor (ASM) light curves of X-ray novae GRO J1655-40. Figure shows that the source has undergone two major outbursts since its discovery in 1994 July. This double-peaked (broad) profile is quite unlike compare to other BH candidates. During first peak in 1996, the source exhibited strong flaring activity with non-thermal emission. In 1997 (second peak), the source spectrum was soft in nature and thermal except at the end of the outburst where the spectrum was hard. After 1997, the source goes beyond the detection level of ASM.

the Crab with 5 PCUs) and unique time resolution of 1μ sec. Each PCU consists of a collimator with 1° FWHM and two gas-filled chambers mounted on top of each other. The first chamber is filled with propane and filters out background electrons (veto layer). The second chamber is filled with Xenon/Methane (mixture) gas and comprises the main X-ray detection part. This chamber contains 4 layers of anode grids separated by cathode wires (per grid 20 anodes are present). The upper 3 layers, each splitted into two (left and right), are used for X-ray detection. The X-rays impacting a Xenon atom trigger a cascade of electrons onto the high voltage anodes. The higher the X-ray photon energy, the more electrons are liberated, and thus the higher the electron pulse-amplitude. The anodes in the grid of the last

layer serve as a discriminator i.e., veto layer for charged particles entering through the detector walls. Major portion of this thesis work depends on the results of timing and spectral properties of X-rays from BH candidates which are observed by *RXTE*/PCA detectors.

2.1.3 High Energy X-ray Timing Experiment (HEXTE)

The HEXTE consists of two clusters each containing four NaI/CsI phoswich detectors with a combined total collecting area of 1600 cm². It operates in the energy range 20 – 200 keV with 15% energy resolution at 60 keV. The HEXTE has provided important spectral information beyond the capability of PCA, but the nominal count rates of HEXTE (e.g., 289 counts sec⁻¹ for the Crab) and low sensitivity (1 Crab = 360 count sec⁻¹ per HEXTE cluster) limit its use for timing studies. In this thesis no major observational data obtained with HEXTE are used. But in Chapter 3 (§3.4.3), we have discussed the high energy spectrum of GRS 1915+105 that was obtained with HEXTE.

2.1.4 Data mode and Screening Criteria

Each ASM and PCA event is processed by an on-board computer, called the Experiment Data System (EDS). The EDS consists of eight Event Analyzers (EAs): six for the PCA data stream and two for that of the ASM. Each EA contains an Intel 80286 processor and associated memory. The EAs can be programmed independently to process incoming events from the instruments in different 8 modes. Two EAs of PCA have preset modes:

1. the Standard-1 data mode provides data in the energy range of 2–60 keV with a time resolution of 0.125 sec and no energy resolution since all 256 channels are combined into one channel,
2. the Standard-2 data mode provides data in the same energy range of 2–60 keV with a time resolution of 16 sec and high spectral resolution (the pulse height is recorded in 129 channels covering the 2 – 60 keV energy range, although maximum energy limit changes from one Epoch to another Epoch).

The modes of the remaining four EAs of PCA could be set by the guest observer or the *RXTE* operation staff. Most of the time, the EA ‘Event’, ‘Binned’ and ‘Single-Bit’ modes are used. In an Event mode, the data is transported to

the ground station as a time series of unevenly spaced events described by arrival time, pulse height, PCU ID etc. and this mode has different configurations like: Generic event (E_31us_16M_50_1s), Good Xenon (Good_Xenon1_2s), Transparent. In a Binned mode, the actual photon arrival time is lost. The events are binned with respect to time, photon energy and detector number. The Generic binned (B_8ms_16A_0_35_H_4P), Standard-1 and Standard-2 are different configurations of Binned data mode. Data of Single-Bit mode consists of a stream of ones and zeros representing detector events and clock ticks (set the time resolution). The generic Single-Bit configurations are designated with a character string beginning with SB (SB_500us_50_249_2s) and it has the same format as that of the Binned mode with higher time resolution between the two events.

Before the start of analyzing the data, it is important to get rid of invalid or unwanted data from the raw data. In practice, this screening business has been done by applying various criteria to create good time intervals (GTI) which includes only the good data. The GTI file is created with `ftool task maketime`. It is also standard practice that the screening criteria are constructed from quantities contained in the filter file which is used as input for the task `maketime`. The `ftool task xtefilt` will create the filter file, automatically consulting the appropriate housekeeping files. This task requires the ObsID no., FITS Master Index (FMI) file and a file listing the Application IDs (appids) as input.

2.2 Analysis

We have analyzed the archival data of *RXTE* Satellite of the sources, i.e., GRS 1915+105, SS 433 and GRO J1655-40, which are available in *High Energy Astrophysics Science Archive Research Center (HEASARC)*, NASA. The unique capabilities of *RXTE* detectors (high time resolution and broad band spectroscopy) help us to diagnose both the temporal and spectral features of the sources. The data reduction and analysis was performed using software (LHEASOFT) FTOOLS version 5.1 and XSPEC version 11.1 (for Epoch 5 = 5/13/00 - present). For details, one could visit at: <http://heasarc.gsfc.nasa.gov/docs/xte/xtegef.html>.

2.2.1 Timing Analysis

Temporal behaviors of the X-ray sources were studied using the Event and Binned mode data. The observed X-ray flux variations with time is known as the 'light curve' and their Fourier transformation in the Power-Frequency plane is known to be the

Power Density Spectra (PDS). To generate the X-ray light curves, we have used the *saextract* task for Binned mode data whereas for Event mode data *seextract* task is used. A typical X-ray light curve of GRS 1915+105 with 1 sec bin time is shown in Figure (2.2). The flux variation (photon counts/sec) is highly quasi-periodic in nature. A powerful ftool task *powspec* calculates the power spectrum density using the Fast Fourier Transformation (FFT) algorithm which is inbuilt in the software. Figure (2.3) shows two PDSs which are generated from the same light curve of GRS 1915+105, but the PDSs are in two different frequency regime. The left-sided PDS is generated with 0.1 sec bin time, whereas the right one is generated with 0.01 sec. Both the PDS shows very strong peaks around ~ 0.02 Hz (left PDS) and ~ 7 Hz (right PDS). Such peaks are due to *quasi-periodic oscillations* (QPOs). QPOs are seem to be the fastest and regular astrophysical phenomena that are observed both in neutron stars and black holes. The signature of QPO features in the PDS is defined as that the features should have coherence parameter $Q = \nu/\Delta\nu > 2$ (FWHM) (van der Klis 1989). Features with lower Q values are regarded as ‘broad power peaks’ which is also there in the PDS around 0.2 Hz (left PDS).

We have also analyzed the Standard-2 data of GRS 1915+105 for the ‘Softness Ratio’ plot (see, Fig. 3.2 in Chapter 3). The procedure to produce the light curves and the ‘Softness Ratio’, the channel selection criteria, time resolution etc. are discussed in the section §3.2.1 .

X-ray observation of SS 433 was carried out during the period of Nov. 2002 to Aug. 2004 with *RXTE*. We have analyzed the archival data as well as the Target of Opportunity (TOO) data. SS 433 was pointed at several times by *RXTE* on our request. We have extracted light curves both from the Good Xenon and the Standard-2 mode data. Background subtracted light curves using Standard-2 data is presented in Figure (4.11) in Chapter 4. We use the Perl script *make_se* to reduce the Good Xenon files as Event files before using the *seextract* task to extract light curves. We have also generated PDS using the Event mode data (higher time resolution), but we didn’t find any quasi-periodicity or QPO like feature in the PDS of X-ray light curves of SS 433.

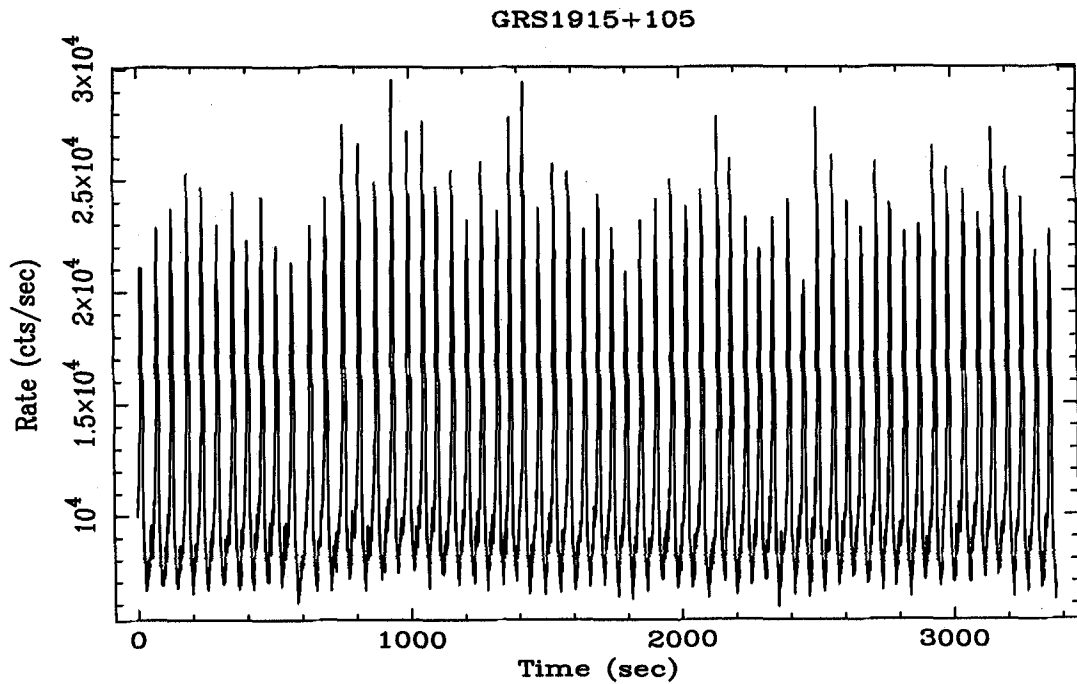


Figure 2.2: A typical X-ray light curves of a black hole candidate GRS 1915+105. The light curve is binned at 1 sec time resolution. Flux variation (photon counts/sec) is highly quasi-periodic in nature.

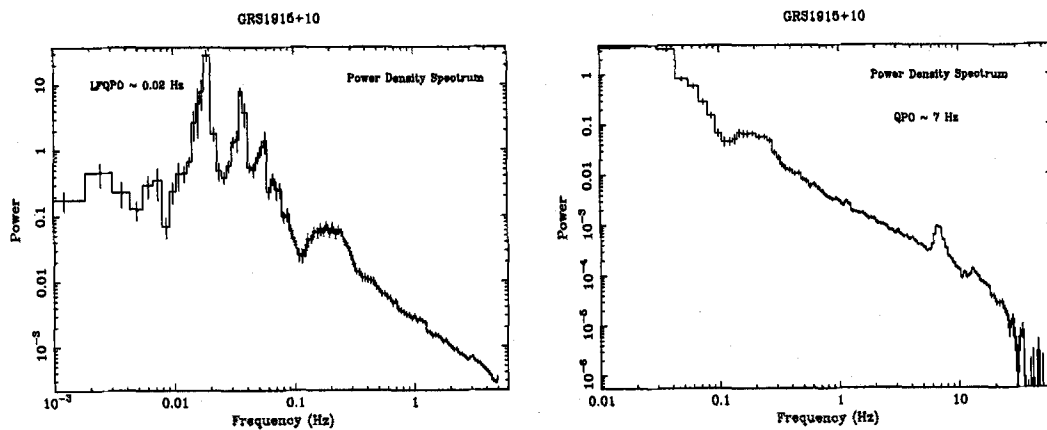


Figure 2.3: Power Density Spectra (PDS) which are generated for the same light curve (Fig. 2.2) of GRS 1915+105. The left-sided PDS shows the low frequency QPO (~ 0.02 Hz) along with the 'broad power peak' around ~ 0.2 Hz, whereas right-sided PDS is drawn to show the high frequency QPO (~ 7 Hz).

2.2.2 Spectral Analysis

The reduction and analysis of *RXTE*/PCA spectra involve several steps, namely: data selection, background estimation, response-matrix generation and finally analysis with the XSPEC package.

The Standard-2 data mode which used for all pointed observations, provides all the key information for accurate spectral analysis (e.g., PCU ID, Anode ID, at least 64 PHA bins). To generate the PCA spectral files i.e., PHA files, we have used the *saextract* task with applying the different filters as input (e.g., GTI information, COLUMN selection of PCUs, time intervals, channel selection etc.).

The background estimation for each spectrum has been done with the latest *pcabackest* task of *ftools*. This task requires the Standard-2 data file, filter file, background models etc. as input. Background model varies from bright sources to faint sources (< 40 cts/sec/PCU) and from one Epoch to another Epoch. Another important input for the background estimation task is the *pca_saa.history* file and it must be included for all the background models except for the bright source model in Epoch 1 and Epoch 2. Ultimately, the *pcabackest* task will produce a background data file from which one can extract light curves and spectra using the *saextract* task.

One of the most important tasks is to generate the detector response matrices which basically bridges the gap between the actual spectrum of the source and the observed spectrum by the instrument/detector. The Perl script *pcarsp* will create the PCA response file (RSP file) which is the product of the Ancillary Response File (ARF) and Redistribution Matrix Function (RMF). The ARF file accounts for the detector windows and collimator response whereas the RMF file accounts for the redistribution of photon energy amongst detector channels by the detecting medium. The response (RSF) file should match with the PHA files (source and background) in PCUs and anode layers and is used by XSPEC for spectral analysis.

Before going to talk about the spectral analysis with XSPEC, it is important to know about the basics of the spectral fitting. The spectrum of a source obtained with the spectrometer on-board satellite, is not the actual spectrum, but rather photon counts (C) within specific detector channels (I). The observed spectrum is related to the actual spectrum of the source ($f(E)$), such that:

$$C(I) = \int_0^{\infty} f(E)R(I, E)dE, \quad (2.1)$$

where $R(I, E)$ is the detector response and is proportional to the probability that an incoming photon of energy E will be detected in channel I . In general, it is very

difficult to determine the actual spectrum of the source ($f(E)$) (for a given set of $C(I)$), by inverting the above equation.

The usual practice is to find out a model spectrum $f(E)$, that can be described in terms of a few parameters (i.e., $f(E, p_1, p_2, \dots)$), and 'fit' it to the observed data ($C(I)$) obtained by the detector instrument. The observed spectrum ($C(I)$) of a particular source is obtained with the few associated XSPEC commands which requires the PHA files of data and background spectral files. Before run the model spectrum in XSPEC to predict the actual spectrum of the source from the background-subtracted count rate, XSPEC requires the RMF file (response matrix) which calibrates the incoming photon energy with the detector channels and we get the energy calibrated observed spectrum. Ultimately, predicted model spectrum ($C_p(I)$) is compared with the observed spectrum ($C(I)$) and a 'fit statistic' is computed from this comparison which enables to judge whether the model spectrum 'fits' the observed data.

The model parameters are then varied to find out the *best-fit parameters* values with the most desirable fit statistic. The model spectrum, $f_b(E)$, made up of the best-fit parameters is considered to be the *best-fit model*. The most common fit statistic used in XSPEC for the *best-fit model* is χ^2 which is defined as,

$$\chi^2 = \sum (C(I) - C_p(I))^2 / (\sigma(I))^2, \quad (2.2)$$

where $\sigma(I)$ is the error for channel I (e.g., if $C(I)$ are counts then $\sigma(I)$ is usually estimated by $\sqrt{C(I)}$). Actually, the χ^2 statistic provides a well-known goodness-of-fit criterion for a given number of degrees of freedom (ν , being the difference between the number of channels and the number of model parameters) to assess the statistical significances of the χ^2 values and hence, the best-fit adequate model is guaranteed for the 'reduced χ^2 ' (χ^2/ν) value to be approximately equal to one. Also, the requirement of an extra model component in the total model is tested using the F-statistic with the *ftest* task within XSPEC. The F-statistic, as defined in Bevington, (1969, pp. 208-209), is the ratio of

$$\begin{aligned} F_\chi &= [\chi^2(m) - \chi^2(m+1)] / [\chi^2(m) / (N - m - 1)], \\ &= \Delta\chi^2 / \chi_\nu^2, \end{aligned} \quad (2.3)$$

where m is the no. of free parameters and $(N - m - 1) = \nu$ is the no. of degrees of freedom. If the F-statistic probability ($P_{F\text{-stat}}$) is low then it is reasonable to add the extra model component. The significance level (S) of this probability is calculated using the following formula,

$$S = \sqrt{\log(1/\sqrt{2\pi}\sigma P)}, \quad (2.4)$$

where P is the F-statistic probability ($P_{F\text{-stat}}$) and σ is given by

$$\sqrt{2\nu_2(\nu_1 + \nu_2 - 2)/\nu_1(\nu_2 - 4)(\nu_2 - 2)^2},$$

where ν_1 and ν_2 are the no. of degrees of freedom (dof) for the initial and final model (after adding an extra model component to the initial model) respectively.

It is also important to know the confidence level of the *best-fit* parameters (p1, p2....) values and how these parameters are correlated with one another. For this, the confidence interval of the *best-fit* parameters values are calculated using the XSPEC *error* command and the *steppar* command is used to generate the $\Delta\chi^2$ values as a function of two different model parameters. Finally, a 2D contour plot of $\Delta\chi^2$ is plotted of the confidence regions of the two parameters to show the correlations.

A best-fit model that is generally acceptable for the SS 433 spectrum (for *RXTE*), is chosen to be the combination of different model components, like,

$$f_b(E) = wabs(bremss + ga + ga)$$

where $f_b(E)$ defined as the sum of the thermal bremsstrahlung spectrum (*bremss*) with two gaussian lines emission (*ga*) features and the whole emission process is modified by the interstellar absorption (*wabs*).

2.3 Indian X-ray Astronomy Experiment (IXAE)

We have also analyzed the X-ray data of GRS 1915+105 that is observed with the *Indian X-ray Astronomy Experiment (IXAE)* and presented a some part of our results in this thesis. The *IXAE* on-board the Indian satellite IRS-P3 was launched using the Polar Satellite Launch Vehicle (PSLV) from Sriharikota Range in India on March 21st, 1996 and since then has carried out observations till the year 2000. The IRS-P3 satellite is placed in a circular polar orbit of 830 km altitude with an orbital inclination of 98° and orbits the earth with a period of 102 mins. Due to the polar orbit of IRS-P3, most of the orbits pass through the high energy charged particle zone, which restricts the observation to about 5 of the 14 orbits per day.

The *IXAE* consists of three Pointed Proportional Counters (PPCs) and one X-ray Sky Monitor (XSM) (Agrawal et al. 1996). The PPCs have a total collecting area of 1200 cm^2 and effective over the energy range 2 – 18 keV with 22% energy resolution at 6 keV. The X-ray observations with PPCs are carried out in two different mode. One is in the nominal mode (N), with 1.0 sec time resolution and other one is the medium mode (M), with 0.1 sec time resolution. The nominal mode observational

data are available for five orbits of the every day and each observation has a duration of about 20 mins., whereas in the medium mode data are usually available only for three orbits due to the limited size of the on-board data storage unit. Each PPC has three different layers, in which X-ray photons are collected in two energy channels of 2–6 keV and 6–18 keV. As a result of the presence of only two energy channels, only two points (one from 2–6 keV photon counts and other one from 6–18 keV photon counts) could be obtained in the spectrum and a so-called ‘mean photon index’ (MPI) s_ϕ (see, Chapter 3 in section §3.3) can be calculated after every second or so. Similarly, 0.1 sec time resolution in the medium mode restricts the observation of QPOs up to 5 Hz only, while the 1 sec time resolution restricts the reporting of QPOs up to 0.5 Hz. Nevertheless, the X-ray light curves of GRS 1915+105 are clear enough and the identification of the specific class can be done without any ambiguity (Paul et al. 1998; Naik et al. 2001, 2002). In *IXAE* data, we found the evidence of class transition (via unknown class) of GRS 1915+105 and presented the results in Chapter 3.

2.4 Observations in Infrared and Radio bands

Observations in Infrared and Radio bands were carried out with the Physical Research Laboratory (PRL) 1.2 meter Mt. Abu infrared telescope equipped with the Near-Infrared Camera and Multi-Object Spectrometer (NICMOS), having a 256×256 HgCdTe detector array cooled to 77 K and the *Giant Meter Radio Telescope (GMRT)* at 1280 MHz (bandwidth 16 MHz), which has 30 antennas each 45 meter in diameter spread over a 25 km region (Swarup et al. 1991) near Pune, India, along a roughly Y-shaped array. The black hole candidate SS 433 was observed both in the wave bands (Infrared and Radio) along with in X-rays as a part of a Multi-wavelength campaign which was conducted on September 2002. We have used the Infrared and radio results in this thesis work just to find out correlation or anti-correlation, if there, with X-rays. In §4.2, we have discussed our multi-wavelength results.

Chapter 3

GRS 1915+105: A FASCINATING ASTROPHYSICAL SOURCE

3.1 GRS 1915+105: A Galactic Microquasar

The transient X-ray source GRS 1915+105 was discovered in 1992 by the WATCH all-sky X-ray monitor on-board GRANAT (Castro-Tirado, Brandt & Lund, 1992) and observations showed that the source was highly variable. At a later time i.e., in *RXTE* era (1996 to till now), *RXTE*/ASM observation shows the same long time scale variability of GRS 1915+105 which is unique and not observed in any other sources. This source is located in the constellation Aquila with the coordinate position *right ascension* ($\alpha_{2000.0}$) = $19^h 15^m 11.60^s$ and *declination* ($\delta_{2000.0}$) = $+10^\circ 56' 44.0''$. The first extensive radio monitoring of the source was carried out (Rodriguez et al. 1995) with the Very Large Array (VLA) and Nancy Radio Telescopes at different frequencies from December 1993 to April 1994. Major outbursts of radio flares (~ 1 Jy) observed in GRS 1915+105 during this period of observation confirmed that it produces superluminal radio jets (Mirabel & Rodriguez, 1994) and the ejected radio blobs are moving away from the source at a speed of $v \approx 0.98c$. At the end of this section, we will discuss little more about the superluminal speed that is observed in this particular source. The maximum X-ray luminosity observed during high-state is $\sim 10^{39}$ ergs/sec and it is confirmed that GRS 1915+105 is one of the high accreting (\sim Eddington rate) black hole candidates. Also, the source shows similar canonical energy spectrum as the other BH candidates and the spectra is modeled by two components : one is multicolor disk blackbody and the other one is the power-law function. Distance measured to the source which is ≤ 13.5 kpc away from us, also confirms its true galactic nature. Another important observation in the near-infrared H and K band identifies that the binary counter-part of GRS

1915+105 is a K-M III star (Greiner et al. 2001), which implies that GRS 1915+105 belongs to the category of low mass X-ray binaries (LMXB). This identification also implies a mass of $M_d = 1.2 \pm 0.2M_\odot$ for the donor. At the same time, with the knowledge of orbital inclination ($i = 70 \pm 2^\circ$), orbital period ($P_{orb} = 33.5$ days) and mass of the donor and knowing the mass function ($f(M) = 9.5 \pm 3.0M_\odot$), the mass of GRS 1915+105 comes out to be $M_c = 14 \pm 4M_\odot$. All these results suggest that GRS 1915+105 is a compact X-ray binary system having a unusually massive(!) black hole at the centre with a low mass donor star that is orbiting around the compact object.

GRS 1915+105 becomes more interesting in X-rays, after the observation starts with *RXTE* in 1996 and at same time with *India X-ray Astronomy Experiment (IXAE)*. Compared to any other BH candidates, GRS 1915+105 displays fascinating and complex X-ray variabilities (short time scale). They are classified in 12 different classes (Belloni et al. 2000; Nandi, Manickam & Chakrabarti, 2000). In the next section, we will discuss about the classification procedure of light curves and focus on the physical basis of origin of the light curves.

There are several observational reports of infrared (IR) and radio observation of GRS 1915+105 in literatures which claims large amplitude variabilities in IR (Fender et al. 1997) and Radio (Rodriguez & Mirabel, 1997; Pooley & Fender, 1997) bands.

Beside this individual energy band observations, a simultaneous observation in different energy bands was carried out by Pooley & Fender (1997) in X-ray/Radio and Eikenberry et al. (1998) in X-ray/IR. Pooley & Fender (1997) first reported that the radio oscillations are really coincident with X-ray dips observed in X-ray light curves. Eikenberry et al. (1998), however, claimed that the quasi-periodicity observed in X-ray/IR flares of ~ 30 mins oscillations is the evidence of disk-jet connection in GRS 1915+105.

In another report by Klein-Wolt et al. (2002), a strong connection was found between radio oscillations and few classes of X-ray light curves. So, the Galactic Black Hole (GBH) GRS 1915+105 has become an astrophysical laboratory to test the theoretical models of black hole physics.

Superluminal motion in GRS 1915+105

The Galactic Black Holes (GBHs) with relativistic jets mimic, on a much shorter time scale, many of the phenomena seen in quasars and are therefore called the *microquasars*.

Superluminal motions i.e., the speed of radio blobs (jets) more than the speed of light, have been observed in quasars for more than 25 years (Pearson & Zensus,

1987; Zensus, 1997). At first this superluminal motions provoked concern because of the fact that it seemed to violate the relativistic effect, but later on these motions were interpreted as relativistic projection effect (Rees, 1966).

The actual feature of the superluminal motions can be understood in terms of the simultaneous ejection of a pair of twin condensations (i.e., matter in the form of radio blobs ejected from the core of the compact objects in two opposite directions) (Mirabel & Rodriguez, 1994; Fender et al. 1999) moving at velocity β ($\beta = v/c$), with the axis of the ejected material making an angle θ ($0^\circ \leq \theta \leq 90^\circ$) with respect to the line of sight of a distant observer. The apparent velocities, due to special relativistic effect, of approaching and receding condensations, v_a and v_r , are given by,

$$v_{a,r} = \frac{v \sin \theta}{1 \mp \beta \cos \theta}, \quad (3.1)$$

and the apparent proper motions of the same approaching and receding condensations can be written as,

$$\mu_{a,r} = \frac{\beta \sin \theta}{1 \mp \beta \cos \theta} \frac{c}{D}, \quad (3.2)$$

where D is the distance from the observer to the source. The above coupled equation can be transformed into two equations,

$$\beta \cos \theta = \frac{\mu_a - \mu_r}{\mu_a + \mu_r} \quad (3.3)$$

and

$$D = \frac{c \tan \theta}{2} \frac{\mu_a - \mu_r}{\mu_a \mu_r}. \quad (3.4)$$

From the above two equations, it is clear that if the proper motions are known, one can easily measure the upper limit of both the angle (θ) and distance (D).

In the case of the bright ejection event of 1994 March 19 for GRS 1915+105 (Mirabel & Rodriguez, 1994), the proper motions measured were $\mu_a = 17.6 \pm 0.4$ mas day⁻¹ and $\mu_r = 9.0 \pm 0.1$ mas day⁻¹ (Note that 1 mas day⁻¹ = 5.61×10^{-14} rad sec⁻¹). From Equation (3.3), we find that $\beta \cos \theta = 0.323 \pm 0.016$, which implies that $\cos \theta \geq 0.323$ or $\theta \leq 71^\circ$, and that $\beta \geq 0.323$. Substituting the upper limit $\theta \leq 71^\circ$ in Equation (3.4), one could derive an upper limit for the distance, $D \leq 13.7$ kpc, confirming the galactic nature of the source. The actual distance to GRS 1915+105 is found to be, from HI absorption studies, 12.5 ± 1.5 kpc (Rodriguez et al. 1995). At this distance the proper motions of the approaching and receding components measured with VLA in 1994 and 1995 imply apparent velocities on the plane of the sky of 1.25 ± 0.15 (superluminal speed) and 0.65 ± 0.08 times the speed of light and

the ejecta move with a actual speed of $\beta = 0.92 \pm 0.08$ at an angle $\theta = 70 \pm 2^\circ$ to the line of sight.

3.2 X-ray variabilities in GRS 1915+105

There have been more than 1000 pointed observations of GRS 1915+105 by the proportional Counter Array (PCA) on-board *RXTE*, till now. Timing analysis of *RXTE*/PCA data shows different types of unique X-ray variabilities (Greiner, Morgan & Remillard, 1996; Morgan, Remillard & Greiner, 1997; Munro, Morgan & Remillard, 1999) and power density spectra (PDS) of time-variability data of GRS 1915+105 shows QPOs with frequency varying from ~ 0.01 Hz. to ~ 67 Hz. Below, we will discuss the classification procedure of the X-ray variabilities and the motivation behind this sort of classification.

3.2.1 Classification of X-ray variabilities of GRS 1915+105

The first attempt to classify the X-ray variabilities (light curves) was presented by Belloni et al. (2000). They analyzed the first two years data of GRS 1915+105 observed with *RXTE* in the period of 1996-1997 and classified the entire light curves into 12 distinct classes based on the photon counts and color characteristics of the individual light curves. These 12 classes have been designated as χ , α , ν , ρ , κ , λ , μ , β , θ , δ , γ and ϕ respectively Figure (3.2a). They plotted the color-color diagram (CD) for two X-ray colors: HR1=B/A and HR2=C/A (A: 2-5 keV, B: 5-13 keV and C: 13-60 keV). From the CD plot, they identified three basic states:

1. A: low count rate, low HR1 and HR2;
2. B: high count rate, high HR1;
3. C: low count rate, low HR1, variable HR2 depending on the length of the event.

These three basic states are the fundamental building blocks of variability transitions among the 12 classes of GRS 1915+105. The possible transitions among these three states are depicted in the Figure (3.1). Belloni et al. (2000) classified the light curves without considering any model i.e., model-independent way. We have analyzed and classified the X-ray light curves in different way which is model-dependent. We have explained the light curves of GRS 1915+105 with the most reasonable and acceptable

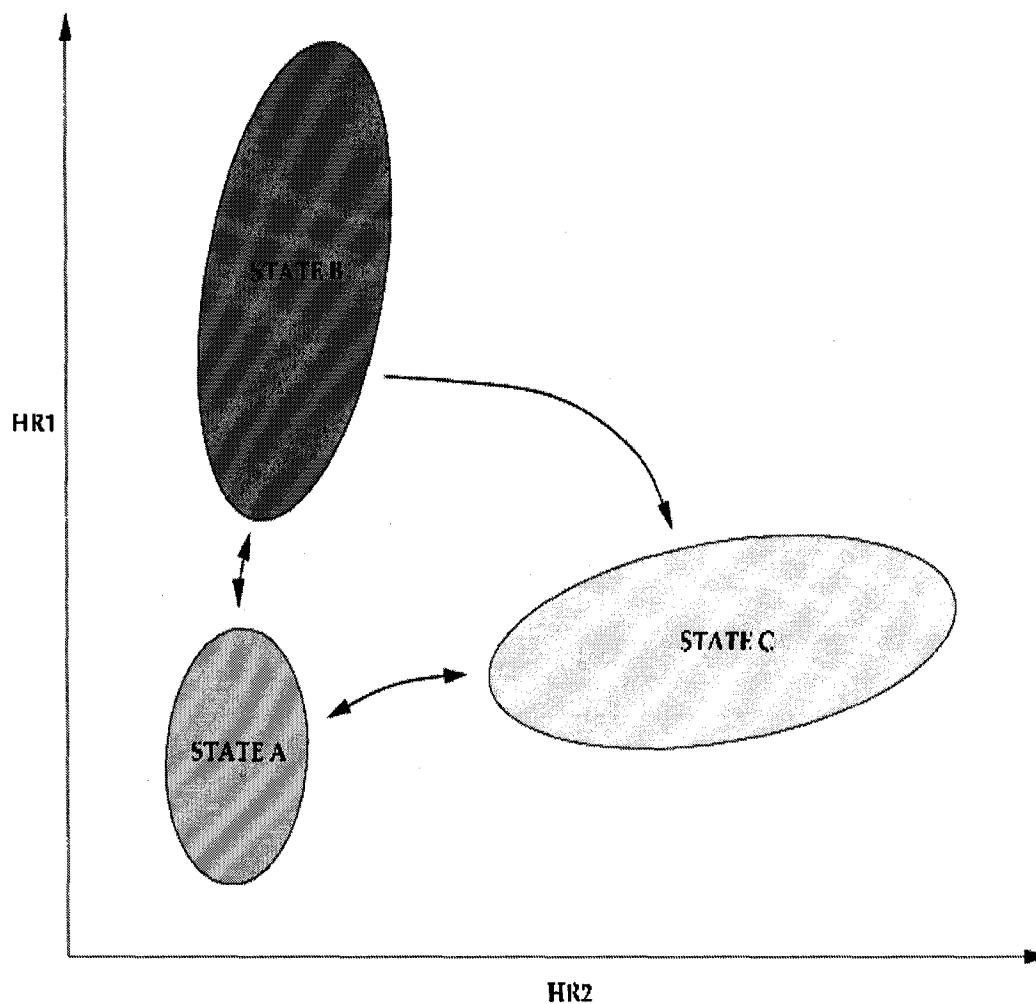


Figure 3.1: X-ray variabilities of GRS 1915+105 are classified in 12 classes (model-independent way) and their color-color diagram ($HR1 \sim HR2$) shows three basic states (A, B and C) with observed transitions. This figure is adopted from Belloni et al. (2000).

model i.e., Advective Flow Paradigm which has all the accretion and winds/outflow features (Chakrabarti & Nandi, 2001; Chakrabarti et al. 2002a). Figure (3.2a) shows all possible variations of the light curves of GRS 1915+105 as observed by *RXTE*/PCA. Twelve panels are marked along with the Belloni's designation. Along X-axis is the time elapsed in seconds and Y-axis is photon counts/sec (rate) in units of 10^3 . Even after one decade of observation with *RXTE*, the source displays only one more extra class (ω , see Naik, Rao & Chakrabarti, 2002; Klein-Wolt et al. 2002) other than the 12 classes. Spectral analysis of the 1st panel (χ) suggests that it is in the hard state. There is a prominent QPO whose frequency changes from time to time and photon count number also changes significantly. GRS 1915+105 remains for a long time in χ class and it is further subdivided into χ_1 , χ_2 , χ_3 and χ_4 by Belloni et al. (2000). Vadawale, Rao & Chakrabarti (2001) showed that there are distinct spectral differences among these sub-classes. They identified two generic sub-classes: χ_{RL} (radio loud) and χ_{RQ} (radio quiet) depending on the radio emissions associated with these two sub-classes. The classes χ_1 and χ_3 belong to the sub-class χ_{RL} whereas χ_2 and χ_4 belong to the sub-class χ_{LQ} . All these four sub-classes show very strong QPO frequencies. Not only that, the power density spectra (PDS) are quite different in χ_{RL} and χ_{LQ} sub-classes. The lower three panels of Figure (3.2a) (10-12) contain light curves of those days on which spectral states are relatively soft. There are no prominent QPOs in these days. Spectral fits indicate high temperature and high photon spectral index. The panels (8-9) contain little complex light curves where always hard dips and soft dips are present. PDS shows QPOs in the hard dips whereas there is no signature of QPOs in the soft dips. Spectral analysis shows that β and θ classes have quite different spectra as compared to the above four classes (χ class). In the remaining six panels (2-7), photons (X-ray flux) jump in between two distinct states, one with a low photon count (Off state) and the other one with a high count (On state).

We have sub-divided the above 12 classes into four sub-classes by studying the 'softness ratio', shown in Figure (3.2b) (Nandi, Manickam & Chakrabarti, 2000). For these, we have analyzed the Standard-2 data which has 16 sec time resolution to produce light curves in three PHA channel intervals: A: 0-7 (1.94-3.00 keV), B: 8-47 (3.35-17.00 keV), C: 47-255 (17.36-60.00 keV). From these we have plotted the 'softness ratio' diagram shown in Figure (3.2b) for individual light curves. Along X-axis B/C is plotted and Y-axis A/C is plotted. Our obvious choice of A, B and C in different energy ranges basically connected with TCAF model. In TCAF, if the pre-shock flow is indeed the source of the soft photons, photons originating in (\leq 3) keV should be roughly proportional to the accretion rate in the cool component

(basically Keplerian). Thus, the photon number may show time variation (due to periodic changes in the ‘accretion rate’). However, no QPO should be seen. This will be discussed in the next section. The harder photons ($E > 3$ keV) would usually come from post-shock region (CENBOL). Since the spectra intersect at around 17 keV and for $E \geq 17$ keV, photon number is not large, we make our choice of A, B and C to be those in energy ranges (0-3) keV, (3-17) keV and (17-60) keV respectively (B and C would be related to sub-Keplerian rate). According to our paradigm, roughly speaking, A, B and C should be proportional to each other, (since B and C produced by interception of soft photons. Of course, soft X-ray absorption makes matter more complex.) and whenever hardness or softness ratios are plotted basically straight lines are expected, instead of very intricate structures of Belloni et al. (2000). One could see from Figure (3.2b) that the plots in panels (10-12) which are soft or nearly soft spectra, are roughly linear and lower-left end starts at sufficiently large number compared to other panels. In panels (8-9), there are two lines with different slopes and one line represents the softness of the spectra of θ and β classes of soft dip regions. PDS plots do not show evidences of QPOs in these light curves except in the hard dip regions of θ and β classes (panel 8-9). Light curves of all other panels with low photon count states show QPOs.

Therefore, the softness diagram could be classified in the following ways:

1. HARD Class (H) : Hard state with a strong power law and a prominent QPO feature in PDS (Panel 1),
2. SOFT Class (S) : Soft state with weak power law and no QPOs (Panel 10-12),
3. INTERMEDIATE Class (I) : Low count to High count transition (off/On transition) and only Off state shows QPO. Assuming outflow from CENBOL, these light curves are well understood (Panels 2-7),
4. SEMI-SOFT Class (SS) : Hard dips with QPO and Soft dips without QPO and these two light curves are related with disk evacuation (Panels 8-9).

Each of these classes have sub-classes in terms of variation in light curves and softness ratios. For instance, in Class H (χ class), photon counts and QPO frequencies vary and the spot mark in Panel 1 moves around. In Class S, the slopes and the coordinates or the lower-left point varies, but the general nature is similar (Panels 10-12). In Class I, the duration of the Off and the On state may vary systematically from one sub-class to another class. The duration of the On-state (high count) may

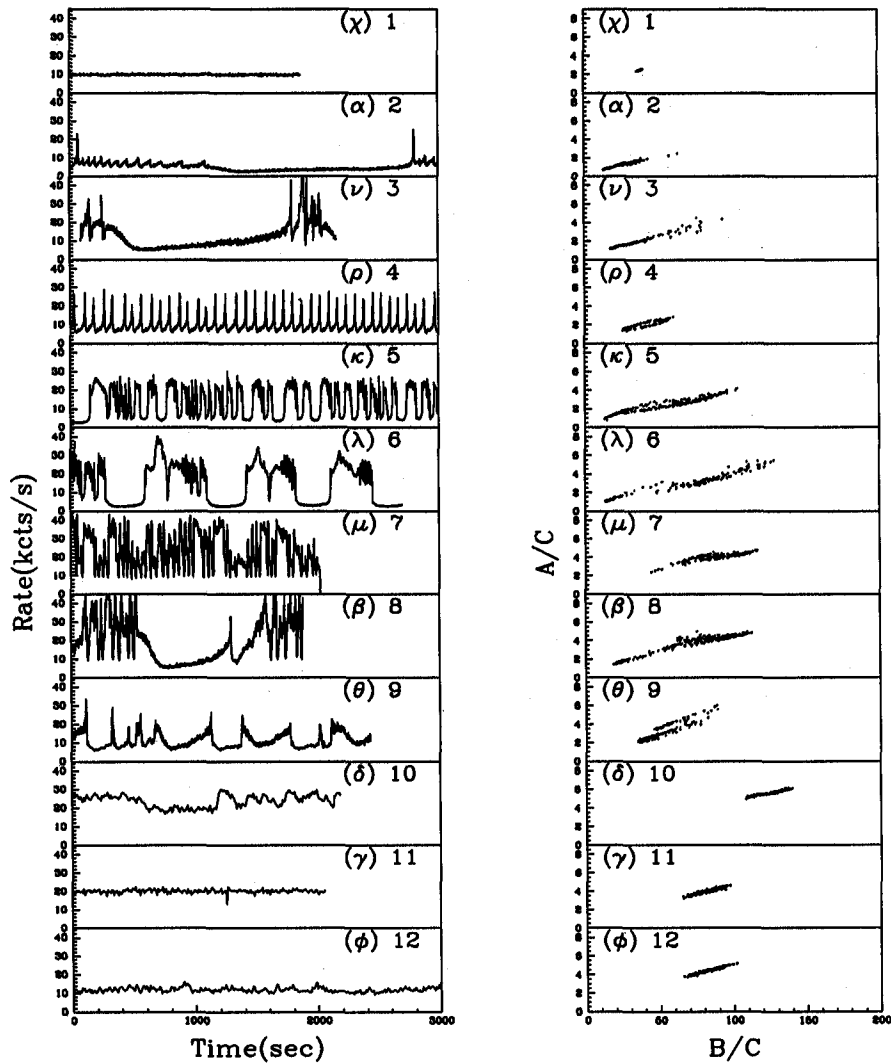


Figure 3.2: All possible light curves of the black hole candidate GRS 1915+105 (left panel). Along X-axis is time in seconds and along Y-axis is photon counts/sec (rate) in units of 10^3 . In right panel, 'softness ratio' A/C vs B/C is plotted for all the 12 classes shown in left panel. A, B and C are photon counts within intervals (0-3) keV, (3-17) keV and (17-60) keV respectively. Panel 1 belongs to Class-H, Panels (10-12) belong to Class-S, Panels (8-9) belong to Class-SS and the rest (Panels 2-7) belong to Class-I (see, text for details in section §3.2.1.)

be almost zero (Panel 4, class ρ). At the same time, the co-ordinate of the lower-left corner point in the softness ratio diagram varies systematically. It is already discussed that soft photon count A is directly related to the accretion rate in the Keplerian disk and hard photon count B is related to the degree of interception, and sum of Keplerian and sub-Keplerian accretion rate (total matter in the CENBOL). Thus, different variations of light curves in this sub-class are related to these accretion rates. The common ground is that the duration of the Off-states in all of these sub-classes are found to obey the correlation with QPO frequency, which will be discussed later. The process of generating light curves purely from theoretical consideration is more involved (as feedback and other non-linear process are present) and we will comment on about this in the subsequent sections.

3.2.2 Advective flow paradigm and GRS 1915+105

In the standard model of a thin disk (SS disk), matter moves in Keplerian orbits. But as matter enters into the horizon of black hole, the accreting flow should be supersonic and thus sub-Keplerian with almost constant angular momentum, i.e. flow deviates from the Keplerian disk. The sub-Keplerian flow with positive specific energy may or may not form a shock at the centrifugal barrier dominated boundary layer or CENBOL. The CENBOL is nothing but the ‘hot’ electron source (Comptonising region) and it intercepts soft photons from the Keplerian disk and reprocesses to hard X-rays (CT95). Depending on whether the Keplerian rate or sub-Keplerian halo rate dominates, the emerging spectra would be softer or harder. When the Keplerian rate is very low ($\sim 0.01 - 0.3\dot{M}_{Edd}$) and the sub-Keplerian rate is high ($\sim 1\dot{M}_{Edd}$), soft photons are fewer in number and electrons in CENBOL remain hot and produces hard X-rays and termed as canonical Hard state. On the other hand, if the Keplerian rate is high enough ($\geq 0.3\dot{M}_{Edd}$), the spectra would be soft and termed as Soft state. In GRS 1915+105, both this two type of spectra is observed. Not only that, the ‘hot’ CENBOL drives outflows from the disk along the vertical axis. When the outflow rate is very high, the sonic sphere (i.e., region of the wind till its first sonic surface) becomes dense enough to cool down due to Comptonisation of the soft photons from the Keplerian disk. Estimation of the rate of wind generation (Chakrabarti, 1998b; Chakrabarti, 1999; Das et al. 2001) shows that in purely soft states no outflow is possible and in purely hard states, outflow is very small. Thus above mentioned cooling of the sonic sphere is not possible. When compression ratio of the shock is intermediate, outflow rate is significant. After the sonic sphere is cooled, the sonic surface comes closer to the black hole and matter below it returns

back to disk, while matter above it separates as blobs. Thus blobby jets are expected in this intermediate states. The return flow acts as feedback on the already accreting flow and the count rate exhibits very interesting behavior. So, keeping all these features and characteristics of TCAF model in the back of our mind, we propose five fundamental modes of accretion/winds configuration to explain most of the observed light curves in GRS 1915+105.

(i) Hard state :

The accretion rate (in units of Eddington rate) in the Keplerian component is low $\dot{M}_K \sim 0.001 - 0.1$ and that of the sub-Keplerian (halo) component is high $\dot{M}_h \sim 1.0$. The combined sub-Keplerian flow encounters centrifugal barrier, thus inner edge is puffed up. Figure (3.3a) shows the schematic diagram of the accretion/wind system. *Spectral signature:* As soft photons are fewer in number and electrons remain hot, the emitted spectrum is hard in nature. If shocks form and oscillate, QPOs could be observed. This is the canonical hard state (H) and class χ belongs to this configuration.

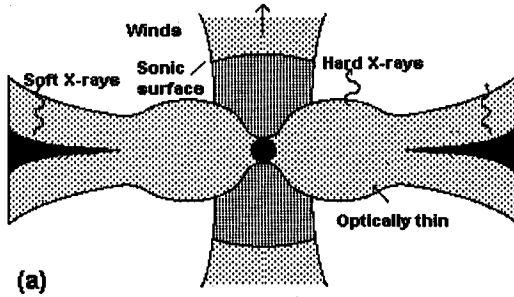
(ii) Off state :

The accretion rates are similar as above, but viscosity is lower than the critical viscosity $\alpha_{ss} \leq 0.01$ (α_{ss} is the Shakura-Sunyaev viscosity parameter) so that shocks may form. If the cooling rate in the post-shock region roughly agrees with the inflow rate, quasi-periodic oscillation of X-rays could be seen. Outflows are produced at a very low but steady rate, which intercepts soft photons from the Keplerian disk. Figure (3.3b) shows the schematic diagram. *Spectral signature:* Spectrum is hard with prominent QPO features. With time the spectrum can get softer if the sonic sphere (region till the sonic point in the outflow) gets filled up gradually. We termed this state as hard-wind (HW) state or Off state (low photon counts).

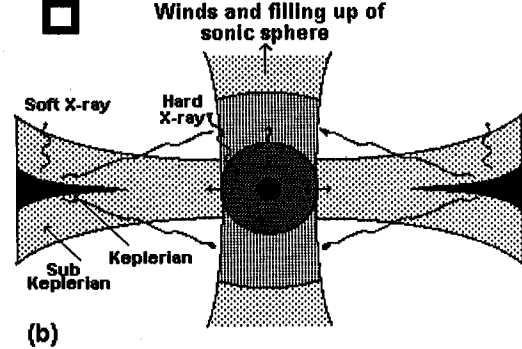
(iii) Dip state :

In this case, Keplerian rates are higher ($\dot{M}_K \sim 0.1 - 0.3$) and viscosity is also higher ($\alpha_{ss} \geq 0.01$) or more so that shocks are weaker. Post-shock flow is partly cooled due to Comptonisation. The outflow till the sonic sphere has sufficient optical depth that it is cooled down by Comptonisation. The sonic point comes down as sound speed goes down in this region. Flow which remains sub-sonic with respect to this sonic sphere loses outward drive and returns back to the disk, while the supersonic flow separates as blobs in the jets. Figure (3.3c) shows the schematic diagram. *Spectral signature:* Emitted spectrum has the tendency towards softer state and larger spectral slope. QPOs may not be visible as the post-shock region is cooler (with longer cooling time scale) while the infall time is shorter since the

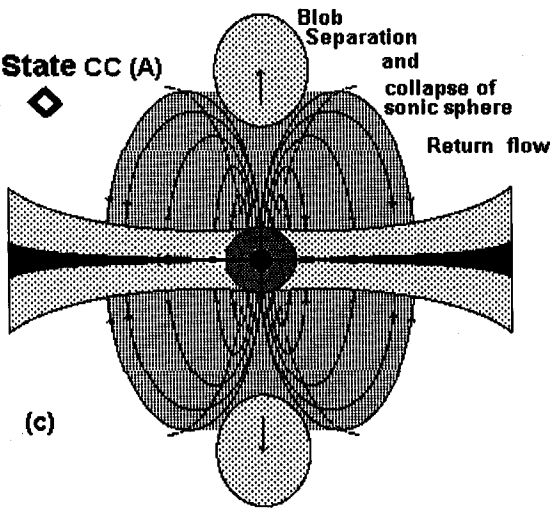
State H



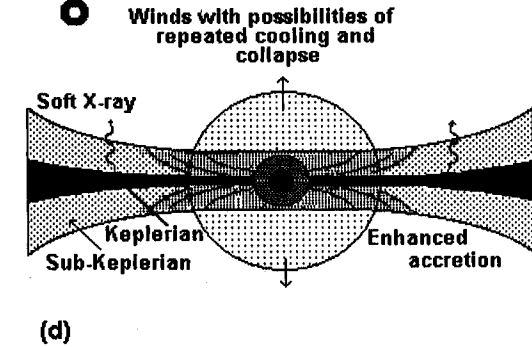
State HW (C)



State CC (A)



State EA (B)



State (S)

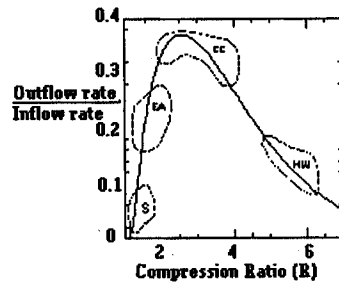
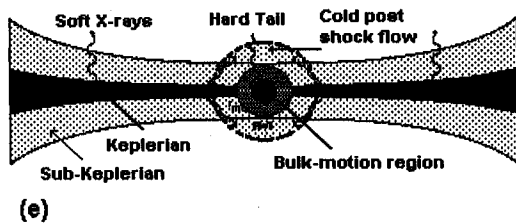


Figure 3.3: Schematic diagram of five possible fundamental modes of accretion-wind configuration. GRS 1915+105 stays most of the time in state HW, and moves CC and EA to form various classes of X-ray light curves. In parenthesis, we mark A, B and C to identify conjectured States of Belloni et al. (2000). The State H and State S represent canonical hard and soft states (see, text for details in section §3.2.2). The last Figure (f) shows variation the of the ratio of outflow to inflow rates as a function of compression ratio (R) (Chakrabarti, 1999).

Keplerian disk moves inward due to larger turbulent and radiative viscosity. This state is termed as ‘Dip’ state or the ‘Compton cool’ (CC) state.

(iv) On state :

In this state, original flow may remain similar to above, but the return flow enhances both Keplerian and sub-Keplerian flow rates in the last few hundred Schwarzschild radii. Figure (3.3d) shows the schematic diagram. Duration of this state is the duration of drainage of the excess accretion from the return flow. *Spectral signature*: Softer state with high photon flux is seen and no QPO should be observed. This high photon counts state is termed as ‘On’ state or the ‘enhanced accretion’ (EA) state.

(v) Soft state :

Accretion rate of the Keplerian component is high $\dot{M}_K \geq 0.3$ and the viscosity is high enough so that Keplerian disk moves in all the way to the inner edge of the disk and post-shock region is completely cooled down. Matter moves almost radially and transfers its momentum to soft photons (bulk motion Comptonisation). Figure (3.3e) shows the schematic diagram. *Spectral signature*: The emitted spectrum is blackbody dominated with a larger spectral slope with a weak power-law hard tail which extends upto high energies. No QPO feature observed in the PDS. This is the canonical soft state (S).

Now, the question is, can we relate the above five accretion/wind configuration with three basic states (A, B and C) of Belloni et al. (2000)? It is clear from the above discussion that three states are quite similar as of our CC, EA and HW respectively (Chakrabarti & Nandi, 2001; Chakrabarti et al. 2002a). It seems that HW (C) state exhibits QPOs. State EA (B) and CC (A) do not exhibit QPO. More interestingly, except for $C \rightarrow B$, all other transitions of states are allowed. In view of our classification of states, we can understand the reason. When the outflow rate is very high, the sonic sphere may be cooled down after the optical depths reaches unity and thus reaching CC from HW (i.e., $C \rightarrow A$). Now, there are two possibilities during this transition, either the flow separates completely as a blob and returns to state HW (i.e., $A \rightarrow C$) or the flow mostly return back to the accretion disk and enhances the accretion (i.e., $C \rightarrow A \rightarrow B$). This may in turn increases the outflow for a short while. As a result, after EA, state CC can form (during this transition shock becomes weaker and outflow is very mild) with enhanced accretion (i.e., $B \rightarrow A$). Similarly, after CC, if the whole matter from the sonic sphere separates as blobs or the enhanced matter is drained out completely, the flow can come back to HW or EA respectively (i.e., $A \rightarrow C$ or $A \rightarrow B$). Since HW state (C) produces

less no. of soft photons, state EA (B) is not directly possible from state HW (C) without first producing return flow and enhanced accretion. This may explain why a transition from $C \rightarrow B$ is difficult. Among all the possible transitions, sometimes $C \rightarrow A$ and $A \rightarrow C$ transitions are explained by studying the magnetic field activity in the accretion disk. In θ and β classes these type of transitions are observed whereas in class β other than C and A, state B i.e., enhanced accretion (EA) mode, is also observed. From the above discussion, it is clear that the complex behavior of GRS 1915+105 necessarily requires both the Keplerian and sub-Keplerian disks for a proper explanation of the light curves. A schematic representation of generating the light curves in GRS 1915+105, is given in Figure (4) of Chakrabarti & Nandi (2001). In some cases, Nandi et al. (2001a) found evidence of QPO in intermittent C state which are embedded in state B and it will be discussed in the next section.

Among other confirmations of the TCAF paradigm, Chakrabarti & Manickam, (2000) (hereafter referred to as CM00) found that the duration of the Off states (low count) strongly depend on the QPO frequency and showed that in low energy (1.9-4) keV QPO is absent. QPO is strongly featured in high energies. This agrees with the understanding that pre-CENBOL (pre-shock) soft photons do not participate in oscillations. This result was tested more stringently in Rao et al. (2000) by actually separating the blackbody photons and Comptonized power-law photons. They found that only Comptonized photons participate in oscillations. Hence, the QPOs observed in PDS of X-ray light curves of GRS 1915+105 are nothing but the oscillation of shocks i.e., the oscillation of CENBOL. Dhawan et al. (2000) observationally demonstrated that jets are originated from very close to the black hole i.e., from the CENBOL. Vadawale et al. (2001) made a detailed spectral study of X-ray dips (using *RXTE* data) observed during the huge radio flares and have presented the evidence for the disappearance of the inner disk i.e., Comptonized component (CENBOL). Such X-ray dips with huge radio flares are classified into θ and β light curves of Belloni et al. (2000). These features will be discussed in the subsequent sections.

3.2.3 Splitting of Peaks in Intermediate Class and related timing properties

According to our classification, α , ν , ρ , κ , λ and μ belong to Intermediate Class. Most of these light curves have two different photon counts state: Off state (low photon count) and On state (high photon count), with different time duration which varies from one class to another class. For instance, ρ class exhibits extremely regular

light curves with broad low count (Off) states and very narrow, spiky (double peak), high count (On) state (Fig. 3.6). Light curves in the ν class is similar to those of ρ , but its peaks are well separated (Fig. 3.5) (Nandi et al., 2001a). A complete ν class is shown in Figure (3.2a) where a long duration HW (C) state is also present. In λ class, both Off and On states are of longer time duration while in κ class these durations are relatively shorter (Fig. 3.2a). In Figure (3.4), we have plotted the subdivisions of a quasi-repetitive structure of the light curve of ν class. It is clear that there is a sharp peak ('first hiccup') at the onset of the On state and there is another sharp peak ('last hiccup') just prior to going to the Off state. Two peaks are marked as 'P1' and 'P2'. The entire light curve (Fig. 3.5) is almost a repetition of this section. Figure (3.5) presents the light curves of ν class (without long duration HW(C) state) clearly showing two peaks P1 and P2 in On state (CC(A) and EA(B)). The time lag between the two peaks is roughly constant on a day (about 10 secs) and we do not find any correlation between this lag and the duration of the Off state. The light curve is shown in four panels: the panels are drawn for channel energies (from top to bottom) 0-5.07 keV, 5.43-6.88 keV, 7.24-9.43 keV and 9.79-13.09 keV respectively (corresponding channels are 0-13, 14-18, 19-25 and 26-35 respectively). Note that while in low energies, photon counts in P1 is much larger compared to P2, in higher energies two peaks are roughly equal, suggesting that the spectrum of P2 is harder. Tamm, Chen & Swank, (1997) also noted the existence of these peaks and that P2 is harder compared to P1. In Figure (3.6), the light curve of ρ class is presented. In this case, the time lag between two peaks (P1 and P2) is about 4 second but other features are quite similar to those of Figure (3.5). The channel energies are marked on each panel.

Power density spectra (PDS) of three different regions (marked in Fig. 3.4) is shown in Figure (3.7) (left-sided). While selecting photons from 'P1' and 'P2' regions we took special care that they are not contaminated by the photons from the Off states. Also, to improve statistics, we added data from many peaks over the entire duration of the observation on that day. Note that in the Off state there is a distinct QPO of frequency $\nu_{qpo} = 7.4$ Hz. Photons in 'P1' also exhibit QPO though it is weaker ($\nu_{qpo} \sim 5.7$ Hz). QPO is completely absent from 'P2'. We also analyzed the light curve of ρ class and the PDS is shown in Figure (3.7) (right-sided). The result is generally the same. The QPO frequency in the Off state is given by $\nu_{qpo} = 6.3$ Hz and in in P1 peak $\nu_{qpo} = 6.8$ Hz. We therefore believe that the observed features may be generic.

One more interesting observation is that whenever the duration of On or high count state is large (i.e., κ and λ class), light curves become noisy and the count

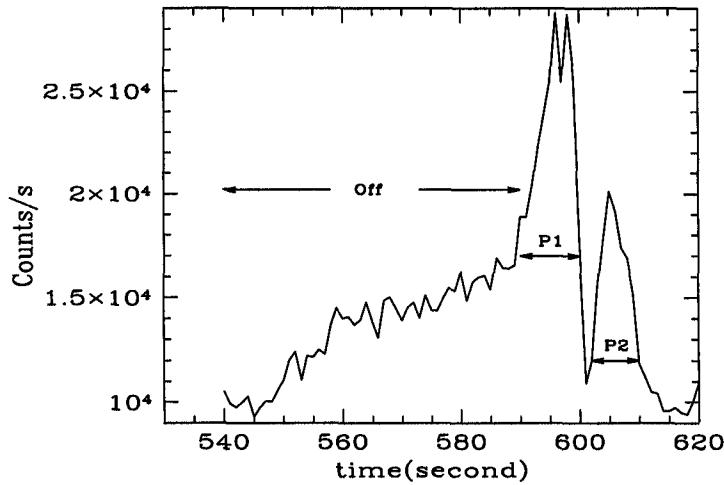


Figure 3.4: Subdivisions of a quasi-repetitive structure of the light curve of Oct. 15th 1996 (ν class). Relatively hard radiations are emitted in the region marked Off (PDS shows strong QPO) with relatively lower count rates. There are typically two major peaks, P1 followed by P2.

rates start oscillating wildly as the Off state is approached. The later half may be termed as 'On⁺⁺' state and Manickam & Chakrabarti, (1999) showed that this region exhibits a weak QPO. In fact, similar to Figure (3.5) and Figure (3.6), where the photons in P2 are harder compared to P1, one finds that On⁺⁺ state is harder compared to the first half of the On state. This is demonstrated in Figure (3.8), where a part of the light curve of κ class is shown. The energy ranges are marked in each panel. Upper four channels are from *RXTE* and the lower two channels are from *IXAE* data. The observation ID for *RXTE* data is 20186-03-01-02. In both the cases one second bin-size is chosen.

First note that *RXTE* and *IXAE* show very similar behaviors throughout the period of overlap of observations. Second, towards the end of each of the On states (which we termed as On⁺⁺ state for brevity), the light curves are noisy and generally oscillatory in nature. This same feature is also observed in λ class. Third, in both the experiments, the relative oscillations are increased with the increasing photon energy in On⁺⁺ state. Fourth, though generally the light curve may be called that of a κ class, several pieces of ρ class is evident. In fact, mini- ρ type light curves are also evident in the On⁺⁺ states giving clear evidence that the light curve in the ρ

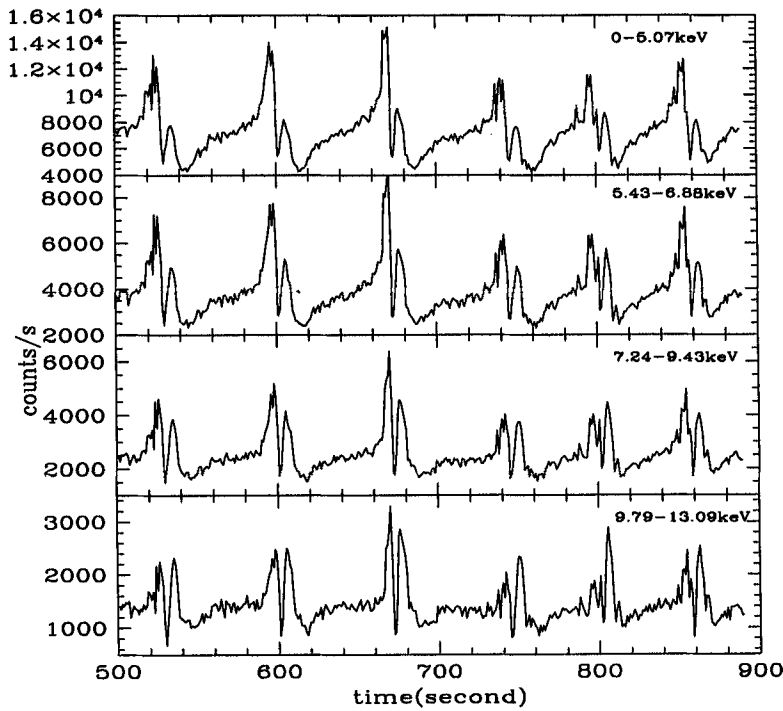


Figure 3.5: Four panels showing light curves of a part of the observation on Oct. 15th 1996 (ν class) at different channels (energies are marked). Note that ratio of photon counts in P1 and P2 tends to become unity at higher energies.

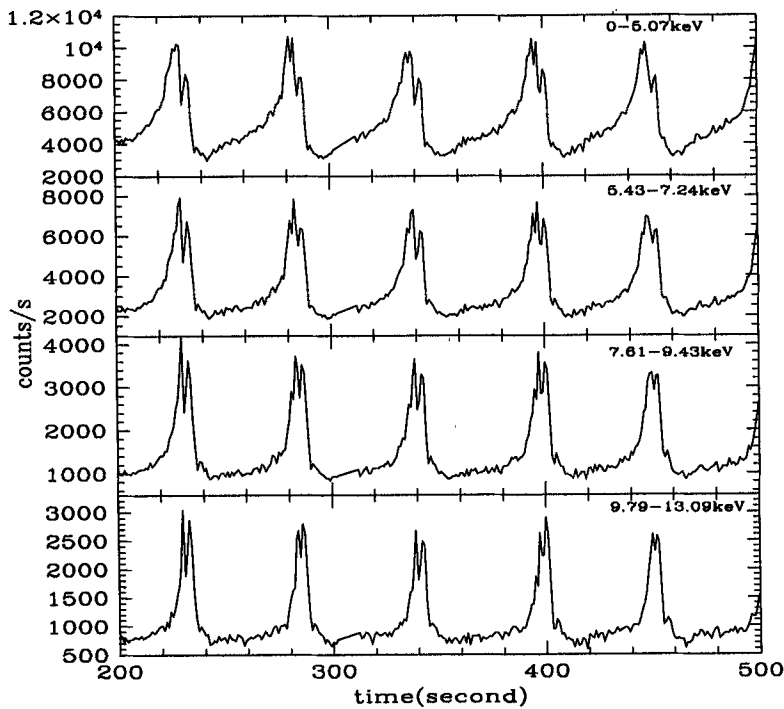


Figure 3.6: Four panels showing light curves of a part of the observation on June 22nd, 1997 (ρ class) at different channels (energies are marked).

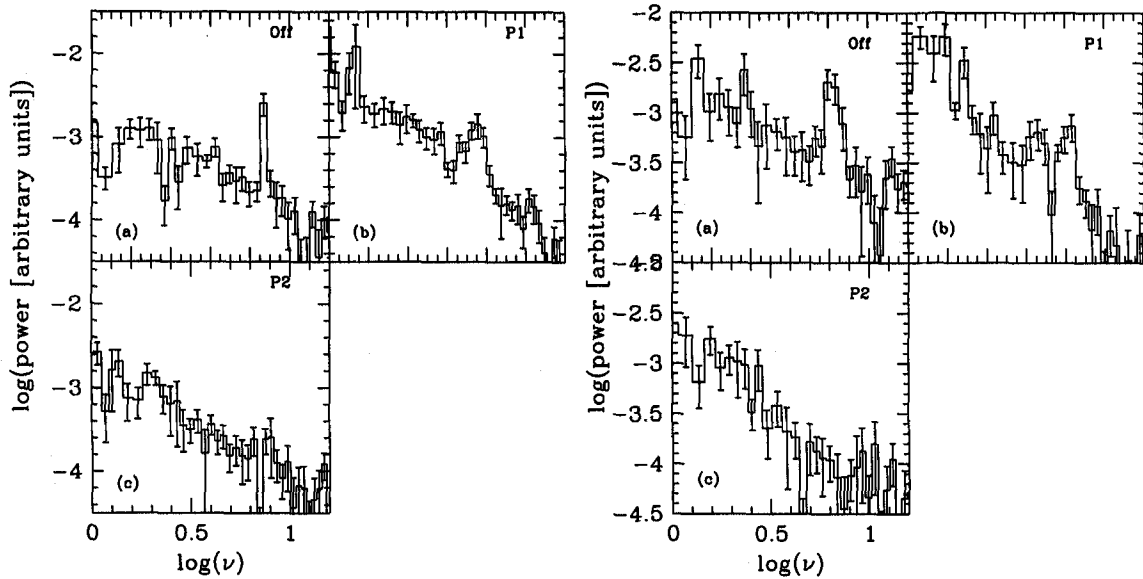


Figure 3.7: Power Density Spectra (PDS) of three regions (left-sided) marked in Fig. 3.4 of the ν class. Several data segments have been added to improve statistics. Right-sided PDS shows three regions (marked as Fig. 3.4) of ρ class (Fig. 3.6). Note the absence of QPOs in P2 in both PDS.

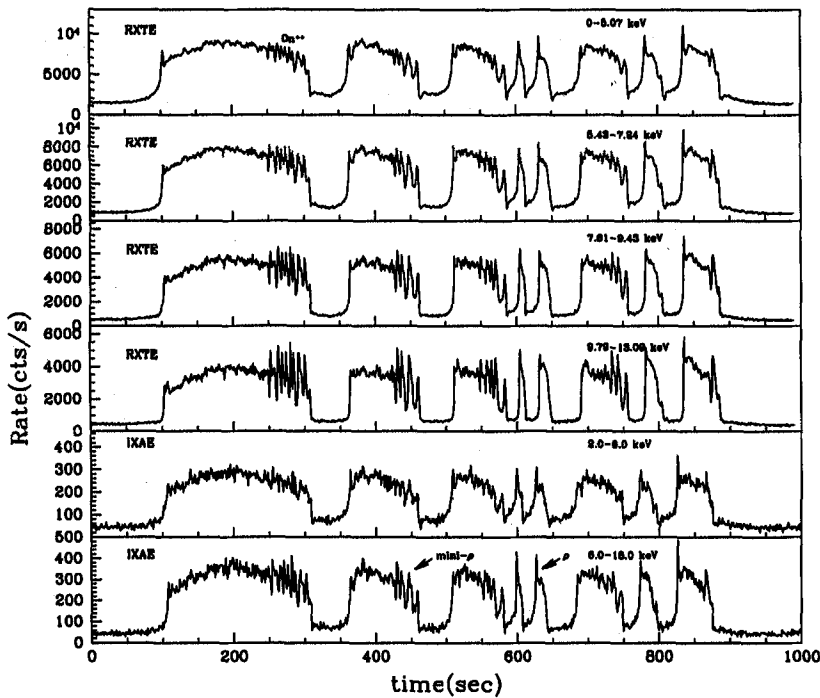


Figure 3.8: A part of the light curve from the κ class is shown. Upper four panels are from *RXTE* and the lower two panels are from *IXAE* data. A small arrow indicates a ρ type burst. Presence of mini- ρ bursts within a κ class (in On states) indicates that ρ may be the *fundamental* type of all burst.

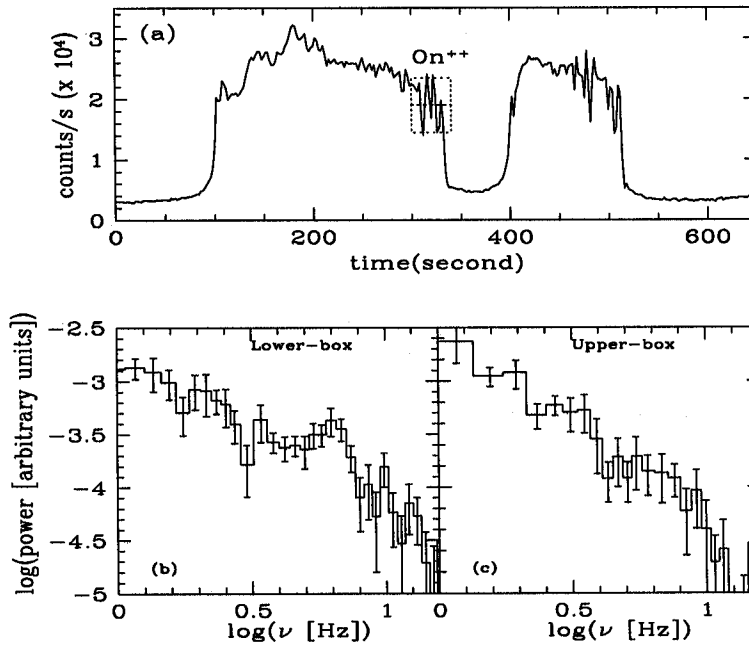


Figure 3.9: A part of the light curve from the so-called κ class is shown. In On^{++} state, two dotted boxes are drawn and below the PDS of each box is plotted. Note the presence of QPO in lower box, which are nothing but mini-off states corresponding to mini- ρ bursts.

class is more primitive. We have found a direct evidence of transition from κ class to ρ class in *IXAE* data. It will be discussed in the section §3.3.

In Figure (3.9), we show a part of the light curve (κ) on the same day, and draw two boxes (in dotted curves) at the On^{++} state. The photons from the upper box show no sign of QPO, while the photons from the lower box shows clear evidence of QPO. Since lower box contains photons which are from mini-Off states of the mini- ρ class mentioned above, it is not surprising that this show QPOs. Indeed, while the Off state on this day shows QPO of frequency 3.09 Hz, these mini-Off states show QPOs of frequency 6.25 Hz. This indicates that towards the end, the shock again starts developing much closer to the black hole giving rise to a higher oscillation frequency and when the shock is fully developed, the Off state (low photon count) begins with a QPO at 3.09 Hz.

An easily missed phenomenon in all these light curves is that most of the On states (high photon count) begin with a ‘hiccup’ or a small peak, which may be linked with ‘P1’ of ν class and also end with another ‘hiccup’ which may be linked

with ‘P2’.

Now, it is clear that since these peaks are separated by a few seconds (in ν and ρ), and generally one has a QPO while the other does not, their origins cannot be same. We believe that these phenomena could be understood easily using paradigm described in section §3.2.2 (see, Fig. 3.3). In these scenario, one may imagine that P1 forms when catastrophic cooling of the CENBOL-sonic sphere system takes place. Since P1 is a continuation of the Off state (HW), QPO is thus expected unless the shock is hidden under the cooler wind. The dip in between the P1 and P2 is due to the Compton cooling (CC) and P2 is due to the steepening of the last bit excess matter on the disk which is delayed by the viscous time scale. The viscous time which a ring of matter takes after it leaves the Keplerian disk from a transition radius (r_{tr} , where the flow deviates from a Keplerian disk, see CT95), and enters the post-shock region is given by $t_{visc} \sim \left(\frac{1}{\alpha_{ss}}\right) \left(\frac{h}{r}\right)^{-2} \left(\frac{r}{v_{Kep}}\right) = 10 \left(\frac{0.01}{\alpha_{ss}}\right) \left(\frac{0.1}{a_s}\right)^2 \left(\frac{r_{tr}}{100}\right)^{1/2}$ sec, where α_{ss} is the SS viscosity parameter, $h(r) \sim a_s r^{3/2}$ is the dimensionless instantaneous height of the disk (in vertical equilibrium) at a radius r (measured in units of $r_g = 2GM/c^2$, the Schwarzschild radius), v_{Kep} is the rotational velocity of the Keplerian orbit, and a_s is the speed of sound in units of velocity of light. As the ring of matter propagates through this region, it is illuminated by soft photons coming out of the Keplerian disk, but since it is outside the shock, its radiations do not participate in the oscillations. On the other hand, since rising side of P1 is in Off state, it shows a QPO. Due to the Compton cooling, the spectrum of P1 is softer. However P2 occurs when the excess matter is almost entirely drained out from the disk. Hence its spectrum is harder. One important thing to note that the viscosity parameter is less than the critical viscosity parameter ($\alpha_c=0.015$) (Chakrabarti, 1990; Chakrabarti & Molteni, 1995; Chakrabarti, 1996b), so our choice of $\alpha_{ss} = 0.01$ to explain the time scale (time lag between P1 and P2) is thus consistent with the presence of shocks in advective flow (i.e., TCAF model).

In general, as excess matter drains out of the CENBOL, its optical depth decreases and spectrum gets harder as well as the QPOs are observed in the On⁺⁺ state of κ and λ classes. This is observed in both the *RXTE* and *IXAE* data (see, Fig. 3.8).

3.3 Evidence of Class transitions in IXAE data

The X-ray observations of GRS 1915+105 were also carried out using the *IXAE*/PPC detectors on-board Indian Satellite IRS-P3 during the period of 1996 to 2000. The

observed X-ray variabilities are strongly similar to the few classes of *RXTE* observations and the variabilities include χ , κ , ρ , α , θ , and β (Paul et al. 1998; Yadav et al. 1999; Naik et al. 2001; 2002) classes. Recently, we have re-analyzed the *IXAE* data and found few evidences of class transition from one class to another (Chakrabarti et al. 2004; 2005). We have also identified some ‘unknown’ classes that basically bridges the gap between the transition of two known class. It is clearly showed in Chakrabarti et al. (2004) that the system probably had ‘predomination’ about the class transition about a few hundred seconds prior to the observation as is evidenced by the presence of drift in low frequency QPO (LFQPO) in the PDS. Not only that, we have also verified the transitions by studying the ‘mean photon index’ (MPI) s_ϕ behavior in detail (Chakrabarti et al. 2005). Basically, s_ϕ is the measure of hardness of light curves. In canonical classes (light curves), s_ϕ varies distinctly, whereas it is noisy during transitions. Figure (3.10) and Figure (3.11) show the transitions, one from κ to ρ class (via unknown class) and other one from χ to θ class.

In Table 3.1, we present the Log of observations which showed class transitions. The first column refers to the name of the Satellite. The second column shows the date of observation and the time when the observation started. The third column gives the orbit numbers (or, the Obs. ID in case of *RXTE*) plotted in the Figures (Fig. 3.10 and Fig. 3.11). Typically the time between two successive observations is around 80 mins. (Yadav et al. 1999). The fourth column gives the exact nature of class transition (Chakrabarti et al. 2005). Since during a transition, a given class is not found to be ‘canonical’ as defined by Belloni et al. (2000), we have put the class-names inside the quotation marks. These are the first results which shows the evidence of class transition from one class to another class in X-ray variabilities of GRS 1915+105.

The possible nature of the accretion flow to explain the class transitions could be understood by noting the variation in the photon count rate in the pre-transition period and the duration of a transition. The variation in the photon count rate points to the variation in the accretion rate while the duration gives an indication of the infall time. Given that there is a gap of more or less 80 min in between two successive observations of *IXAE*, the duration T_d could be at most $\sim 3-5$ hours i.e., 10000 – 20000 seconds. This is short even for a free falling gas from the outer edge of the disk located at $r_d \sim 1.5 \times 10^6$ in units of $r_g = 2GM/c^2$, the Schwarzschild radius of the central black hole of mass $M \approx 14 \pm 4M_\odot$ since this is around

$$T_{infall} \sim r_d^{3/2}(r_g/c) \sim 2.6 \times 10^5 \left(\frac{r_d}{1.5 \times 10^6} \right)^{3/2} \left(\frac{M}{14M_\odot} \right) \text{sec.} \quad (3.5)$$

The viscous time for a Keplerian disk of similar size must be at least ten to a hundred

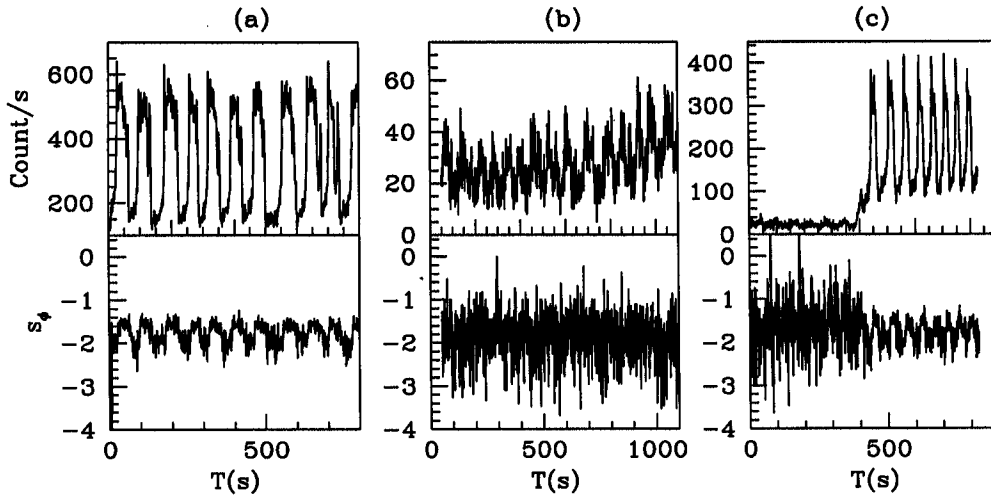


Figure 3.10: 2 – 18 keV light curves as observed by *IXAE* (upper panel) and mean photon spectral index s_ϕ (lower panel) in 1st, 3rd and 5th orbits of June 22nd, 1997. GRS 1915+105 was (a) in the κ class, (b) in an unknown class and (c) went to the ρ class on that day. Lower panels show how s_ϕ distinctly change. Specifically it is noisy during transition.

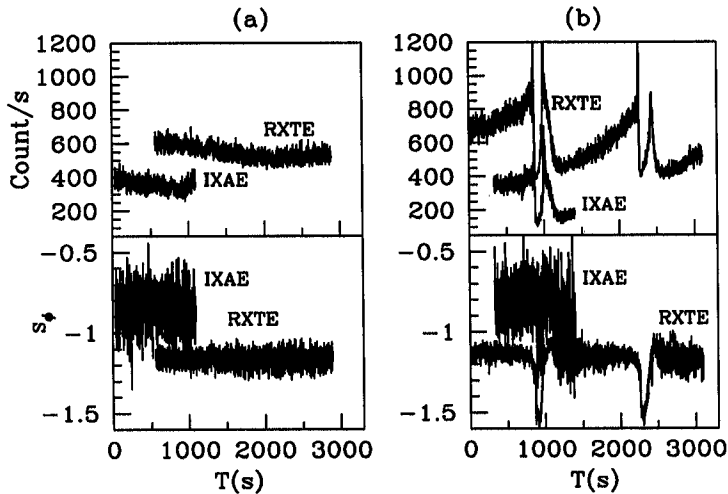


Figure 3.11: Class transition as seen from *IXAE* and *RXTE* observations on the 8th of June, 1999 in two successive orbits (marked). *RXTE* photon counts are divided by 50 and shifted upward by 200 cts/sec for comparison. In (a), there was no significant variation in light curve or spectral index. GRS 1915+105 was in a class similar to χ but the counts were a factor of 10-20 times higher. There is a gap of 44 min. in the two *RXTE* data presented in (a) and (b). In (b), the source is distinctly in θ class. *RXTE* data is less noisy than the *IXAE* data because of higher counts. It was binned in 2 – 6 keV and 6 – 15 keV before computing s_ϕ in order that comparison with *IXAE* could be made (for details, see Chakrabarti et al. 2005).

Table 3.1: Log of obs. of GRS 1915+105

Satellite	Date Time (UT) ^a	Orbit No. ObsID	Class transition
IXAE	22th June, 1997 12:12:24	1, 3, 5	$\kappa - > \rho$
IXAE	25th June, 1997 11:12:05	3, 4, 5	' χ ' - > ρ
IXAE	08th June, 1999 11:02	2, 3	' χ ' - > θ
RXTE	08th June, 1999 11:02	40702-01-03-00	' χ ' - > θ
IXAE	25th June, 2000	1, 2, 3	$\rho - > \alpha$

a) Starting time of the observation

times larger, i.e., few $\times 10^6$ seconds for any reasonable viscosity. This indicates that if the transition takes place in 10^4 seconds, the accretion flow must be nearly freely falling, i.e., sub-Keplerian, and must originate from intermediate distances, rather than from the outer edge, i.e., out of Keplerian disk through energy deposition or otherwise. This flow is neither a static corona, nor a flow which is radiatively less efficient. Smith et al. (2001, 2002) indeed found observational signatures of the nearly free-falling matter in several black hole candidates which causes dynamical spectral state changes. We thus believe that the variation of the rate of the sub-Keplerian matter may be responsible for the class transitions we discussed here.

3.4 Spectral variabilities in GRS 1915+105

As GRS 1915+105 is unique in X-ray variabilities, one could expect that this source would also show richness in spectral properties. Detailed spectral studies show that the spectral properties are different in different classes of light curves. In section §3.2.2, we have already discussed the timing characteristics of GRS 1915+105 and explained the variabilities with the help of Advective Flow Paradigm. Here we are going to study the spectral properties of GRS 1915+105 to show that the spectral variabilities of GRS 1915+105 couldn't be well explained without the accretion/outflows configurations that we have proposed (Chakrabarti & Nandi, 2001; Chakrabarti et al. 2002a). Detailed spectral studies show that λ , κ classes are associ-

ated with outflows and β , θ classes are linked with jets which are produced/launched from the post-shock region i.e., CENBOL.

3.4.1 Spectral signature of Outflows from CENBOL: A theoretical study

It is quite well known that accretion and outflows/jets are common in systems that include black holes. It is already discussed that in Advective Flow Paradigm, CENBOL is responsible for the outflows and the jets. So it is natural to ask a question, what could be the spectral signature of a CENBOL which is losing matter to hot winds or that is gaining matter from the cooler winds? On the one hand, one might imagine that a CENBOL with lesser electron density and therefore optical depth would be hotter and harder. But, in presence of a large number of soft photons from the pre-CENBOL flow, fewer electrons of CENBOL would be easier to cool. Using this argument, Chakrabarti (1998a) computed the spectrum taking loss of matter due to the winds from CENBOL into account and showed that emergent spectrum become softer. Similarly, when cooler matter of the subsonic region of the outflow falls back by a return flow, enhanced optical depth of the CENBOL makes it harder to cool it down by the same number of soft-photons emerging from the Keplerian disk in the pre-CENBOL region and the resultant spectrum should be hardened in comparison to the spectrum in the high/soft state. Thus, *softening of the hard state spectrum and hardening of the soft state spectrum could indicate that accretion rate is not preserved within CENBOL— i.e., matter is lost or gained* (We refer this as ‘SH-HS’ phenomenon for brevity.) (Chakrabarti et al. 2002c). Of course, the degree by which the spectrum changes depends on mass loss/gain. Figure (3.12) shows the cartoon diagrams of the possible disk-wind connection. A detailed description of this configuration is already given in section §3.2.2 to explain the Off/On transitions (λ and κ class) which are observed in GRS 1915+105. As a result, the crossover energy point between hard and soft states (spectrum) shifts towards the higher energy in the Off/On states. In Figure (3.13), we present two sets of calculated spectra to illustrate this. Disk accretion rates for the soft and the hard states are $0.1\dot{M}_{Edd}$ and $0.02\dot{M}_{Edd}$, respectively. The halo accretion rate is kept fixed at $0.2\dot{M}_{Edd}$, and the shock is located at $R_s = 6$ and $R_s = 40$, respectively, in high/soft and low/hard states (*dotted curves*). This is in line with the general conclusions that the inner edge moves in during soft states. The solid curves are drawn to mimic the Off (mass-loss) and On (mass-gain) state spectra. In these cases, the disk accretion rates are kept as before, but 20% of CENBOL matter is assumed

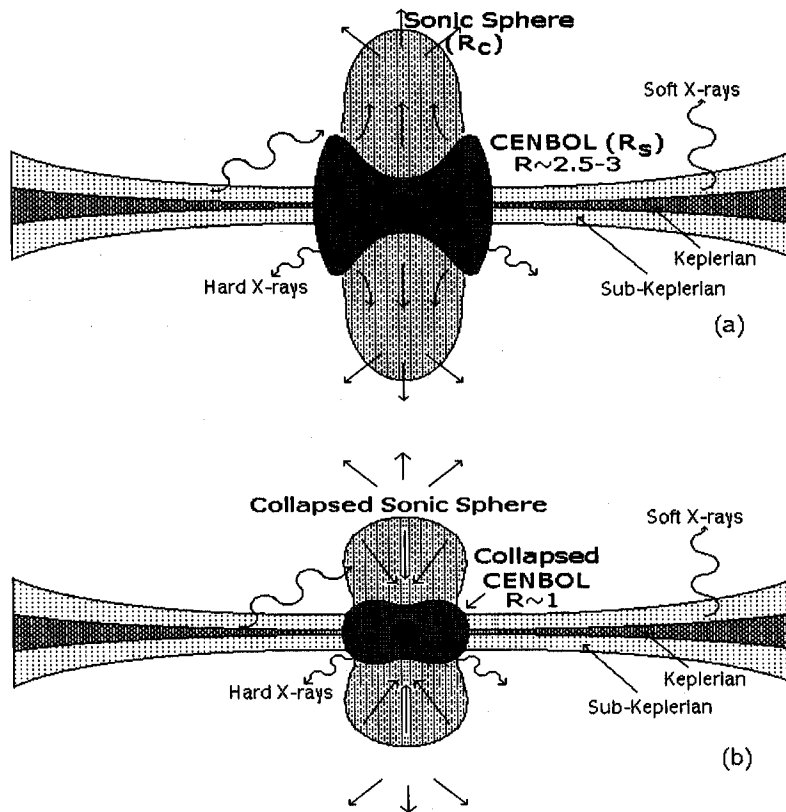


Figure 3.12: Cartoon diagrams of the accretion disk near a black hole that includes a boundary layer (surface of the CENBOL). Panel (a) shows the 'Off' state where the outflow material fills up the region to the sonic point R_c . Panel (b) shows cases with prominent 'On' states where the material in the subsonic region cools and falls back on the CENBOL and takes time to drain.

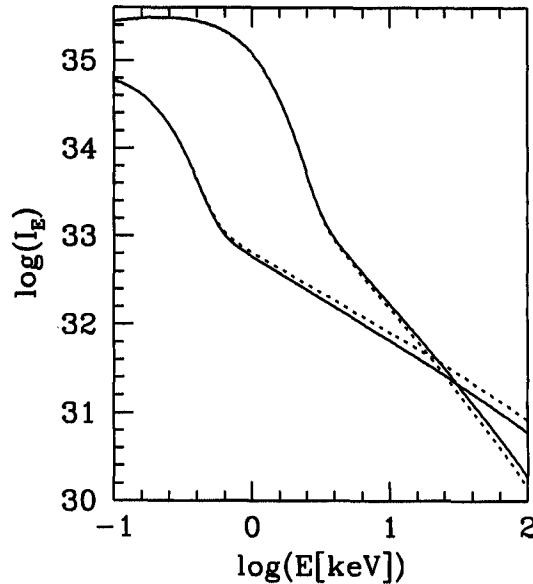


Figure 3.13: Typical nature of calculated spectra (uncorrected for absorption) for Off and On states (*solid curves*) and low/hard and high/soft states (*dotted curves*). In the Off state, the spectrum appears to be softened with respect to low/hard state, and in On state, the spectrum appears to be hardened with respect to high/soft state. As a result, the pivoting point shifts toward higher energy.

to be lost in wind in the Off state (see, e.g., Molteni, Lanzafame & Chakrabarti, 1994), and 10% (for illustration purpose) of matter in the outflow is assumed to be falling back on the halo in the On state. Because of the selective softening and hardening, the intersection point (pivot) is located at higher energy.

3.4.2 Evidence for winds/outflows in the spectra of GRS 1915+105

We have analyzed the *RXTE* public archive data. The source was in a low/hard state from 1996 December up to 1997 March. The spectral and temporal behavior during the low state was stable, characterized by a hard spectrum (with the power-law photon index of ~ 2 , and the total flux in the power-law component being $\sim 80\%$) and 1 – 10 Hz QPOs (Trudolyubov, Churanov, & Gilfanov, 1999; Munro, Morgan & Remillard, 1999). Since the source was in similar state on several occasions (1996 July-August; 1997 October; 1998 September-October), we treat this state as the low/hard state of GRS 1915+105. These observations belong to the χ class. The

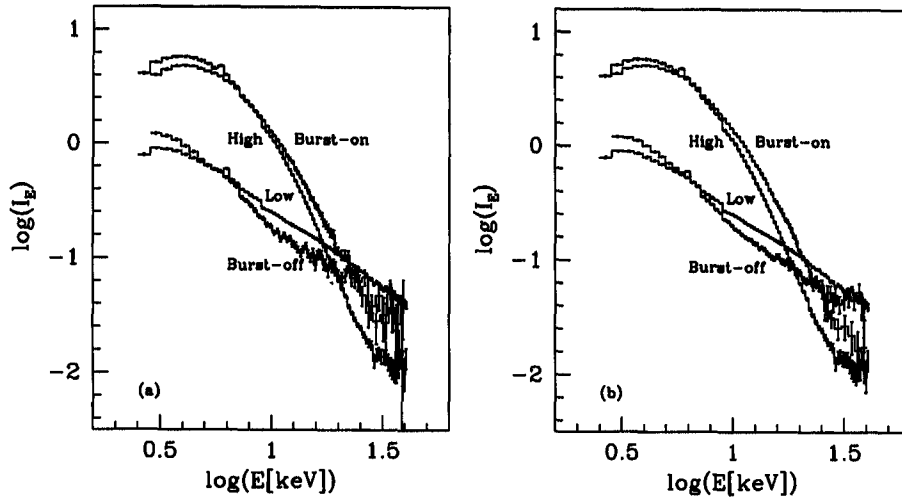


Figure 3.14: Unfolded *RXTE*/PCA spectra of GRS 1915+105 obtained during the low/hard and high/soft states compared with Off and On states spectra during the irregular bursts observed on (a) 1997 June 18, (b) 1997 July 10. The histogram shows the fitted model. During the Off/On transitions, the pivoting occurs at a higher energy.

source reached a high state in August 1997. During this period of observation, light curves of GRS 1915+105 belong to the γ and δ class. We have selected one observation each from the low/hard state and high/soft state to quantify the spectral parameters. The low state (χ_2) observation was carried out on 1997 March 26 with ObsID no. 20402-01-21-00 (Muno et al. 1999; Trudolyubov et al. 1999). The high state (δ) observation was carried out on 1997 August 19 with ObsID no. 20402-01-41-00 (Muno et al. 1999). Spectra of these two states are shown in Figure (3.14) and are marked.

During the transition between these two states, GRS 1915+105 exhibited several types of bursting behavior. The light curves are classified as ρ , κ , λ etc. (Intermediate class). It was seen that for about a month the source was in a burst mode with a slow transition from regular bursts to irregular bursts and then again to a regular burst of shorter duration (Yadav et al. 1999). In Yadav et al. (1999), it was postulated that the irregular bursts are manifestations of rapid state changes. As discussed earlier, CM00 explained the Off/On transitions (similar to the Burst-off and Burst-on transition of Yadav et al. 1999) in terms of the repeated filling of the

outflow region and its abrupt cooling due to inverse Comptonisation. We present the spectral properties of GRS 1915+105 during the irregular bursts observed on 1997 June 18 (ObsID: 20402-01-33-00) in Figure (3.14a) and on 1997 July 10 (ObsID: 20402-01-36-00) in Figure (3.14b). The light curves of this two observation belong to κ and λ class.

We have generated the 129 channel energy spectra from the Standard-2 mode of the PCA for each of the above observations. Standard procedures for data selection, background estimation and response matrix generation have been applied. PCA consists of five units and data from all the units are added together. We have fitted the energy spectrum of the source using a model consisting of disk-blackbody and power-law with absorption by intervening cold material parameterized as equivalent Hydrogen column density, N_H . The value of N_H has been kept fixed at $6 \times 10^{22} \text{ cm}^{-2}$. We have included a Gaussian line near the expected K_α emission from iron and absorption edge due to iron. These features help to mimic the reflection spectrum usually found in other Galactic black hole candidate sources like Cygnus X-1 (Gierlinski et al. 1997). Systematic errors of 1 – 2 % have been added to the data. XSPEC version 10.0 has been used to fit the spectra.

The resultant unfolded spectra for the two spectral states presented in Figure (3.14) shows that in the low state, the disk blackbody component has lower temperature ($kT_{in} = 0.60 \pm 0.05 \text{ keV}$) and a larger inner disk radius ($R_{in} = 115 \pm 2 \text{ km}$) compared to the high state, which has the inner disk temperature of $1.95 \pm 0.01 \text{ keV}$ and the inner disk radius of $26 \pm 1 \text{ km}$. The inner disk parameters are calculated using a distance to the source of 10 kpc and inclination to the disk of 70° . The power-law index in the low state (2.40 ± 0.01) is much flatter than that seen in the high state (3.61 ± 0.02). (The quoted errors are for nominal 90% confidence levels obtained by the condition of $\chi^2_{min} + 2.7$). The disk blackbody component has a 3 – 26 keV flux of <10% of the total flux in the low state, which increase to >65%. The two spectra intersect at around 17 keV. It should be noted here that the disk-blackbody inner radius gives systematically lower value when scattering effects are not considered and PCA generally shows steeper spectrum due to uncertainties in the response matrix. The results presented here, however, highlights the broad changes in the spectral states.

The corresponding unfolded spectra during the irregular burst of June 18, 1997 presented in Figure (3.14a) shows that the burst-off state has spectral parameters similar to that of the low state ($kT_{in} = 0.76 \text{ keV}$, index = 2.76) and the burst-on state spectrum resembles that of the high state ($kT_{in} = 2.2 \text{ keV}$, index = 3.1). At the same time it is clear that the spectrum of the burst-off state is softer than that

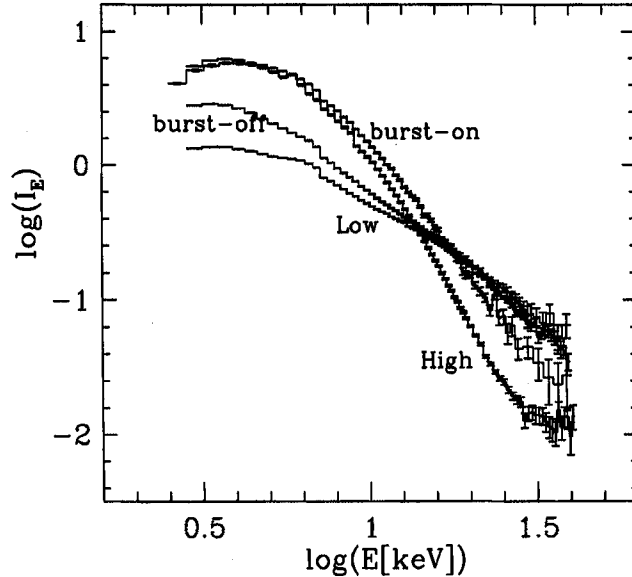


Figure 3.15: Same as Fig. 3.14, except that the observation ID of the On/Off and low states are chosen close to 1997 October 31 when IR/Radio flares were observed (Dhawan et al. 2000). The spectral slope variations are also seen on this days.

of the low state and the spectrum of the burst-on state is harder than that of the high/soft state. As a result, the energy at which the two spectra pivot is much high (~ 26 keV). The same behavior is seen also in Figure (3.14b). The low/hard and high/soft states have been kept as above. The intersection in all these cases during the burst-on/burst-off transition is around 25 keV, far above the low/high intersection.

A direct correlation between the *RXTE*/ASM and IR/Radio observations were confirmed by Dhawan et al. (2000). The activity of radio emission at around 500AU made on 1997 October 31 would be perturbed by the CENBOL activity of around 1997 October 28.5 if perturbation propagates with 0.98c. This activity is associated with the β class. In the next section, we will discuss about the spectral properties of θ and β classes which are found to be associated with the huge flare activity in GRS 1915+105. Unfortunately, no PCA data is available for 28th or 29th of October. Figure (3.15) shows the spectral properties on 1997 October 30 (ObsID: 20402-01-52-02). To compare with the high/low spectrum, we chose the low state observation closest to this day, namely, 1997 October 25 (ObsID: 20402-01-52-00; χ_3 class),

and we chose the same high state as mentioned above. The spectral slopes of the high, low, on and off states are 3.61 ± 0.02 , 2.76 ± 0.018 , 3.34 ± 0.021 and 2.85 ± 0.013 , respectively. This again shows the softening of the hard states and the hardening of the soft states. The intersection of the spectra of low and high states is at around 14 keV (the pivotal point changes due to the different low state observation; χ_2 is radio-quiet and χ_3 is radio-loud) whereas that of the On and Off states of β class (On and Of states refer to Class B (EA) and Class C (HW) of Belloni et al. 2000) is at around 17 keV. Thus, the effect of winds/jets could be significant here as well.

3.4.3 Inner disk disappearance in GRS 1915+105: Spectral study

After its discovery in X-rays in 1992, the galactic black hole GRS 1915+105 was then observed in the radio band, where plasma ejection activity was observed (Mirabel & Rodriguez, 1994) and the source earned the name *microquasar*, because of its phenomenological resemblance with a quasar but scaled down in mass, luminosity etc. by several orders of magnitude. Later on, using simultaneous observation in different wave-bands, several authors (Pooley & Fender, 1997; Fender & Pooley, 1998; Eikenberry et al. 1998) were able to correlate the X-ray variability with the radio and IR emissions and their claim about the disk-jet connection was further established when Feroci et al. (1999) reported the disappearance of inner accretion disk during a small radio flare. It has been noticed that huge radio flare activity observed in GRS 1915+105 was associated with the θ and β light curves of X-ray variability (Mirabel & Rodriguez, 1999; hereafter referred to MR99; Dhawan et al. 2000; Naik et al. 2001). One such simultaneous observation in X-ray/IR/Radio is shown in Figure (3.16). The observation was carried out on 1997 September 09 and the X-ray variability observed is the β class of Belloni et al. (2000). The infrared flare starts just after the recovery from the hard X-ray dip (QPO is seen in PDS), when a sharp, isolated X-ray spike is observed i.e., mass is ejected from the inner disk during the hard X-ray dip. The subsequent soft X-ray dip (QPO is not seen in PDS) with the chaotic X-ray variation in X-rays, is connected with the replenishment of the inner accretion disk. Thus the relativistic plasma clouds that observed as synchrotron emission at IR first and later at radio, are originated from the inner part of the accretion disk.

More recently, Vadawale et al. (2001) made a detailed spectral study of X-ray dips of θ class during the huge radio flares (~ 450 mJy) using the PCA and HEXTE data of *RXTE* and have presented the evidence for the disappearance of the inner accretion disk. From their analysis, it was clear that there was lack of photon counts

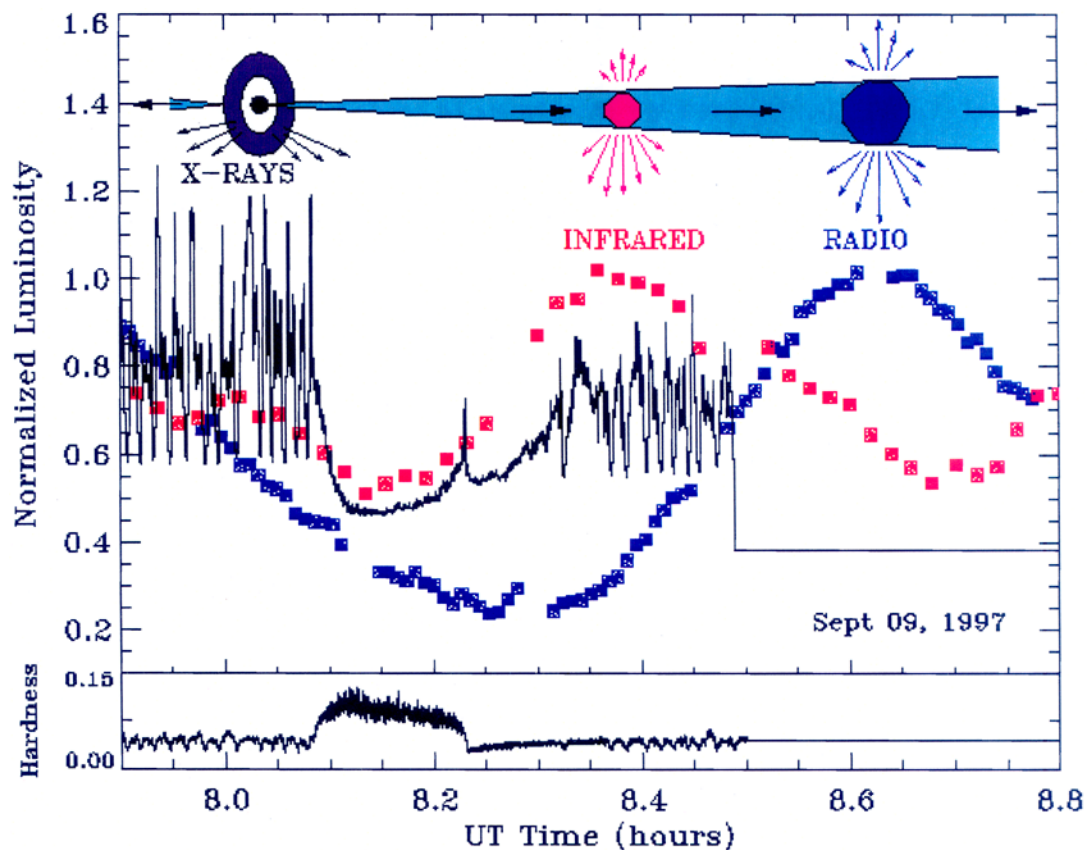


Figure 3.16: The simultaneous observation of GRS 1915+105 in Radio, infrared and X-rays on 1997 September 9. The X-ray light curve belongs to β class of Belloni et al. (2000). The infrared flare starts during the recovery from the hard X-ray dips, when a sharp, isolated X-ray spike is observed. These observations also show that there is anti-correlation between the hard X-rays and Radio emissions, suggesting that during huge radio flares, the inner part of the accretion disk is evacuated in the form of jets. This Figure is adopted from Mirabel & Rodriguez (1999) (MR99).

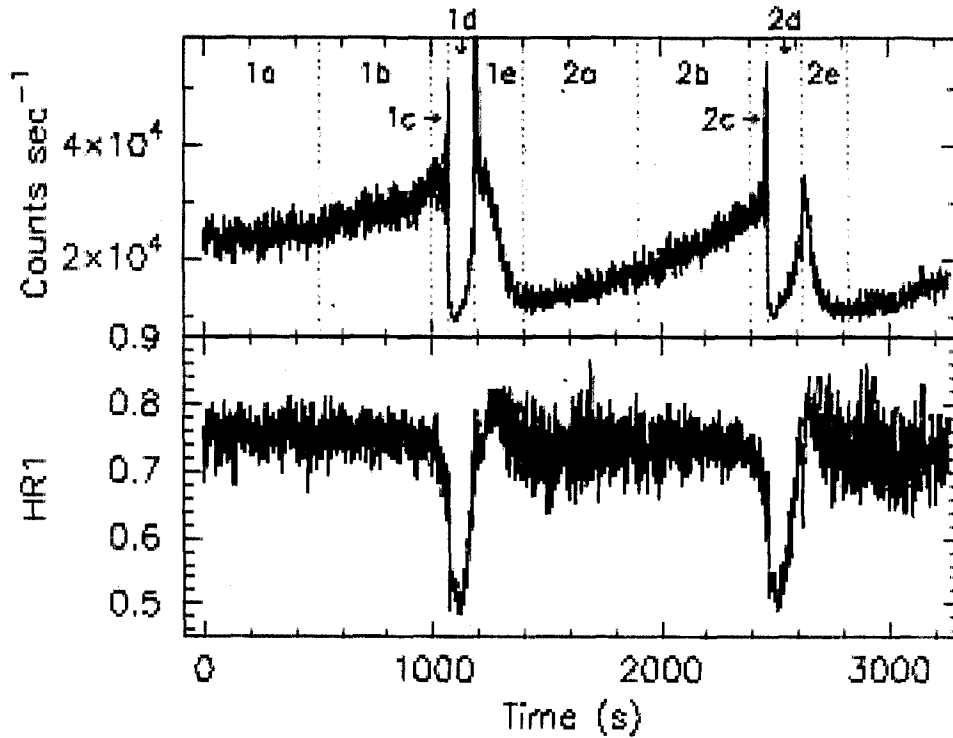


Figure 3.17: X-ray light curve (θ class) (top panel) and hardness ratio (HR1: 6 – 15 keV/2 – 6 keV) (bottom panel) of GRS 1915+105 obtained on 1999 June 8 using *RXTE*/PCA. The region chosen for proving the assertion of inner disk disappearance are shown in top panel, separated by dotted lines (see, Vadawale et al. 2001). The bottom panel shows that the hard X-rays are strongly reduced during the ‘soft dips’ in the light curve.

in the energy range 8 – 30 keV during the soft X-ray dips. The *RXTE*/PCA light curve (θ class) along with the hardness ratio (HR1) is shown in Figure (3.17). In the top panel, light curve (time in X-axis and photon counts/sec in Y-axis) and in the bottom panel hardness ratio HR1 (6 – 15 keV/2 – 6 keV) are plotted. It is seen that during the soft dips (marked as ‘1d’ and ‘2d’) when the count rate went down, the hard X-ray flux itself went down. From the spectral analysis, Vadawale et al. (2001) also showed that the Comptonised component gets suppressed during the soft dips, whereas it is strong in hard dips (the combined segment of a, b, c) (see, Figure (2) of Vadawale et al. 2001). In fact, the timing analysis also suggests that the 0.1 – 10 Hz QPO is present in the hard dips and it disappears during the soft dips.

It has already been proven that the hard X-rays and QPOs are directly related with the CENBOL activity (CM00; Rao et al. 2000). Thus this analysis establishes the fact that the inner part of accretion disk i.e., Comptonised region (CENBOL) is ejected away and it starts re-building itself during the soft dips (in time segment '1d').

Since the disappearance of the inner disk is seen to be correlated with intense radio activity, the role of the magnetic field becomes important inside the disk to understand the system completely. So we investigated the magnetic flux tube dynamics inside the disk to explain the disk evacuation phenomenon. This study is throughly discussed in *Chapter 5*.

Chapter 4

SS 433: ENIGMA OF THE PAST CENTURY

4.1 The Black Hole Candidate SS 433

The enigmatic and the most unusual galactic source Stephenson-Sanduleak 433 (SS 433), was first noted in an objective prism survey (Stephenson & Sanduleak, 1977) as one of the many emission line objects with strong $H\alpha$ (6562.8\AA). This was identified as the optical counterpart of a variable radio source (Clark & Murdin, 1978; Ryle et al. 1978; Seaquist et al. 1979). The X-ray emission from the source was also variable (Seward et al. 1976; Forman et al. 1978; Marshall et al. 1979). The observations in different wave-bands Radio/optical/X-ray have given the confirmation of a single and same source, named SS 433, where from all the radiations are coming out and its association with the supernova remnants (SNR), W50. The source SS 433, also known as V1343 Aquilae, is located in the constellation Aquila with the coordinate position *right ascension* (α_{2000}) = $19^h 11^m 49.56^s$ and *declination* ($\delta_{2000.0}$) = $+04^\circ 58' 57.6''$. The discovery of SS 433 and several historical accounts associated with this source are precisely written in an excellent book *The Quest for SS433* by David H. Clark (1985). Figure (4.1) shows the Very Large Array (VLA) radio map of SNR W50 (upper one). The radio counterpart of SS 433 is the bright unresolved source at the centre of the image ($\alpha_{1950} = 19^h 09^m 21.28^s$ and $\delta_{1950.0} = +04^\circ 53' 54.0''$). In lower part of Figure (4.1), the complex optical spectrum of SS 433 is presented where blue-shifted and red-shifted lines of $H\alpha$ and $H\beta$ are clearly seen along with the stationary lines.

The extraordinary complexity of SS 433, which made the object unique in nature, arises from the detailed optical spectrum study. Margon and his collaborators (Margon et al. 1979) showed, in addition to very strong, broad Balmer ($H\alpha$) line, that the optical spectrum of SS 433 contains a pair of broad emission features of unfamiliar wavelengths. These unknown emissions are found to be consistent with

Doppler-shifted Balmer ($H\alpha$) line: one is red shifted $H\alpha$ and other one is blue shifted $H\alpha$. Not only that, the Doppler-shifted line features are seen to change in wavelengths in a periodic manner of a time scale of ~ 164 days. Another important feature is that the ‘moving’ lines show huge amplitude variations. The red-shifted line achieves a maximum of about $50,000 \text{ km sec}^{-1}$ whereas the blue-shifted one achieves a minimum of $30,000 \text{ km sec}^{-1}$. It is also noticed that the average, or mean, velocity of the sum of the red and blueshift systems remains approximately constant at a value of about $12,000 \text{ km sec}^{-1}$ ($z = 0.034$). A compilation of optical spectra of SS 433 is shown in Figure (4.2). It is clear that the principal Balmer line ($H\alpha$) appears to stay fixed throughout, while the blue and redshifted lines drift through the spectrum from one night to the next.

The above unique features observed in SS 433 are well explained by ‘kinematic model’ which hypothesizes that the matter is ejected from the star (compact object) in two opposing jets that are collimated and oppositely aligned to within a few degree (Fabian & Rees, 1979; Milgrom 1979). At the same time, Abell & Morgan (1979) able to provide the solutions for the free parameters of the proposed ‘kinematic model’. The parameters include the ejection velocity (v_j) of matter of $0.26c$, rotation of the jet axis with a period (P) of ~ 164 days, the inclination angle (i) 79° between the central axis of the rotation cone and the line of sight and the half-angle (θ) 20° of the cone (angle between the central axis and the jet axis). At the end of this section, we will discuss the ‘kinematic model’ for SS 433 in detail. The knowledge of the ‘kinematic model’ is necessary for us to understand the system completely. The profiles (e.g broadness, time variability and asymmetry of the lines, see Fig. 4.2) of the ‘moving’ lines are generally described by the time overlap of multiple discrete ejection components, commonly referred to as the ‘bullets’ (Margon, Grandi & Downes, 1980; Murdin, Clark & Martin, 1980; Vermeulen et al. 1993b). The bullet-like features and the precession of the relativistic jets of SS 433 are also verified from the study of radio observation. The radio observation of SS 433 with VLA showed that the central radio source is surrounded by the extended (ejecting) components which moved with time. The extended (ejecting) components were found to move outwards in two opposite directions in a *corkscrew* like motion, shown in Figure (4.3) (Hjellming & Johnston, 1981a; 1981b). Their result also suggests that the source is 5.0 kpc away. Later on, using VLBI observations of radio jets (‘bullets’), Vermeulen et al. (1993a) independently confirmed the *precessional* and *relativistic* nature of the jets of SS 433 and also derived an accurate distance to the source of about $4.85 \pm 0.2 \text{ kpc}$. The free parameters derived by Abell & Margon (1979), almost 25 years ago, remain consistent with the ‘kinematic model’ even after

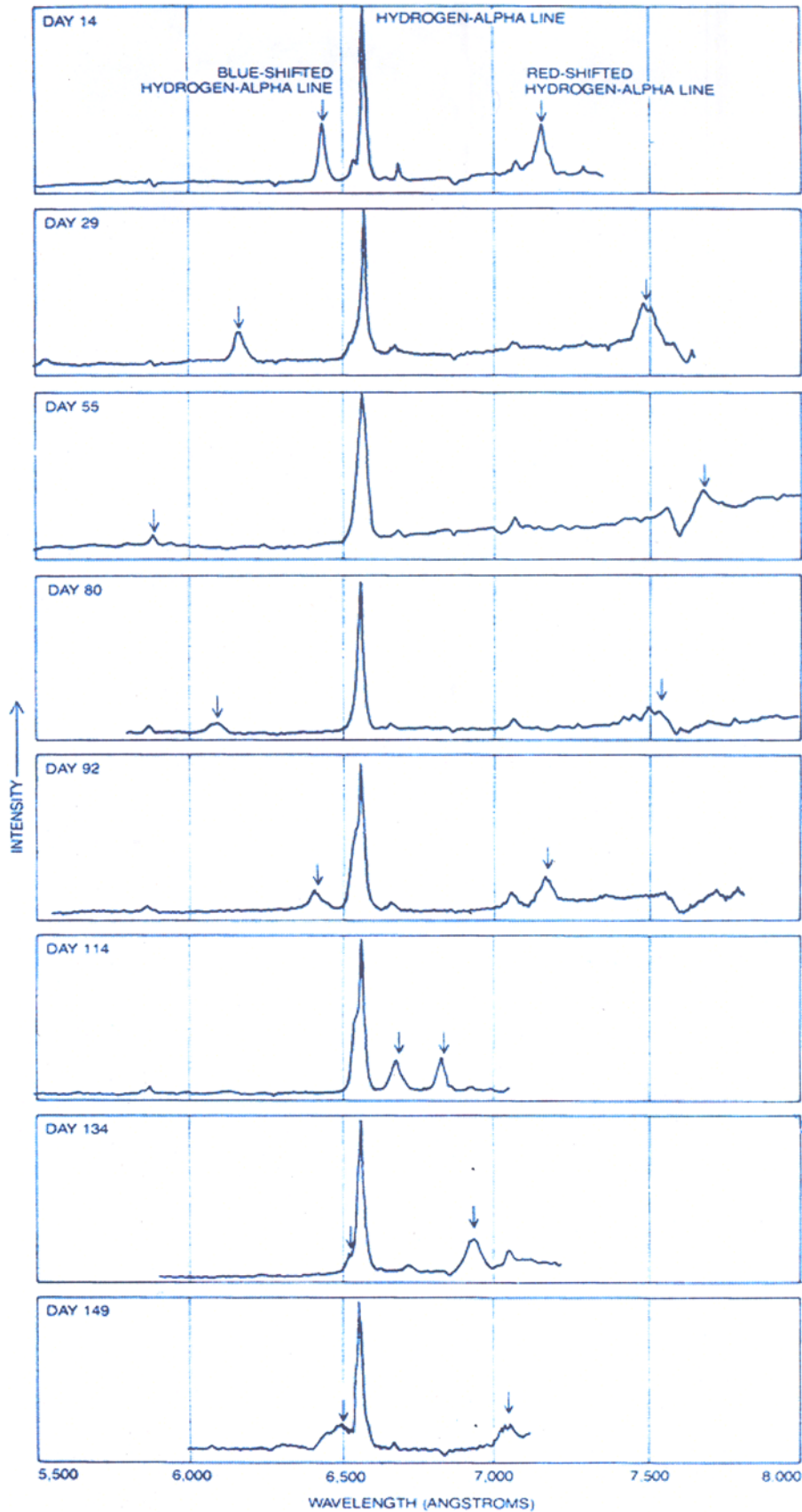


Figure 4.2: A compilation of optical spectra of SS 433 obtained with a 5 month period from Lick Observatory. The principle H α line is fixed. The periodic motion, in opposite directions, of the blue and red moving lines is clear.

a one decade (Margon & Anderson, 1989) and two decade (Eikenberry et al. 2001) of observation of SS 433.

Apart from the *precessional* periodicity (P) in SS 433, Margon, Grandi & Downes (1980) also found another periodicity of 13.5 ± 0.5 days of strengths of the low velocity ‘stationary’ Balmer lines ($H\alpha$), which was in good agreement with the 13.1 days low-amplitude radial velocity period discovered by Crampton, Cowley & Hutchings (1980), and strongly suggests that SS 433 is a binary system related to the better studied galactic X-ray sources. The precise measurement of the *precessional* period of the jets and *orbital* period of the binary companion are given in Anderson, Margon & Grandi (1983), Katz et al. (1982) and Goranskii et al. (1998). SS 433 also exhibits ‘nodding’ motion of the jets on a ~ 6.3 days period (Katz et al. 1982) due to the nutation of the accretion disk. This motion is obvious in disk-jet system of SS 433, because it is a closed binary system and the binary *orbital* period is not negligible compared with the *precessional* period of the jets.

It is clear from the above discussion (see, also the excellent reviews by Margon, 1984 and Cherepashchuk, 1988), why SS 433 is a unique object and is known to be the enigma of the past century. Still there remains various puzzles concerning SS 433: the nature of the compact object (a black hole or a neutron star), the nature of the accretion disk (e.g., thick or slim/thin), the origin of disk-jet precession (a master disk or a slaved disk), and the collimation and formation of jets.

So, to understand the physical processes operating in SS 433 binary system and the evolutionary status of this object, it is necessary to know the masses of the components in the system. The mass-losing star (donor star) is probably massive with a mass of at least $10M_{\odot}$, since the mass loss rate in the system is enormous $\sim 10^{-4}M/\text{year}$ (van den Heuvel, 1981), and as a consequence, supercritical accretion onto the compact object takes place.

The first attempt to understand the nature of the compact object in SS 433, was made by Goncharskii et al. (1984). They have analyzed the optical light curves of SS 433 using a geometrically thin accretion disk and have estimated a mass $M_c \approx 6M_{\odot}$ for the compact object in this binary system, suggesting the presence of a black hole. In a different approach, Antokhina & Cherepashchuk (1985) interpreted the optical light curves of SS 433 for a geometrically thick and precessing disk, and their estimation of mass $M_c \geq 4M_{\odot}$ for the compact object, confirmed that SS 433 is a possible black hole candidate.

At a later time, another attempt was made to estimate the mass function of SS 433 system by several authors (Mazeh et al. 1987; Antokhina & Cherepashchuk,

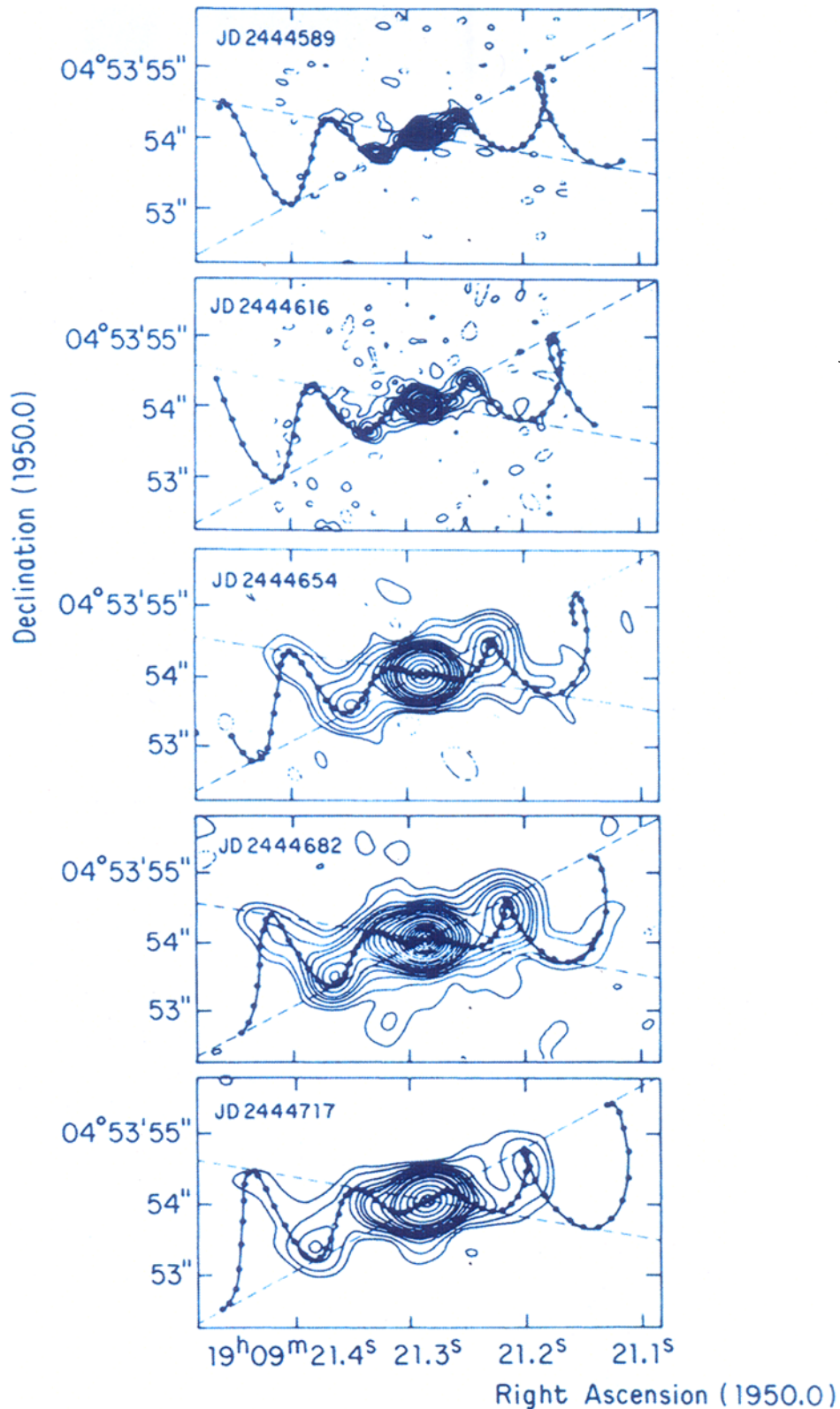


Figure 4.3: VLA maps of SS 433 produced over a 4 month period showing the growth of the radio lobes as predicted by the *corkscrew* motion of the precessing relativistic jets in the kinematic model (Hjellming & Johnston, 1981a; 1981b).

1987). The mass function derived from the He II ($\lambda 4686$) emission line indicates that the donor star mass is greater than $8M_{\odot}$ (Fabrika & Bychkova, 1990). These results conclude that SS 433 is a high mass X-ray binary (HMXB) system. The whole system is embedded in a gaseous shell of SNR W50 (see, Fig. 4.1).

Recently, Gies et al. (2002) pointed out from their UV spectroscopic study of the mass donor star of SS 433 that the nature of the companion is probably an evolved A-type star (i.e., massive donor) with a black hole of mass $M_c = 11 \pm 5M_{\odot}$ as the primary. Most recent estimates (Hillwig et al. 2004) suggest that the central object could be a low mass black hole ($2.9 \pm 0.7M_{\odot}$) with a high mass ($10.9 \pm 3.1M_{\odot}$) companion.

Even after the extensive optical and radio monitoring of the source, which has provided the basic parameters to describe the disk-jet system, still there are few things to be addressed for the relativistic jet source SS 433. To find out the consistency of the ‘kinematic model’ in X-ray emissions, it is also important to observe the source in X-rays. Detailed temporal and spectral studies of X-ray observations made with *RXTE* will be discussed in section §4.3 and it is found that our analysis strongly supports the ‘kinematic model’. It is already discussed about the observational supports for the ‘bullet-like’ ejections in SS 433 in optical band as well as in the radio band. In the next section (§4.2), we are going to present the possible photometric evidence of the ‘bullet-like’ ejections which is inferred from the X-ray, IR and radio observations. Before going to present our multi-wavelength results, now we will discuss about the ‘kinematic model’ for SS 433.

Kinematic model for SS 433

SS 433, the enigma of the last century, has attracted many astrophysicists due to its bizarre optical spectrum. It has been observed that the X-ray binary SS 433 exhibits an extraordinary optical spectrum with a very intense, stationary H α emission line along with two other Doppler-shifted emission lines, one is associated with the blue-shift system and other one is with the red-shift system. After an extensive optical monitoring, during late 80’s of the last century, a group of astrophysicists noticed that the two Doppler-shifted lines drift slowly as the observed night progress and the lines come to their original positions after every ~ 164 days and the observed range of Doppler-shifts corresponds to velocities from 0 to $-30,000 \text{ km sec}^{-1}$ in the blue-shift system and 11,000 to $48,000 \text{ km sec}^{-1}$ in the red-shift system. Thereafter, they came up with an idea that the radiation with variable Doppler shift is emitted from hot matter ejected by the central object of SS 433 system at high but nearly constant velocity in oppositely directed narrow beams and rotation of the beam axis

basically provides the observed radial velocity variations. This model is known as 'kinematic model' for SS 433 and is still applicable to this system even after 25 years of its discovery.

To calculate the Doppler shift (z) of the emission lines, a schematic representation of the 'kinematic model' of SS 433 with different notations and system components are shown in Figure (4.4). Now, let us assume that the beam axis rotates with an angular velocity $\omega = 2\pi/p$ ($p = 164$ days be the precessional period of the jets) and the line-of-sight (from Earth) lie along a unit vector \hat{e} , inclined at an angle i to the beam rotation axis (i.e., in the direction of unit vector \hat{n} , ON direction). As the beam axis rotates, the jets of the ejected matter which is in the direction of \hat{r} (OP direction), oriented at an angle θ to the beam rotation axis, describe a conical motion about the axis, with a period of 164 days. Let \mathbf{v} be the velocity of the matter stream in the jet which is in the same hemisphere as \hat{e} , and let the beam of the matter stream (i.e., the jet) at a particular time of rotation is along the unit vector of \hat{r}' (OQ direction). The direction cosine, l , of the angle between \hat{r}' and \hat{e} is

$$\begin{aligned} l = \hat{r}' \cdot \hat{e} &= [\hat{n}(\hat{n} \cdot \hat{r}) + [\hat{r} - \hat{n}(\hat{n} \cdot \hat{r})]\cos\omega t + (\hat{r} \times \hat{n})\sin\omega t] \cdot \hat{e} \\ &= \cos i \cos\theta + [\cos(i - \theta) - \cos i \cos\theta]\cos\omega t \\ &= \sin\theta \sin i \cos\omega t + \cos\theta \cos i. \end{aligned} \quad (4.1)$$

The corresponding direction cosine, l' , of the angle between line of sight and the opposite matter stream (i.e. the jet is pointing opposite to the unit vector \hat{r}' , not shown in Fig. 1.5) is

$$l' = -l = -\sin\theta \sin i \cos\omega t - \cos\theta \cos i. \quad (4.2)$$

Now, it is easy to write down the Doppler shift (z) formula for the emission lines as the direction cosine is known to us. The classical Doppler shift is $z = lv$, where v is the velocity of the matter. But, when the matter velocity (v) is a large fraction of velocity of light (c), we must use the result from special relativity and the corresponding shift is known as relativistic Doppler shift which can be written as,

$$1 + z = \gamma(1 + lv), \quad (4.3)$$

where l must be direction cosine in the observer's frame and $\gamma = (1 - v^2)^{-1/2}$ is the Lorentz factor. Therefore, the observed Doppler shifts of the matter streams with direction cosines l and l' are

$$1 + z = \gamma(1 \pm v\sin\theta \sin i \cos\omega t \pm \cos\theta \cos i). \quad (4.4)$$

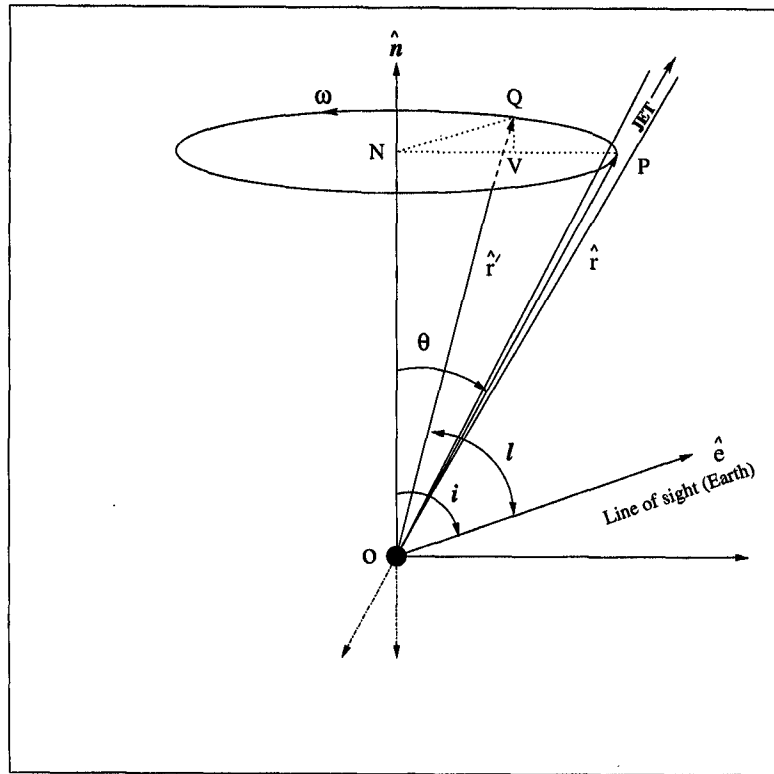


Figure 4.4: Schematic representation of kinematic model of SS 433 (see, section §4.1 for different notations). Figure shows the almost narrow beam (one-sided jet in the direction of OP) emanating along the rotation axis of an accretion disk which precesses with an angular velocity ω (jets precess with 164 day period).

The solution of the above equation which describes the 'kinematic model' for SS 433, depends on few free parameters (e.g., v , θ , i and p). The Doppler shifts (z) of emission lines of SS 433 observed for a long period during 1978-83 follow exactly the above equation with the best fit parameter values for $v/c = 0.2601$, $\theta = 19.85^\circ$, $i = 78.83^\circ$ and $p = 162.532$ days. As the jet precess in ~ 164 days, the precessional phase (ψ) of the jet can be calculated from the following formula,

$$\psi = 2\pi(t - t_0)/p, \quad (4.5)$$

where t_0 refers to the epoch of zero precessional phase (i.e., $\psi = 0$) which corresponds to the greatest radial velocity separation and greatest disk opening angle. Figure (4.5) shows the variation of Doppler shifts (z) of the two oppositely directed

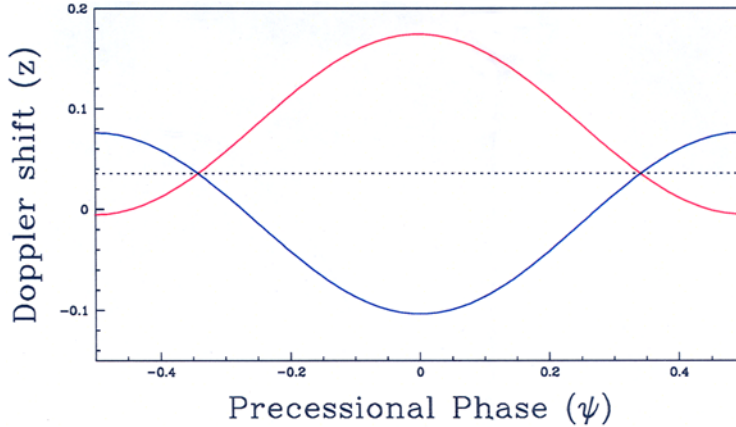


Figure 4.5: The variation of Doppler shifts (z) with the precessional phase (ψ). Red and blue curves correspond to Doppler shifted values of the moving emission lines that are originated from the receding (red jet) and approaching (blue jet) jets respectively. The average velocity of the moving lines is about $12000 \text{ km sec}^{-1}$ which is almost constant and it is marked as dashed line ($z=0.034$).

jets with their precessional phases (ψ) which are calculated using Equation (4.4), (4.5) and the best fit parameters values. Here, we have used the value of $t_0 = \text{HJD } 2451458.12$ (Goranski et al. 1998) as a epoch of $\psi = 0$.

4.2 Photometric evidence of ejection of ‘bullet-like’ features

SS 433 is the only object which has the strong observational support for the ejection of matter in a bullet-like fashion (Grandi, 1981; Brown et al. 1991; Vermeulen, 1993b). Since the bullets of energy $\sim 10^{35}$ ergs do not change their speed for a considerable time ($\sim 1 - 2$ days), Chakrabarti et al. (2002b) postulated that they must be ejected from accretion disk itself. They presented a mechanism to produce quasi-regular bullets, which will be discussed in the next chapter. These bullets would be ejected from X-ray emitting region and propagate through optical, infrared ($\sim 10^{13-14}$ cm) and finally to radio emitting region at $\gtrsim 10^{15}$ cm (roughly the distance covered in a day with $v \sim v_{jet}$) or so. Thus if the object is in a low or quiescence state, each individual bullet flaring and dying away in a few minutes time scale, should be observable not only in optical wavelengths (Grandi, 1981; Margon,

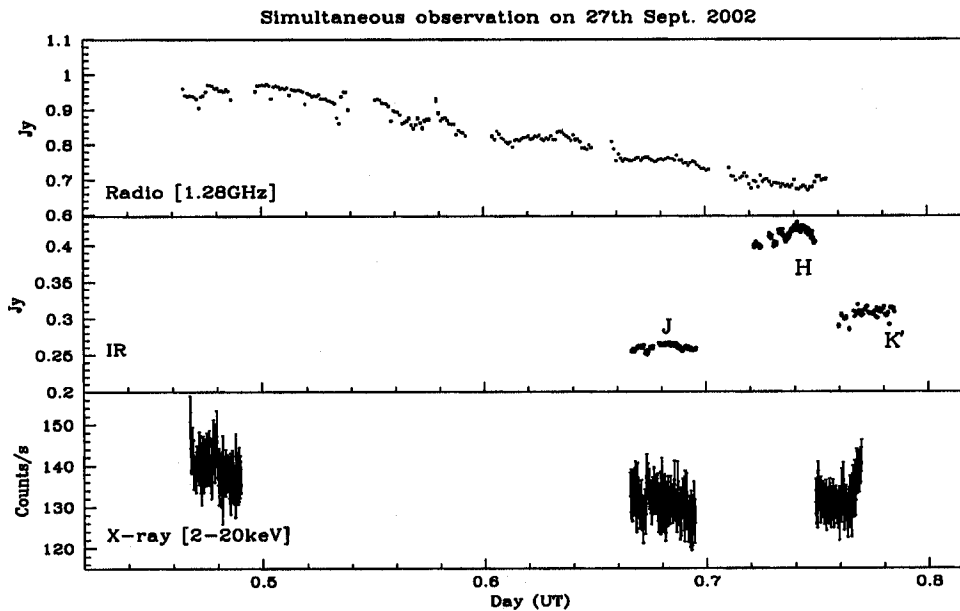


Figure 4.6: Multi-wavelength observation of short time variability in SS 433 by radio (top), IR (middle) and X-ray (bottom) on 2002 September 27. The observations were made at the *GMRT*, Pune, at 1.28 GHz (radio), 1.2 m Mt. Abu infrared telescope at *J*, *H* and *K'* bands and with the *RXTE* satellite (2 – 20 keV), respectively.

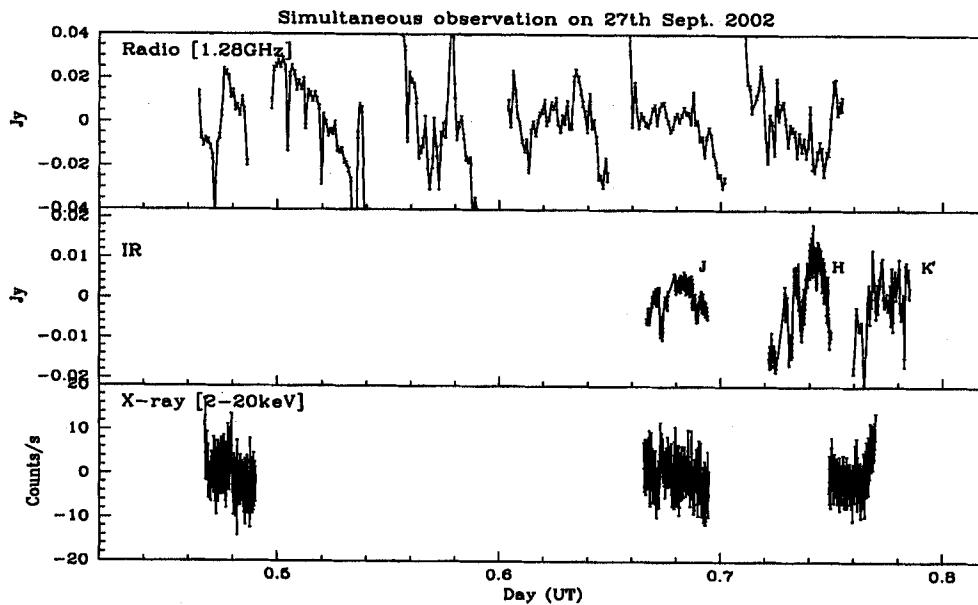


Figure 4.7: Observations in Fig. 4.6 are plotted around the mean taken in each spell of observation. Considerable variations at a time scale of a few minutes are observed. (for details, see Chakrabarti et al. 2003).

1984; Brown et al. 1991) but also in all the wavelengths, including X-ray, IR and radio emitting regions.

Here, we present the results from the X-ray, infrared (IR) and radio observations of 27th and 29th of September, 2002. Our results indicate that there are considerable variations in the timescale of minutes in all the wavelengths. These may be called micro-flares and indeed we are able to catch such flares both in X-ray and Radio observations. The observations carried out in different wave bands and the data reduction techniques were discussed in Chakrabarti et al. (2003).

4.2.1 Results on short time-scale variabilities

The observational result of September 27th, 2002 is shown in Figure (4.6) with UT (Day) along the X-axis. The upper and middle panels show the radio and IR fluxes (uncorrected for reddening) in Jansky and the lower panel shows X-ray counts per second in 2 – 20 keV.

These observations correspond to an average flux of 10^{-14} ergs $\text{cm}^{-2}\text{sec}^{-1}$, 5×10^{-10} ergs $\text{cm}^{-2}\text{sec}^{-1}$ and 10^{-10} ergs $\text{cm}^{-2}\text{sec}^{-1}$ respectively. Observations in radio and IR were carried out during 25-30th September, 2002 and no signature of any persistent ‘flare’ was observed. The radio data clearly showed a tendency to go down from 1.0 Jy to 0.7 Jy reaching at about 0.3 Jy on 28th/29th, while the X-ray data showed a tendency to rise towards the end of the observation of the 27th. The IR data in each band remained virtually constant. The H-band result was found to be higher compared to the J and K’ band results during 25th-29th September, 2002.

In Figure (4.7), we present the same light curves as in Figure (4.6) but plotted around the ‘local’ mean, i.e., mean values taken in each ‘spell’ of observation. We note that there are significant variations in a matter of minutes in observations at all the wavelengths. From an eye-estimate, we see the variability time-scale to be $T_{var} \sim 2 - 8$ minutes. The error-bars include errors in individual measurements plus the standard deviation of the flux variation in the light curve. To impress that the variability is real, we show in Figure (4.8) the differential flux density variation of IR observations in the J and H bands during 27 September 2002 using differential photometry and we compare the differential flux variation between SS 433 and two brightest standard stars (std1 and std2) for the whole light curve and we found the variation in the IR light curves of SS 433 is likely to be intrinsic and the analysis shows above 2σ level variability in both the bands (Chakrabarti et al. 2003).

4.2.2 X-ray and radio flares in support of the bullet-like features

Could these variations be due to individual bullets? In order to be specific, we present in Figure (4.9a), one ‘micro-flare’-like event in radio from the data on 29th of Sept., 2002, when radio intensity was further down ~ 0.3 Jy so that the micro-flares could be prominently seen. We observe brightening the source from 0.35 Jy to 0.8 Jy in ~ 75 sec which faded away in another ~ 75 sec. That is, the intensity became more than doubled in ~ 1 minute ! Similarly in Figure (4.9b), where we presented a ‘micro-flare’ from the 2nd (central) ‘spell’ of X-ray data of 27th Sept. 2002 (Fig. 4.6-4.7), we also observed significant brightening and fading in ~ 100 sec. The count rate went up more than 15% or so in about a minute. We calculated the energy contained in the individual radio and X-ray micro-flare to be 1.1×10^{33} ergs and 2.7×10^{35} ergs respectively. Since the radio luminosity is very small, even when integrated over 0.1 to 10 GHz radio band (with a spectral index of ~ -0.5) (Vermeulen et al. 1993a) we find that almost all the injected energy at X-ray band is lost on the way during its passage of $\sim 1 - 2$ day.

In order to establish that the features we observe are really due to ‘bullets’ emitting at different wave bands, one should find correlations among them, or try to ‘follow’ them from one band to the other. Unfortunately, cross-correlation among our observations did not yield sharp peaks, partly because the observations were of short duration. Main problem is that the locations of the IR/radio emitting regions themselves are very uncertain. Also, the average duration of an ‘event’ (\sim minute) and average interval of the events (2 – 8 minutes) are very very short compared to the travel time of the bullets to IR ($\sim 10^4$ sec) or radio ($\sim 10^5$ sec) regions. However, we can exclude that the variabilities to be due to ‘fluctuations’ at the inner regions of the accretion disk – the typical time-scale of such variabilities (say, at $r \sim 3r_g$, where, $r_g = 2GM/c^2$, M , G and c being the mass of the black hole, G being the gravitational constant and c being the velocity of light) of an $M = 10M_\odot$ object would be $\sim 2\pi r/c \sim 20GM/c^3 \sim 10^{-3}$ sec, i.e., of much shorter duration than what we see. Similarly, if it were due to random or flicker noise, we should have seen $1/f^\alpha$ ($\alpha \sim 1$) dependence of the PDS (PDS does not show any QPO like features). However, the best fit of PDS has $\alpha \sim 1.6 - 1.8$ instead. Thus, the origin of these features must be different and could be due to ‘bullet-like’ ejections from the disk.

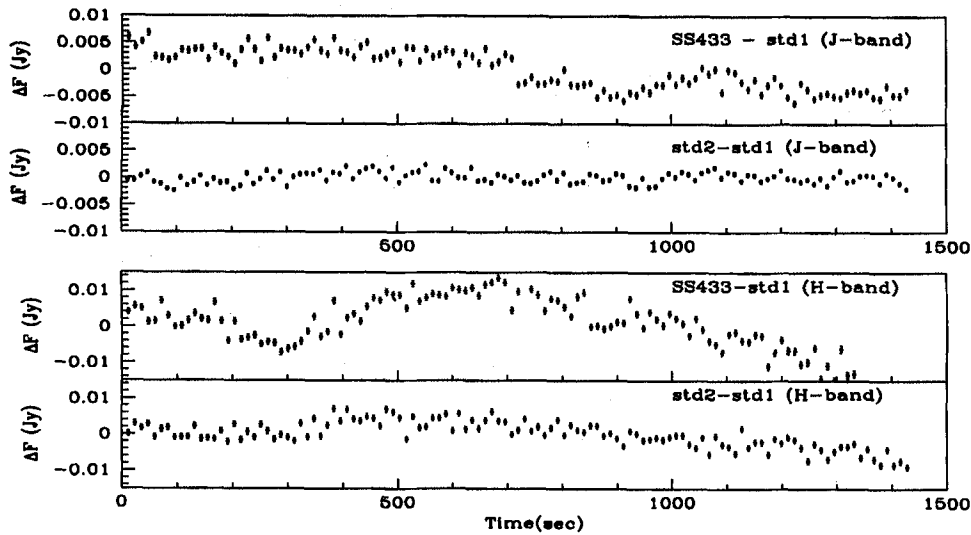


Figure 4.8: Differential photometry of SS 433 with respect to the two brightest standard stars (std1 and std2) in the same frame of object is plotted. Different curves are marked on the top right corner in each panel. The error bar for each individual differential measurement is also shown. Differential flux variation of SS 433 is above the 2σ level in comparison with that of standards.

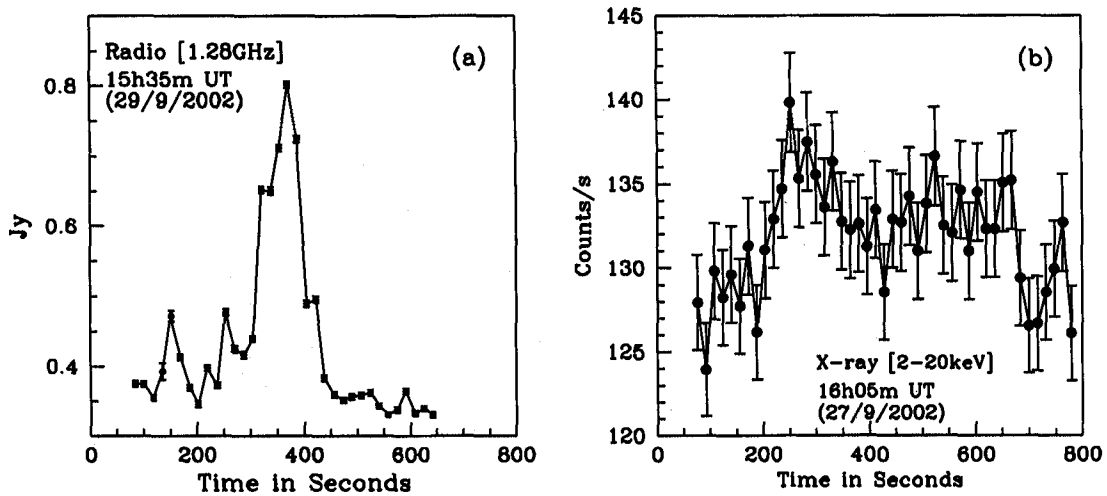


Figure 4.9: Individual flares in very short timescales are caught. (a) A radio flare lasting 2.5 minutes (observed on 2002 September 29) and (b) an X-ray flare (observed on 2002 September 27) lasting for about 3.5 minutes. Each bin size is 16 sec.

4.3 X-ray observation of SS 433 with *RXTE*

In X-rays, SS 433 is a relatively weak source and is not generally observable in hard X-rays beyond ~ 30 keV. Recently, SS 433 is observed with the *INTEGRAL* and for the first time this source shows a hard spectrum upto 100 keV (Cherepashchuk et al. 2003). SS 433 was first identified as an X-ray source with the *HEAO-A* (Marshall et al. 1979). The X-ray luminosity ($\sim 10^{36}$ ergs sec $^{-1}$) was found to be vary by a factor of 2 on a time scale of 6 months, and the *HEAO-A* spectrum of the source could be modeled as thermal bremsstrahlung emission ($kT = 14.3$ keV) with an emission line (~ 7 keV) due to Fe-K transition. Later on, the observations with *EXOSAT*, *Ginga*, *ASCA* confirmed the existence of the Doppler- shifted emission lines features (Watson et al. 1986; Yuan et al. 1995; Kotani et al. 1994) in the X-ray spectrum of SS 433. The shifting of the Fe-line was found to be consistent with the predictions of the ‘kinematic model’. This therefore indicated that the X-ray emitting material is physically associated with the jets. With this idea, Brinkmann et al. (1991) and Kotani et al. (1996) developed the model that the X-ray emission originates near the base of the jets that are adiabatically expanding and cooling until kT drops to about 100 eV, at which point the jet is thermally unstable. Kotani et al. (1996) also found that the red-shifted Fe XXV line was fainter relative to the blue-shifted line than expected from Doppler intensity conservation, leading them to conclude that the redward jet (receding jet) must be obscured by the neutral material in the accretion disk of SS 433. A soft X-ray image of W50/SS 433 taken with the *ROSAT/PSPC* is shown in Figure (4.10). The compact object SS 433 is seen as the black object at the centre of the image alongwith the two prominent X-ray jets that are oppositely directed from the central object. Recently, the *Chandra* observation of SS 433 spectrum (Marshall et al. 2002; Namiki et al. 2003) shows a very much complex behavior with a large number of blue and red-shifted lines. The ‘kinematic model’ was also established, but higher velocity was required for the line emitting gases. Iron line emission from the extended region of the jet also been observed by *Chandra* (Migliari, Fender and Méndez, 2002). On the other hand, the above observations does not show any considerable temporal variations in X-ray flux of SS 433 in the short time scale, whereas *Ginga* observation (Yuan et al. 1995) shows X-ray flux variation with a larger time scale (in units of days) during the X-ray eclipse of the source. In the next sections, we will present the *RXTE* results which are based on temporal and spectral characteristics of SS 433 observations.

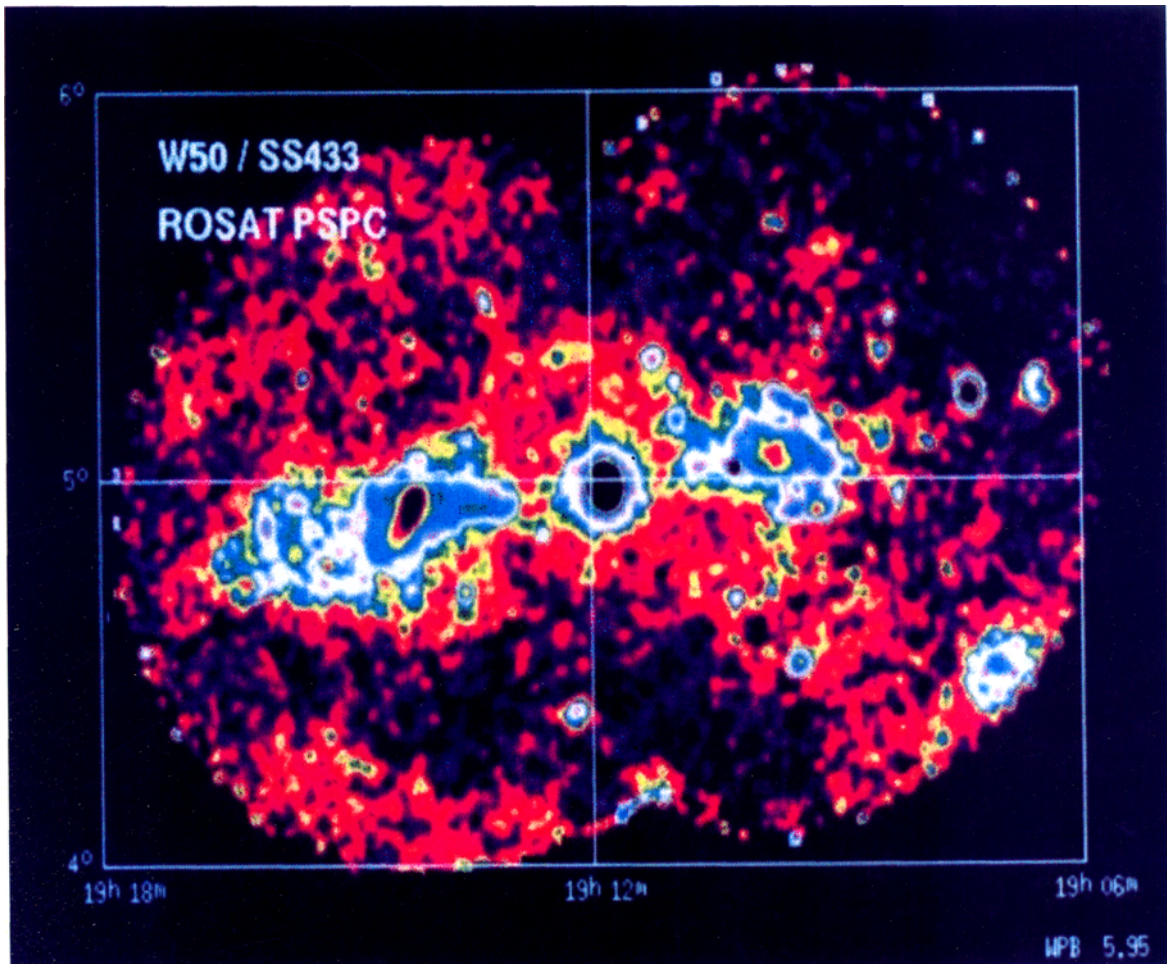


Figure 4.10: The picture above is a soft X-ray image of the SNR W50/SS 433 system taken with the *ROSAT* X-ray observatory. SS 433, the compact object is seen as the black object at the center of the image along with the two prominent X-ray jets that are oppositely directed from the central object. The material in the jet on the left is speeding towards the Earth, while the jet on the right is directed away from the Earth. Image also shows the large scale diffuse X-ray emission produced by the supernova remnant (SNR), which surrounds the compact object, SS 433 (Courtesy: NASA).

4.3.1 Temporal features of SS 433 in different phases

SS 433 was pointed at several times by *RXTE*/PCA. We present the results obtained using the *RXTE* satellite, compiling archival data as well as TOO data triggered by us. Most importantly, for the first time, the observation was carried out during (a) the *inferior conjunction* (when the central compact object and the base of the jet is blocked exactly by the companion; i.e., the orbital phase $\phi = 0$) and at the same time, when the precessional phase, ψ was also 0 and (b) the *superior conjunction* (when the companion is hidden by the disk and the jet is completely exposed to us, i.e., the orbital phase $\phi = 0.5$) and at the same time, when the precessional phase, ψ was also 0 are presented and analyzed. In these special days, the jet was directly pointing towards us emitting lines with the highest possible Doppler shifts. These data were obtained on Oct. 2nd, 2003 and on Mar. 13th, 2004. So, one could expect that the X-ray photon counts (flux) should be high on Mar. 13th, 2004 compare to Oct. 2nd, 2003 observation. Figure (4.11) displays this feature very clearly. We have analyzed the *RXTE*/PCA observational data since November, 2001. In order to avoid biasing the analysis, we selected only those observations which were taken by the same units of PCA detector, namely, 2 & 3. We made the analysis by adding data from these two PCUs together. Figure (4.11) shows the background-subtracted light curves for different *precessional* phase (ψ) and *orbital* phase (ϕ) values. The error-bars obtained from $\text{counts}^{1/2}/\text{binsize}$ are included. We extracted the light curves both from the Good Xenon and Standard-2 mode data. The binsize was chosen to be 16 sec. Data extraction procedure is already discussed in Chapter 2.

A log of selected observation is given in Table 4.1. The first Column gives the log of observation begins (in MJD) along with the *RXTE* Observation ID. To calculate the precessional phase (ψ) and orbital phase (ϕ), at the beginning time of these observations, we adopt the following ephemeris (Goranskii et al. 1998): HJD 2451458.12 + 162.15E for ψ and HJD 2450023.62 + 13.0821E for ϕ . These are given in Column 3. Observations I (made on Oct. 2nd, 2003) and observation K (made on Mar. 13th, 2004) had $\phi \sim 0.0$ and $\phi \sim 0.5$ respectively both having $\psi \sim 0$. TOO observations G-L were triggered at our request. A recent TOO data (Observation M made on 25th of March, 2004) is also included. We also re-analyzed the archival data of Nov. 2001. The spectra were fitted with a thermal bremsstrahlung and iron line(s) and the temperature is given in Column 4 (see, next section for details of the fitting procedure.) The total integrated flux of X-rays in 3 – 25 keV range in units of $10^{-10} \text{ergs cm}^{-2} \text{sec}^{-1}$ is presented in Column 5. During the recent superior conjunction when the jet was exposed to us (March 13th, 2004), the net flux was

found to be more than twice as high compared to that in the inferior conjunction (Oct. 2nd, 2003). The net flux remained high for at least another orbital period indicating that SS 433 may be undergoing a flaring activity.

One can compare the X-ray flux by *RXTE* observations with earlier results of *EXOSAT* (Watson et al. 1986) and *Chandra* (Namiki et al. 2003). For instance, in the same unit as in Table 4.1, at $\psi \sim 0$, the 2 – 6 keV flux of *EXOSAT* was 1.5 while our fluxes vary from 1.07 – 1.6 depending on ϕ in the same range of 2 – 6 keV. *Chandra*, on the other hand, found the total integrated flux in 1 – 10 keV at $\psi \sim 0.4$ to be 0.9. We did not make any observation at this phase, and our result at phase $\psi \sim 0$ in 3 – 9 keV is 1.6 – 3. Thus the fluxes measured by *RXTE* are comparable to previous measurements, although an actual comparison requires observation to be carried out at the same precessional and orbital phases as well.

Previous observation other than *RXTE* revealed no variability on time scales shorter than 300 sec. For the first time, Safi-Harb & Kotani (2003), using the PCA Nov. 2001 data, found the fast time variability of ≤ 300 sec in X-ray observation of SS 433. We have also found such short time scale variabilities (≤ 100 sec) which are shown in Figure (4.11) (marked as panel K and L). The X-ray light curve of Sep. 27th. 2002 (panel G) observation was already presented in the previous section, where, it was found that the X-ray photon counts showed a very rapid change (around 15%) in a matter of minutes. The panels of Observations H and I show the light curves of Oct. 1st, 2003 and Oct. 2nd 2003 respectively, the second observation being at the donor inferior conjunction. While these light curves also show similar rapid variation, there appears to be an overall modulation of X-ray photon counts. At least 25% of the flux modulation occurs in 6-7 minutes timescale. Given that the companion star is directly blocking the base of the jet, and the X-rays received may be passing through the star's atmosphere this could even be due to some kind of oscillation in the atmosphere of the star.

By analyzing both the Good Xenon and Standard-2 mode data, we could not detect any quasi-periodicity in the power density spectra (PDS). The panel of Observation K shows the light curve of March the 13th, 2004 when the companion was right behind the disk. The jet pointing towards the observer had the highest blue-shift and the base of the jet was totally exposed. The X-ray flux was more than twice as high compared to average flux of past observations. The X-ray count was also much higher on this date and a variation of $\sim 30\%$ was observed in a matter of few minutes. Similar result persisted on the next day (Observation L of 14th of March, 2004; see, Fig. 4.11) when short time-scale variability was more prominent. In fact, the X-ray flux remained high even after one orbital period (Observation M).

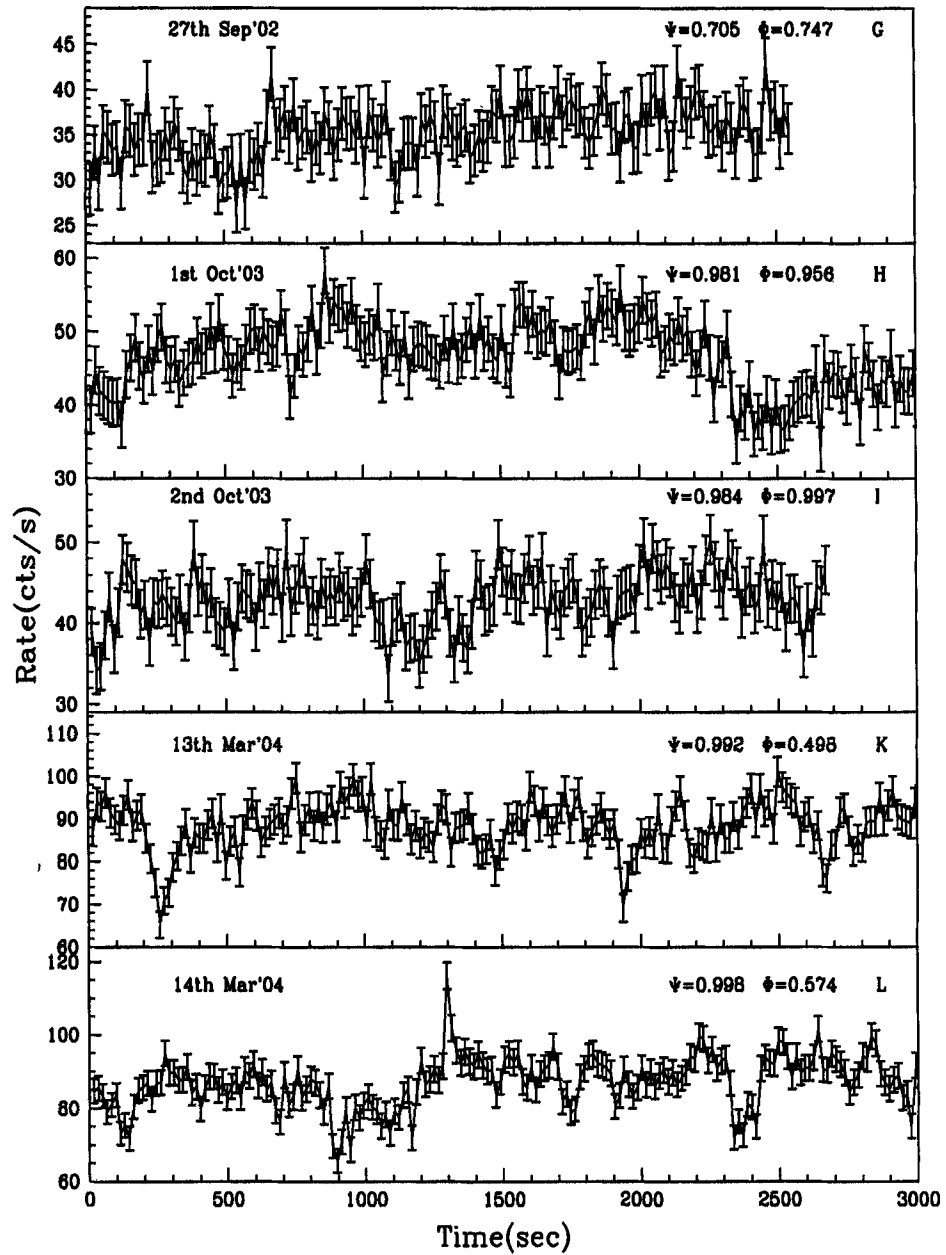


Figure 4.11: X-ray light curves (background subtracted) extracted from **Standard-2** data of SS 433 for observations G, H, I, K and L (marked). Along X-axis is time (in seconds) and along Y-axis is photon counts/sec (rate). Short time-scale variabilities are observed (see, panel K and L).

Table 4.1: RXTE Observation log^a

Obs. log	MJD(UT) (Date)	ψ	kT_b	Flux ^b
	ObsID	ϕ	(keV)	
A	52222(07:10:27) (09th Nov'01)	0.716	23.02	2.824
	60058-01-01-00	0.106	+1.19 -1.10	
B	52224(06:47:29) (11th Nov'01)	0.728	27.03	2.966
	60058-01-03-00	0.257	+1.85 -1.56	
C	52227(06:11:11) (14th Nov'01)	0.747	26.91	3.436
	60058-01-06-00	0.485	+1.62 -1.41	
D	52228(06:00:16) (15th Nov'01)	0.753	24.01	3.480
	60058-01-07-00	0.561	+1.45 -1.19	
E	52234(08:03:15) (21st Nov'01)	0.790	25.93	2.786
	60058-01-12-00	0.025	+7.53 -4.44	
F	52235(07:54:37) ^c (22nd Nov'01)	0.796	27.63	3.547
	60058-01-13-00	0.102	+1.83 -1.54	
G	52545(15:57:34) (27th Sep'02)	0.705	13.92	2.375
	70416-01-01-01	0.747	+0.57 -0.71	
H	52914(16:41:24) (01st Oct'03)	0.981	17.23	3.183
	80429-01-01-00	0.956	+0.71 -0.65	
I	52914(05:20:00) ^d (02nd Oct'03)	0.984	17.50	2.993
	80429-01-01-01	0.997	+0.91 -0.81	
J	53077(18:55:12) (12th Mar'04)	0.986	51.35	7.557
	90401-01-01-01	0.423	+5.00 -3.18	
K	53078(18:33:04) ^e (13th Mar'04)	0.992	44.93	6.912
	90401-01-01-00	0.498	+2.60 -2.19	
L	53079(18:12:00) (14th Mar'04)	0.998	40.10	6.778
	90401-01-01-02	0.574	+1.99 -1.72	
M	53089(01:51:28) (25th Mar'04)	0.062	46.41	7.592
	90401-01-02-01	0.363	+4.17 -3.40	

a) Error bars in temperature are at 90% confidence level; b) Flux is in the range (3 – 25 keV) in units of 10^{-10} ergs cm⁻² sec⁻¹; c) Massive radio flare observed (Safi-Harb & Kotani, 2003); d) TOO observation at $\psi \sim 0$ and $\phi \sim 0$; e) TOO observation at $\psi \sim 0$ and $\phi \sim 0.5$

The short time scale variability of 50 – 100 sec indicates a length $\leq 10^{12}$ cm, which could be length scale of the X-ray jets.

In the next section, we present the results of spectral analysis of *RXTE*/PCA observation of SS 433.

4.3.2 Spectral fits of *RXTE* observation of SS 433

It has been pointed out by Marshall et al. (2002), using *Chandra* observation, that the X-ray spectrum of SS 433 is very complex. The line emissions from different materials do show blue- and red-shifted components. Migliari et al. (2002) also reported the *Chandra* observation of iron line features emitted from extended regions of the jets. Our analysis of *RXTE* spectral data also shows the Doppler shifted iron line features which roughly match with the predictions of the ‘kinematic model’.

The data reduction and analysis was performed with the software HEASOFT 5.1 consisting of FTOOLS 5.1 and XSPEC 11.1. We extracted energy spectra from PCA **Standard-2** data. For each spectrum, we have followed the standard procedures to generate the background spectra and PCA detector response matrices. We performed fitting the spectra simultaneously with different combination of models such as thermal bremsstrahlung, line contribution, disk-blackbody spectrum and the power-law spectrum modified by interstellar absorption (WABS model, Morrison & McCammon, 1983).

During fitting, we find that the so-called ‘traditional model’ are best fitted with a minimum reduced χ^2 value. We find good fitting while keeping the hydrogen column density fixed at $2.4 \times 10^{22} \text{cm}^{-3}$ except on the Oct. 1st-2nd, 2003, when $1.6 \times 10^{22} \text{cm}^{-3}$ was needed. We did not set any systematic error. We also found that reduced χ^2 is smaller if two lines are included instead of a single line. We have included in the Table 4.2 the normal χ^2 values and the degrees of freedom (dof) as well as the reduced χ^2 when one (denoted by χ_1^2 in Column 3) or two (denoted by χ_2^2 in Column 4) lines are fitted. We find that χ_2^2 is always smaller than χ_1^2 .

In Figures 4.12(a-c), we present the spectra of observations G (Fig. 4.12a), I (Fig. 4.12b) and K (Fig. 4.12c) respectively. For all observations, for the best fitting, two additional line features were tried out on the top of thermal bremsstrahlung fit. The requirement of two line fitting in the spectrum is tested using the F-statistics with the *f_{test}* task within XSPEC. P_{F-stat} is the F-statistic probability for the addition of the 2nd Gaussian line to the same model with a single line. This is given in Column 5 of Table 4.2. The significance is given under this *P* value and is denoted

Table 4.2: Results^a of RXTE observations of SS 433

Obs. log	z_{blue} z_{red}	χ^2_1 (χ^2/dof)	χ^2_2 (χ^2/dof)	$PF-stat$	E_{obs} (keV)	σ_{line} (keV)	F_{line}^b ($\times 10^{-3}$)	z FeXXVI	z FeXXV
A	0.005 0.066	0.742 (35.6/48)	0.633 (28.5/45)	1.7×10^{-2} (2.1 σ)	$6.822^{+0.038}_{-0.039}$	$0.692^{+0.054}_{-0.053}$	$2.536^{+0.144}_{-0.135}$	0.020 $^{-0.005}_{+0.005}$	-0.021
B	-0.001 0.073	0.966 (46.4/48)	0.682 (31.4/46)	4.9×10^{-4} (2.8 σ)	$6.905^{+0.138}_{-0.153}$ $6.819^{+0.002}_{-0.001}$	$1.050^{+0.209}_{-0.169}$ 0.309 ± 0.0	$2.026^{+0.269}_{-0.271}$ $0.808^{+0.330}_{-0.480}$	0.009 $^{-0.019}_{+0.021}$ 0.021	-0.033 -0.020 $^{-0.0003}_{+0.0002}$
C	-0.012 0.083	1.261 (60.5/48)	0.775 (35.6/46)	5.1×10^{-8} (3.5 σ)	$6.976^{+0.081}_{-0.088}$ $6.891^{+0.084}_{-0.099}$	0.125 ± 0.0 $1.159^{+0.132}_{-0.114}$	$0.613^{+0.179}_{-0.164}$ $3.216^{+0.262}_{-0.246}$	-0.002 $^{-0.012}_{+0.013}$ 0.011	-0.044 -0.031 $^{-0.012}_{+0.015}$
D	-0.015 0.087	1.819 (87.3/48)	1.265 (58.2/46)	3.6×10^{-4} (2.9 σ)	$6.986^{+0.087}_{-0.074}$ $6.837^{+0.128}_{-0.170}$	0.246 ± 0.0 $1.209^{+0.198}_{-0.160}$	$0.894^{+0.184}_{-0.213}$ $2.632^{+0.305}_{-0.271}$	-0.003 $^{-0.009}_{+0.011}$ 0.018	-0.045 -0.023 $^{-0.019}_{+0.025}$
E ^c	-0.036 0.107	1.373 (65.9/48)	1.027 (47.2/46)	1.7×10^{-3} (2.6 σ)	$7.281^{+0.136}_{-0.154}$	$1.227^{+0.184}_{-0.171}$	$3.212^{+0.745}_{-0.595}$	-0.045 $^{-0.019}_{+0.022}$	-0.089
F ^d	-0.039 0.111	1.011 (48.5/48)	0.745 (34.3/46)	3.3×10^{-4} (2.9 σ)	$6.950^{+0.092}_{-0.104}$ $6.876^{+0.119}_{-0.147}$	0.257 ± 0.0 $1.128^{+0.206}_{-0.168}$	$0.708^{+0.198}_{-0.264}$ $2.403^{+0.390}_{-0.268}$	0.002 $^{-0.013}_{+0.015}$ 0.013	-0.039 -0.029 $^{-0.018}_{+0.022}$
G	0.011 0.060	1.202 (54/45)	0.831 (35.7/43)	1.4×10^{-4} (3.0 σ)	$7.012^{+0.106}_{-0.105}$ $6.802^{+0.104}_{-0.125}$	$0.939^{+0.140}_{-0.118}$ 0.125 ± 0.0	$2.059^{+0.113}_{-0.226}$ $0.518^{+0.163}_{-0.181}$	-0.007 $^{-0.015}_{+0.015}$ 0.023	-0.049 -0.018 $^{-0.015}_{+0.018}$
H	-0.102 0.173	1.596 (76.6/48)	0.789 (36.3/46)	2.0×10^{-7} (3.9 σ)	$7.722^{+0.099}_{-0.108}$ $5.359^{+0.186}_{-0.212}$	$1.191^{+0.107}_{-0.099}$ 0.544 ± 0.0	$2.747^{+0.259}_{-0.227}$ $0.647^{+0.135}_{-0.164}$	-0.108 $^{-0.014}_{+0.015}$ 0.230	-0.155 0.198 $^{-0.028}_{+0.032}$
I ^e	-0.103 0.174	1.691 (81.2/48)	0.845 (38.9/46)	1.9×10^{-7} (4.0 σ)	$7.731^{+0.099}_{-0.115}$ $5.221^{+0.238}_{-0.262}$	$1.181^{+0.128}_{-0.119}$ 0.615 ± 0.0	$2.594^{+0.308}_{-0.266}$ $0.748^{+0.166}_{-0.173}$	-0.110 $^{-0.016}_{+0.018}$ 0.250	-0.157 0.219 $^{-0.035}_{+0.039}$
J	-0.103 0.174	3.768 (180.9/48)	1.693 (76/45)	1.5×10^{-8} (4.3 σ)	$7.693^{+0.085}_{-0.070}$ $5.333^{+0.148}_{-0.146}$	$1.073^{+0.065}_{-0.069}$ $0.567^{+0.211}_{-0.167}$	$6.149^{+0.387}_{-0.388}$ $1.487^{+0.556}_{-0.376}$	-0.104 $^{-0.012}_{+0.010}$ 0.234	-0.151 0.202 $^{-0.022}_{+0.022}$
K ^f	-0.103 0.174	3.570 (171.4/48)	1.628 (73.3/45)	2.1×10^{-8} (4.2 σ)	$7.587^{+0.054}_{-0.032}$ $5.323^{+0.132}_{-0.141}$	$1.011^{+0.056}_{-0.055}$ $0.495^{+0.148}_{-0.132}$	$5.731^{+0.282}_{-0.284}$ $1.103^{+0.305}_{-0.244}$	-0.089 $^{-0.008}_{+0.005}$ 0.236	-0.135 0.204 $^{-0.020}_{+0.021}$
L	-0.103 0.175	3.176 (152.5/48)	1.597 (72.9/45)	1.8×10^{-7} (4.0 σ)	$7.523^{+0.085}_{-0.058}$ $5.352^{+0.136}_{-0.069}$	$1.031^{+0.081}_{-0.061}$ $0.462^{+0.158}_{-0.154}$	$5.804^{+0.293}_{-0.322}$ $1.010^{+0.336}_{-0.247}$	-0.080 $^{-0.009}_{+0.008}$ 0.231	-0.126 0.199 $^{-0.020}_{+0.010}$
M	-0.096 0.168	1.454 (69.8/48)	0.845 (38/45)	4.4×10^{-8} (3.5 σ)	$7.570^{+0.114}_{-0.099}$ $5.453^{+0.209}_{-0.207}$	$1.014^{+0.104}_{-0.104}$ $0.439^{+0.234}_{-0.237}$	$6.202^{+0.589}_{-0.591}$ $1.204^{+0.589}_{-0.446}$	-0.087 $^{-0.016}_{+0.014}$ 0.217	-0.132 0.184 $^{-0.031}_{+0.031}$

a) Error bars are at 90% confidence level; b) Total photons $\text{cm}^{-2} \text{sec}^{-1}$ in the line; c) the fitting of the lower energy component was uncertain; d) Massive radio flare observed (Safi-Harb & Kotani, 2003); e) TOO observation at $\psi \sim 0$ and $\phi \sim 0$; f) TOO observation at $\psi \sim 0$ and $\phi \sim 0.5$

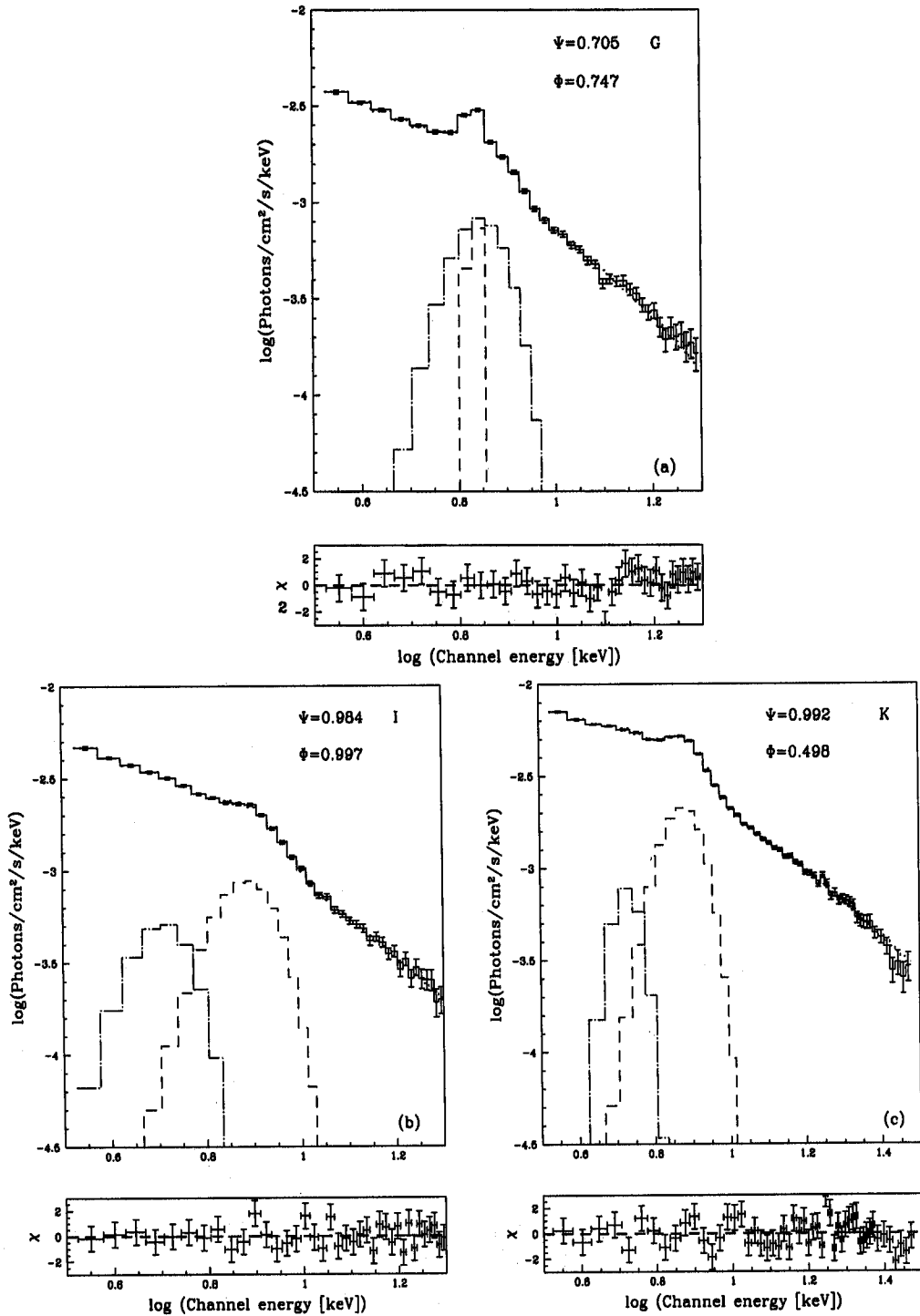


Figure 4.12: Unfolded X-ray spectrum of SS 433 with different model components on (a) Obs. G on 27th September 2002, (b) Obs. I on 2nd of October 2003 (inferior conjunction) and (c) Obs. K on 13th of March 2004 (superior conjunction). While in (a), the precession/orbital phases were generic (see Table 4.1), in (b), the phases were very close to zero when the companion blocked the central object and in (c), the precession phase is close to zero but the orbital phase is close to 0.5. The model components are: thermal bremsstrahlung (solid histogram) and two Fe lines (dashed

in parenthesis. Based on the significance value we find that all the observations favour the two-line model except Obs. A and Obs. E as these fits are significant only at 2.1σ and 2.6σ levels respectively. Indeed, we observe that on MJD 52234 (Observation E), the X-ray flux is very low. Given that it takes about a day for the jet to arrive from the X-ray emitting region to the radio emitting region, it is possible that the massive radio flare on MJD 52335 (Observation F. See, Safi-Harb & Kotani, 2003) actually was ejected on the previous day. Similar behavior of anti-correlation between Radio and X-ray fluxes has been reported by Mirabel & Rodriguez (1999) (MR99). During the final fit of the observations B, C, D, F and G, we froze the narrower line width. In our fit, there was no signature of any soft-X-ray bump characteristics of a Keplerian disk. As has been pointed out earlier (Chakrabarti et al. 2002b), there is evidence that the flow is actually from a wind accretion and thus possibly sub-Keplerian. This is also required for the production of the observed jets (Chakrabarti, 1999). The line energies (in keV) we obtained are given in Column 6. The residuals given in the lower panels of Figs. 4.12(a-c) indicate that the fits are satisfactory. Note that in Observations J-K-L, there are significant contributions from high energy (~ 30 keV) photons and the flux is also much higher (see, Table 4.1). This behavior persisted even after one orbital period (Observation M). Columns 7 and 8 give the line width (keV) and line strength (in units of photons $\text{cm}^{-2} \text{sec}^{-1}$) respectively for each line. It has been noted earlier (Kotani et al. 1996; Marshall et al. 2002; Namiki et al. 2003) from the *ASCA* and *Chandra* observations that the FeXXV lines are on an average 2-3 times (or more) stronger compared to FeXXVI lines. In our *RXTE* observations C, D and F (when $\psi \sim 0.7$), we find roughly a similar result when we identify both the lines to come from the approaching jet components. However, in observations B and G, where the lines were similarly identified as above, the FeXXV line is found to be weaker compared to the FeXXVI line. In observations H-M the jets are pointing towards the observer ($\psi \sim 0$) and we find that two lines are roughly agreeing with the prediction of the kinematic model provided the line with higher energy (brighter component) is identified with FeXXVI of the approaching jet and the lower energy (dimmer component) is identified with FeXXV of the receding jet. In Observation E, we could fit with only one line, possibly because of certain disturbances of the inner disk and the jet one day ahead of the massive radio flare reported by Safi-Harb & Kotani (2003).

In Fig. 4.13(a-b), we have drawn contour plots of $\Delta\chi^2$ for Obs. C in the (a) line width (σ) vs. line energy (E_{obs}) plane and (b) line width (σ) vs. line flux (F_{line}) plane to show the correlations. Similarly, in Fig. 4.14(a-b), we have drawn the

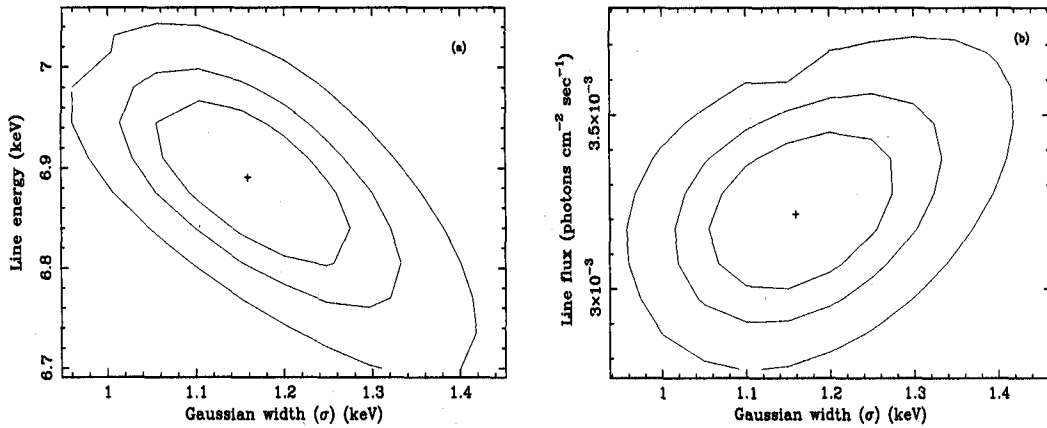


Figure 4.13: Two parameter confidence region of the broad FeXXVI (a) line energy vs. Gaussian width and (b) line flux vs. Gaussian width from spectral fitting to the *RXTE*/PCA data of Obs. C. Contours correspond to 68%, 90% and 99% confidence.

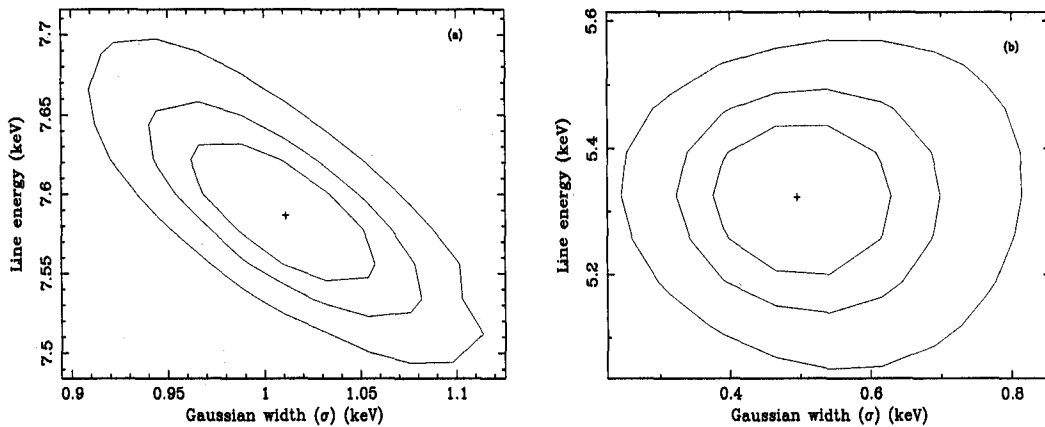


Figure 4.14: Two parameter confidence region of the broad FeXXVI (a) line energy vs. Gaussian width and (b) line flux vs. Gaussian width from spectral fitting to the *RXTE*/PCA data of Obs. C. Contours correspond to 68%, 90% and 99% confidence.

contour plots of $\Delta\chi^2$ for Obs. K in the line width (σ) vs. line energy (E_{obs}) plane for the (a) broad line and (b) narrow line. The contours are of 68%, 90% and 99% confidence level. It can be seen that the lines are resolved at the 90% confidence level.

While comparing with the absolute line strength with previous observations, we note that *Chandra* (Marshall et al. 2002) obtained a red-jet FeXXV line (1s2p - 1s²) flux of ~ 0.13 in the same unit chosen in Table 4.2, while we obtained the value of ~ 1.2 (Observation M), both observations being at a similar precessional phase of $\psi \sim 0.06$ if the same ephemeris (Goranskii et al. 1998) were used. This high value may be because (a) the SS 433 was intrinsically brighter in X-ray in our observation and (b) blending of lines which *RXTE* was unable to resolve especially there could be always a significant contribution from the neutral Fe line emitted from regions at rest in the observed frame (Kotani et al. 1996; Marshall et al. 2002).

In Columns 9-10 we present the computed red- and blue-shift factors (z) of the observed lines, had their origins been the FeXXVI (Ly α transition at 6.965 keV) or the FeXXV line (1s2p - 1s² transition at 6.684 keV), respectively. In bold faced letters we have highlighted the probable identification of the lines. Generally speaking, the line with higher energy could be identified with the blue-shifted FeXXVI line quite satisfactorily (Fig. 4.15a). However, the line with lower energy could be fitted with red-shifted FeXXV lines when $\psi \sim 0$ and with blue-shifted FeXXV line elsewhere (Fig. 4.15b). The error-bars (at 90% confidence level) drawn in Fig. 4.15(a-b) are given in Table 4.2. The data has been folded with 162.15 day periodicity for convenience. Superimposed are the solid and dotted curves representing the Doppler shifts (Eqn. 4.4) of the jet component pointing towards us and the component pointing away from us respectively. Though the poor resolution in *RXTE*/PCA detector may be the main cause of the deviation of the fitted shifts from that of the kinematic model, one can assume that the lines energies are correct in order to estimate the possible variation of jet velocity, if any, which may be responsible for this deviation, when other system parameters are kept unchanged. We plot the short and long-dashed curves in Figs. 4.15(a-b) for $v_j = 0.286$ and $v_j = 0.234$ respectively which are 10% away from the velocity $v_j = 0.2602$ of the standard model. The horizontal lines correspond to the intrinsic red-shifts for these velocities. Since at $\psi \sim 0$, the blue jet seems to have a large scattering of velocity, while the red jet seems to have a higher velocity, we could not conclude with certainty if the jets have truly different velocity than that of the standard 'kinematic model', even though there are reports (e.g., Marshall et al. 2002) that the jet velocity could be higher close to the compact object.

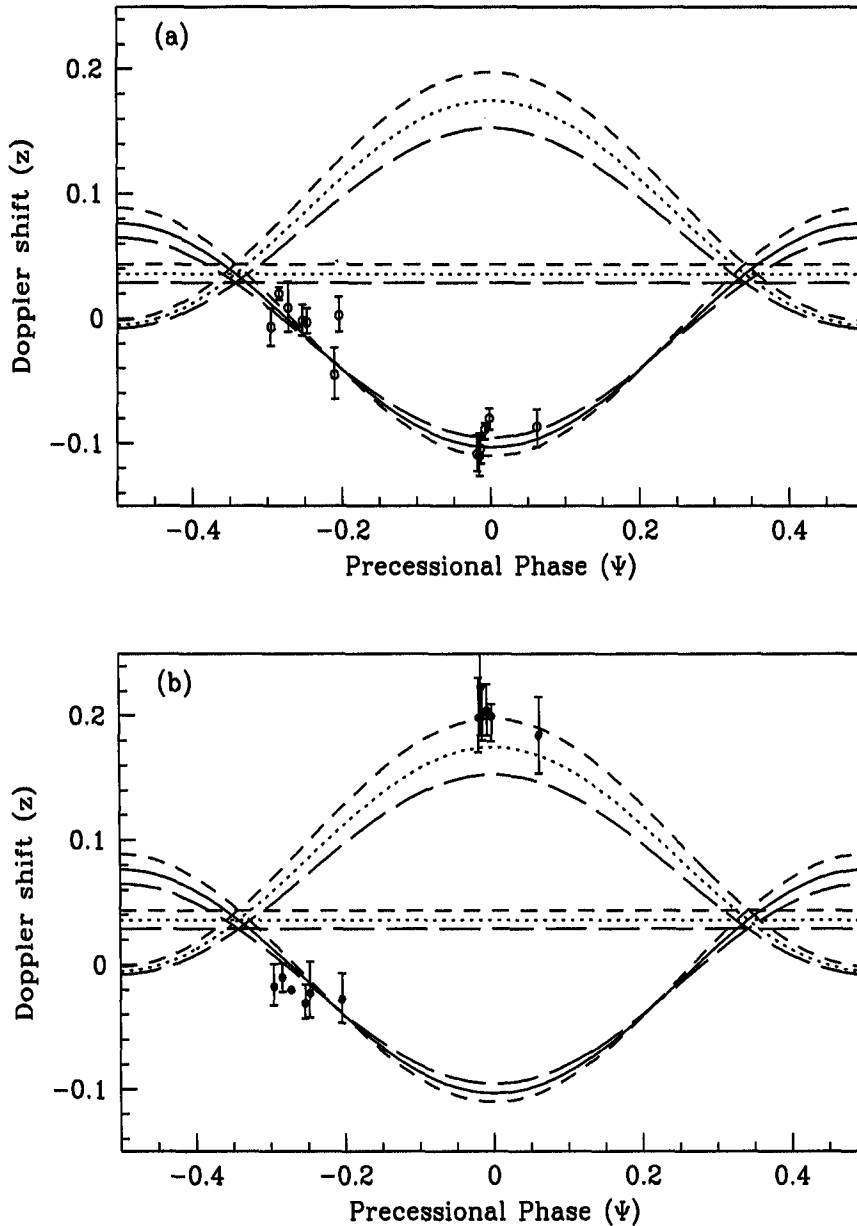


Figure 4.15: Observed Doppler shifts (y-axis) of (a) FeXXVI and (b) FeXXV lines from the approaching (solid curve) and receding (dotted curve) jets super-imposed on the prediction from the ‘kinematic model’ with standard parameters (see, §4.1) as a function of the precessional phase ψ . Also shown in short-dashed and long-dashed curves the shifts obtained by respectively reducing and enhancing the jet velocity by ten percent. The horizontal curves represent intrinsic red-shifts for the corresponding jet velocities. See §4.3.2 for detailed criteria used in line-identifications. All the observations were plotted against the same precessional phase for clarity of the plot of the lines.

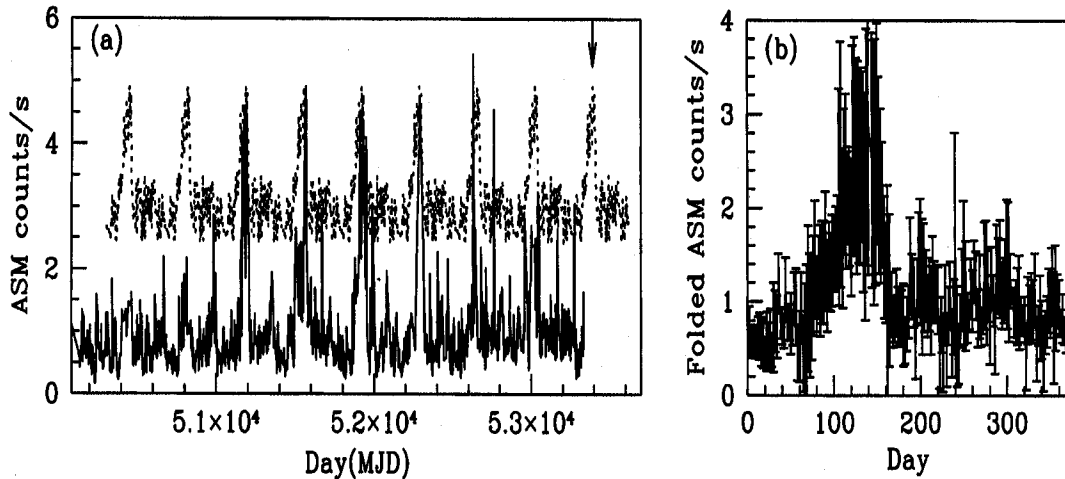


Figure 4.16: (a) ASM counts/s of SS 433 since 1996 till Oct. 26th, 2004. For clarity, we plotted only those points when the count over the background rate is positive. We superpose (with a shift of 2/sec along y-axis) the mean light-curve when folded around 368 days to show the periodic nature of a strong flare which repeats after every 368 days interval (This could be an artefact of the ASM observation). (b) Average ASM light curve obtained by folding around 368 days showing the presence of the strong flare.

We also examined if the lines could be fitted with NiXXVII ($1s2p - 1s^2$ transition at 7.788 keV). However, except for the lower energy component of observation F, none seems to be satisfactory. It may be noted that near $\psi \sim 0$, RXTE observation showed the evidence of both the components of the jet which has not been reported before.

4.4 X-ray Flares in SS 433?

During the recent TOO campaign of 12-14th March, 2004, the X-ray flux is found to be very high. This may indicate that SS 433 was undergoing some kind of X-ray 'flare'. In fact a cursory look at the entire ASM rate profile since 1996 till Sept., 2004 (Fig. 4.16a) where we plotted (solid) only those points when the count over the background rate is positive, shows that there had been a few occurrences of flaring activities in the past. One spike on MJD 52086 was removed as it had a very unusual count (11.5/s). In Fig. (4.16b), we folded the ASM light curve around

368 days of interval and taken the mean count along with standard deviation as the error bars to indicate that there are indeed some indication of periodicity. This mean is plotted as dashed curve in Fig. (4.16a), just to show that the periodicity is real. While there are at least two other weaker peaks with this periodicity, they do not appear to be significant. We predicted that the next flare should take place during Dec. 21st, 2004 till Feb. 8th, 2005 (By an arrow it is indicated in the Fig. 4.16a), and we indeed observed such flare in the ASM light curve (not included in the Figure).

Chapter 5

OUTFLOWS AND JETS IN MICROQUASARS

5.1 Outflows and Jets in Black Holes

Outflows and Jets are common phenomena in galactic black holes, also known as *microquasars*, because of its resemblance with the scale down version of physical properties of quasars. It has been observed that many of the black holes possess a relativistic jet whose velocity is a significant fraction ($\geq 0.1c$) of the velocity of light. Sometimes the jet velocity is highly relativistic ($\geq 0.9c$) i.e., the case of GRS 1915+105, GRO J1655-40, XTE J1748-288 etc. and sometimes it is mildly relativistic ($\sim 0.26c$) as observed in SS 433. The relativistic nature of the jet in GRS 1915+105 was confirmed from the extensive monitoring in the radio band (Mirabel & Rodriguez 1994; Pooley & Fender 1997; Fender et al. 1999) and importantly it was also noticed that the jet velocity in GRS 1915+105 changes from time to time. On the other hand, the jet velocity in SS 433 is found to be remarkably constant ($\sim 0.26c$) in the optical band (see, review by Margon 1984). However, both the microquasars GRS 1915+105 and SS 433 possess radio jets and their appearance is very different, with GRS 1915+105 appearing to have a continuous or discontinuous jet, where SS 433 has a knotty, precessional jet corresponding to discrete ‘bullets’ of matter ejected from the central engine of SS 433. Also, there are clear observational supports that both the jets in GRS 1915+105 and SS 433 are produced from vicinity of the black holes (Dhawan et al. 2000; Marshall et al. 2002; Chakrabarti et al. 2003).

It is almost confirmed that outflows/jets are produced in hard spectral states of black holes. Several attempts have been made to associate the radio emission, presumably coming from the jets, to the X-ray emission from the accretion disk of GRS 1915+105 (Fender et al. 1999; Naik et al. 2001; Naik & Rao, 2000; Klein-Wolt et al. 2002). There are also evidence of disappearance of inner accretion disk

in GRS 1915+105 during radio flares (Feroci et al. 1999; Vadawale et al. 2001). Since the disappearance of the inner disk is seen to be correlated with intense radio activity, the role of magnetic field must be studied in order to understand the system completely. Rodriguez and Mirabel (1999) estimated the field in radio blobs to be around tens of mG at 500 – 1000 AU (in 1994 observation). Fender et al. (1997) requires the field to be around 8G at around 1 AU (in 1996 observation). From similarity of ~ 30 min oscillations in IR and Radio, they concluded that the radio blobs are adiabatically expanding and are independently ejected from the disk in every 30 – 40 minutes. If the trapped field inside a radio blob is of roughly $1/r$ (for toroidal field) then its interpolated value close to a black hole is around 10^7 G at around $10r_g$ which is comparable to an equipartition value. Thus, one needs to correlate fields ejected from the disk with those observed inside the radio blobs.

In the next section, we examine the mass ejection based on the TCAF model in presence of magnetic field (we call this as Magnetized TCAF or MTCAF model) amplified due to strong shear at the transition radius of the Keplerian and a sub-Keplerian flow.

5.2 The magnetized TCAF model for matter ejection

5.2.1 Basic assumptions

Based on the global solutions of the most general advective accretion disk solution (Chakrabarti, 1990; 1996b; 1996c), Chakrabarti & Titarchuk (1995) presented a TCAF model of accretion onto black holes. The basic assumptions of the TCAF model are discussed already in Chapter 1 (§1.5.4). Figure (5.1) schematically shows the TCAF model along with its all different components. In TCAF, the centrifugal pressure supported boundary layer (or, CENBOL for short) which acts like a ‘virtual boundary’ of black hole, has most of the features of a thick accretion disk although in advective disks, advection is included self-consistently and in thick disks advection is totally ignored. This is because at CENBOL surface, matter undergoes a supersonic to sub-sonic transition and it moves very slowly in the radial direction. In some phases of accretion, matter can bring in a large amount of stochastic magnetic field. The field is sheared due to strong azimuthal velocity and the toroidal field becomes very strong. These field lines will have very little matter within it and would likely to be buoyant and emerge from various parts of the accretion disk. Figure (5.1) schematically shows this behavior. Toroidal magnetic flux tubes released from the Keplerian disk are sheared, amplified and are advected in the sub-Keplerian flow.

Due to centrifugal the barrier, the matter stays away from the axis. Thus a so-called funnel wall is created exactly as in a thick accretion disk (Paczynski & Wiita, 1980). Chakrabarti and D'Silva (1994, hereafter CD94) computed the nature of their trajectories inside a thick accretion disk. They showed that in the event a strong flux tube enters a hot region with ion temperature $T_i \gtrsim 10^{10}\text{K}$, the magnetic tension becomes the strongest force and the flux tube catastrophically collapses. Because of strong similarity of the thick accretion disk and the CENBOL, we believe that similar mechanism could be working and the flux tube collapse would take place.

5.2.2 Governing equation of motion of the flux tubes

We have considered the motion of the flux tubes on the equatorial plane of an accretion flow around a Schwarzschild black hole described by Paczynski-Wiita (1980) pseudo-Newtonian acceleration $g = -1/2(x-1)^{-2}$. We use the geometric units. Masses are measured in units of the mass of the central black hole, M_{BH} ; distances from the axis (x) are measured in units of the Schwarzschild radius $r_g = 2GM_{BH}/c^2$; and the time scales are measured in units of r_g/c . Inside the disk, we choose the polytropic equation of state, $P = K\rho^\gamma$, where K and γ are constants. The magnetic flux tubes brought in by advection are assumed to be sheared and *axisymmetric* toroidal flux tubes of random shape and size could be produced inside the flow. We however assume that the flux tubes are thin, i.e., the flux tube cross-sectional radius σ is smaller than the local pressure scale height of the disk. Close to a black hole, angular momentum of the flow remains constant (Chakrabarti, 1996b) even in the presence of a moderate viscosity. Thus, we choose the specific angular momentum λ in the sub-Keplerian region to be constant. The equations of motion for the thin flux tubes have been written down in CD94 and we do not repeat here. For the sake of completeness, we write down the radial equation only valid for the equatorial plane ($\theta = \pi/2$),

$$\ddot{x} + \frac{X}{(1+X)}[-x\dot{\phi}^2 - 2x\omega\dot{\phi}] = \frac{X}{(1+X)}\left\{\frac{M_b}{X}[g - x\omega^2] - \frac{1}{m_i}\frac{\psi^2}{2\pi\sigma^2} - \frac{D_x}{\pi\sigma^2\rho_e}\right\}, \quad (5.1)$$

where $X = m_i/m_e$, $m_i = 2\pi^2\sigma^2x\rho_i$ and $m_e = 2\pi^2\sigma^2x\rho_e$ are the masses of the fluid inside and the fluid displaced by the flux tube respectively, ρ_i and ρ_e being the corresponding densities. Subscripts e and i indicate whether the relevant quantity is of the ambient (external) medium or within the flux tube (internal medium). $\psi = \pi\sigma^2B$, B being magnetic field of the tube and $\dot{\phi}$ is the intrinsic angular velocity

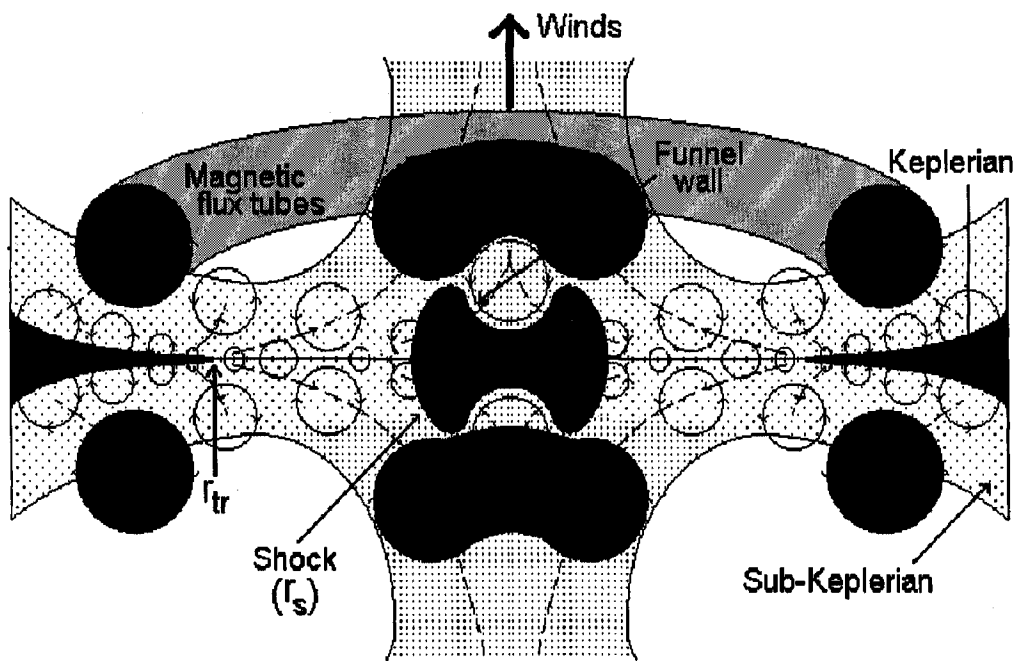


Figure 5.1: A cartoon diagram of the accretion disk near a black hole which includes a shock (r_s), a sub-Keplerian and a Keplerian disk with a boundary at r_{tr} . Stochastic magnetic fields are sheared and amplified as they leave a Keplerian disk. In a hot, sub-Keplerian flow, these toroidal flux tubes catastrophically collapse squirting matter along the axis, and thereby evacuating the disk and producing outflows/jets. Dashed curves show typical trajectories (see, CD94 for details).

of the flux tube inside the disk. The drag term is assumed to be similar to the drag experienced by a cylinder moving perpendicular to its axis in a fluid, and the drag per unit length in radial direction is given by,

$$D_x = -\frac{1}{2}C_D\rho_e\sigma(\dot{x} - u)^2, \quad (5.2)$$

where $C_D \sim 0.4$ (Goldstein 1938). The pre-shock, sub-Keplerian flow is assumed to have a radial velocity,

$$u \sim \beta/\sqrt{(x-1)}, \quad (5.3a)$$

and the post-shock sub-Keplerian flow,

$$u \sim 1/R\sqrt{(x-1)}. \quad (5.3b)$$

Here, β is a factor by which sub-Keplerian matter slows down compared to a freely falling flow. $\beta \sim 1$ for very low angular momentum cool flow. R is the compression ratio of the shock by which matter is assumed to be slowed down inside the CENBOL.

From Eqn. (5.1), we note that there are four forces in operation: (i) The second term inside the bracket of the left hand side is the Coriolis force $F_c = 2v_\phi\omega$, where $\omega = \lambda/x^2$ is the angular velocity of the flow. The Coriolis acceleration is given by (CD94),

$$a_C = \frac{\rho_i}{\rho_i + \rho_e} \frac{2\lambda^2}{x} \left[\frac{1}{x_0^2} - \frac{1}{x^2} \right]. \quad (5.4)$$

A flux tube brought from x_0 to x inside a flow of constant angular momentum would feel no Coriolis force if the motion is along the direction of constant angular velocity since $x_0 \sim x$ for rotating bodies. A magnetic flux tube with buoyancy factor $M_b (= \frac{\rho_e - \rho_i}{\rho_e}) = 1 - X$, will feel the (ii) Magnetic Buoyancy force (first term on the right hand side inside the curly bracket). The corresponding acceleration is (CD94):

$$a_{MB} = \frac{M_b}{1+X} \left[\frac{1}{2(x-1)^2} - \frac{\lambda^2}{x^3} \right]. \quad (5.5)$$

The tube will emerge out of the disk if a_{MB} dominates over a_C . The middle term on the right hand side of Eqn. (5.1) is the (iii) force due to Magnetic Tension. The corresponding acceleration is a_T (CD94):

$$a_T = -\frac{1}{m_i + m_e} \frac{\Psi^2}{2\pi\sigma^2} = -\frac{B^2}{4\pi x(\rho_i + \rho_e)}. \quad (5.6)$$

The final and very important force is represented by the final term of Eqn. (5.1). It is called the (iv) Drag Force exerted due to the motion of a rigid tube inside a flow. The corresponding acceleration is (CD94):

$$a_D = -\frac{1}{2} \frac{C_D \rho_i \sigma (\dot{x} - u)^2}{2\pi \sigma^2 (\rho_i + \rho_e)} \sim -\frac{C_D \rho_i u^2}{2\pi \sigma (\rho_i + \rho_e)}. \quad (5.7)$$

Here we used $\dot{x} \sim 0$ for computing the maximum value of the drag force.

Equating the acceleration due to buoyancy (Eqn. 5.5) with that due to magnetic tension (Eqn. 5.6) on the equatorial plane, we get the critical temperature of the external gas as (CD94),

$$T_{p,0} = \frac{m_p c^2 [\lambda_K^2(x_0) - \lambda^2]}{8kx_0^2}, \quad (5.8)$$

above which the tension dominates over buoyancy and the flux tubes rush towards the funnel wall catastrophically. Here we used the mean electron number per ion to be $\mu = 1/2$ and k is the Boltzmann constant. Subscript 0 specifically indicates that the flux tube will behave like an over stretched rubber-band only after it crosses $x = x_0$, where $T > T_{p,0}$. Note that since we are dealing with a sub-Keplerian disk, $T_{p,0} > 0$ in the entire region of interest. For typical values $x_0 = 100$, $\lambda_0 = 1.8$, one obtains $T_{p,0} \sim 6 \times 10^9$ K. For an adiabatic disk, this assumption remains valid even when the flux tube collapses very rapidly since its internal temperature will increase adiabatically in the same way as in the external disk. For an efficiently cooled two-temperature flow, the above proton temperature would correspond to an electron temperature of $T_e \sim \sqrt{m_e/m_p} T_p$. This is around 14 keV which is very reasonable for the temperature of the sub-Keplerian region. When the flux tubes fall radially, neither Coriolis force nor the drag term could be neglected. In fact, accelerated flux tubes would have high \dot{x} in the drag term as they move faster than the bulk radial motion. Meanwhile, assuming that internal mass of a flux tube is roughly constant, the cross-section $\sigma \sim 1/\sqrt{x}$ increases as the flux tube approaches the black hole. So, this will also increase the drag term. As a result, we expect that the flux tube would slow down somewhere close to the black hole and buoyancy would eject the flux tube out of the disk perpendicularly as shown in Figure (5.1). Typical trajectories of the flux tubes, based on numerical integrations in CD94, are shown in Figure (5.1).

The buoyancy timescale t_b is estimated from Eqn. (5.5): $a_{MB} \sim h/t_b^2 = \frac{M_b}{(1+X)x^3} (\lambda_K^2 - \lambda^2)$, where, $h \sim a_s x^{3/2}$ is the half thickness of the disk in vertical equilibrium at x and $a_s \sim x^{-1/2}$ is the speed of sound. Note that t_b is very large in a Keplerian disk ($\lambda_K \sim \lambda$). For a sub-Keplerian flow, $\lambda/\lambda_K \sim 0.4$ with $\lambda = 1.8$ at $x = 30$, $X \sim 0.1$, $M_b \sim 0.9$, $t_b \sim 240$.

Collapse time t_f of a flux tube is estimated in the following way: When tension is the most dominant force, the radial equation of the flux tube (Eqn. 5.1) is simplified to:

$$\ddot{x} + a_T = 0. \quad (5.9)$$

Putting $\ddot{x} \sim x/t_f^2$, we see that the velocity of collapse of the flux tube v_f is,

$$v_f \sim \left(\frac{B^2}{4\pi\rho_e}\right)^{1/2} \sim v_a, \quad (5.10)$$

where v_a is the Alfvén velocity. Thus, flux tube collapses in Alfvén speed. Since $B \propto x^{-2}$, magnetic pressure is $\propto x^{-4}$, while the gas pressure $p_e \propto x^{-5/2}$, the ratio of magnetic to gas pressure $f \propto x^{-3/2}$, increasing with the decrease of x . As the flux tube leaves the Keplerian disk, large shear at the transition region and in the sub-Keplerian flow quickly intensifies the flux tube to $M_b \sim 1$ during infall. On the other hand, if $f \sim 1$ at $x \sim 300$ where the flow deviates from a Keplerian disk, $f \sim 30$ at $x = 30$, inside the CENBOL. The Alfvén speed $v_a \sim \left(\frac{B^2}{4\pi\rho_e}\right)^{1/2} \sim (f/\gamma)^{1/2}a_s \sim 5a_s$ where we used $\gamma = 4/3$. Since, inside a CENBOL, the velocity of matter v_m is highly sub-sonic, it is therefore high sub-Alfvénic: $v_m \ll v_a$. Thus, $v_f/v_m \gg 1$ and the flux tube collapses catastrophically. This justifies the conjecture made earlier that the rubber-band effect could evacuate the disk (Chakrabarti, 1994; 1996c; 2000). For $a_s \sim x^{-1/2}$, $t_f \sim x^{3/2}/5 \sim 30$ at $x = 30$. Thus inside the CENBOL $t_b \gg t_f$.

So far, we have ignored many non-axisymmetric effects such as Parker instability (1979 and references therein) and shearing instability (e.g., Balbus & Hawley, 1991). Foglizzo & Tagger (1995) treated this problem comprehensively in the context of a standard disk embedded in a large scale field. They found that (a) if the wavelength is larger than the disk thickness then the flux tube is very unstable and buoyantly comes out of the disk and (b) instability is strongest if the field is weaker. According to Parker (1979), submerged field tubes may break up into filaments in timescales of around $3\Lambda/v_a$, where Λ is the scale height and the field is able to escape from the gas in timescales $t_P \sim \Lambda/v_a$. If $\Lambda \sim h \sim x$, which is especially true in CENBOL region, the time scale of the escape of the field may be comparable to the t_f as obtained above. As a result, the flux not only collapses catastrophically, but also escapes upwards following a curved trajectory as depicted in Figure (5.1). In presence of a differential rotation, Balbus and Hawley (1991) suggested that even a small initially vertical field would be amplified to create all the components in dynamical timescale $t_d \sim 1/\omega = x^2/\lambda \sim 50$ (at $x = 30$, $\lambda = 1.8$). Numerical simulation (Hawley, Gammie & Balbus, 1995) has verified this instability neglecting the tension effects. Even though the time scales of the collapse, Parker instability

and shear instability are of the same order, we believe that the rubber-band effect would still be important for the destruction of the inner disk.

5.2.3 Estimation of the ejected mass from the inner accretion disk of GRS 1915+105

Vadawale et al. (2001) have shown that during the soft X-ray dips a thermal-Compton component in the X-ray spectrum gets suppressed. Several workers in the literature talked about the disk-evacuation (e.g., Belloni et al. 1997; Feroci et al. 1999) in this context. We like to understand this using Two Component Advective Flow (TCAF) models of Chakrabarti & Titarchuk (1995) in presence of Magnetic field (i.e., MTCAF model) and its time variability properties described in Molteni, Sponholz & Chakrabarti (1996); Ryu, Chakrabarti & Molteni (1997; hereafter referred to as RCM97) and Chakrabarti & Manickam (2000). The observation of possible disk-evacuation is clearly in line with the TCAF model and the shock oscillation model of the quasi-periodic oscillations (CM00; see also, Rao et al. 2000) which showed that the Comptonising post-shock region participates in oscillation. The sub-Keplerian region in the pre-shock flow does not emit much radiation and it is possible that some of this region may also be disrupted during the rapid collapse of the flux tube. Once we accept the destruction of the sub-Keplerian region by magnetic rubber-band effect, we can compute the mass of this region in the following way:

The shock location is computed by equating the infall time from the shock with the time scale of QPO. This time scale t_{ff} can be written in the form (CM00):

$$t_{ff}^{-1} = \frac{1}{R} \frac{1}{r_s^\alpha} \frac{cv_0}{r_g}, \quad (5.11)$$

where, R is the compression ratio (see also, Eqn. 5.3b), r_s is the shock location, v_0 is a dimensionless constant. Here, $\alpha = 3/2$ for free-fall motion and $\alpha = 1$ for a flow of constant velocity cv_0/R in the post-shock region. Using this assumption, the shock location in the pre-dip and the post-dip flow (for parameters in these flow see, Vadawale et al. 2001) are $\sim 45r_g$ and $\sim 66r_g$ respectively. CM00 proposes that a better fit in the correlation between the duration of the QPO and the frequency of QPO requires more or less constant velocity in the post-shock region with a rough velocity of $0.066c/R$. This produces the shock in the pre-dip and the post-dip flow at $79r_g$ and $140r_g$ respectively. Using the parameters of Vadawale et al. (2001), and the location of the shock as given above, the electron number density

in the Comptonising region is found to be $n_e \sim 10^{17} \text{ cm}^{-3}$. The corresponding mass ($\frac{4}{3}\pi r_s^3 m_p n_e r_g^3$) of the region is $M_{CENBOL} \sim 2 - 3 \times 10^{18} \text{ gm}$ depending on the model of the inflow. How much of this matter is squirted out of the disk along the axis? Again, in the absence of the size distribution of the flux tubes, the answer is difficult. However, because of centrifugal force, matter is unlikely to enter within the ‘funnel wall’ (CD94) even after compression, sudden collapse of large flux tubes [$\sigma \sim h(r_s)$] would be expected to displace the whole CENBOL region parallel to the funnel wall. The outflow rate would be $\dot{M}_{out} \sim M_{CENBOL}/t_f$ which may be very large compared to the inflow rate for a short duration of t_f . In case flux tubes are smaller in size, since the collapse velocity is much larger than the speed of sound, matter will still be displaced but would be refilled in free-fall time, unless there are many near-simultaneous flux collapse events.

In case the magnetized sub-Keplerian disk is removed by imploding flux tubes as described in the earlier Section, one requires to know the location of the inner edge of the Keplerian disk to estimate the complete mass involved. From the model fit (Vadawale et al. 2001), the Keplerian disk temperature turns out to be $T_K \sim 1.5 \text{ keV}$. With a hardening factor of around 1.7 (Shimura and Takahara, 1995), mass of the black hole as $10M_\odot$ and Shakura-Sunyaev viscosity parameter $\alpha_{SS} = 0.01$, the above temperature corresponds to a transition radius at around $r_{tr} \sim 320r_g$ (Shakura and Sunyaev, 1973). Assuming density falling off as $\rho \sim \rho_0(\frac{x_0}{x})^{3/2}$, the mass of the sub-Keplerian flow of size x_{tr} ($\int 4\pi x h(x) \rho dx$ with $h(x) \sim x$) is around 10^{20} g . These computations assume no pair production, i.e., there is exactly one electron for each proton in the Comptonising region.

Once the evacuation is complete, the disk is filled in quickly by sub-Keplerian matter in the timescale of:

$$t_{visc} \sim \frac{1}{\alpha_{SS}} \left(\frac{h(x)}{x}\right)^{-2} \frac{x}{v_{Kep}} = 192 \left(\frac{0.01}{\alpha_{SS}}\right) \left(\frac{0.03}{a_s}\right)^2 \left(\frac{x_{tr}}{300}\right)^{1/2} \frac{M_{BH}}{10M_\odot} \text{ s}. \quad (5.12)$$

Here, $h(x) \sim a_s x^{3/2}$ (a_s is the speed of sound) is the local vertical height of the disk. The time scales seem to be reasonable, since the dips have been seen to be filled up in matter of 150 to 200 seconds. It is to be noted that Dhawan et al. (2000) using disk-instability model of Belloni et al. (1997) obtained the missing inner disk region to be only 180 km. This distance is about $6r_g$ and with $10^{18} \text{ gm s}^{-1}$ accretion rate which they employ, the mass of this region cannot be enough to create the 10^{23} gm blob (or, even 10^{18} gm mini-blobs) observed by Mirabel & Rodríguez (1999). This is particularly because the region $1 - 3r_g$ is definitely supersonic and sub-Keplerian and therefore is of very little mass. We believe that the missing region should be much larger, possibly order of a $100 r_g$ or so.

In the next section, we will discuss the plausible mechanisms to produce ‘bullet-like’ ejecta from the precessing disk in SS 433 system.

5.3 Ejection mechanism of bullets in SS 433

It is already discussed that SS 433 is a HMXB having companion of OB-type or evolved A-type star, which is losing mass at the rate of about $10^{-4}M_{\odot}\text{yr}^{-1}$ (van den Heuvel 1981), corresponding to extremely super-Eddington accretion regardless of the mass of the compact object. The jets in SS 433 have curious properties that it is ejected almost continuously in a ‘bullet’ like fashion (Borisov & Fabrika 1987; Vermeulen et al. 1993b; Paragi et al. 1999; Gies et al. 2002), with a surprisingly nearly constant radial velocity of about $0.26c$. The radial velocity is less than the maximally allowed sound speed of $c/\sqrt{3}$, and thus hydrodynamic acceleration could, in principle, explain its ejection features. Therefore one may not require a magnetic or electrodynamic acceleration process (Belcher & MacGregor 1976; Lovelace 1976). However, the good collimation of the jets (Margon 1984; Paragi et al. 1999) and the massive radio flares which are rare events in SS 433 (Safi-Harb & Kotani 2003), support the idea of presence of toroidal flux tubes in the disk.

It was already pointed out by Chakrabarti (1999) and Das et al. (2001) that significant outflows are produced only when the accretion rate is such that the X-rays source is in a low/hard state, and all the observational indications in other microquasars also suggest that the jets are indeed produced in low/hard states (Corbel et al. 2001; Klein-Wolt et al. 2002). However, it is difficult to imagine how SS 433 manages to remain in the low/hard state with $10^{-4}M_{\odot}\text{yr}^{-1}$ of wind matter ejected from its companion. The answer to this quandary probably lies in the recent results of Paragi et al. (1999) and Blundell et al. (2001), whose high resolution radio maps show that there is a large region of roughly 50 AU in radius that is filled with enough gas and dust to obscure the accretion disk and the base of the jets. They also found an equatorial outflow. Gies et al. (2002) present an additional evidence from observations of the ‘stationary’ $\text{H}\alpha$ and He I lines for an extended ‘disk wind’. So it is distinctly possible that most of the matter from the donor is rejected either by the centrifugal force (Chakrabarti 2002) or by the radiation force far outside the central accretion disk, and thus the compact object receives only a few times the Eddington rate (\dot{M}_{Edd}) of its companion’s wind matter to accrete. This consideration finds further support from the fact that the kinematic luminosity of the jet itself is around 10^{39} ergs sec^{-1} (Margon 1984), which corresponds to about 1 Eddington rate for a $10M_{\odot}$ compact object.

In numerical simulations of supercritical winds by Eggum, Coroniti & Katz (1985) designed to model SS 433, it was shown that only a fraction of the percent of the infalling matter is ejected from a radiation pressure-supported Keplerian disk, which indicates that the accretion rate must be at least $100\dot{M}_{Edd}$ if the accretion takes place through a Keplerian disk. Recent, *Chandra* and *RXTE* data does not show any signature of a Keplerian disk (Marshall et al. 2002; Nandi et al. 2005). On the other hand, numerical simulations of a sub-Keplerian disk by Molteni, Lanzafame & Chakrabarti (1994) suggest that about 15%-20% of matter is ejected as an outflow, indicating that the accretion rate onto the compact object in SS 433 need be at most a few times \dot{M}_{Edd} . Similar simulations with different parameters yield situations where no steady shocks can form, even though two saddle-type sonic points are present (RCM97); under these conditions, large scale shock oscillations produce intermittent outflows instead of continuous outflows. Since the compact object is a wind accretor, a low angular momentum, sub-Keplerian flow is most likely description of the accretion flow. Indeed, the presence of sub-Keplerian flows in several other HMXBs has now been verified (Smith, Heindl & Swank 2002).

The basic ejection in SS 433 is bullet-like, and since the size of the X-ray emitting region (X-ray jet) is smaller than $l_x \sim 10^{12}$ cm within which the material in the jets is already accelerated to $v_{jet} \sim 0.26c$ (Watson et al. 1986; Stewart et al. 1987), although it is found that the jet velocity in X-rays is little larger than $0.26c$ (Marshall et al. 2002, Nandi et al. 2005), the bullets are not expected to be delayed by more than $l_x/v_{jet} \sim 100$ sec. Indeed, the observations of SS 433 indicated variability on timescales of 50 – 1000sec (Safi-Harb & Kotani 2003), roughly corroborating this picture. Recently, Nandi et al. 2005 also found the same short time scale variability in *RXTE* data. In fact, a simultaneous measurement of massive flare at 2 GHz in the radio (Kotani & Trushkin 2001) and in hard X-rays (Safi-Harb & Kotani 2003) indicated a strong anti-correlation of radio and X-ray fluxes, similar to what is observed in GRS 1915+105 (MR99; Vadawale et al. 2001). Moreover, the X-ray luminosity is very low ($\sim 10^{36}$ ergs sec $^{-1}$) and is believed to come from the base of the jets. All the previous and recent observations made with *EXOSAT*, *Ginga*, *ASCA*, *Chandra* and *RXTE* suggest that the X-ray spectrum of the jet is well fitted with thermal bremsstrahlung model with $kT \sim 30keV$. The overall spectral shape suggests that the source has always been in a standard low/hard state, and so far no signature of thermal emission from ‘Keplerian disk’ has been detected. From the interaction of the jet with the SNR W50, the lower limit of the kinematic luminosity is found to be at least 10^{39} ergs sec $^{-1}$ (Biretta et al. 1983; Davidson & McCray 1980). This means that the mean mass outflow rate is around 10^{18} gm sec $^{-1}$, and if most of

it is in the form of bullets ejected at 50 – 1000 sec intervals, the mass accumulated in each bullet should be in the range of $10^{19} - 10^{21}$ gm.

Therefore, it is clear from the above discussion that the essential features that one must explain when attempting to produce bullets out of the accretion disks are (i) the disk should be a sub-Keplerian flow, (b) the object (black hole) and its surrounding should be in a low/hard state, (c) bullets should be ejected in 50 – 1000 s timescales under normal circumstances, (d) the mass of each bullet should be around $10^{19} - 10^{21}$ gm, and, finally, (e) there should be occasional flaring with an anti-correlation of radio and X-ray emission. We now discuss several scenarios and present what we believe to be the most possible picture of what is going on in SS 433. The four process are schematically shown in Figures 5.2 (a-d).

5.3.1 Cooling of the base of the jet by Comptonisation and separation of blobs

It was shown by several numerical simulations that significant outflows are produced from regions very close to the inner edge of the accretion flow, possibly from the CENBOL (Molteni et al. 1994, 2001). These jets are launched subsonically but quickly pass through the inner region to become supersonic. In the subsonic region while the matter moves slowly, the density is high and the optical depth could be large enough ($\tau \geq 1$) to undergo Comptonisation cooling (Fig. 5.2a) *provided there is a Keplerian disk underneath to supply soft photons*. A part of the outflow, which was subsonic previously, becomes supersonic because of this rapid cooling and separates from the base of the jet. This separation of blobs is expected to occur at the sonic surface r_c which is $\sim (2 - 3)r_s$, where r_s is the size of the centrifugal barrier (see, Chakrabarti 1999).

This possibility, though attractive, and in fact likely to be a major mechanism for rapid state change in objects like GRS 1915+105 (CM00), is untenable in SS 433 because the latter is a wind accretor: thus no significant Keplerian disk is expected in this system to supply the soft photons, and none has been detected so far (Watson et al. 1986; Yuan et al. 1995; Marshall et al. 2002; Nandi et al. 2005).

5.3.2 Resonance oscillation of accretion shocks in the presence of bremsstrahlung cooling

Numerical simulations of accretion flow show that in cases where the cooling timescale nearly matches the infall timescale, a shock forms, but it then starts oscillating and ejects matter quasi-periodically (Langer, Chanmugam & Shaviv 1983; MSC96; see, Fig. 5.2b). In order to have an oscillation period of around 50 sec, the shock must be located at the large distance of $r_{s,MSC} \approx 6400r_g$ for a black hole of mass $M_c = 10M_\odot$, where $r_g = 2GM/c^2$. The mass of the postshock region is computed by equating the bremsstrahlung (which we assume to be the major cooling mechanism) cooling time and the infall time in the postshock region (MSC):

$$T_{MSC} \simeq \frac{\epsilon}{\dot{\epsilon}} \simeq \frac{r_{s,MSC}}{v_f} \simeq \left(\frac{Rr_{s,MSC}}{r_g} \right)^{3/2} \frac{r_g}{c}, \quad (5.13)$$

where ϵ is the specific thermal energy, v_f is the infall velocity, and $R = (\gamma + 1)/(\gamma - 1) \simeq 4-7$ (these limits are for a strong shock with $\gamma = 5/3$ and $\gamma = 4/3$, respectively) is the compression ratio at the shock. Assuming the gas density (n) and temperature (T) scale as $n \sim r^{-3/2}$ and $T \sim r^{-1}$, respectively, the mass of the sub-Keplerian region of $r \leq r_s$ turns out to be 7×10^{19} gm (with $M = 10M_\odot$, $\gamma = 5/3$). This is indeed of the same order as the mass of the bullets observed in SS 433. However, one has to have both the angular momentum and energy of the injected material comparable to the marginally bound values determined by the central object in order to achieve such oscillation. On the other hand, if the mass expulsion from the system takes place at the similar radius of $r_{ex} \sim 10^4 r_g = 2 \times 10^9 M/M_\odot$ cm due to the centrifugal force, the specific angular momentum of the flow is approximately $[r_{ex}/(2r_g)]^{1/2} r_g c \sim 70 r_g c$, which is very large compared to the marginally bound value of $2r_g c$. So it is unlikely that this mechanism works in SS 433.

5.3.3 Nonsteady and nonlinear shock oscillation

A standing shock can form in sub-Keplerian flow only if there are two saddle-type sonic points and the Rankine-Hugoniot relation is satisfied at least at one point in between these two sonic points. However, Chakrabarti (1990) showed that there is a large region of the parameter space where there are two saddle-type sonic points but the shock conditions are not satisfied. Even an initially supersonic accretion (such as the wind from the companion) can fall into this category.

What will happen to such a realistic flow, especially when the specific entropy at the inner sonic is greater than that at the outer sonic point? RCM97 discovered that

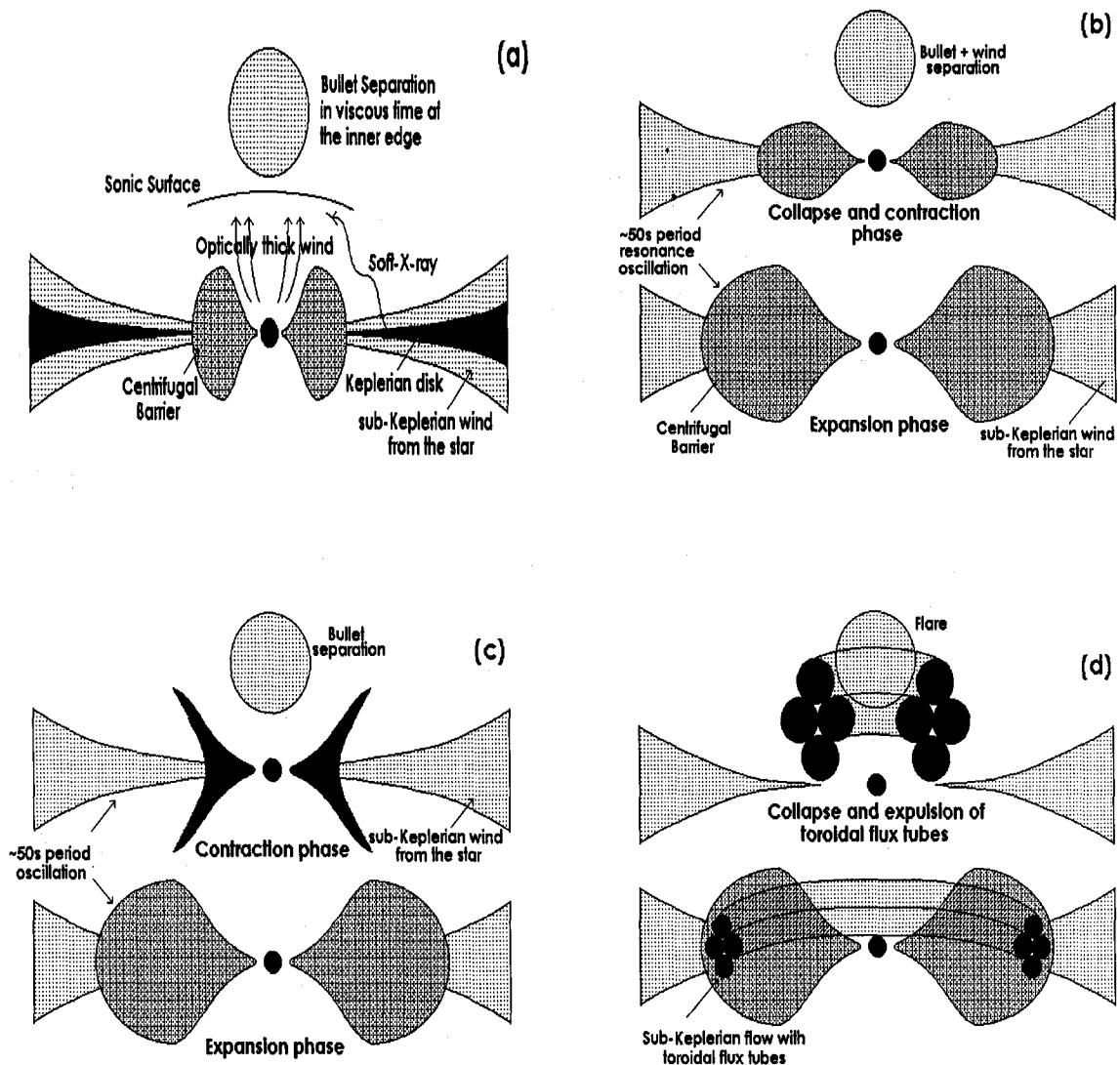


Figure 5.2: Schematic representation of the bullet separations in SS 433 are shown. (a) The base of the jet is cooled down by soft photons from a Keplerian disk and it is detached when it becomes supersonic. (b) Resonance oscillation of the sub-Keplerian region due to the near matching of the infall time with the cooling time produces discrete ejecta during the phase when centrifugal barrier contracts. (c) Nonsteady motion of the centrifugal barrier due to the inability of the flow to find a steady shock solution. (d) Magnetic tension from toroidal flux tubes (shown as shaded narrow tori) causes them to collapse catastrophically in a hot ambient medium in rapid succession, which evacuates the centrifugal barrier. The recurrence time of (a) is the viscous timescale in the inner part of the disk, ~ 10 sec; (b-c) is ~ 50 sec; and (d) is random and dictated by the enhanced magnetic activity.

a flow injected with these parameters exhibits yet another type of shock oscillation (Fig. 5.2c). Here the shock searches for a stable location and oscillates without finding it. In the first half of the cycle, the shock recedes far away, the postshock region fills up, but the accretion is essentially completely blocked. In the second half of the cycle, the shock pushes the matter into the black hole, thereby evacuating the postshock region. In a realistic simulation, RCM97 find that while the ratio of actually accreted matter to the amount available from the companion, $R_{ai} \equiv \dot{M}_{acc}/\dot{M}_{inj}$, would be 0.2 during the first half-cycle, $R_{ai} \sim 1.3$ in the second half-cycle. The outflow was also found to be very large. The timescale of oscillation was found to be $T_{RCM} \sim (4000 - 6000)r_g/c$ for a $r_s \simeq 20r_g$ whose infall time is only about $T_{MSC} \simeq (Rr_s/r_g)^{3/2}(r_g/c) \sim (350 - 400)r_g/c$. Thus, this type of oscillation takes about a factor of $R_T = T_{RCM}/T_{MSC} \sim 15$ times longer than the resonance oscillation discussed in the previous section (§5.3.2). For a 50 sec oscillation, the location of the shock should be obtained from $(r_{s,RCM}/r_g)^{3/2} \simeq (1/R)(50\text{sec}/R_T)(c/r_g) \sim 10^4$, which gives $r_{s,RCM} \sim 450r_g$ for a $10M_\odot$ black hole, a more physically reasonable value. Even though the size of the oscillating region goes down by a factor of 10 or so, compared with that involved in the resonance oscillation, the ejected mass need not go down (even for the same accretion rate as in the earlier case). This is because nearly all of the accretion flow is accumulated in half the cycle (~ 25 sec in this case) before being ejected (see, Fig. 2 of RCM97).

Another importance of this type of nonsteady shock oscillation is that it is driven by centrifugal force and not by thermal cooling. Hence the result is generally independent of the accretion rate. Thus, as long as the viscosity remains low, equivalent to having the Shakura-Sunyaev (1973) parameter $\alpha_{ss} \leq \alpha_c \simeq 0.015$ (Chakrabarti 1990), and \dot{M}_{inj} remains fairly constant, this oscillation, once established, could be sustained indefinitely.

5.3.4 Magnetic rubber-band effect

In the event of increase in magnetic activity of the disk, as could happen for a instance when the accretion disk bends towards the binary companion during its precessional motion, it is not unlikely that a strong magnetic field will be first intercepted, and then advected, toward the inner edge of the disk. In this the field will preferentially become toriodial due to shear in the rotating flow. Then, as has already been discussed in section §5.2.2 (CD94; Nandi et al. 2001b), the acceleration

due to the magnetic tension,

$$a_T = -\frac{B_\phi^2}{4\pi r(\rho_i + \rho_e)} \sim -\frac{B_\phi^2}{4\pi r\rho_e}, \quad (5.14)$$

would be the dominant force in the postshock region of the sub-Keplerian flow (Fig. 5.2d). Here r is the major radius of the toroidal flux tube and ρ_i and ρ_e are the densities of the medium internal and external to the flux tube, respectively. The last step in equation (5.14) is written because $\rho_i \ll \rho_e$ for a strong flux tube. Since $B_\phi \propto 1/r$ and $\rho_e \propto r^{-3/2}$, we get

$$a_T = r^{-3/2}, \quad (5.15)$$

thus increasing rapidly as the tube comes closer to the black hole, and even surpassing the magnetic buoyancy,

$$a_{MB} = \frac{(1-X)}{(1+X)} \left(\frac{\lambda_K^2 - \lambda^2}{r^3} \right) \simeq \frac{\lambda_K^2 - \lambda^2}{r^3}, \quad (5.16)$$

where $X = \rho_i/\rho_e \rightarrow 0$ and λ_K and λ are, respectively, the specific angular momentum of a Keplerian disk and the disk under consideration. The accelerations in equations (5.15) and (5.16) do cross over, since at a location very close to a black hole, $\lambda \rightarrow \lambda_K$ for a sub-Keplerian flow.

The effect of magnetic tension is dramatic, and the inner part of the disk is evacuated in the Alfvén timescale: $r/v_A \sim (r/a_T)^{1/2} \lesssim 0.1$ sec, for a $10M_\odot$ black hole with a realistic Alfvén speed, $v_A \simeq 0.1c$ (Nandi et al. 2001b). The enhanced plasma ejection along the axis presumably causes sporadic magnetic-flare events that would be observable as radio outbursts, at the same time reducing the X-ray emission from the disk that forms the base of the jet. Such effects may have been seen (Safi-Harb & Kotani 2003) in SS 433 where simultaneous observations of 2 GHz radio and 2 – 20 keV X-ray fluxes from SS 433 have been made, and a clear dip in X-ray flux is seen at the same time a strong radio flare is observed. It is worth noting that similar anticorrelated variations are common during flares in GRS 1915+105 (Feroci et al. 1999; MR99; Vadawale et al. 2001), and we suggest that the flares in SS 433 originate in the same way.

In the next Chapter, we will draw our conclusions on the basis of the results that are presented in this thesis.

Chapter 6

CONCLUSIONS AND DISCUSSIONS

As has been mentioned in the introduction itself, the goal of the thesis is to study the spectral and timing properties, mostly in X-rays, of accretion flows around black holes. So, we started with giving description of the compact objects (white dwarfs, neutron stars and black holes). We specially discuss the galactic black holes that are found in X-ray binaries. In §1.2, we gave an account of the historical developments of X-ray astronomy instruments. We also discussed the importance of astronomy missions how it strengthened our views about X-ray observation of compact objects. In §1.3, we talked about different radiative processes, the knowledge of which are essential to explain most of the observed X-ray features that are associated with the black holes. In §1.4, we presented the general overview of the accretion processes and their implication to calculate luminosity, temperature, mass of the central object etc. Finally, we discussed various models of accretion onto compact objects, starting from Bondi flow to TCAF paradigm.

In Chapter 2, we discussed the data acquisition and analysis techniques. As this thesis work is based on the use of X-ray data obtained with the *RXTE* satellite, we gave a detail description of the satellite components (i.e., ASM, PCA and HEXTE). The All-Sky Monitor (ASM) has proved to be a unique instrument on-board *RXTE* due to its fascinating first-results or quick look capability, such as detection of a new source in the sky, state change of known sources and quasi-periodic of high flux variation in a longer time scale etc. On the other hand, the Proportional Counter Array (PCA) has the unique capability of tagging the X-ray events with microsecond accuracy over the broad energy range 2–60 keV which enables *RXTE*/PCA to probe the fundamental physical processes which are going on closed to the compact objects as well as the geometry of the systems, nature and characteristics of the compact objects itself. We also discussed different data mode and screening criteria to get rid of invalid or unwanted data from raw data. Once this procedure is done, the raw data

becomes useful for the main analysis. In §2.2, we presented the analysis technique in detail. Both the timing and the spectral analysis techniques are discussed in this section and we gave an account of step-wise analysis techniques for the different data modes. The data reduction and analysis was performed using the software (LHEASOFT) FTOOLS version 5.1 and XSPEC version 11.1.

In this section, we also talked about the spectral fitting procedure along with the χ^2 minimization technique that are done with XSPEC package in LHEASOFT. In §2.3 and §2.4, we briefly discussed the *IXAE* payload on IRS-P3 and *GMRT* radio telescope at Pune and Infrared telescope at Mt. Abu respectively. We re-analyzed the *IXAE* X-ray data and found the evidence of class transitions in GRS 1915+105 light curves. Other data from two telescopes are used as a part of the Multi-wavelength Campaign of SS 433 to see the correlation in different wave bands i.e., X-rays, Infrared and Radio emission.

In Chapter 3, we began with discussing the fascinating observed properties of GRS 1915+105 which is a massive stellar mass black hole of mass $14 \pm 4M_{\odot}$. *RXTE*/*ASM* shows that the long time scale variability is very complex, which is not observed any other sources. VLA observation in radio band confirmed its superluminal ejection of matter in the form of jets with a true speed of $v \approx 0.98c$. The maximum luminosity observed in GRS 1915+105 is $\sim 10^{39}$ ergs/sec which also confirmed that the source is one of the high accreting black hole candidates. GRS 1915+105 becomes more interesting in X-rays, in the era of *RXTE*, due to its fascinating short time scale variabilities (light curves). The X-ray variabilities of GRS 1915+105 and their timing properties are discussed in §3.2. The light curves of GRS 1915+105 are classified in 12 classes by Belloni et al. (2000) (model independent way) and they found three basic states which are responsible for all the variabilities. Here, we analyzed the light curves in different way that is model dependent. In the light of advective flow paradigm (TCAF paradigm), we classified the light curves just in 4 classes (states) and proposed five fundamental modes of accretion/wind configurations to explain most of the observed light curves. We also mapped these fundamental modes with Belloni's three basic states and discussed timing and spectral properties of each light curves. In §3.3, we presented the results from *IXAE* and found the direct evidence of class transitions in GRS 1915+105 (e.g., $\kappa \rightarrow \rho$) and explained such transitions by means of predominant variation of the sub-Keplerian accretion rate alone though smaller variation of Keplerian flow cannot be ruled out.

Beside the X-ray variabilities (temporal characteristics), GRS 1915+105 also shows spectral variabilities which we presented in §3.4. We analyzed the spectral data and invoked that the spectral variabilities are quite well understood only when

the outflows/winds are generated from the CENBOL, not from the entire disk. In the same section, we discussed the spectral study of X-ray dips of θ class of GRS 1915+105 during huge radio flares. It is found that during soft ‘dips’ the Comptonized component (8 – 30 keV photon counts) is suppressed and there is no signature of QPO. We argued that the absence of Comptonized component in the soft X-ray dips (in θ and β class), is the evidence for the disappearance of the inner accretion disk (i.e., CENBOL).

We also analyzed the archival data of GRO J1655-40 and found the spectral variabilities which are quite similar in nature with GRS 1915+105. We didn’t present these results in this thesis.

In Chapter 4, we studied both the temporal and spectral properties of X-ray data that are obtained with *RXTE*. In §4.1, we talked about various features of the enigmatic and most unusual galactic source SS 433. Here, we discussed all the bizarre properties of the source in all wavelengths. This source remains unique for the last 25 years due to its two attracting features: one is ‘bullet-like’ ejection in the form of jets, which move with almost constant velocity ($\sim 0.26c$) and the other one is the precession of the jets (in ~ 164 days period) which follows the ‘kinematic model’ for SS 433. In §4.3, we presented the results from the Multi-wavelength campaign of 27th and 29th September 2002 in X-rays, Infrared and Radio bands and found the photometric evidence of ejection of ‘bullet-like’ features in SS 433.

In the same Chapter (§4.3), we presented most intriguing results that were obtained from *RXTE* X-ray observation. From the temporal analysis, we found the short time scale variability of 50 – 100 sec indicates a length $\leq 10^{12}$ cm, which could be the length scale of the X-ray jets. It was also found that the X-ray flux varies with the precessional phase as well as the orbital phase of the SS 433 binary system. We didn’t find any quasi-periodic behavior in the PDS of X-ray light curves of SS 433. From the spectral analysis, we detected the iron line features in the X-ray spectrum. We found that the iron line energy (including blue/red shifts) match with the shifts predicted from the ‘kinematic model’. This therefore indicated that the X-ray emitting material is physically associated with the jets. The total X-ray spectrum of SS 433 is modeled with the thermal bremsstrahlung and iron line features. No signature of Keplerian disk is found in the spectrum. All the results that we presented in this Chapter, are obtained from *RXTE* for the first time. We also found some kind of flaring activity in the *RXTE*/ASM data.

As the Jets and Outflows are common phenomena in galactic black holes (e.g., GRS 1915+105, SS 433), in Chapter 5, we gave an account of production of jets

from the vicinity of black holes. According to TCAF paradigm, CENBOL plays the crucial role for the production of jets/outflows from the disk. Since the inner disk evacuation phenomenon is seen to be correlated with an intense radio activity, the role of magnetic field must be studied in order to understand the system completely. So we investigated the magnetic flux tube dynamics inside the TCAF disk (we termed it as Magnetized- TCAF disk or MTCAF) to explain the disk evacuation phenomena. We showed that close to the black hole, where the flow could be very hot ($\geq 10^{10}$ K) (i.e., inside the CENBOL) the tubes move at least with the Alfvén speed and may catastrophically collapse like a stretched rubber band. We conjectured that such a rapid collapse would assist evacuation of matter from the disk and cause X-ray ‘dips’ seen in the light curves of GRS 1915+105. In §5.2.3, we estimated the mass of the ejecta which agrees with observations. In §5.3, we presented few scenarios leading to the ejection of matter as ‘bullets’ in SS 433. We discussed four possible ways to create blobs of matter originating from the disk and concluded that periodic ejection of the blobs by the large scale oscillations of an accretion shock may be the fundamental production mechanism of the ‘normal’ bullets. The irregularly observed rapid flaring (Vermeulen et al. 1993a) and massive radio flare events (Safi-Harb & Kotani, 2003) could be understood in terms of the catastrophic collapse of toroidal magnetic flux tubes, very similar to what has been argued to be occurring in GRS 1915+105.

All the observed features in GRS 1915+105 and SS 433 are quite well explained with the TCAF paradigm. So we believe that the TCAF paradigm is the most promising one to explain most of the X-ray features observed in other black holes as well.

Bibliography

- Abell, G. O. & Margon, B., *Nature*, **279**, 701 (1979)
- Abramowicz, M. A., Czerny, B., Lasota, J. P. & Szuszkiewicz, E., *Astrophys. J.*, **332**, 646 (1988)
- Agrawal, P. C., Paul, B., Rao, A. R., et al., *Journal of the Korean Astronomical Society*, **29**, S429 (1996)
- Anderson, S. F., Margon, B. & Grandi, S. A., *ApJ*, **273**, 697 (1983)
- Antokhina, E. A. & Cherepashchuk, A. M., *SvAL*, **11**, 4 (1985)
- Antokhina, E. A. & Cherepashchuk, A. M., *AZh*, **64**, 562 (1987)
- Balbus, S.A. & Hawley, J.F., *ApJ*, **376**, 214 (1991)
- Belcher, J. W. & MacGregor, K. B., *ApJ*, **210**, 498 (1976)
- Belloni, T., Mendez, M., King, A. R., van der Klis, M. & van Paradijs, J., *ApJ*, **479**, L145 (1997)
- Belloni, T., Klein-Wolt, M., Mendez, M., van der Klis, M., & van Paradijs, J., *A&A*, **355**, 271 (2000)
- Beloborodov, A. M., *MNRAS*, **297**, 739 (1998)
- Bevington, P. R., *Data reduction and error analysis for the physical sciences*, (Published by McGraw-Hill, New York), p-208 (1969)
- Biretta, J. A., Cohen, M. H., Unwin, S. C. & Pauliny-Toth, I. I. K., *Nature*, **306**, 42 (1983)
- Blundell, K. M., Mioduszewski, A. J., Muxlow, T. W. B., Podsiadlowski, P. & Rupen, M. P., *ApJ*, **562**, 79 (2001)
- Bondi, H., *Mon. Not. Roy. Astron. Soc.*, **112**, 195 (1952)

- Borisov, N. V. & Fabrika, S. N., *Soviet Ast. Lett.*, **13**, 200 (1987)
- Brinkmann, W., Kawai, N., Matsuoka, M. & Fink, H. H., *A&A*, **241**, 112 (1991)
- Brown, J. C., Cassinelli, J. P. & Collins, G. W., *ApJ*, **378**, 307 (1991)
- Castro-Tirado, A. J., Brandt, S. & Lund, N., *IAU Circ.*, 5590 (1992)
- Chakrabarti, S. K., *Theory of Transonic Astrophysical Flows*, (World Scientific Publishing, Singapore) (1990)
- Chakrabarti, S. K. & Molteni, D., *ApJ*, **417**, 671 (1993)
- Chakrabarti, S.K., *Proceedings of 17th Texas Symposium*, Edited by Böhringer, H., Morfill, E. & Trümper, J., (New York Academy of Sciences, New York), p. 546 (1994)
- Chakrabarti, S.K. & D'Silva, S., *ApJ*, **424**, 138 (1994) [CD94]
- Chakrabarti, S. K. and Titarchuk, L., G., *ApJ*, **455**, 623 (1995) [CT95]
- Chakrabarti, S.K. and Molteni, D., *Mon. Not. R. Astron. Soc.*, **272** 80 (1995)
- Chakrabarti, S. K., *Mon. Not. Roy. Astron. Soc*, **283**, 325 (1996a)
- Chakrabarti, S. K., *ApJ*, **464**, 664 (1996b)
- Chakrabarti, S. K., *Phys. Rep.*, **266**, 318 (1996c)
- Chakrabarti, S. K., *Ind. Journ. Phys.*, **72B(6)**, 565 (1998a)
- Chakrabarti, S. K., *Proceedings of Observational Evidence for Black Holes in the Universe*, edited by Chakrabarti, S. K., (Kluwer Academic Publisher, Dordrecht, 1998b)
- Chakrabarti, S. K., *Astron. Astrophys.*, **351**, 185 (1999)
- Chakrabarti, S.K., *Class. Quant. Grav.*, **17**, 2427 (2000)
- Chakrabarti, S.K. & Manickam, S., *ApJ*, **531**, L41 (2000) [CM00]
- Chakrabarti, S. K. & Nandi, A., *Indian J. Physics*, **75B (1)**, 1 (2001) *astro-ph/0012526*
- Chakrabarti, S.K., Manickam, S., Nandi, A. & Rao, A. R., *Proceedings of the Ninth Marcel Grossmann Meeting*, Edited by Gurzadyan, V. G., Jantzen, R. T. & Ruffini, R., (World Scientific, Singapore) (2002a) *astro-ph/0012525*

- Chakrabarti, S. K., in *IAU Colloq., Exotic Stars as Challenges to Evolution*, Edited by Vanhamme, W. & Tout, C., 187 (2002)
- Chakrabarti, S. K., Goldoni, P., Wiita, P., Nandi, A., & Das, S., *ApJ*, **576**, L45 (2002b)
- Chakrabarti, S. K., Nandi, A., Manickam, S., Mandal, S. & Rao, A. R., *ApJ*, **579**, L21 (2002c)
- Chakrabarti, S. K., Pal, S., Nandi, A., Anandarao, B. G. & Mondal, S., *ApJ*, **595**, L45 (2003)
- Chakrabarti, S. K., Nandi, A., Choudhury, A. & Chatterjee, U., *ApJ*, **607**, 406 (2004)
- Chakrabarti, S. K., Nandi, A., Chatterjee, A., Choudhury, A. & Chatterjee, U., *A&A*, **431**, 825 (2005)
- Chen, X. M., Abramowicz, M. A. & Lasota, J. P., *ApJ*, **476**, 61 (1997)
- Cherepashchuk, A. M., *AdSpR*, **8**, 591 (1988)
- Cherepashchuk, A. M., Sunyaev, R. A., Seifina, E. V., et al., *A&A*, **411** L 441 (2003)
- Clark, D. H. & Murdin, P., *Nature*, **276**, 44 (1978)
- Clark, D. H., *The Quest for SS433*, (Viking Penguin Inc., New York) (1985)
- Corbel, et al., *ApJ*, **554**, 43 (2001)
- Crampton, D., Cowley, A. P. & Hutchings, J. B., *ApJ*, **235**, L131 (1980)
- Das, S., Chattopadhyay, I., Nandi, A. and Chakrabarti, S. K., *Astron. Astrophys.*, **379**, 683 (2001)
- Davidson, K. & McCray, R., *ApJ*, **241**, 1082 (1980)
- Dhawan, V., Mirabel, I. F. & Rodriguez, L. F., *ApJ*, **543**, 373 (2000)
- Dubner, G. M., Holdaway, M., Goss, W. M. & Mirabel, I. F., *AJ*, **116**, 1842 (1998)
- Eggum, G. E., Coroniti, F. V. & Katz, J. I., *ApJ*, **298**, 41 (1985)
- Eikenberry, S. S., Matthews, K., Morgan, E. H., Remillard, R. A. & Nelson, R. W., *ApJ*, **494**, L61 (1998)

- Eikenberry, S. S. et al., *ApJ*, **561**, 1027 (2001)
- Esin, A. et al., *ApJ*, **505**, 854 (1998)
- Fabian, A. C. & Rees, M. J., *MNRAS*, **187**, 13 (1979)
- Fabrika, S. N. & Bychkova, L. V., *A&A*, **240**, L5 (1990)
- Fender, R. P., Pooley, G. G., Brocksopp, C. & Newell, S. J., *MNRAS*, **290**, L65 (1997)
- Fender, R. P. & Pooley, G. G., *MNRAS*, **300**, 573 (1998)
- Fender, R. P., Garrington, S. T., McKay, D. J., et al., *MNRAS*, **304**, 865 (1999)
- Feroci, M., Matt, G., Pooley, G. et al., *A&A*, **351**, 985 (1999)
- Foglizzo, T. & Tagger, M., *A&A*, **301**, 293 (1995)
- Forman, W., Jones, C., Cominsky, L., et al., *ApJ Suppl.*, **38**, 357 (1978)
- Friedman, H., Lichtman, S. & Byram, E., *Phys. Rev.*, **83**, 1025 (1951)
- Giacconi, R., Gursky, H., Paolini, F. R. & Rossi, B. B., *Phys. Rev. Lett.*, **9**, 439 (1962)
- Giacconi, R., Kellogg, E., Gorenstein, P., Gursky, H. & Tananbaum, H., *Astrophys. J.*, **165**, L27 (1971)
- Gierlinski, et al., *MNRAS* **288**, 958 (1997)
- Gies, D. R., McSwain, M. V., Riddle, R. L., Wang, Z., Wiita, P. J. & Wingert, D. W., *ApJ*, **566**, 1069 (2002)
- Goldstein, S., *Modern Developments in Fluid Mechanics*, (Oxford:Clarendon Press) (1938)
- Goncharskii, A. V., Metlitskaya, Z. Y. & Cherepashchuk, A. M., *SvA*, **28**, 74 (1984)
- Goranskii, V. P., Esipov, V. F., & Cherepashchuk, A. M., *Astron. Rep.*, **42**, 209 (1998)
- Grandi, S., *Vistas Astron*, **25**, 7 (1981)
- Greiner, J., Morgan, E. H. & Remillard, R. A., *ApJ*, **473**, L107 (1996)

- Greiner, J., Cuby, J. G., McCaughrean, M. J., Castro-Tirado, A. J. & Mennickent, R. E., *A&A*, **373**, L37 (2001)
- Hawley, J. F., Gammie, C. F. & Balbus, S. A., *ApJ*, **440**, 742 (1995)
- Hillwig, T. C., Gies, D. R., Huang, W., et al., *ApJ*, **615**, 422 (2004)
- Hjellming, R. M. & Johnston, K. J., *Nature*, **290**, 100 (1981a)
- Hjellming, R. M. & Johnston, K. J., *ApJ*, **246**, 141 (1981b)
- Jahoda, K., Swank, J. H., Giles, A. B., et al., *SPIE*, **2808**, 59 (1996)
- Jaroszyński, M., Abramowicz, M. A. & Paczyński, B., *Acta Astr.* **30**, 1 (1980)
- Katz, J. I., Anderson, S. F., Grandi, S. A. & Margon, B., *ApJ*, **260**, 780 (1982)
- Klein-Wolt, M., et al., *MNRAS*, **331**, 745 (2002)
- Kotani, T., Kawai, N., Aoki, T. et al., *PASJ*, **46**, L147 (1994)
- Kotani, T., Kawai, N., Matsuoka, M. & Brinkman, W., *PASJ*, **48**, 619 (1996)
- Kotani, T. & Trushkin, S., *IAU Circ.*, 7747 (2001)
- Langer, S. H., Chanmugam, C. & Shaviv, G., *ApJ*, **258**, 289 (1982)
- Levine, A. M., Bradt, H., Cui, W., et al. *ApJ*, **469**, L33 (1996)
- Lovelace, R. V. E., *Nature*, **22**, 507 (1976)
- Manickam, S. & Chakrabarti, S. K., *Indian J. Phys.*, **73**(6), 967 (1999)
- Malzac, J., Beloborodov, A. M. & Poutanen, J., *MNRAS*, **326**, 417 (2001)
- Margon, B., Stone, R. P. S., Klemola, A., et al., *ApJ*, **230**, 41 (1979)
- Margon, B., Grandi, S. A. & Downes, R. A., *ApJ*, **241**, 306 (1980)
- Margon, B., *Ann. Rev. Astron. Astrophys.*, **22**, 507 (1984)
- Margon, B. & Anderson, S. F., *ApJ*, **347**, 448 (1989)
- Marshall, F. E., Swank, J. H., Boldt, E. A., Holt, S. S & Serlemitsos, P. J., *ApJ*, **230**, L145 (1979)
- Marshall, H. L., Canizares, C. R. & Schulz, N. S., *ApJ*, **564**, 941 (2002)

- Mazeh, T., Kemp, J. C., Leibowitz, E. M., Meninger, H. & Mendelson, H., *ApJ*, **317**, 824 (1987)
- Migliari, S., Fender, R. & Méndez, M., *Sci*, **297**, 1673 (2002)
- Milgrom, M., *A&A*, **78**, L9 (1979)
- Mirabel, I. F. & Rodríguez, L. F., *Nature*, **371**, 46 (1994)
- Mirabel, I. F. & Rodríguez, L. F., *ApJ*, **511**, 398 (1999)
- Mirabel, I. F. & Rodríguez, L. F., *Ann. Rev. Astron. Astrophys.*, **37**, 409 (1999) [MR99]
- Molteni, D., Lanzafame G. & Chakrabarti, S. K., *ApJ*, **425**, 161 (1994)
- Molteni, D., sponholz, H. & Chakrabarti, S. K., *ApJ*, **457**, 805 (1996) [MSC96]
- Molteni, D., Acharya, K., Kuznetsov, O., Bisikalo, D. & Chakrabarti, S. K., *ApJ*, **563**, L57 (2001)
- Morgan, E. H., Remillard, R. A. & Greiner, J., *ApJ*, **482**, 993 (1997)
- Morrison, R. & McCammon, D., *ApJ*, **270**, 119 (1983)
- Muno, M.P., Morgan, E.H., & Remillard, R.A., *ApJ*, **527**, 321 (1999)
- Murdin, P., Clark, D. H. & Martin, P. G., *MNRAS*, **193**, 135 (1980)
- Namiki, M., Kawai, N., Kotani, T. & Makishima, K., *PASJ*, **55**, 281 (2003)
- Naik, S. & Rao, A. R., *A&A*, **362**, 691 (2000)
- Naik, S., Agrawal, P. C., Rao, A. R., Paul, B., et al., *ApJ*, **546**, 1075 (2001)
- Naik, S., Agrawal, P. C., Rao, A. R., Paul, B., *MNRAS*, **330**, 487 (2002)
- Naik, S., Rao, A. R. & Chakrabarti, S. K., *JApA*, **23**, 213 (2002)
- Nandi, A., Manickam, S. G. & Chakrabarti, S. K., *Indian J. Phys.*, **74B(5)**, 331 (2000) *astro-ph/0012523*
- Nandi, A., Manickam, S. K., Rao, A. R. & Chakrabarti, S.K., *MNRAS*, **324**, 267 (2001a)
- Nandi, A., Chakrabarti, S.K., Vadawale, S.V. and Rao, A.R., *A&A*, **380**, 245 (2001b)

- Nandi, A., Chakrabarti, S.K., Belloni, T. & Goldoni, P., *MNRAS*, (in press) (2005)
astro-ph/0409662
- Novikov, I. D. and Thorne, K. S., *Black Hole Astrophysics, in Black Holes* edited by Dewitt, C. and Dewitt, B., (Gordon and Breach New York, New York) (1973)
- Parker, E. N., *Cosmical Magnetic Fields* (Clarendon press, Oxford) (1979)
- Paczyński, B. and Wiita, P., *Astron. Astrophys.*, **88**, 23 (1980)
- Paragi, Z., et al., *A&A*, **348**, 910 (1999)
- Paul, B., et al., *ApJ*, **492**, L63 (1998)
- Pearson, T. J. & Zensus, J. A., *In Superluminal Radio Sources, CUP*, Edited by Zensus, J. A. & Pearson, T. J., p.1, (1987)
- Pooley, G.G. & Fender, R.P., *MNRAS*, **292**, 925 (1997)
- Rao, A.R., Naik, S., Vadawale, S.V. & Chakrabarti, S.K., *A&A*, **360**, L25 (2000)
- Rees, M. J., *Nature*, **211**, 468 (1966)
- Remillard, R. A., Morgan, E. H., McClintock, J. E., et al., *ApJ*, **522**, 397 (1999)
- Rodriguez et al., *ApJ Suppl.*, **101**, 173 (1995)
- Rodriguez, L. F. & Mirabel, I. F., *ApJ*, **474**, L123 (1997)
- Rothschild, R. E., Blanco, P. R., Gruber, D. E., et al., *ApJ*, **496** 538 (1998)
- Rybicki, G. B. and Lightman, A. P., *Radiative Processes in Astrophysics*, (A Wiley-Interscience Publication, New York) (1979)
- Ryle, M., Hine, G., Shakeshaft, J. & Caswell, J. L., *Nature*, **276**, 571 (1978)
- Ryu, D., Chakrabarti, S.K. & Molteni, D., *ApJ*, **474**, 378 (1997) [RCM97]
- Safi-Harb, S. & Kotani, T., *in New Views of Microquasars*, Edited by Durouchaux, P., Fuchs, Y. & Rodriguez, J. (Centre for Space Physics: Kolkata), p. 279 (2003)
- Seaquist, E. R., Garrison, R. F., Gregory, P. C., Taylor, A. R. & Crane, P. C., *AJ*, **84**, 1037 (1979)
- Seward, F. D., Page, C. G., Turner, M. J. L. & Pounds, K. A., *MNRAS*, **177**, 13 (1976)

- Shakura, N. I., *Astron. Zhur.*, **49**, 921 (1972)
- Shakura, N. I. & Sunyaev, R. A., *Astron. Astrophys.*, **24**, 337 (1973)
- Shapiro, S. L. and Teukolsky, S. A., *Black Holes, White Dwarfs and Neutron Stars: The Physics of Compact Objects*, (A Wiley-Interscience Publication, New York) (1983)
- Shimura, T. & Takahara, F., *ApJ*, **445**, 780 (1995)
- Smith, D. M., Heindl, W.A. Markwardt, C. B. & Swank, J. H., *ApJ*, **554** L41 (2001)
- Smith, D. M., Heindl, W.A. & Swank, J.H., *ApJ*, **569** 362 (2002)
- Sobczak, G. J., McClintock, J. E., Remillard, R. A., et al., *ApJ*, **520**, 776 (1999)
- Stephenson, C. B. & Sanduleak, N., *ApJ Suppl.*, **33**, 459 (1977)
- Stewart, G. C., Watson, M. G., Matsuoka, M., et al., *MNRAS*, **228**, 293 (1987)
- Swarup, G., et al., *Curr. Sci.*, **60**, 95 (1991)
- Tamm, R., Chen, X. -M. & Swank, J., *ApJ*, **485**, 83 (1997)
- Trudolyubov, S. P., Churazov, E. M. & Gilfanov, M. R., *Astron. Lett.*, **25**, 718 (1999)
- Vadawale, S.V., Rao, A.R. & Chakrabarti, S.K., *A&A*, **372**, 793 (2001)
- Vadawale, S.V., Rao, A.R., Nandi, A. & Chakrabarti, S.K., *A&A*, **17**, L370 (2001)
- van den Heuvel, E. P. J., *Vistas Astron.*, **25** 95 (1981)
- van der Klis et al., *Nature*, **316**, 225 (1985)
- van der Klis. M., *Annu. Rev. Astron. Astrophys.*, **27**, 517 (1989)
- Vermeulen, R. C. et al., *A&A*, **270**, 177 (1993a)
- Vermeulen, R. C. et al., *A&A*, **270**, 204 (1993b)
- Watson, M. G., Stewart, G. C., Brinkmann, W. & King, A. R., *MNRAS*, **222**, 261 (1986)
- Yadav, J.S., Rao, A.R., Agrawal, P.C., Paul, B. Seetha, S. & Kasturirangan, K., *ApJ*, **517**, 935 (1999)
- Yuan, W., Kawai, N., Brinkmann, W. & Matsuoka, M., *A&A*, **297**, 451 (1995)

Zdziarski, A. A., in *Highly Energetic Physical Processes Proceedings of the IAU symposium*, **195**, 153 (2001)

Zensus, J. A., *Annu. Rev. Astron. Astrophys.*, **35**, 607 (1997)

Classification of light curves of the black hole candidate GRS 1915+105

Anuj Nandi, Sivakumar G Manickam and Sandip K Chakrabarti¹

S. N. Bose National Centre for Basic Sciences, JD Block, Salt Lake, Sector-III, Calcutta-700 098, India

E-mail : chakraba@boson.bose.res.in

Received 4 August 2000, accepted 10 August 2000

Abstract : The black hole candidate GRS 1915+105 exhibits a rich variety of variability. Assuming that the earlier paradigm of black hole accretion which includes a shock is applicable for this system as well, one can classify these variabilities into four classes. We present light curves of these classes and discuss the basis of our classification.

Keywords : Black holes, X-ray sources, outflows.

PACS Nos. : 97.60.Lf, 98.70.Qy, 04.70.-s

1. Introduction

GRS 1915+105 is a stellar mass black hole candidate in our galaxy which exhibits very rich time-variability. It is termed as a micro-quasar since it has most of the features of a quasar, such as a superluminal jet which moves at a speed of 98 percent of the velocity of light [1,2]. Morgan *et al* [3] pointed out that the source is sometimes in low-hard state, but in other times it goes to flare state with considerable variations in amplitude and quasi-periodic oscillation frequency. They showed that there are several time-scales of quasi periodic oscillations (QPO) ranging from 67 Hz to 0.01 Hz (sec, also, Muno *et al* [4]). Recently, it has been pointed out [5–7] that there is a distinct correlation between the oscillation frequency and the duration of oscillation. This correlation has been explained by invoking repeated formation and cooling of the wind generated from the centrifugal pressure dominated boundary layer (CENBOL) of the black hole [5,7]. (Wind production from accretion flows are also discussed in Das and Chakrabarti [8]). Several types of oscillations have been plotted in Manickam and Chakrabarti [6].

Given that accretion disk models around black holes are pretty well understood [9,10], and variation of accretion rates, out flow rates, shock locations, cooling processes *etc.* can make spectral change dramatically, it is not perplexing as to why GRS 1915+105 exhibits such a rich variety of oscillations. It was already pointed out [11,12] that oscillation of shock waves could be responsible for the QPO. Later, this model was proven to be correct [6,7] where it was shown

that soft X-rays (0–4 keV) emitted from the pre-shock region, do not participate in QPOs and only hard X-rays (4–13 keV) show quasi-periodic behaviour.

In this *Rapid Communication*, we present a classification of the light curves based on our understanding of the black hole accretion process according to which not only Keplerian matter, but also substantial amount of sub-Keplerian matter accretes into a black hole and the sub-Keplerian flow often produces stationary or non-stationary shocks. We find that although there are several types of light curves, the number of classes could be as few as four. In our picture, the post-shock flow is heated up and puffed up and intercepts soft photons from the pre-shock region. In the pre-shock region, Keplerian disk is situated in the equatorial plane and is flanked by poorly emitting sub-Keplerian matter above and below. The post-shock flow produces winds and outflows, rates of which depend on the spectral states of the black hole [13]. In the hard states, there is a continuous outflow at a smaller rate, while in the soft states, no outflow is produced. When the compression ratio of the shock is intermediate, outflow rate is maximum and flares and variabilities are prominent.

That the outflows are originated from CENBOL has now been confirmed by several workers. Mirabel and Rodriguez [2] and Dhawan *et al* [14] found evidence of IR flares and radio flares which are directly correlated with the X-rays produced by inverse-Comptonization at the base of the jet. Similarly, Fender [15] concluded that the base of the jet is the same place where X-rays are originated. Junor *et al* [16]

¹ Also, Honorary Scientist at Centre for Space Physics, IA-212, Salt Lake City, Sector-III, Calcutta-700 097, India

found that jets in M87 must be originated within a few tens of Schwarzschild radii.

If our paradigm as described above is correct, and the X-ray variability is primarily due to variability of the hard X-rays, then it is conceivable that the light curves could be classified according to the photon counts from pre- and post-shock flows. This is precisely what we do. In the next Section, we briefly present the theory of photon emission from the pre- and post-shock flows. In Section 3, we plot the light curves and the softness ratios and classify the light curves into four classes. Finally, in Section 4, we draw our conclusions.

2. Brief theory of photon emission from an accretion disk around black holes

For a Keplerian disk, the surface flux of soft X-rays emitted is given by [17],

$$F = 5 \times 10^{26} \left(\frac{\dot{M}_{17}}{M^2} \right) r^{-3} I \text{ erg cm}^{-2} \text{ sec}^{-1}. \quad (1)$$

Here, M is the mass of the black hole, measured in units of M_{\odot} , the mass of the sun, \dot{M}_{17} is the mass accretion rate of the Keplerian component in units of 10^{17} gms/sec, r is the distance from the black holes measured in units of $r_s = GM_{BH}/c^2$ (M_{BH} is the mass of the black hole, G is the gravitational constant, c is the velocity of light all measured in cgs units), $I = 1 - (6/r)^{1/2}$. For an optically thick flow, the black body radiation that is emitted locally is that of temperature

$$T_e(r) = [4F(r)/a]^{1/4} \\ = 5 \times 10^7 M^{-1/2} (\dot{M}_{17})^{1/4} r^{-3/4} I^{1/4} \text{ K}. \quad (2)$$

Here a is the radiation constant. Close to $r = 20$ and for $M = 10$, the temperature is roughly 1.4 keV which corresponds to soft X-ray radiation. A part of this radiation is intercepted by the post-shock region [18] and is re-emitted after being energized by inverse-Comptonization process. If the accretion rate is very small, inverse-Comptonization still leaves the post-shock region hotter and hard radiation as well as winds are produced. If both the Coulomb heating and inverse-Comptonization are important, the electrons are roughly $(m_p/m_e)^{1/2}$ times cooler than the protons: $T_e \sim (m_e/m_p)^{1/2} T_p$. In the post-shock region: $T_p \sim 10^{11}$ K and $T_e \sim 2 \times 10^9$ K. Power-law radiation emitted by successive scattering can produce radiation starting from 2 to 200 keV or more. Even higher energy radiations can be emitted by synchrotron processes.

When Keplerian accretion rate is very high, they cool the post-shock electrons completely and the shock vanishes. The post-shock region also resembles like an optically thick Keplerian flow, but the inner edge of the disk ($r < 6$) produces hard radiation due to bulk-motion Comptonization [18].

In the event of oscillating shocks, the winds produced may not leave the system and stalled jets are produced.

Matter in the subsonic region of the wind falls back to equatorial disk as soon as it is cooled due to inverse-Comptonization. This periodicity gives an expression for the duration of QPOs which is found to be well correlated with the QPO frequency [5,7]. Various types of QPOs which are observed could be due to variations of accretion rates in Keplerian and sub-Keplerian components and shock location (which is determined by the specific energy and specific angular momentum of the inflow).

3. Classification of light curves

Figure 1 shows possible variations of the light curves of GRS 1915+105 as observed by the RXTE satellite. Twelve panels are marked. Panels 3 and 6 have more than one light curve (separated by dashed line), as they are similar but with subtle

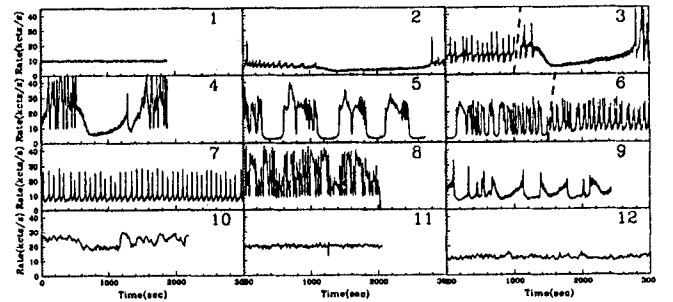


Figure 1. All possible light curves of the black hole candidate GRS 1915+105. Along X-axis is time in seconds and along Y-axis is photon counts in units of 10^3 . In Panels 3 and 6, two days of curves differing slightly, have been shown.

difference. Along X-axis is the time elapsed in seconds since the beginning of the observation. Spectral analysis of the 1st panel suggests that it is purely in hard state. There is a prominent QPO whose frequency may change from time to time and photon count number may also change significantly. Final three panels (10–12) contain light curves of those days on which spectral states are soft. There are no QPOs in these days. Spectral fits indicate high temperature and high photon spectral index. The ninth panel contains a light curve where two semi-soft spectra with different photon counts are seen. Count rate varies very significantly. In the remaining seven panels (2–8) photons jump in between two distinct states, one with a low photon count (off state) and the other with a high photon count (on state). These twelve types have been designated as χ , α , ν , β , λ , κ , ρ , μ , θ , δ , γ and ϕ respectively by Belloni *et al* [19]. They also plot hardness ratios of these cases where (B/A) vs (C/A) were depicted. Here, A , B , C are photon counts in (0–5) keV, (5–12) keV and (12–60) keV ranges. These hardness ratios show various well known features such as Atoll, Z-type *etc.* very similar to what was observed in neutron star candidates.

According to the paradigm of Keplerian/sub-Keplerian flow, the following should be happening close to a black hole [18]: Keplerian flow moves in the equatorial plane while sub-Keplerian flow moves above and below the plane. The Keplerian flow itself becomes sub-Keplerian close to the

black hole. The combined sub-Keplerian flow then continues to move towards the black hole and forms a standing or oscillating shock if the specific energy is positive. Otherwise, the combined flow forms a smaller centrifugal barrier dominated region and passes through the inner sonic point. The post-shock region reprocesses soft photons from the Keplerian disk and emits essentially hard radiation provided Keplerian accretion rate is small enough, otherwise, the post-shock region also cools down [18]. While hot, the post-shock region produces winds. If the outflow rate is large enough, it may intercept soft and hard photons and re-process. If the outflow is 'failed', namely, do not pass beyond the sonic point due to various factors such as cooling down by inverse Comptonization [5,7], it may fall back onto the post-shock region and the object may behave as if the accretion rate had gone up. Most of the on/off transitions can be easily interpreted in this way.

If the pre-shock flow is indeed the source of the soft photons, photons originating in (0–3) keV range should be roughly proportional to the accretion rate in the cool component (basically Keplerian). Thus, photon number may show time variation (due to periodic change in the 'accretion rate'). However, no QPO should be seen. Chakrabarti and Manickam [7] demonstrated this. This harder photons ($E > 3$ keV) would usually come from the post-shock flow. Since spectra intersect at around 17 keV, and for $E > 17$ keV, photon number is not large, we make our choice of A , B and C to be those in ranges (0–3) keV, (3–17) keV and (17–60) keV respectively. According to our paradigm, roughly speaking, A , B and C should be proportional to each other, (since B and C produced by interception of soft photons. Of course, soft X -ray absorption makes matter more complex.) and whenever hardness or softness ratios are plotted basically straight lines are expected, instead of Atoll, Banana and Z shapes which do not give any insight into the problem. Figure 2 shows twelve panels (in the same sequence as in Figure 1) where B/C is plotted along X -axis and A/C is plotted along the Y -axis. We call this a 'softness ratio' diagram. In some of the panels (No. 2–4, 6–8), the ratio is zoomed in to show details. One observes that panels (9–12), which are for soft or nearly soft spectra, the plots are roughly linear and the lower-left end starts at sufficiently large number compared to the other panels. Power density plots do not show evidence of QPO in these types of light curves. Light curves of all other panels show QPO.

The softness diagrams could be classified into the followings :

1. HARD Class (H) : Panel 1
2. SOFT Class (S) : Panels 10–12
3. SEMI-SOFT Class (SS) : Panel 9
4. INTERMEDIATE Class (I) : Panels 2–8

Each of these classes have subclasses in terms of variation in light curves and softness ratios. For instance, in Class H, counts and QPO frequencies vary and the spot mark in

Panel 1 moves around. In Class S, the slopes and the coordinates of the lower-left point varies, but the general nature is similar (Panels 10–12). In Class I, the duration of the off

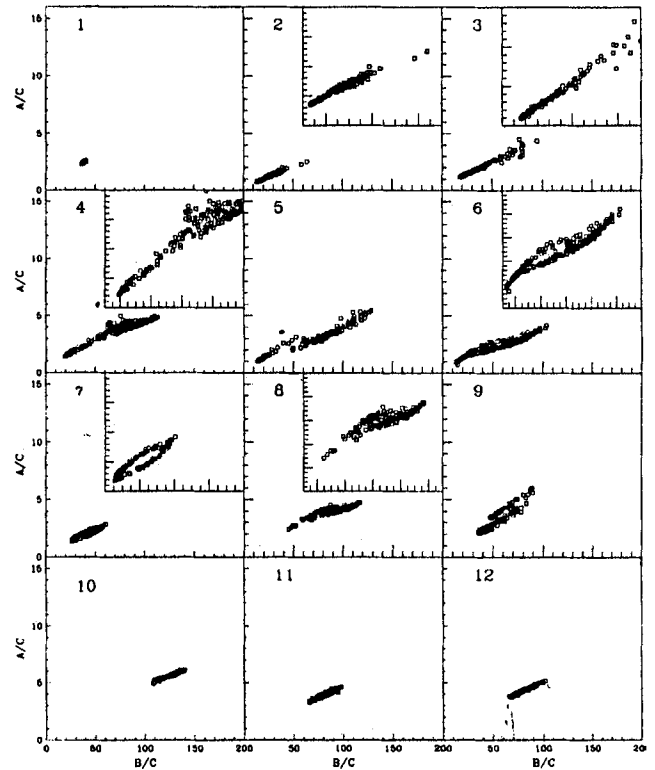


Figure 2. Softness Ratio A/C vs B/C is plotted for all the 12 panels shown in Figure 1. A , B , and C are photon counts within intervals (0–3) keV, (3–17) keV and (17–60) keV respectively. Panel 1 belongs to Class-II, Panel 9 belongs to Class-SS, Panels (10–12) belong to Class-S and the rest belong to Class-I. See, text for details.

and the on state may vary systematically from one sub-class to the next. The duration of the on-state (high count) may be almost zero (Panel 7). At the same time, the co-ordinate of the lower left corner point in the softness ratio diagram varies systematically. As discussed in Section 2 [eq.(1)], soft photon count A is directly related to the accretion rate in the Keplerian disk and hard photon count B is related to the degree of interception, and sum of Keplerian and sub-Keplerian accretion rate (total matter in the post-shock region). Thus, different members of this sub-class are directly related to these accretion rates. The common ground is that the duration of the off-states in all of these sub-classes are found to obey the correlation with QPO frequency [7]. The process of generating light curves purely from theoretical consideration is more involved (as feedback and other non-linear processes are present) and would be reported in future.

4. Concluding remarks

We have presented all possible types of light curves and divided them into four classes according to the nature of light curves and the softness ratios. We find that the black hole candidate GRS 1915+105 stays most of the time in Class H

state (which has QPO), while touring around other classes (only off states of which have QPOs), depending on the accretion rates in the Keplerian and sub-Keplerian flows. In Class S, the black hole is in soft state and no QPO is observed. Our simplified classification is based on the black hole accretion paradigm that explains the spectral state transitions as well as QPOs. In future, detailed theoretical modeling would be presented.

Acknowledgments

SGM acknowledges a grant 'Quasi-Periodic Oscillations of Black Holes' from the Indian Space Research Organisation and AN acknowledges a Department of Science & Technology grant No. SP/S2/K-14/98 for supporting their Fellowship.

References

- [1] I F Mirabel and L F Rodríguez *Nature* **371** 46 (1994)
- [2] I F Mirabel and L F Rodríguez *Ann. Rep. Astron. Astrophys.* **37** 409 (1999)
- [3] E H Morgan, R A Remillard and J Greiner *Astrophys. J.* **482** 993 (1997)
- [4] M P Muno, E H Morgan and R A Remillard *Astrophys. J.* **527** 321 (1999)
- [5] S K Chakrabarti *Indian J. Phys.* **73B** 931 (1999)
- [6] L G Manickam and S K Chakrabarti *Indian J. Phys.* **73B** 967 (1999)
- [7] S K Chakrabarti and S G Manickam *Astrophys. J.* **531** L41 (2000)
- [8] T Das and S K Chakrabarti *Class. Quant. Grav.* **16** 3879 (1999)
- [9] S K Chakrabarti *Phys. Rep.* **266** 229 (1996)
- [10] S K Chakrabarti *Indian J. Phys.* **72B** 183 (1998)
- [11] D Molteni, H Sponholz and S K Chakrabarti *Astrophys. J.* **457** 805 (1996)
- [12] D Ryu, S K Chakrabarti and D Molteni *Astrophys. J.* **474** 378 (1997)
- [13] S K Chakrabarti *Astron. Astrophys.* **351** 185 (1999)
- [14] V Dhawan, I F Mirabel and L F Rodríguez *Astrophys. J.* (submitted) (2000)
- [15] R Fender in *Proc. ESO Workshop on Black Holes in Binaries and Galactic Nuclei* eds. L Kaper, E P J van den Heuvel and P A Woudt (Berlin : Springer-Verlag) (in press) (2000)
- [16] W Junor, J A Biretta and M Livio *Nature* **401** 891 (1999)
- [17] S L Shapiro and S A Teukolsky *Black Holes, White Dwarfs and Neutron Stars--the Physics of Compact Objects* (New York : John Wiley) (1983)
- [18] S K Chakrabarti and L G Titarchuk *Astrophys. J.* **455** 623 (1995)
- [19] T Belloni, M-K Wolt, M Méndez, M van Der Klis and J van Paradijs *Astron. Astrophys.* **355** 271 (2000)

On the source of quasi-periodic oscillations of the black hole candidate GRS 1915+105: some new observations and their interpretation

Anuj Nandi,^{1★} Sivakumar G. Manickam,^{1★} A. R. Rao^{2★} and Sandip K. Chakrabarti^{1,3★}

¹*S. N. Bose National Centre for Basic Sciences, JD-Block, Sector III, Salt Lake, Calcutta 700098, India*

²*Tata Institute of Fundamental Research, Homi Bhabha Road, Colaba, Mumbai 400005, India*

³*Centre for Space Physics, 114/w/1A Raja S. C. Mullick Rd, Calcutta 700047, India*

Accepted 2001 January 8. Received 2001 January 4; in original form 2000 October 18

ABSTRACT

A few classes of the light curve of the black hole candidate GRS 1915+105 have been analysed in detail. We discover that unlike the previous findings, quasi-periodic oscillations (QPOs) occasionally occur even in the so-called ‘On’ or softer states. Such findings may require a revision of the accretion/wind scenario of the black hole candidates. We conjecture that considerable winds that are produced in ‘Off’ states cool down as a result of Comptonization and fall back to the disc, creating an excess accretion rate and producing the so-called ‘On’ state. After the drainage of the excess matter, the disc goes back to the ‘Off’ state. Our findings strengthen the shock oscillation model for QPOs.

Key words: accretion, accretion discs – black hole physics – stars: individual: GRS 1915+105 – stars: oscillations.

1 INTRODUCTION

The black hole candidate GRS 1915+105 continues to excite astrophysicists by having one of the most, if not the most mysterious light curves. In a matter of days, the light curve changes its character, and within each day, photon counts show variations of a factor of 2 to 5 or more (Belloni et al 1997; Morgan, Remillard & Greiner 1997; Paul et al. 1998; Manickam & Chakrabarti 1999). The power density spectra shows clear evidence of quasi-periodic oscillations (QPOs) with frequency ranging from ~ 0.001 to 67 Hz (see, e.g., Morgan, Remillard & Greiner 1997; Chakrabarti & Manickam 2000, hereafter CM00, and references therein).

The origin of the QPOs cannot be a complete mystery, because there is very clear evidence that sub-Keplerian flows, which must occur in a black hole accretion, exhibit very wild time-dependent behaviour, including large amplitude shock oscillations. This is especially true when the infall time matches the cooling time (Molteni, Sponholz & Chakrabarti 1996; Ryu, Chakrabarti & Molteni 1997; Paul et al. 1998; Remillard et al. 1999a,b; Muno, Morgan & Remillard 1999). This became more evident when it was observed that the QPOs are absent in low-energy photons but are very strong at high energies, supporting the view that the photons participating in QPOs originate at hot post-shock flow (CM00, Rao et al. 2000). It has also been observed that QPOs are seen mostly when the photon counts are low (‘Off’ states) and QPO is very weak or absent in the On states when the photon

counts are about two to five times larger. In the present paper, we mean by On and Off states the high and low count states of the light curves. This nomenclature is not related to spectral states.

Because of the presence of the On and Off states in the light curves, explanation of QPOs using radial oscillation of the centrifugal pressure supported shocks alone (which produce the right amplitude and frequency for the QPOs) cannot be the complete story. The very fact that the Off states terminate and the On states emerge on almost (but not exactly) regular bases gives rise to another time-scale which must, at the same time, be dependent on disc/jet parameters. This is because Belloni et al. (2000) found that at least 12 types of light curves are seen, and within each type, the duration and behaviour of the On and the Off (if both exist) states were not at all fixed. For instance, ρ class exhibits extremely regular light curves (Taam, Chen & Swank 1997; Vilhu & Nevalainen 1998) with broad Off or low-count states and very narrow, spiky, high-count or On states. Light curves in the ν class is similar to those of ρ , but are highly irregular. In λ class, both Off and On states are of longer time duration (Belloni et al. 1997) while in κ class these durations are relatively shorter. Nandi, Manickam & Chakrabarti (2000) using a completely different procedure divided the light curves into four fundamental types (Hard, Soft, Semi-soft and Intermediate). The Intermediate class shows On–Off transitions. Chakrabarti (1999a,b) and Chakrabarti & Manickam (2000) showed that outflow rates from the centrifugal barrier must play a major role in deciding the duration, as the wind matter at least up to the sonic sphere can be Comptonized and cooled down. Most of this cold matter (below the sonic surface of the cooler wind) can fall back on the immediate vicinity of the disc increasing its accretion rate temporarily while the rest must

* E-mail: anuj@boson.bose.res.in (AN); sivman@boson.bose.res.in (SGM); arrao@tifr.res.in (ARR); chakraba@boson.bose.res.in (SKC)

separate out at a supersonic speed. As this excess matter drains out, the Off state together with the QPO start appearing again.

In this paper, we analyse light curves in detail and find that QPOs may be observed at very unlikely times in the light curves. For instance, we find that very often, there is a sharp peak ('first hiccup') at the onset of the On state and there is a sharp peak ('last hiccup') just prior to going to the Off state. The first peak, though in the On state, very often shows QPOs while the last peak, though the radiation is much harder, does not show a QPO. We also note that the radiation progressively hardens in the On state. In several cases, using data from both the *Rossi X-ray Timing Experiment (RXTE)* and *Indian X-ray Astronomical Experiment (IXAE)*, ρ -class curves (mostly mini- ρ type) are seen to be peeled off from a κ class. In κ and λ , the On state duration is long and just before going to the Off state, the light curve becomes noisy and oscillatory in nature, and the features indicate as though the light curve is made up of 'sums' of ρ types. Only the lower half of the oscillations (local Off states of mini- ρ states) exhibit QPO! We believe that these observations definitely point to the drainage of extra matter in the disc which was accumulated from the wind.

One of the problems in analysing data of one of the most complex objects, such as GRS 1915+105 is that one has to ask the right questions, and ask as many of them as possible. Once a paradigm is kept in the back of one's mind, asking questions become easier. We therefore concentrate on models which required sub-Keplerian and Keplerian flows simultaneously and where winds are also produced self-consistently. In the next section, we present some of the 'subtle' observational results which have not been reported by workers before (despite the fact that GRS 1915+105 is probably the most studied object in recent years). In Section 3, we interpret these observations in terms of the advective disc paradigm. In Section 4, we draw our conclusions.

2 OBSERVATIONS

2.1 Properties of two peaks in the On state

GRS 1915+105 exhibits both broad and narrow On states (Paul et al. 1998; Yadav et al. 1999; Belloni et al. 2000; CM00). When

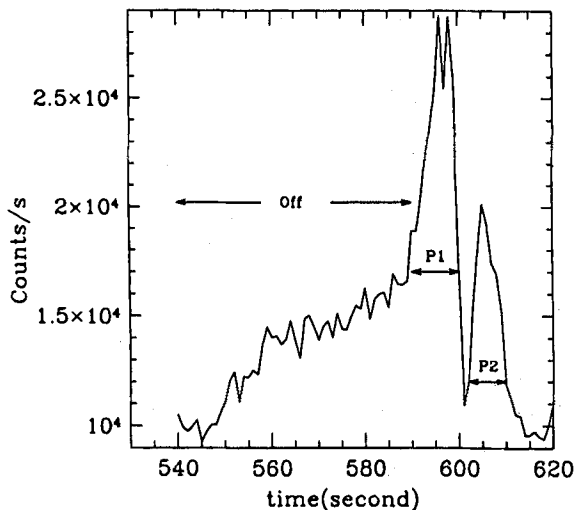


Figure 1. Subdivisions of a quasi-repetitive structure of the light curve of 1996 October 15 (ID: 10408-01-41-00). Relatively hard radiations are emitted in the region marked 'Off' with relatively lower count rates. There are typically two major peaks, P1 followed by P2.

the On state is narrow or spiky, i.e. the duration with high photon counts is very small, very often a second peak is observed just after transition from On to Off states. This has also been cursorily reported by Paul et al. (1998). Fig. 1 shows details of a narrow section of the all-channel light curve corresponding to the *RXTE* observation of 1996 October 15 (the observation ID number is

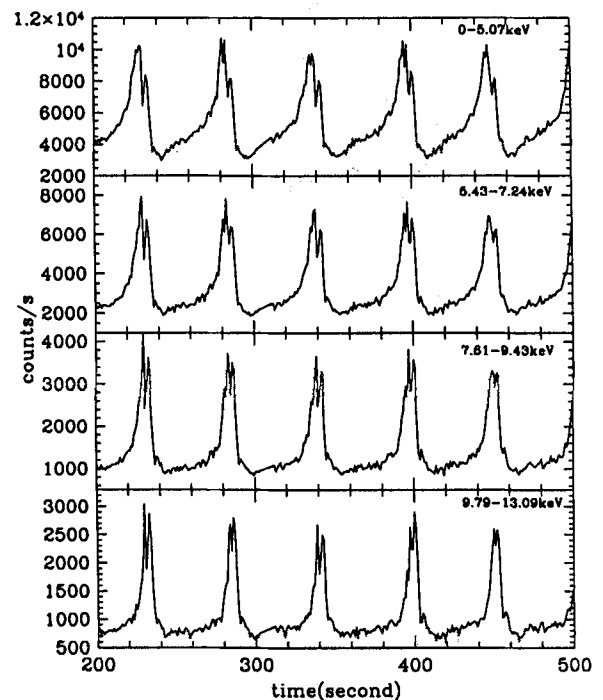
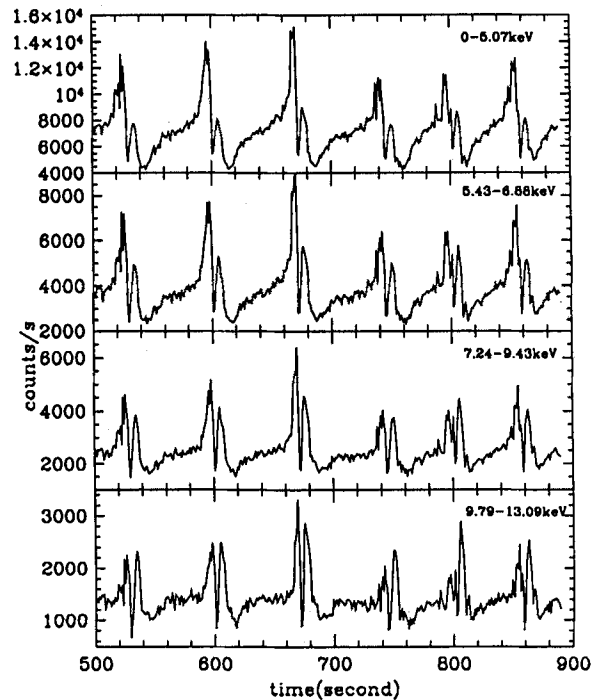


Figure 2. (a) Four panels showing light curves of a part of the observation on 1996 October 15 (ID: 10408-01-41-00) at different channels (energies are marked). Note that the ratio of photon counts in P1 and P2 tends to become unity at higher energies. (b) Four panels showing light curves of a part of the observation on 1997 June 22 (ID: 20402-01-34-01) at different channels (energies are marked).

10408-01-41-00). We denote the peak that appears first as the primary peak (P1 for short) and the peak following P1 as the secondary peak (P2 for short). The words Off, 'P1' and 'P2' are marked. The entire light curve is almost a repetition of this section. Fig. 2(a) presents the light curves of this data clearly showing two peaks P1 and P2 in the On state. The time-lag between the two peaks is roughly constant (in this case about 10 s) on a given day, and we do not find any correlation between this lag and the duration of the Off state. The light curve is shown in four panels of Fig. 2: the panels are drawn for channel energies (from top to bottom) 0–5.07, 5.43–6.88, 7.24–9.43, and 9.79–13.09 keV respectively (corresponding channels are 0–13, 14–18, 19–25 and 26–35 respectively).

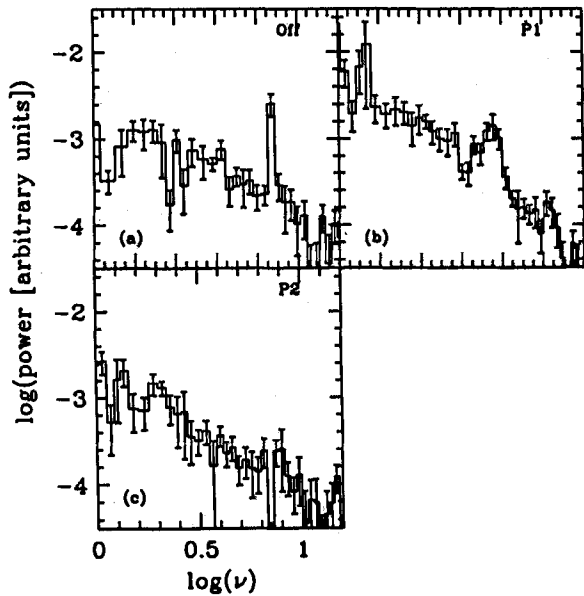


Figure 3. Power density spectrum (PDS) of the three regions marked in Fig. 1 of the observation dated 1997 June 22. Several data segments have been added to improve statistics. Note the absence of QPO in P2.

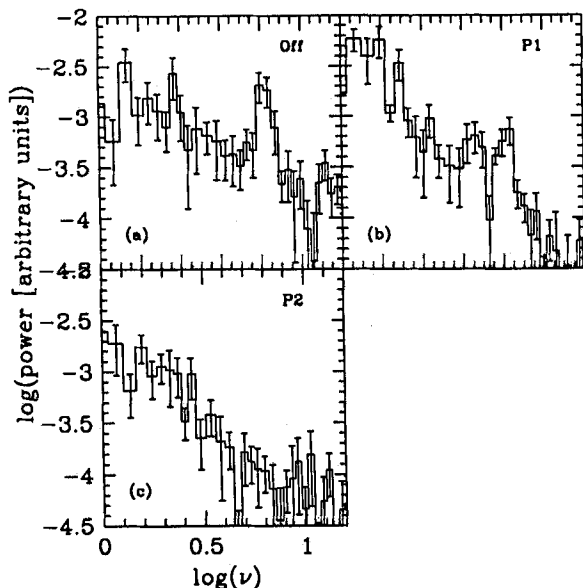


Figure 4. Power density spectrum (PDS) of three regions marked in Fig. 1 of the observation dated 1996 Oct 15. Several data segments have been added to improve statistics. Note the absence of QPO in P2.

26–35). Note that while in low energies, photon counts in P1 is much larger compared to P2; in higher energies they are roughly equal, suggesting that the spectrum of P2 is harder. Taam et al. (1997) also noted the existence of these peaks and that P2 is harder compared to P1. A similar light curve is shown in Fig. 2(b), for the *RXTE* observation of 1997 June 22 (see also Vilhu & Nevalainen 1998 and Yadav et al. 1999 for displaying this light curve). The corresponding observation ID is 20402-01-34-01. In this case, the time-lag is about 4 s but other features are similar to those of Fig. 2(a). The channel energies are marked on each panel (corresponding channels numbers are 0–13, 14–19, 20–25 and 26–35 respectively).

Figs 3(a)–(c) show the power density spectra (PDS) of the three regions marked in Fig. 1. While selecting photons from 'P1' and 'P2' regions, we took special care that they are not contaminated by the photons from the Off states. Also, to improve the statistics, we added data from many peaks over the entire duration of the observation on that day. Note that in the Off state there is a distinct QPO of frequency $\nu_{\text{QPO}} = 7.4$ Hz. Photons in 'P1' also exhibit QPO though it is weaker ($\nu_{\text{QPO}} \sim 5.7$ Hz). QPO is completely absent from 'P2'. We examined the *RXTE* data of 22nd June, 1997 also, the PDS of which is shown in Fig. 4(a)–(c). The result is generally the same. The QPO frequency in the Off-state is given by $\nu_{\text{QPO}} = 6.3$ Hz and in P1 peak $\nu_{\text{QPO}} = 6.8$ Hz. We therefore believe that the observed features may be generic.

2.2 Properties of On⁺⁺ state

It is generally observed that whenever the duration of On or the high-count state is large, light curves become very noisy and count rates start oscillating wildly as the Off state is approached. The later half may be termed as 'On⁺⁺' state and Manickam & Chakrabarti (1999) showed that this region exhibits a weak QPO. In fact, similar to Fig. 2(a)–(b) above, where the photons in P2 are harder compared to P1, one finds that the On⁺⁺ state is harder compared to the first half of the On state. This is demonstrated in Fig. 5, where a part of the light curve from the so-called κ state is shown. The energy ranges are marked in each panel. The upper four channels are from *RXTE* and the lower two channels are from *IXAE* data. The observation ID for *RXTE* is 20186-03-01-02. In both the cases a bin-size of 1 s is chosen.

First, note that the *RXTE* and *IXAE* data show very similar behaviour throughout the period of overlap of observations. Secondly, towards the end of each of the On states (which we term as the On⁺⁺ states for brevity), the light curves are noisy and generally oscillatory in nature. Thirdly, in both the experiments the relative oscillations are increased with the increasing photon energy in the On⁺⁺ state. Fourthly, though the light curve may generally be termed as κ class (Belloni et al. 2000), several pieces of ρ class are evident. In fact, mini- ρ type light curves are also evident in the On⁺⁺ states, giving clear evidence that the light curve in the ρ class is more primitive. In the next section we discuss the possible interpretations of this important observation.

In Fig. 6, we show a part of the light curve on the same day, and draw two boxes (in dotted curves) at the On⁺⁺ state. The photons in the upper box show no sign of QPOs, while the photons in the lower box show clear evidence of QPOs. As the lower box contains photons which are from mini-Off states of the mini- ρ class mentioned above, it is not surprising that they show QPOs. Indeed, while the Off state on this day shows QPOs of frequency 3.09 Hz, these mini-Off states show QPOs of frequency 6.25 Hz.

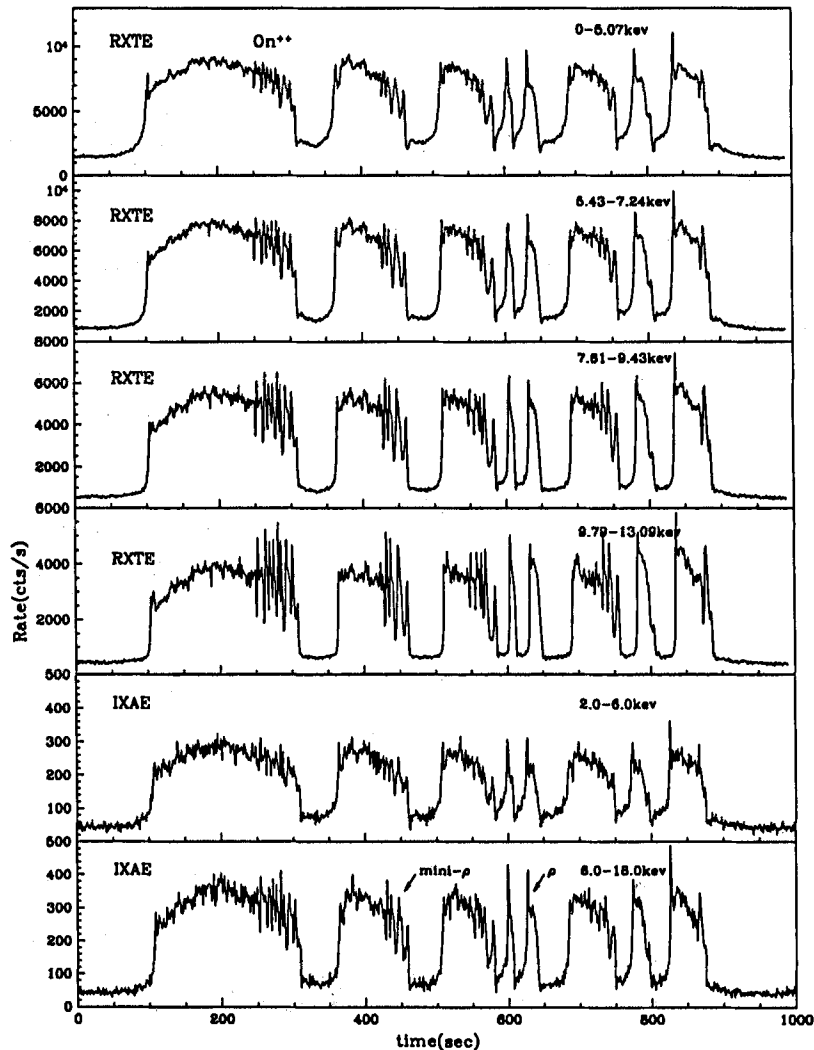


Figure 5. A part of the light curve from the so-called κ state is shown. The energy ranges are marked in each panel. The upper four panels are from *RXTE* data and the lower two panels are from *IXAE* data. Note that in On^{++} states light curves are noisier and more oscillatory, more so for photons at higher energy. A small arrow indicates a ρ -type burst. Presence of mini- ρ bursts within a κ -type On states indicates that ρ may be the *fundamental* type of all bursts.

This indicates that towards the end, the shock starts developing much closer to the black hole again and gives rise to a higher oscillation frequency. When the shock is fully developed, the Off state begins with a QPO at 3.09 Hz.

An easily missed phenomenon in all these light curves is that most of the On states begin with a ‘hiccup’ or a small peak, which may be likened to ‘P1’ of ρ or ν class, and also end with another ‘hiccup’ which may be likened with ‘P2’.

3 POSSIBLE INTERPRETATIONS OF THESE OBSERVATIONS

3.1 The paradigm

While there is as yet no fully self-consistent model which includes discs, winds and radiative transfer simultaneously, one can collect bits and pieces of the solutions and construct a viable model for the system. Chakrabarti (1996) and more recently Chakrabarti (2000) have discussed such solutions in detail. Fig. 7 shows a cartoon diagram of an accretion/wind system of GRS 1915+105. Generally, it is assumed the accretion is advective in nature and

has a centrifugal barrier dominated region which may or may not have become a fully developed shock (at $r = r_s$) throughout the period of observation. Chakrabarti (1999) showed that the centrifugal barrier dominated boundary layer (CENBOL for short) is not only responsible for the Comptonized radiation, but also responsible for the wind/jet formation. A very simple analysis which envisages an isothermal wind at least up to the sonic surface (at $r = r_c$) shows that winds should not be emitted in soft states, and very hard states should have very little winds. If the shock is of intermediate strength, outflow rate is very much high.

If the outflow rate is high enough, it can fill the sonic sphere (of size $r_c \sim 2-3r_s$; subsonic region up to the sonic surface) rapidly until the optical depth as a result of Compton scattering becomes larger than unity. Comptonization cools down this region rapidly. CM00 suggests that the duration of the Off state is the time in which this region achieves this threshold of cooling. As the specific energy and angular momentum of the flow decide shock location and its strength (Chakrabarti 1989), a small variation of the overall viscosity would change the shock location and therefore cause the variation of the duration and the QPO frequency from one Off state to another. The correlation between

duration and frequency based on this consideration has been discussed in CM00. An important by-product of all this is that as the disc loses matter (and pressure) from the post-shock region in the form of outflows, the shock, as well as the inner edge of the

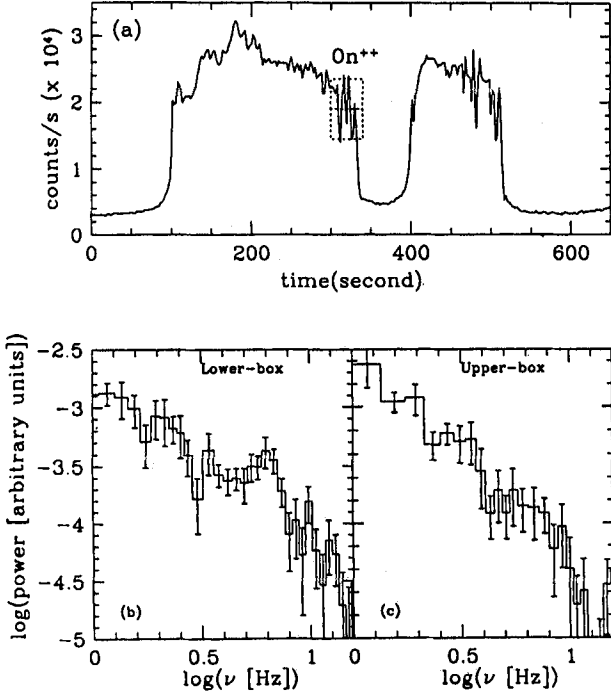


Figure 6. A part of the light curve from the so-called κ state is shown. In On^{++} states, two dotted boxes are drawn and below them the PDS of each box is plotted. Note the presence of QPOs in the lower box, which are nothing but mini-Off states corresponding to mini- ρ bursts.

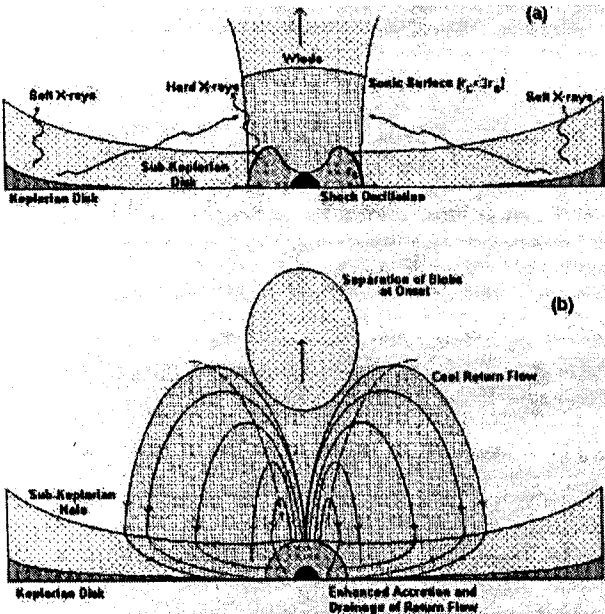


Figure 7. A cartoon diagram showing possible physical processes close to a black hole during an average time of the (a) Off and (b) On states. Centrifugal barrier or CENBOL produces winds. Subsonic region is cooled and falls back on the disc while supersonic region separates out as blobs. Excess accretion in the inner part causes higher counts in On states.

Keplerian disc moves inwards, gradually increasing the QPO frequency. This has been demonstrated by the dynamic power density spectra (e.g., Muno et al. 1999; Trudolyubov et al. 1999).

A part of the wind that does not reach escape velocity must return back to the disc and the accretion rate of the disc is temporarily modulated. This has been demonstrated by two-dimensional simulations of advective discs (Molteni, Lanzafame & Chakrabarti 1994; Molteni, Ryu & Chakrabarti 1996; Ryu, et al. 1997). This feedback mechanism becomes more complex in the presence of radiative cooling of the outflow. After the wind is cooled down, the sound speed is reduced, and location of the sonic surface comes closer to the black hole very abruptly. Part of the originally subsonic outflowing matter still remains below the new sonic surface and falls back because it loses the drive needed to escape. The rest becomes supersonic (because of reduced sound speed) and separates into the form of blobs. Thus, blobs are produced at the end of the off-states. This conjecture has been tested by multiwavelength observations (Dhawan, Mirabel & Rodriguez 2000).

During the On states, the shock and the CENBOL are non-existent and hence the QPOs are generally absent. Towards the end of the On state, in the so-called On^{++} state, the shocks start forming close to the black hole because of heat generated by excess accretion. The shock then rapidly recedes to a distance consistent with the steady-state solution as soon as the excess matter is drained out of the disc. This causes the onset of the Off state. This process of receding is regularly seen in numerical simulation of sub-Keplerian flows (Chakrabarti & Molteni 1993; Molteni, Lanzafame & Chakrabarti 1994).

3.2 Origin of hiccups or P1 and P2 peaks

It is clear that because these peaks are separated by a few seconds, and generally one peak has a QPO while the other does not, their origins cannot be the same. From the paradigm described above, one may imagine that P1 forms when catastrophic cooling of the CENBOL-sonic sphere system takes place. As P1 is a continuation of the Off state, QPO is thus expected unless the shock is hidden under the cooler wind. P2 is caused by the steepening of last bits of excess matter on the disc which is delayed by the viscous time-scale. The viscous time which a ring of matter takes after it leaves the Keplerian disc from a transition radius r_{tr} , where the flow deviates from a Keplerian disc (Chakrabarti & Titarchuk 1995), and enters the post-shock region is given by

$$t_{\text{visc}} \sim \frac{1}{\alpha} \left(\frac{h}{r} \right)^{-2} \frac{r}{v_{\text{Kep}}} = 10 \left(\frac{0.01}{\alpha} \right) \left(\frac{0.1}{c_s} \right)^2 \left(\frac{r_{tr}}{100} \right)^{1/2} \text{ s},$$

where α is the Shakura–Sunyaev viscosity parameter, $h(r) \sim c_s r^{3/2}$ is the dimensionless instantaneous height of the disc (in vertical equilibrium) at a radius r (measured in units of $R_g = 2GM/c^2$, the Schwarzschild radius), v_{Kep} is the rotational velocity of the Keplerian orbit, and c_s is the speed of sound in units of the velocity of light. As this ring of matter propagates through this region it is illuminated by soft photons coming out of the Keplerian disc, but because it is outside the shock its radiations do not participate in the oscillation. On the other hand, because the rising side of P1 is in the Off state, it shows QPO. As a result of Compton cooling, the spectrum of P1 is softer. However, P2 occurs when the excess matter is almost entirely drained out from the disc. Hence its spectrum is harder.

It is to be noted that whether or not shocks form depends on

viscosity. It has been shown (Chakrabarti 1990, 1996; Chakrabarti & Molteni 1995) that there is a critical viscosity parameter α_c below which shocks can form and this parameter is ~ 0.015 . Beyond this shocks disappear and Keplerian flows directly enter into the black hole. Our choice of $\alpha = 0.01$, chosen as such to explain the time-scale, is thus consistent with the presence of shocks.

In general, as excess matter drains out of the CENBOL, its optical depth decreases and the spectrum gets harder in the On^{++} state. This is observed in both *RXTE* and *IXAE* data.

3.3 Origin of ρ type light curve

One of the reasons we plotted Fig. 5 using the particular region of κ -class observations is that it may hold the key to understanding the general light curves. The figure clearly indicates that ρ -type regions are peeled off gradually in On^{++} states of the κ -class light curve. The arrows in Fig. 5 indicate that the forms of rise and fall are qualitatively similar, but quantitatively one is a miniature version of a fully developed ρ -type of bursts. Details of the modelling is discussed elsewhere (Chakrabarti et al. 2000).

Briefly, when the entire CENBOL behaves like a single blob, its light curve is of ρ -type: the count rate goes up in a Comptonization time-scale and rapidly drops in an infall time-scale. However, in the presence of strong winds and subsequent return of matter on the disc, turbulence is generated and one may imagine that each of the turbulent cells, after being steepened into small shocks, produce mini- ρ light curves, depending on the shapes and sizes of the turbulent cells. Each mini-shock produces a mini- ρ curve after filling smaller sonic surface.

4 CONCLUDING REMARKS

In this paper, we have pointed out some new and interesting characteristics of the light curve of the black hole candidate GRS 1915+105. We showed that the On states of ρ and ν types of light curves very often produce more than one peak, which behave differently. For instance, the first peak may show QPOs whereas the second peak shows no QPOs. The second peak also has a harder spectrum. In the κ and λ classes where the On state duration is longer, the On state shows very noisy and oscillatory behaviour towards the end, which we term as the On^{++} state. What is more, photons from the upper half of these light curves do not show QPOs, while those from the lower half do.

Though these observations are related to very small regions of the overall light curves, they help us understand the behaviour of matter close to a black hole. If one assumes that the duration of the Off states are determined by the time in which the optical depth of the sonic sphere becomes unity, as CM00 suggested, then many puzzles are solved. In this picture, part of the cooler matter of the out-flowing wind falls back on the CENBOL and the pre-shock disc, and its drainage time gives rise to the On states. It is possible that the first catastrophic cooling gives rise to the first hiccup in the On state, and the last significant density perturbation, caused by the fallen matter, may cause the final hiccup. This can explain why P1 often shows QPO, but P2 does not. The duration of the On

states in between may vary, depending on drainage time, giving rise to various classes of light curves. Also, towards the end of the drainage period, i.e. in On^{++} states, the excess matter is depleted and the signs of QPO starts appearing. What is most interesting is that mini- Off states show QPOs while mini- On states do not, indicating that states with broader 'On' are possibly made of ρ -type bursts.

ACKNOWLEDGMENTS

This work is partly supported by the Indian Space Research Organization (ISRO) through a project entitled 'Quasi-Periodic Oscillations in Black Holes'. AN's work is supported by a DST project entitled 'Analytical and Numerical Studies of Astrophysical Flows Around Compact Objects'. We gratefully acknowledge the use of *RXTE* data from public archive of GSFC/NASA.

REFERENCES

- Belloni T., Méndez King A. R., van der Klis M., van Paradijs J., 1997, *ApJ*, 488, L109
- Belloni T., Klein Wolt M., Méndez M., van Der Klis M., van Paradijs J., 2000, *A&A*, 355, 271
- Chakrabarti S. K., 1989, *ApJ*, 347, 365
- Chakrabarti S. K., 1990, *MNRAS*, 243, 610
- Chakrabarti S. K., 1996, *Phys. Rep.*, 266, 229
- Chakrabarti S. K., 1999a, *Indian J. Phys.*, 73B, 6, 931
- Chakrabarti S. K., 1999b, *A&A*, 351, 185
- Chakrabarti S. K., 2000, *Il Nouvo Cimento*, 115B, 897
- Chakrabarti S. K., Manickam S. G., 2000, *ApJ*, 531, L41 (CM00)
- Chakrabarti S. K., Molteni D., 1993, *ApJ*, 417, 671
- Chakrabarti S. K., Molteni D., 1995, *MNRAS*, 272, 80
- Chakrabarti S. K., Titarchuk L. G., 1995, *ApJ*, 455, 623
- Chakrabarti S. K., Manickam S. G., Nandi A., Rao R., 2000, in Ruffini R., ed., *Proc. 9th Marcel Grossman Conf.* World Scientific, Singapore, in press
- Dhawan V., Mirabel I. F., Rodriguez L. F., 2000, *ApJ*, submitted
- Manickam S. G., Chakrabarti S. K., 1999, *Indian J. Phys.* 73, 967
- Molteni D., Lanzafame G., Chakrabarti S. K., 1994, *ApJ*, 425, 161
- Molteni D., Ryu D., Chakrabarti S. K., 1996, *ApJ*, 470, 460
- Molteni D., Sponholz H., Chakrabarti S. K., 1996, *ApJ*, 457, 805
- Morgan E. H., Remillard R. A., Greiner J., 1997, *ApJ*, 482, 993
- Muno M. P., Morgan E. H., Remillard R. A., 1999, *ApJ*, 527, 321
- Nandi A., Manickam S., Chakrabarti S. K., 2000, *Indian J. Phys.*, 74B, 5, 3312
- Paul B., Agrawal P. C., Rao A. R., Vahia M. N., Yadav J. S., Seetha S., Kasturiragan K., 1998, *ApJ*, 492, L63
- Rao A., Naik S., Vadawale S. V., Chakrabarti S. K., 2000, *A&A*, 360, L25
- Remillard R. A., McClintock J. E., Sobczak G. J., Bailyn C. D., Orosz J. A., Morgan E. H., Levine A. M., 1999a, *ApJ*, 517, L127
- Remillard R. A., Morgan E. H., McClintock J. E., Bailyn C. D., Orosz J. A., 1999b, *ApJ*, 522, 397
- Ryu D., Chakrabarti S. K., Molteni D., 1997, *ApJ*, 474, 378
- Taam R., Chen X.-M., Swank J., 1997, *ApJ*, 485, 83
- Trudolyubov S., Churazov E., Gilfanov M., 1999, *A&A*, 25, 718
- Vilhu O., Nevalainen J., 1998, *ApJ*, 508, L85
- Yadav J. S., Rao R., Agrawal P. C., Paul B., Seetha S., Kasturiragan K., 1999, *ApJ*, 517, 935

Fundamental states of accretion/jet configuration and the black hole candidate GRS1915+105

Sandip K Chakrabarti^{1*} and Anuj Nandi

S N Bose National Centre for Basic Sciences, JD Block, Salt Lake, Sector-III, Calcutta-700 098, India

E-mail : chakraba@boson.bose.res.in, anuj @ boson.bose.res.in

Received 24 October 2000, accepted 30 November 2000

Abstract : Advective disk paradigm of black hole accretion includes self-consistent formation of shocks and outflows from post-shock region. We apply this paradigm to understand rich variation of the light curve of the black hole candidate GRS1915+105. We propose that out of five possible *fundamental states* the black hole candidate GRS1915+105 moves around among three of them creating all possible observed light curves.

Keywords : Black holes, X-ray sources, stars : individual (GRS1915+105)

PACS Nos. : 04.70.-s, 97.60.Lf, 98.70.Qy

1. Introduction

Chakrabarti [1,2] pointed out that considerable amount of outflow could be generated from the centrifugal pressure supported boundary layer (CENBOL) of a black hole. Indeed, it was shown that when the shock is weak (compression ratio $R \sim 1$), the outflow must be negligible and when the shock is strong ($R \sim 4-7$), the outflow is small but non-negligible. However, for the intermediate shock strength ($R \sim 2-3$), the outflow rate is very large—close to thirty percent of the inflow rate. Subsequently, Chakrabarti [3] showed that the slope of the hard-tail of the spectrum of a black hole must become larger in presence of outflows from the CENBOL region and conversely, if external matter is added to CENBOL for the same intensity of soft photons (from the Keplerian disk), the spectral slope must become smaller. In other words, hard-state spectrum should be softened and soft-state spectrum should be hardened. This has also been observed to be the case [4].

Another important phenomenon involving outflow is its periodic cooling by Compton scattering. When the outflow rate is large, the slowly moving subsonic region could be catastrophically cooled down by soft photons from the

Keplerian disk [3,5]. The sonic surface of the cooler outflow comes closer to the black hole horizon and the flow separates into two parts. Matter from the region above the new sonic sphere separates supersonically as blobs, and matter below the new sonic sphere returns back to the accretion disk. This causes enhancement of accretion rates of the disk temporarily in a very short time-scale and could produce interesting temporal variation of the photon flux.

Meanwhile, Belloni *et al* [6] (hereafter B2000) and Nandi *et al* [7] (hereafter N2000) classified all possible types of light curves of a very exciting black hole candidate GRS1915+105. B2000 divided the light curves in twelve types (termed as $\phi, \chi, \gamma, \mu, \delta, \theta, \lambda, \kappa, \rho, \nu, \alpha$ and β) and N2000 divided the light curves in four fundamental classes (Hard, Soft, Semi-Soft and Intermediate). B2000 mentioned that from the spectral point of view, however, one could imagine that there are three types of States : *A, B* and *C* combining which these light curves could be generated. In the present *Rapid Communication*, we claim that existence of these *fundamental states* cannot be understood by a standard Keplerian disk model and can be easily understood from the advective disk paradigm. In the next Section, we

*Corresponding Author

¹ Also, Honorary Scientist at Centre for Space Physics, 114/V/1A, Raja S. C. MULLICK Road, Kolkata-700 047, India

present the backbone solutions of the advective disk. In §3, we discuss five fundamental states which are formed out of these backbone solution and show that the states *A*, *B* and *C* of the black hole candidate GRS1915+105 [6] comprise three of them. Finally in §4, we draw our conclusions.

2. Backbone solutions of advective accretion

Equations governing advective accretion disks in pseudo-Newtonian geometry and in Kerr geometry were presented elsewhere and will not be repeated here [8,9]. It is observed that there are a total of eight different types of solutions [9] which are denoted as :

O : Flow passing through the outer sonic point only.

I : Flow passing through the inner sonic point only.

SA : Flow has two saddle type sonic points, and a steady shock forms in accretion.

NSA : Same as *SA* but no steady shocks can form. Shocks are oscillatory.

SW : Same as *SA* but steady shocks form only in winds.

NSW : Same as *SW* but oscillatory shocks form in winds.

*I** : Incomplete solution with inner sonic point.

*O** : Incomplete solution with outer sonic point.

In Figure 1, one solution (in Kerr geometry) from each type is shown in Mach number (*y*-axis) vs $\log(r)$ (*x*-axis)

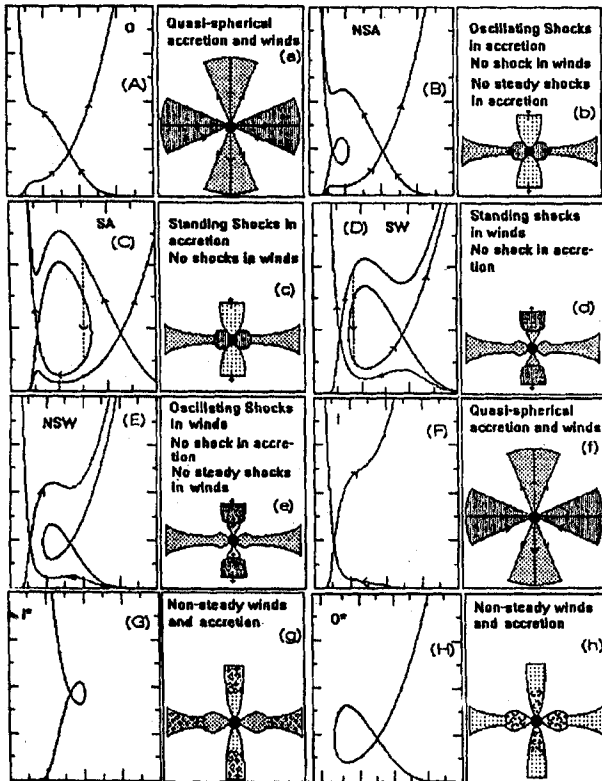


Figure 1. All possible representative solutions of an inviscid advective flow (A-H) and the nature of the disk-jet system (a-h). In the solutions, Mach numbers (*y*-axis) are plotted against logarithmic radial distance (*x*-axis).

plane. Vertical equilibrium and axi-symmetry have been assumed. For each of the solutions, we also present the schematic diagram of the nature of the flow. Transverse thickness is estimated from the assumption of vertical equilibrium $h \sim ar^{1/2}(r-1)$, where *r* is the radial distance in units of Schwarzschild radius $r_g = 2GM_B/c^2$ (M_B is the black hole mass and *G* and *c* are the gravitational constant and velocity of light respectively.). One notes that close to the black hole, matter is puffed up since its temperature is higher. Non-steady solutions have been represented by turbulence [in (g) and (h)].

When viscosity is added, closed topology of the solutions shown above open up [8] and the flow can join with a Keplerian disk. The specific energy of a Keplerian flow is :

$$\varepsilon = \frac{1}{2}v^2 + na^2 + \frac{\lambda^2}{2r^2} - \frac{1}{2(r-1)}, \quad (1)$$

where *n* is the polytropic constant, *v* is the radial velocity, *a* is the sound velocity and λ is the specific angular momentum respectively. For a cooler flow, ε is negative, but for a hotter flow, particularly away from the equatorial plane (so that the last term in eq. (1) is small), the energy could be positive. In case matter brings in magnetic field, its dissipation would raise the energy to a positive value so that shocks may form in a steady flow. In a non-steady flow, such restrictions do not apply and oscillating shocks may form even with bound flows [10,11].

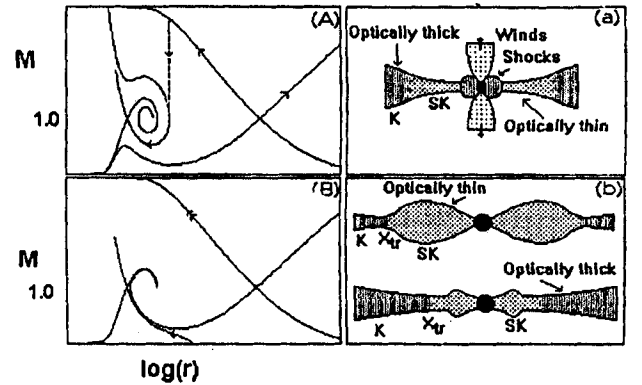


Figure 2. Same as Figure 1 but for a viscous flow. (a) Viscosity smaller than the critical value and (b) larger than the critical value.

Figure 2 shows representative solutions in a viscous flow and how a realistic disk looks like. In (a), flow viscosity is smaller than the critical value [8] and shocks can form and outflows are produced from CENBOL as in Figure 1. In (b), flow viscosity is higher than the critical value [8] and there are two solutions : one is mostly Keplerian (optically thick) till it passes through the inner sonic point, and the other is Keplerian farther out and passes through the outer sonic point. This is the optically thin branch of the solution.

3. Fundamental states of a realistic accretion flow

One could combine solutions in 1(a–h) and 2(a–b) to obtain realistic accretion-wind systems around a black hole. Viscosity is considered to be high in the equatorial plane and smaller away from the plane. From Figure 2(b) equatorial flow will be Keplerian closer to the black hole, and solutions of Figure 2(a) would cover above and below. There are several possibilities for reasonable parameters of a black hole accretion. We name these states according to the way they are commonly perceived in the literature.

(i) Hard state :

The accretion rate (in units of Eddington rate) in the Keplerian component is low $\dot{M}_K \sim 0.001 - 0.1$ and that of the sub-Keplerian component is high $\dot{M}_s \sim 1$. The combined sub-Keplerian flow enters into the black hole without forming a shock. Figure 3(a) shows the schematic diagram of the accretion-wind system. *Spectral signature* : Hard state without quasi-periodic oscillation of X-rays. If shocks form and oscillate, Quasi Periodic Oscillations (QPOs) could be observed.

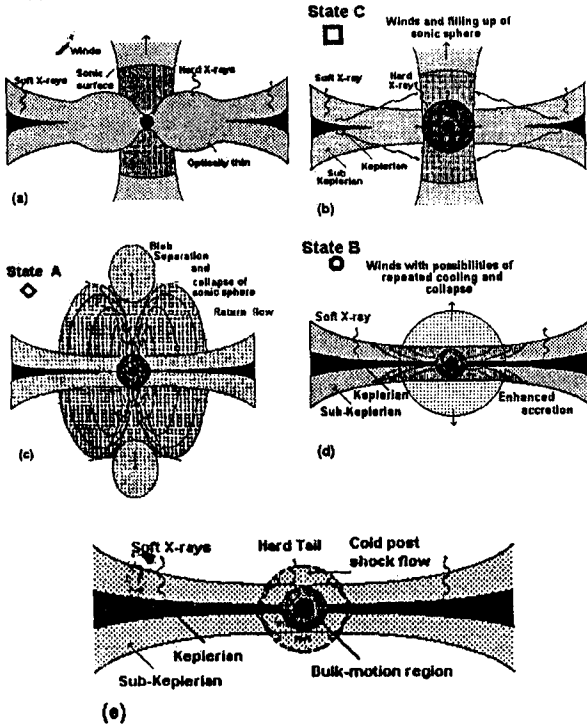


Figure 3. Fundamental States of the black hole accretion-jet system obtained by combining backbone solutions of Figure 1 and Figure 2. (a) Hard State, (b) Off State, (c) Dip State, (d) On State and (e) Soft State.

(ii) Off state :

The accretion rates are similar as above, but viscosity is lower than the critical $\alpha \leq 0.01$ (α is the Shakura-Sunyaev [12] viscosity parameter) so that shocks may form. If cooling rate in the post-shock region roughly agrees with the inflow rate, quasi-periodic oscillation of X-rays could be seen.

Outflow is produced which intercepts soft photons from Keplerian disk. Figure 3(b) shows that schematic diagram. *Spectral signature* : hard state with QPO. With time, the spectrum can get softer if the sonic sphere (region till the sonic point in the outflow) gets filled up gradually.

(iii) Dip state :

Keplerian accretion rates are higher $\dot{M}_K \sim 0.1 - 0.3$ and viscosity is also higher $\alpha \geq 0.01$ or more so that shocks are weaker. Post-shock flow is partly cooled due to Comptonization. Outflow till the sonic sphere has sufficient optical depth that it is cooled by Comptonization. The sonic point comes down as sound speed goes down in this region. Flow which remains sub-sonic with respect to this sonic sphere loses outward drive and returns back to the disk, while the supersonic flow separates as blobs in the jets. Figure 3(c) shows the schematic diagram. *Spectral signature* : tendency towards softer state and large spectral slope. QPO may not be visible as the shock is cooler (with longer cooling time scale) while infall time is shorter since the Keplerian disk moves inward due to larger viscosity.

(iv) On state :

Original flow may remain similar to above, but the return flow enhances both Keplerian and sub-Keplerian disk rates last few hundred Schwarzschild radii. Figure 3(d) shows the schematic diagram. Duration of this state is the duration of drainage of the excess accretion from return flow. *Spectral signature* : softer state with high photon flux. QPO is absent.

(v) Soft state :

Accretion rate of the Keplerian component is high $\dot{M}_K \geq 0.3$ and the viscosity is high enough so that Keplerian disk moves in all the way to the inner edge of the disk (Figure 2b). Matter moves almost radially and transfers its momentum to soft photons (bulk motion Comptonization [13]). Figure 3(e) shows the schematic diagram. *Spectral signature* : soft state spectrum without QPO with a weak power-law hard-tail.

Color-Color diagrams [HR1 vs HR2 diagrams where $HR1 = b/a$ and $HR2 = c/a$ ($a : 2 - 5$ keV, $b : 5 - 13$ keV, $c : 13 - 60$ keV)] showed very intricate structures (shapes of atoll, banana, etc.) [6]. From these, B 2000 conclude that there are three distinct States of GRS 1915 + 105 : *A* (low rate and low HR1, HR2), *B* (high rate, high HR1) and *C* (low rate, low HR1, variable HR2 depending on length of the event). According to classifications of Nandi *et al* [7], this would correspond to different regions in the softness ratio diagram. It seems that the State *C* exhibits QPO. State *A* and State *B* do not exhibit QPO. More interestingly, except for $C \rightarrow B$ transition, all other transitions of states are allowed. Nandi *et al* [14] found evidence of QPO in intermittent state *C* which are embedded in state *B*.

A comparison of the description of the States given above and the description of the fundamental States (1–5), it seems that, for GRS1915+105, data obtained so far suggests that the fundamental states 1 and 5 are missing, States 2–4 can be identified with States C, A and B of B2000 respectively. One can understand a typical evolution of States in the following way : Suppose we start with the State 2 described above. If the accretion rate is generally increased, shock is weakened (compression ratio goes down). There could be two types of high count states (State 3 [Dip] and State 4 [On]). After the winds of State 2 fills in the sonic sphere and cools it down by Comptonization, CENBOL and the region till the sonic sphere collapse. This is the State 3. Now there are two possibilities [5] : either the flow separates completely as a blob and returns to State 2 or the flow mostly returns back to the accretion disk and enhances the accretion. This would be the State 4. This may in turn increase the outflow [1,2]. But shock becomes weaker because of post-shock cooling, hence the outflow is very mild, but may remain at the threshold so that a bit more outflow can cause the sonic sphere to collapse again. Thus, occasional trips to State 3 from State 4 is possible. This is regularly observed [6]. Once the enhanced matter is drained out and the shock bounces back to roughly the original location (compatible with its specific energy and angular momentum), State 2 forms again. Since State 2 produce fewer soft photons, State 4 is not directly possible from State 2 without first producing return flow and enhanced accretion. This may explain why a direct transition from State 2 to State 4 is not seen [6].

It is clear that the complex behaviour of GRS1915+105 necessarily requires both Keplerian and sub-Keplerian disks for a proper explanation of the light curve. The return-flow from the cooler wind acts as a nonlinear feedback which can be represented schematically in Figure 4. Here, \dot{M}_K , \dot{M}_S , \dot{M}_{in} , \dot{M}_{rf} , \dot{M}_{out} and \dot{M}_{BH} represents Keplerian accretion rate, sub-Keplerian accretion rate, total accretion rate, rate

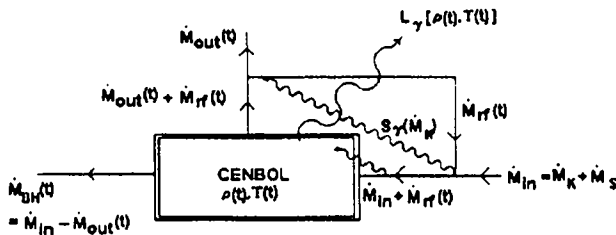


Figure 4. Schematic diagram stressing non-linearity induced by the return flow from the jet to the disk. Varieties of the light curve of GRS1915+105 is expected to be generated because of this non-linearity.

of return flow outflow rate and the rate of actual accretion to the black hole respectively. The soft photon intensity S_γ intercepted by the sonic sphere and the CENBOL is a function of the Keplerian rate.

4. Concluding remarks

We have presented the fundamental states of a viscous advective disk which includes radiative transfer. We identify that trips through States 2–4 cause the variable light curves in GRS 1915+105. Outflow seems to be a determining factor in switching these states. Numerical simulations showed existence of such outflows [15]. We already noted that the spectral states are related to the outflow rates [5]. Observations also suggest such a possibility [16, 17]. We believe that non-linear feed-back from the outflowing wind is essential to understand the variable light curves observed in this black hole candidate. Detailed modeling of these light curves would be presented elsewhere.

Acknowledgment

This project is partly supported by a DST grant No. SP/S2/K-14/98.

References

- [1] S K Chakrabarti *Indian J. Phys. (Review)* **72B** 183 (1998a)
- [2] S K Chakrabarti *Astron. Astrophys.* **351** 185 (1999a)
- [3] S K Chakrabarti *Indian J. Phys.* **72B** 565 (1998b)
- [4] S K Chakrabarti, S G Manickam, A Nandi and A R Rao *Astron. Astrophys* (submitted)
- [5] S K Chakrabarti *Indian J. Phys.* **73B** 931 (1999b)
- [6] T Belloni, M K Wolt, M Méndez, M van Der Klis and J van Paradijs *Astron. Astrophys.* **355** 271 (2000)
- [7] A Nandi, S G Manickam and S K Chakrabarti *Indian J. Phys.* **74B** 331 (2000)
- [8] S K Chakrabarti *Astrophys. J.* **464** 646 (1996)
- [9] S K Chakrabarti *Il Nuovo Cim.* **115** 897 (2000)
- [10] D Molteni, H Sponholz and S K Chakrabarti *Astrophys. J.* **457** 805 (1996)
- [11] D Ryu, S K Chakrabarti and D Molteni *Astrophys. J.* **474** 378 (1997)
- [12] N I Shakura and R A Sunyaev *Astron. Astrophys.* **24** 337 (1973)
- [13] S K Chakrabarti and L G Titarchuk *Astrophys. J.* **455** 623 (1995)
- [14] A Nandi, S G Manickam, A R Rao and S K Chakrabarti *Mon. Not. Roy. Astron. Soc.* (in press)
- [15] D Molteni, G Lanzafame and S K Chakrabarti *Astrophys. J.* **425** 161 (1994)
- [16] V Dhawan, I F Mirabel and L F Rodriguez *Astrophys. J.* **543** 373 (2000)
- [17] R Fender in *Proc. ESO Workshop 'Black Holes in Binaries and Galactic Nuclei'* (eds) L Kaper, E P J van den Heuvel and P A Woudt (Berlin : Springer-Verlag) (in press)

Observational evidence for mass ejection during soft X-ray dips in GRS 1915+105

S. V. Vadawale¹, A. R. Rao¹, A. Nandi², and S. K. Chakrabarti²

¹ Tata Institute of Fundamental Research, Homi Bhabha Road, Mumbai (Bombay) 400 005, India

² S.N. Bose National Center for Basic Sciences, Salt Lake, Calcutta 700 091, India

Received 8 January 2001 / Accepted 1 March 2001

Abstract. We investigate the connection between the X-ray and radio properties of the Galactic microquasar GRS 1915+105, by analyzing the X-ray data observed with RXTE, during the presence of a huge radio flare (~ 450 mJy). The X-ray lightcurve shows two dips of ~ 100 s duration. Detailed time resolved spectral analysis shows the existence of three spectral components: a multicolor disk-blackbody, a Comptonized component due to hot plasma and a power-law. We find that the Comptonized component is very weak during the dip. This is further confirmed by the PHA ratio of the raw data and ratio of the lightcurves in different energy bands. These results, combined with the fact that the 0.5–10 Hz QPO disappears during the dip and that the Comptonized component is responsible for the QPO lead to the conclusion that during the dips the matter emitting Comptonized spectrum is ejected away. This establishes a direct connection between the X-ray and radio properties of the source.

Key words. accretion, accretion disks – black hole physics – stars: winds, outflows – stars: individual: GRS 1915+105 – X-rays: stars

1. Introduction

The Galactic microquasar GRS 1915+105 is a bright X-ray source and it is a subject of intense study in all wavelengths, particularly in radio and X-ray wavelengths (see Mirabel & Rodriguez 1999 and references therein). It has been exhibiting different types of X-ray variability characteristics (Morgan et al. 1997; Munro et al. 1999; Yadav et al. 1999; Belloni et al. 2000a). The radio emission from this source also demonstrates its chaotic nature by means of time to time huge radio flares (Mirabel & Rodriguez 1994; Fender et al. 1999), long episodes of high/low emissions and periodic oscillations (Pooley & Fender 1997). There were several attempts in the past to correlate the radio and X-ray emission characteristics. Pooley & Fender (1997) reported short period radio oscillations coincident with X-ray dips. Fender & Pooley (1998) showed that the IR emission, interpreted as the high-energy tail of a synchrotron spectrum, also varies on similar time scales. Feroci et al. (1999) reported disappearance of inner accretion disk during a small radio flare. Thus, so far there are many evidences for the morphological correlation between X-ray emission and small radio oscillations or flares. However, in the case of huge radio flares, exhibited by this source from time to time, there is no strong morphological identification with

detailed X-ray emission characteristics. Fender et al. (1999) suggested that the repeated ejections of the inner accretion disk (Belloni et al. 1997) might be responsible for such flares. It was pointed out that such oscillations, having hard dips are not always accompanied by high radio emission (Naik & Rao 2000; Yadav et al. 1999). This suggests that some other mechanism is responsible for such huge radio flares. Recently, Naik & Rao (2000) made a systematic study of the morphology of different types of X-ray emission and accompanying radio emission and found an one to one correspondence between the soft dips in X-rays (observed during classes β and θ) and high radio emission. Naik et al. (2001) have suggested that the huge radio flares might be produced due to a number of such soft dip events.

In this *Letter* we propose an evidence of mass ejection, during the soft X-ray dips, by performing a detailed time resolved X-ray spectroscopy of the RXTE archival data observed simultaneously with a huge radio flare. We identify three components in the spectrum and show that the Comptonized component disappears during the dips. We explain this as ejection of the inner cloud and thus establish a direct connection between huge radio flares and X-ray emission from this source.

2. Analysis and results

GRS 1915+105 exhibits huge radio flares from time to time, the most recent of which occurred on 1999 June 8.

Send offprint requests to: S. V. Vadawale,
e-mail: santoshv@tifr.res.in

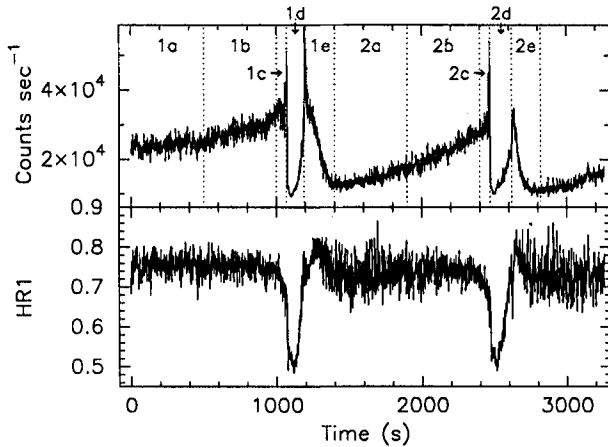


Fig. 1. Lightcurve (top panel) and hardness ratio (6–15 keV/2–6 keV; bottom panel) of GRS 1915+105 obtained on 1999 June 8 using *RXTE-PCA*. The regions chosen for time resolved spectral and temporal studies are shown in the top panel, separated by dotted lines

The PPC detectors of IXAE (Agrawal et al. 1997) observed the source during the entire episode of this radio flare, including the low-hard state of the source just prior to the flare. The IXAE observations revealed the presence of regular soft dips in the X-ray lightcurve during the radio flare. During these dips the X-ray flux decreases by a factor of three within ~ 5 s, remains low for ~ 30 –60 s and then gradually recovers to the maximum (Naik et al. 2001). Inspired by this observation, we obtained the *RXTE* data observed on 1999 June 8 (ObsID: 40702-01-03-00) to study, in detail, the spectral properties of the dips during the radio flare. This is the only pointed *RXTE* observation during this flare (Naik et al. 2001). The *PCA* (Jahoda et al. 1996) lightcurve and hardness ratio for this observation is shown in Fig. 1. It shows that this observation belongs to class θ as defined by Belloni et al. (2000a). The class θ shows almost regular soft dips of 40–100 s duration (defined as state A) and variable low-hard state (defined as state C) outside the dip.

We have attempted a wide band, time-resolved X-ray spectroscopy of the dip events by making spectral fits to the data from different portions of the lightcurve during both the observed cycles. We have divided each cycle into five intervals: pre-pre-dip (a, 500 s), pre-dip (b, 500 s), edge (c, 80 s), dip (d, 100 s and 140 s) and post-dip (e, 200 s). Figure 1 (top panel) shows the selection of these time intervals. For wide band spectral fitting we have extracted 129 channel spectra from *PCA* and 64 channel spectra from *HEXTE*. We have used data from cluster 0 of *HEXTE* and have added 2% systematic error to *PCA* spectra (Vadawale et al. 2001; Gierlinski et al. 1999). The spectra during very short intervals e.g. dip and edge, were rebinned to fewer number of channels in order to improve the statistics. We have fitted the *PCA* (3–50 keV) and

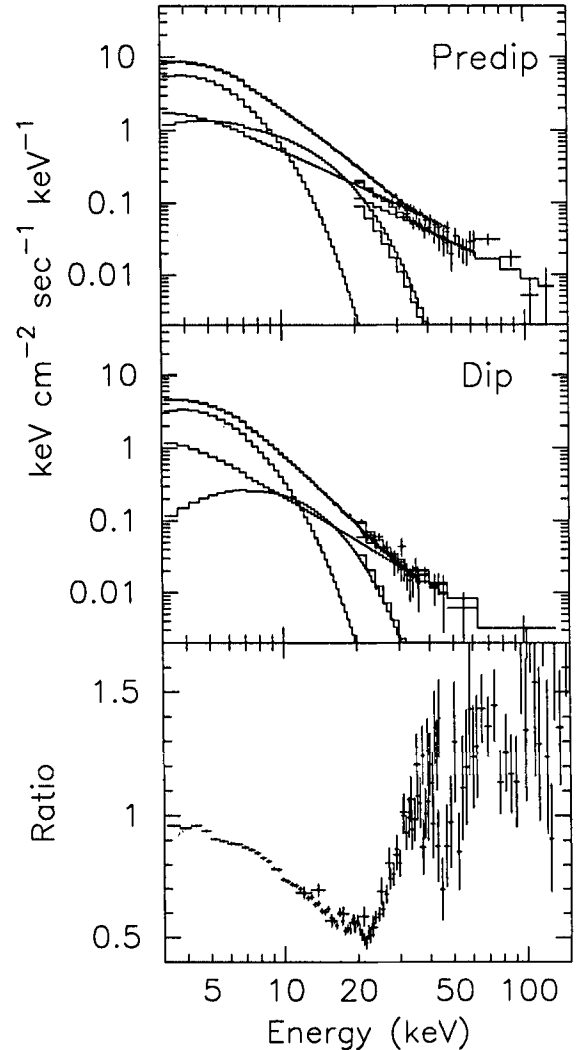


Fig. 2. The deconvolved X-ray spectra of GRS 1915+105 during the last 80 s before the dip (top panel) and 100 s during the dip (middle panel). The model consists of a disk blackbody, Comptonization due to hot plasma, and a power-law. The bottom panel shows the ratio of observed count rates (dip to pre-dip ratio) normalized at 30 keV, which highlights the lack of counts in the range 8–30 keV during the dip

HEXTE (15–150 keV) spectra simultaneously with different models (see Vadawale et al. 2001; Rao et al. 2000).

We find that the X-ray spectrum cannot be fitted by the “standard” model for the Black Hole Candidates (BHCs), consisting of a disk-blackbody and a power-law. It is also known previously that the X-ray spectra of radio loud states are peculiar and cannot be described by the standard model (Muno et al. 1999; Belloni et al. 2000b) and hence it is necessary to look for more complex models. We find that a three component model consisting of a disk-blackbody, a Comptonization due to hot plasma (CompST – see Sunyaev & Titarchuk 1980) and a power-law is necessary for statistically and physically acceptable fit to the X-ray spectra of the current observation.

Table 1. Results of temporal and spectral analysis¹ of RXTE data of GRS 1915+105 during class θ on 1999 June 8

Region	ν_{QPO} Hz	P_{QPO} rms %	kT_{in} (keV)	kT_{e} (keV)	τ	Γ_{X}	2–50 keV Flux (10^{-8} erg cm^{-2} s^{-1})			
							Total	Diskbb	CompST	Power-law
1a	5.99	3.10	1.51	3.35	16.77	2.81	6.69	2.00	1.13	3.56
1b	6.68	2.47	1.58	3.55	12.92	2.86	7.71	2.46	1.55	3.70
1c	8.34	1.89	1.51	3.18	12.85	2.61	8.80	4.25	2.20	2.34
1d	-	-	1.50	2.58	36.28	3.11	4.07	2.49	0.45	1.12
1e	4.67	3.44	1.56	3.52	12.86	2.75	6.27	2.12	1.28	2.86
2a	4.71	6.74	1.36	3.60	13.69	2.74	4.17	0.98	0.68	2.50
2b	5.60	3.76	1.50	3.64	12.75	2.84	6.18	1.66	1.08	3.44
2c	7.27	1.65	1.45	3.14	21.53	2.60	7.52	3.66	1.90	1.96
2d	-	-	1.44	2.40	35.30	2.93	3.95	2.35	0.53	1.06
2e	4.20	6.57	1.42	3.52	13.66	2.61	4.44	1.42	0.96	2.06

¹The model components are disk blackbody (diskbb), thermal-Compton (CompST) and power-law. Typical errors: inner disk temperature kT_{in} : ± 0.03 ; temperature of the Compton cloud kT_{e} : ± 0.15 ; optical depth of the Compton cloud τ : ± 0.40 ; power-law photon index Γ_{X} : ± 0.05 ;

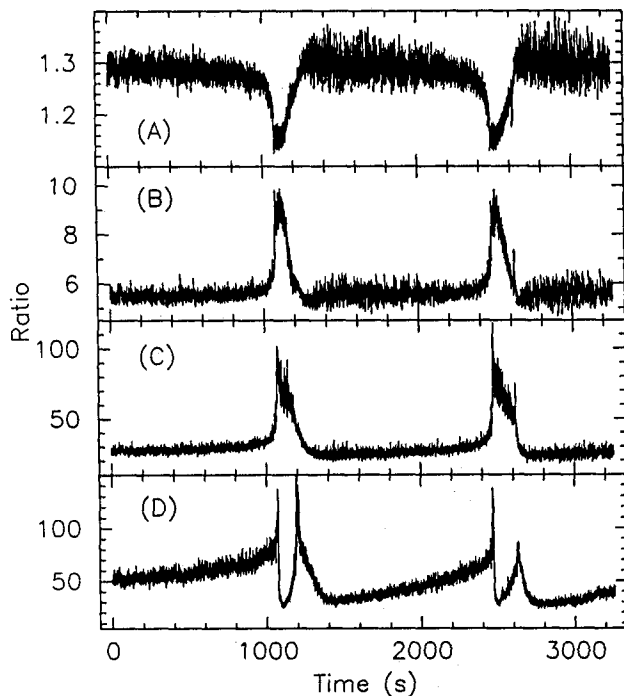


Fig. 3. Ratio of the lightcurves of GRS 1915+105 a) std-1/2–8 keV b) std-1/8–15 keV c) std-1/15–25 keV d) std-1/25–60 keV. Opposite shape of the dip in the top/bottom and middle two panels suggests that during the dip, relative decrease of counts in the middle energy ranges is larger than that in the low/high energy range

For example, in the pre-dip1 region, a model consisting of a disk-blackbody and a power-law gives $\chi^2 = 272$ for 89 degrees of freedom (dof), a model consisting of a disk-blackbody and a CompST gives $\chi^2 = 191$ for 88 dof, whereas the model consisting of three component: a disk-blackbody, a CompST and a power-law gives $\chi^2 = 85$ for 86 dof. The spectral fits improve by similar orders in the other regions as well, by using the three component

model. The same model is used by Vadawale et al. (2001) and Rao et al. (2000) to describe the radio loud low-hard state of this source, and they give a detailed justification for the existence of the third component. It should be mentioned here that the wide band (3–150 keV) spectral fitting is critical for identification of all the three components. Vadawale et al. (2001) have suggested the origin of the additional power-law as the very high-energy tail of the synchrotron radiation responsible for the radio emission. Our results strengthen their conclusion that the high radio emission manifests itself in X-ray spectra as an additional power-law component. The parameters of the best fit model are shown in Table 1 along with the component-wise X-ray flux for each region separately. The observed values of QPO frequency and the rms power in the QPO are also given in the table.

The two dip periods are particularly interesting because of the very weak CompST component and the absence of QPO. The absence of QPO (also reported earlier by Munro et al. 1999; Markwardt et al. 1999), combining with the result that only the CompST is responsible for the QPO (Rao et al. 2000), suggests that the CompST should also be absent during the dips. The same is indicated by the large decrease in the CompST flux compared to other two component fluxes (Table 1). A small CompST flux in the dip could be due to the inclusion of the recovery period in the dip spectrum. It is not possible to get the combined PCA and HEXTE-CL0 spectra during the first ~ 60 s of dip minima due to the rocking motion of the HEXTE clusters. However, spectral analysis of the dip minima using only PCA data shows that a disk-blackbody + power-law model gives statistically acceptable fit ($\chi^2 = 84$ for 60 dof), whereas the same model, for the pre-dip1 PCA data, gives unacceptable fit ($\chi^2 = 220$ for 64 dof). This leads to a hypothesis that the CompST is really absent in the beginning of the dip and slowly reappears during the later part of the dip.

To verify this hypothesis, we examined various ratios of the raw data. First two panels of Fig. 2 show the

unfolded spectra of pre-dip and dip intervals, obtained for the first dip, whereas the bottom panel shows the ratio of the observed count rate during the dip period to that during the pre-dip period, normalized at 30 keV. This ratio clearly shows that the dip period has fewer counts in the middle energy range (10–30 keV), in which the spectrum is dominated by CompST component, compared to the low and high energy range. This justifies our hypothesis that only CompST vanishes during the dip. To examine the temporal behavior of the dip in different energy ranges, we show in Fig. 3, the ratio of the PCA Standard-1 lightcurve (consisting of photons of all energy) to the lightcurve in different energy ranges. First panel of this figure shows that, during the dip, decrease in the count-rate in 2–8 keV range is less than that in the total count-rate, whereas the second and third panel show that, during the dip, decrease in the count-rate in 8–25 keV range (where CompST is a dominant component) is more than that in the total count-rate. Opposite shape of the dip in the first two panels shows that the decrease in the count-rate during the dip is strongly energy dependent and is most in the range where CompST is dominating. The shape of the dips in the fourth panel, which are shallower than the dips in the total lightcurve and thus show the effect of the dips in the lightcurve above 25 keV, is also opposite to that in the third panel. This provides further evidence to our hypothesis by showing that the decrease in the count-rate at high energies, is less than that in the middle energies.

Thus Figs. 2 and 3 provide strong support to our hypothesis, made from the time resolved spectroscopy, that the CompST component disappears during the dips. This can be interpreted as the ejection of the matter of the Compton cloud.

3. Discussion

Microquasars are thought to be the Galactic analogues of the distant quasars and AGNs. Because of their very low mass, compared to the AGNs, they provide a unique opportunity to probe the astrophysics of the AGNs in very short time scales. GRS 1915+105 is one of the most active microquasars, and shows all possible modes of the mass inflow and outflow, exhibited by means of highly complex emission throughout the electromagnetic band. Belloni et al. (2000a) classified the different types of the X-ray emission from this source in 12 different classes and the present observation belongs to the class θ , which predominantly consists of the low-hard state and soft dips. Our finding, that the X-ray spectrum of the low-hard state outside the dips in this observation is best described by three component model corroborates the conclusion drawn by Vadawale et al. (2001), who found that the X-ray spectra of all radio-loud low-hard states require the three component model.

The vanishing of the Comptonized component during the dip leads to the interpretation that the matter responsible for the Comptonized component is ejected away from the inner region of the accretion disk and the ejected

matter emits the synchrotron radiation which is observed as the radio flare. As time progresses, this matter is replenished and the Comptonized component reappears. Nandi et al. (2001) estimate a mass of $\sim 10^{18}$ g to be ejected during a dip event, based on the TCAF model, and they give a physical basis for such an ejection. The radio flare which occurred on 1999 June 8 is fairly large, with flux at 2.25 GHz reaching up to 500 mJy, which are previously observed only during the superluminal ejection from this source. Rodriguez & Mirabel (1999) have estimated a typical mass of the superluminal ejecta of the order of 10^{22} – 10^{23} g and hence a collection of a large number of such dips can cause the ejection of the superluminal ejecta. These results give a concrete support to the suggestion made by Naik et al. (2001) that the huge radio flares are produced by multiple dip events.

We wish to point out here that the hard state (state C) outside the soft dips, and variations in them, are also associated with radio emission in GRS 1915+105. Yadav (2001) has found a correlation between the X-ray hardness ratio in state C and the strength of radio emission for various X-ray variability classes. Belloni et al. (2000b) have estimated the mass accretion rate from the changes in the sizes of the inner accretion disk and have associated them with the outflow rates. In this work, we have found a definite evidence from X-ray spectroscopic analysis for a particular emission region disappearing during the soft dips (state A). It is quite possible that the state C (and variations in them) is associated with flat spectrum radio emission (see also Vadawale et al. 2001) and the soft dips are associated with steep spectrum radio emission coming from the superluminally moving ejecta. A continuous X-ray and radio observations during a superluminal jet emission episode should throw further light on the origin of radio emission in GRS 1915+105.

4. Conclusion

In this *Letter* we have shown that during soft X-ray dips, decrease in the count rate in the middle energy range (8–25 keV) is significantly greater than that in the low/high energies. We explain this as an ejection of a Compton cloud, whose radiation dominates in the middle energy range. We suggest that a collection of a large number of such dips can eject the required mass of the superluminally moving blobs.

Acknowledgements. We thank referee for useful comments and suggestions to improve the presentation of this paper. This research has made use of data obtained through the High Energy Astrophysics Science Archive Research Center Online Service, provided by the NASA/Goddard Space Flight Center.

References

- Agrawal, P. C., et al. 1997, *J. Korean Astrono. Soc.*, 29, S429
- Belloni, T., Klein-Wolt, M., Mendez, M., van der Klis, M., & van Paradijs, J. 2000a, *A&A*, 355, 271
- Belloni, T., Migliari, S., & Fender, R. P. 2000b, *A&A*, 358, L29

- Belloni, T., Mendez, M., King, A. R., van der Klis, M., & van Paradijs, J. 1997, *ApJ*, 479, L145
- Chakrabarti, S. K., & Titarchuk, L. G. 1995, *ApJ*, 455, 623
- Fender, R. P., & Pooley, G. G. 1998, *MNRAS*, 300, 573
- Fender, R. P., Garrington, S. T., McKay, D. J., et al. 1999, *MNRAS*, 304, 865
- Feroci, M., Matt, G., Pooley, G., et al. 1999, *A&A*, 351, 985
- Gierlinski, M., Zdziarski, A. A., Poutanen, J., & Coppi, P. S. 1999, *MNRAS*, 309, 496
- Jahoda, K., et al. 1996, *SPIE*, 2808, 59
- Markwardt, C. B., Swank, J. H., & Taam, R. E. 1999, *ApJ*, 513, L37
- Mirabel, I. F., & Rodriguez, L. F. 1994, *Nature*, 371, 46
- Mirabel, I. F., & Rodriguez, L. F. 1999, *ARA&A*, 37, 409
- Morgan, E. H., Remillard, R. A., & Greiner, J. 1997, *ApJ*, 482, 993
- Muno, M. P., Morgan, E. H., & Remillard, R. A. 1999, *ApJ*, 527, 321
- Naik, S., & Rao, A. R. 2000, *A&A*, 362, 691
- Naik, S., Agrawal, P. C., Rao, A. R., et al. 2001, *ApJ*, 546, 1075
- Nandi, A., Chakrabarti, S. K., Vadawale, S. V., & Rao, A. R. 2001, *A&A*, submitted
- Pooley, G. G., & Fender, R. P. 1997, *MNRAS*, 292, 925
- Rao, A. R., Naik, S., Vadawale, S. V., & Chakrabarti, S. K. 2000, *A&A*, 360, L25
- Rodriguez, L. F., & Mirabel, I. F. 1999, *ApJ*, 511, 398
- Vadawale, S. V., Rao, A. R., & Chakrabarti, S. K. 2001, *A&A*, submitted
- Sunyaev, E. A., & Titarchuk, L. 1980, *A&A*, 86, 121
- Yadav, J. S., Rao, A. R., Agrawal, P. C., et al. 1999, *ApJ*, 517, 935
- Yadav, J. S. 2001, *ApJ*, 548, 876

Computation of outflow rates from accretion disks around black holes

S. Das, I. Chattopadhyay, A. Nandi, and S. K. Chakrabarti*

S. N. Bose National Centre for Basic Sciences, Salt Lake, Kolkata 700098, India

Received 15 May 2001 / Accepted 30 August 2001

Abstract. We self-consistently estimate the outflow rate from the accretion rates of an accretion disk around a black hole in which both the Keplerian and the sub-Keplerian matter flows simultaneously. While Keplerian matter supplies soft-photons, hot sub-Keplerian matter supplies thermal electrons. The temperature of the hot electrons is decided by the degree of inverse Comptonization of the soft photons. If we consider only thermally-driven flows from the centrifugal pressure-supported boundary layer around a black hole, we find that when the thermal electrons are cooled down, either because of the absence of the boundary layer (low compression ratio), or when the surface of the boundary layer is formed very far away, the outflow rate is negligible. For an intermediate size of this boundary layer the outflow rate is maximal. Since the temperature of the thermal electrons also decides the spectral state of a black hole, we predict that the outflow rate should be directly related to the spectral state.

Key words. X-rays: stars – stars: winds, outflows – black hole physics

1. Introduction

Most of the galactic black hole candidates are known to undergo spectral state transitions (Tanaka & Lewin 1995; Chakrabarti & Titarchuk 1995, hereafter CT95; Ebisawa et al. 1996). Two common states are the so-called hard state and the soft state. In the former, soft-X-ray luminosity is low and the energy spectral index $\alpha \sim 0.5$ ($E_\nu \propto \nu^{-\alpha}$) in the 2–10 keV range. In the latter state, the soft-X-ray luminosity is very high, and hard-X-ray intensity is negligible. There is also a weak power-law hard-tail component with an energy spectral slope $\alpha \sim 1.5$. In the two component advective flow (TCAF) model (CT95), the viscous Keplerian disk resides in the equatorial plane, while the weakly viscous sub-Keplerian flow flanks the Keplerian component both above and below the equatorial plane. The two components merge into a single component when the Keplerian disk also become sub-Keplerian. It is suggested (Chakrabarti 1990) that close to a black hole, at around $10\text{--}15 r_g$, ($r_g = 2GM_{\text{BH}}/c^2$ is the Schwarzschild radius, M_{BH} and c are the mass of the black hole and the velocity of light respectively) the sub-Keplerian flow slows down due to the centrifugal barrier and becomes hotter. Chakrabarti (1999, hereafter Paper I) shows that this centrifugal pressure-supported boundary layer (CENBOL for

short) region could be responsible for the generation of thermally-driven outflowing winds and jets and computed the ratio of the outflow to the inflow rate assuming a simple conical accretion disk model.

In the present paper, we compute the *absolute* value of the outflow rate as a function of the rates of the two inflow components, Keplerian and sub-Keplerian. This we do analytically following the recently developed procedure of obtaining shock locations (Das et al. 2001). By dynamically mixing these two components using solutions of the viscous transonic flows we obtain the specific energy and angular momentum of the sub-Keplerian region. We use these pair of parameters to locate shocks in the flow, compute the compression ratio and from this, the outflow rate. We note that as Keplerian matter is increased in the mixture, the shock compression ratio goes down, and the outflow rate decreases. This is also the case even from a radiative transfer point of view – when the Keplerian rate is high, the CENBOL region is completely cooled and the shock compression ratio $R \sim 1$. Hence in the soft state, which is due to increase of the Keplerian rate, outflow should be negligible.

In the next section, we present the governing equations to compute the outflow rates using a purely analytical method. We compute results for both the isothermal and adiabatic outflows. In Sect. 3, we present our results for a single component sub-Keplerian flow. We also produce examples of realistic disks with Keplerian and sub-Keplerian components and obtain outflow rates as functions of the

Send offprint requests to: S. K. Chakrabarti,
e-mail: chakraba@boson.bose.res.in

* *Honorary Scientist*, Centre for Space Physics, 114/v/1A
Raja S.C. Mullick Rd., Kolkata 700047.

inflow parameters. In Sect. 4, we discuss our results and draw conclusions.

2. Model equations

We consider matter accreting on the equatorial plane of a Schwarzschild black hole. Spacetime around the black hole is described by the Paczyński-Wiita pseudo-Newtonian potential $\phi = \frac{GM_{\text{BH}}}{r - 2GM_{\text{BH}}/c^2}$ (Paczyński & Wiita 1980) where M_{BH} is the mass of the black hole and G , c are the gravitational constant and velocity of light respectively. Here, r is the radial distance from the origin of the coordinate in which the black hole is treated at the centre. We use geometric units in which all the length, time and velocity scales are measured in units of $2GM_{\text{BH}}/c^2$, $2GM_{\text{BH}}/c^3$ and c respectively. In future, we use r to denote non-dimensional distance, ϑ and a to denote the non-dimensional radial velocity and adiabatic speed of sound respectively. In accretion or outflow, we assume that the viscous stress is negligible so that matter moves with a constant specific angular momentum. Indeed, even if viscosity is not negligible, the transport of angular momentum is slow compared to the infall timescale. Hence, matter can have almost constant specific angular momentum.

In this case, the radial momentum equation for a non-dissipative flow in vertical equilibrium is given by (Chakrabarti 1989),

$$\vartheta \frac{d\vartheta}{dr} + \frac{1}{\rho} \frac{dP}{dr} - \frac{\lambda^2}{r^3} + \frac{1}{2(r-1)^2} = 0. \quad (1)$$

Integrating this, we obtain the conserved specific energy of the flow,

$$\mathcal{E}_v = \frac{1}{2}\vartheta^2 + na^2 + \frac{\lambda^2}{2r^2} - \frac{1}{2(r-1)}, \quad (2)$$

where n is the polytropic index of the inflow and λ is the specific angular momentum. In Eq. (1), P and ρ are thermal pressure and density respectively, v is the infall velocity and $a = \sqrt{\gamma P/\rho}$ is the adiabatic sound speed.

The mass flux conservation equation in a flow which is in vertical equilibrium is given by,

$$\dot{M}_{\text{in}} = 4\pi\rho\vartheta rh(r) = \Theta_{\text{in}}\rho_s\vartheta_s r_s^2, \quad (3)$$

where $\Theta_{\text{in}} (= \sqrt{\frac{2n}{n+1}} 4\pi a_s r_s^{1/2})$ is the solid angle subtended by the inflow at the CENBOL boundary. Subscripts “s” denote the quantities at shock (CENBOL boundary) and $h(r) = \sqrt{\frac{2}{\gamma} ar^{1/2}(r-1)}$ is the half-thickness of the disk in vertical equilibrium at a radial distance r .

A sub-Keplerian flow with a positive energy will pass through the outer sonic point and depending on whether the Rankine-Hugoniot condition is satisfied or not, a standing shock may form (Chakrabarti 1990; Chakrabarti 1996). If a standing shock forms, then the post-shock flow would become hotter and would emit hard X-ray radiation. This CENBOL region behaves similarly to the boundary of a normal star; it would be expected to drive

outflows. Using Eqs. (2) and (3), it is easy to obtain shock locations (i.e., outer surface of the CENBOL) analytically. Briefly, the procedure to obtain shocks involves the following steps:

(a) For a given pair of specific energy \mathcal{E}_v and angular momentum λ , one obtains a quartic equation for the sonic point and solves it for the three sonic points located outside the horizon. Two of them are saddle type or “X” type sonic points and one is a centre type or “O” type sonic point.

(b) From the inner and the outer “X” type points, Mach numbers are expressed as polynomials of radial distance r . These Mach number expressions satisfy constraints that they must have appropriate values at the sonic points.

(c) In addition, it is enforced that the Mach number invariants at the shock location are also satisfied (r_s).

(d) The resulting equation becomes quartic in r_s and the shock locations are obtained from its solution.

Details are discussed in Das et al. (2001). We consider only the region of the inflow parameter space (\mathcal{E}_v , λ) that is able to produce standing shocks.

In the pre-shock region, matter is cooler and is sub-Keplerian. Assuming $\mathcal{E}_v \sim 0$ (freely falling condition) and $a \sim 0$ (cool gas) in presence of angular momentum, matter will fall with a velocity,

$$\vartheta(r) = \left[\frac{1}{r-1} - \frac{\lambda^2}{r^2} \right]^{1/2}. \quad (4)$$

Using this, from Eq. (3) the density distribution can be obtained.

At the shock $r = r_s$, i.e., the boundary of the CENBOL, the compression ratio is given by,

$$\mathcal{R} = \frac{\Sigma_+}{\Sigma_-} = \frac{h_+(r_s)\rho_+(r_s)}{h_-(r_s)\rho_-(r_s)} = \frac{\vartheta_-}{\vartheta_+}, \quad (5)$$

where subscripts “-” and “+” refer, respectively, to quantities before and after the shock. Here, Σ is the density of matter integrated vertically ($\Sigma \sim \rho h$) and the second “=” sign was written using the mass flux conservation equation given above (Eq. (3)).

At the shock, the total pressure (thermal and ram pressure) is balanced:

$$W_-(r_s) + \Sigma_-(r_s)\vartheta_-^2(r_s) = W_+(r_s) + \Sigma_+(r_s)\vartheta_+^2(r_s), \quad (6)$$

where W is the pressure of the gas integrated vertically.

We assume that in the pre-shock region, the thermal pressure is small in comparison to the ram pressure,

$$W_+(r_s) = \frac{R-1}{R}\Sigma_-(r_s)\vartheta_-^2(r_s). \quad (7)$$

The isothermal sound speed in the post-shock region is obtained from:

$$C_s^2 = \frac{W_+}{\Sigma_+} = \frac{R-1}{R^2}\vartheta_-^2 = \frac{1}{f_0} \left[\frac{r_s^2 - \lambda^2(r_s-1)}{r_s^2(r_s-1)} \right], \quad (8)$$

where, $f_0 = \frac{R^2}{R-1}$.

Up to the sonic point matter moves slowly and the density is higher. Since the outflow would take place in a sea of radiation, the momentum deposition is likely to be effective. With the electron number density $n_e \propto r^{-3/2}$, yet photon number density $n_\gamma \propto r^{-2}$, it is easier to deposit momentum only close to the black hole. In radiation driven outflows from the stellar surface, it is customary to assume flows to be isothermal until the sonic point. We first compute outflow rates making this assumption. Later we drop this assumption and show that the general behaviour remains similar. In addition, we assume that there is very little rotation in the outflow. There is no a priori reason to assume this, except that there is no observational support of rotation in the jet and it is possible that due to radiative viscosity most of the angular momentum is transported very close to the black hole. Furthermore, it has been observed that the effect of angular momentum in the outflow is to bring the sonic points closer to the black hole, especially away from the axis (Sakurai 1985; Chakrabarti 1986). The general effect would produce a transverse structure in the jet which we ignore in the present solution. It was shown (Das & Chakrabarti 1999) that in presence of angular motion the conical outflow is to be replaced by an annular flow confined by the centrifugal barrier and the funnel wall. Generally speaking, the outflow surface varies as $r^{3/2}$. However, the inflow surface area is still proportional to r^2 . Because of this asymmetry, the problem is no longer tractable analytically and is beyond the scope of the present paper.

2.1. When the outflow is isothermal

The radial momentum balance equation in the outflow is given by

$$\vartheta \frac{d\vartheta}{dr} + \frac{1}{\rho} \frac{dP}{dr} + \frac{1}{2(r-1)^2} = 0, \quad (9)$$

and the continuity equation is given by

$$\frac{1}{r^2} \frac{d}{dr} (\rho \vartheta r^2) = 0. \quad (10)$$

From above equations we get

$$\frac{d\vartheta}{dr} = \frac{N}{D}, \quad (11)$$

where

$$N = \frac{2C_s^2}{r} - \frac{1}{2(r-1)^2} \quad \text{and} \quad D = \vartheta - \frac{C_s^2}{\vartheta}. \quad (12)$$

To obtain the sonic point condition, we put $N = 0$ and $D = 0$ and get, $\vartheta(r_c) = C_s$, and $r_c = \frac{1+8C_s^2 \pm \sqrt{1+16C_s^2}}{8C_s^2}$, where the subscript c denotes the quantities at the sonic point in the outflow.

Integrating the radial momentum equation, considering the sonic point condition, we have,

$$C_s^2 \ln \rho_+ - \frac{1}{2(r_+ - 1)} = \frac{1}{2} C_s^2 + C_s^2 \ln \rho_c - \frac{1}{2(r_c - 1)}. \quad (13)$$

Here, we have ignored the radial velocity in the outflow at the boundary of the shock. Using the notations $\rho(r_c) = \rho_c$ and $\rho(r_+) = \rho_+$, we obtain,

$$\rho_c = \rho_+ \exp[-f], \quad (14)$$

$$\text{where } f = \frac{1}{2} - \frac{1}{2C_s^2} \frac{r_+ - r_c}{(r_+ - 1)(r_c - 1)}.$$

The outflow rate is given by

$$\dot{M}_{\text{out}} = \Theta_{\text{out}} \rho_c \vartheta_c r_c^2, \quad (15)$$

where Θ_{out} is the solid angle subtended by the outflow.

From Eqs. (2) and (15) we get,

$$\frac{\dot{M}_{\text{out}}}{\dot{M}_{\text{in}}} = R_{\dot{m}} = \frac{\Theta_{\text{out}}}{\Theta_{\text{in}}} \left[\frac{r_+^2 (r_+ - 1)}{r_+^2 - \lambda^2 (r_+ - 1)} \right]^{-1/2} \frac{RC_s r_c^2}{r_+ (r_+ - 1)} \times \exp[-f]. \quad (16)$$

The above relation is very similar to that obtained in Paper I when the effects of rotation in the inflow were ignored. However, there the ratio $R_{\dot{m}}$ was a function of R alone. In the present analysis, R is computed self-consistently from the specific energy and the specific angular momentum of the flow:

$$R = \frac{\Sigma_+}{\Sigma_-} = \frac{\vartheta_-}{\vartheta_+} = \left[\frac{\frac{1}{2} M_+^2 + n}{\frac{1}{2} M_-^2 + n} \right]^{1/2}, \quad (17)$$

where pre-shock and post-shock Mach numbers $M_-(\mathcal{E}, \lambda)$ and $M_+(\mathcal{E}, \lambda)$ are computed analytically from Das et al. (2001).

2.2. When the outflow is adiabatic

At the other extreme, when the energy of the outflow does not change, one can also obtain an analytical expression for the outflow rate assuming the $r_+ \gg \lambda^2$. In this case, the entropy density of the flow in the post-shock region is the same as the entropy density of the entire outflow and the specific energy is also conserved along the outflow. We assume that the turbulence generated at the CENBOL has effectively transported angular momentum away. Thus, the energy conservation equation gives

$$n a_s^2 - \frac{1}{2r_+} = \frac{2n+1}{2} a_c^2 - \frac{1}{2r_c}, \quad (18)$$

where the left hand side is the energy at the CENBOL ($r = r_+$) and the right hand side is at the sonic point ($r = r_c$) of the outflow where $u_c = a_c$ has been used. $n = \frac{1}{\gamma-1}$ is the polytropic constant. In a Bondi (in or out) flow, $a_c^2 = 1/4r_c$. At the CENBOL, $a_s^2 = \gamma C_s^2$, where C_s is the isothermal sound speed (Eq. (8)). Using these, one obtains (assuming $r_+ \gg \lambda^2$)

$$\frac{r_c}{r_+} = \frac{2n-3}{4\left(\frac{2n\gamma}{f_0} - 1\right)}, \quad (19a)$$

and

$$\frac{a_c^2}{a_s^2} = \frac{f_0 r_+}{4\gamma r_c}. \quad (19b)$$

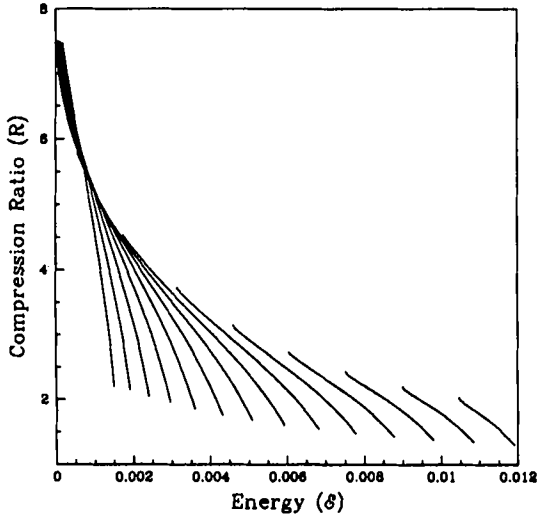


Fig. 1. Variation of the compression ratio of the shocks as a function of specific energy \mathcal{E} and angular momentum λ as obtained from the analytical solution. λ varies from 1.57 (right) to 1.79 (left). Curves are drawn at intervals of $d\lambda = 0.02$.

In an adiabatic flow with an equation of state $P = K\rho^\gamma$ (where K is a constant and a measure of entropy), one obtains, assuming, $K_c = K_s$,

$$\frac{\rho_c}{\rho_s} = \left(\frac{a_c^2}{a_s^2} \right)^n. \quad (20)$$

From these relations one obtains the ratio of the outflow to the inflow rate as

$$R_m = \frac{\Theta_o}{\Theta_i} \left(\frac{f_o}{4\gamma} \right)^3 \frac{R}{2} \left\{ \frac{4}{3} \left[\frac{8(R-1)}{R^2} - 1 \right] \right\}^{3/2}. \quad (21)$$

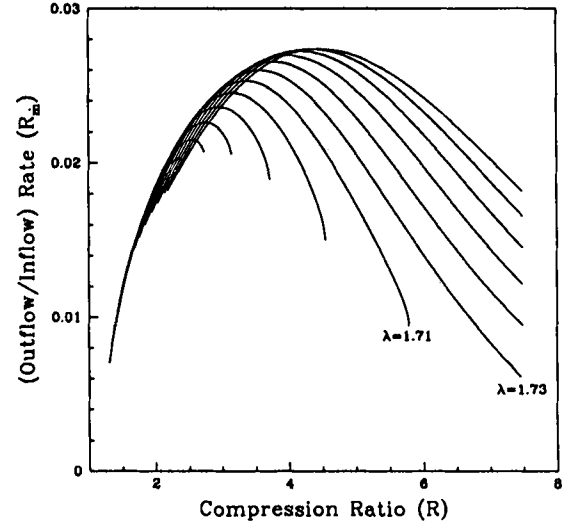
Here, we have used $n = 3$ for a relativistic flow. The nature of this function will be discussed below.

3. Outflow rates from inflow parameters

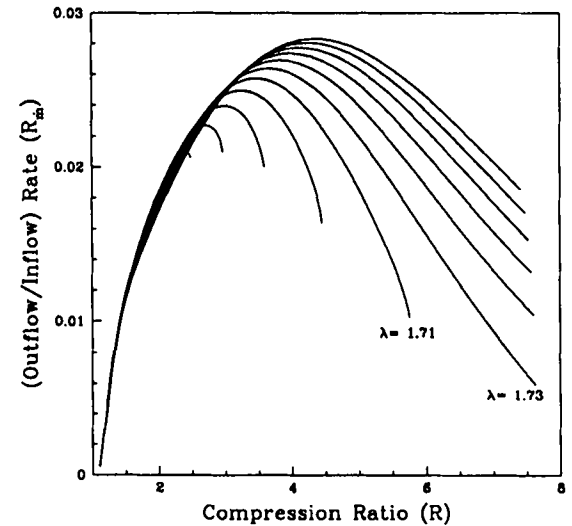
In Eq. (16), we presented the outflow/inflow rate ratio as a function of the compression ratio of the flow at the shock. The compression ratio is obtained from the specific energy and angular momentum using Eq. (17). First, we employ analytical means to obtain this for a single component sub-Keplerian disk. Second, we use a two component Keplerian/sub-Keplerian disk to actually compute these parameters from more fundamental parameters such as accretion rates and viscosity.

3.1. Single component sub-Keplerian flows

In Fig. 1, we plot the analytical solution of the compression ratio R as a function of the flow parameters: specific energy \mathcal{E} and the specific angular momentum λ . The shock strength generally increases when energy decreases and the angular momentum increases. This is because for low energy, the outer sonic point and the shock form very



(a)



(b)

Fig. 2. a) Variation of the ratio of outflow to inflow rates R_m as a function of compression ratio for various specific angular momenta. $\lambda = 1.57$ (inner most) to 1.83 (outer most). Curves are drawn at intervals of $d\lambda = 0.02$. Outflow rate is maximum at some intermediate compression ratio; b) Same as Fig. 2a except that curves are drawn for the exact numerical solution.

far away and the Mach number jumps from a very large number to a very small number. If the angular momentum is decreased, shock is produced only if the specific energy is high, i.e., if the sonic points and the shocks are very close to the black hole. Here, flow becomes subsonic before its Mach number could be very high.

Figure 2a shows the principle result of our work when only one sub-Keplerian accretion is chosen as the inflow. We plot the ratio R_m for a large number of specific angular momenta of the flow ranging from 1.57 (innermost) to 1.83 (outermost) at intervals of $d\lambda = 0.02$. The curves are

drawn for all ranges of specific energy \mathcal{E} for which shocks are formed. Along the X -axis the compression ratio R of these shocks is written. Here to compute solid angles of the inflow and the outflow, we assume the half opening angle of the outflow to be 10° . Therefore, $\Theta_{\text{out}} = \pi^3/162$. Θ_{in} is given in the discussion following Eq. (2). In Paper I, the compression ratio R was assumed to be a parameter and no angular momentum was assumed a priori. Presently, we show the dependence on angular momentum. The general character, namely, that the outflow rate is negligible when the shock is weak ($R \sim 1$) and falls off gradually for strongest shock ($R \rightarrow 7$), remains the same as in Paper I, however. There is a peak at about $R_{\text{in}} \sim 2.8\%$. Note that for a given R , R_{in} increases monotonically with specific angular momentum λ . This is because density of CENBOL rises with λ . The curves corresponding to $\lambda = 1.71$ and 1.73 are specially marked since there is a clear difference in tendency of the variation of R_{in} . For instance, below $\lambda \sim 1.72$, very strong shocks are not possible at all and as a result the outflow rate has a lower limit. For $\lambda \gtrsim 1.72$ such a limit does not exist.

The general behaviour of the outflow rate can be understood in the following way: when shocks are strong, they form very far out, and thus, even though the CENBOL area (which is basically the area of the base of the jet) increases, the net outflow rate is low. When the shock forms very close to the black hole, the temperature is high, and thus the outflow velocity is larger, but the CENBOL surface area goes down. Thus the product is low. For the intermediate cases the net effect is larger.

For comparison with the analytical work presented in Fig. 2a, in Fig. 2b we present a similar diagram drawn using a numerical computation of the shock locations (Chakrabarti 1989). Excellent agreement between these two figures implies that the approximations on which the analytical work was based are justified. All the features are reproduced well in Fig. 2a, except that for the weakest shocks outflow rate is not as low as in the numerical calculation of Fig. 2b.

We now present the nature of R_{in} when the outflow is also chosen to be adiabatic in Fig. 3. We used $\Theta_{\text{o}}/\Theta_{\text{i}} \sim 0.1$ for reference. We observe that the peak is still located at around $R \sim 4$ and the outflow rate drops for very strong ($R \sim 7$) and very weak ($R \sim 1$) shocks. We therefore believe that our conclusion about the behaviour of R_{in} is generic.

3.2. Two component advective flows

Chakrabarti & Titarchuk (1995) proposed that the spectral properties are better understood if the disk solutions of sub-Keplerian flows are included along with the Keplerian flows. Recently, Smith et al. (2001a), Smith et al. (2001b), Miller et al. (2001) found conclusive evidence of these two components in many of the black hole candidate accretion flows. While the matter with higher viscosity flows along the equatorial plane as a Keplerian

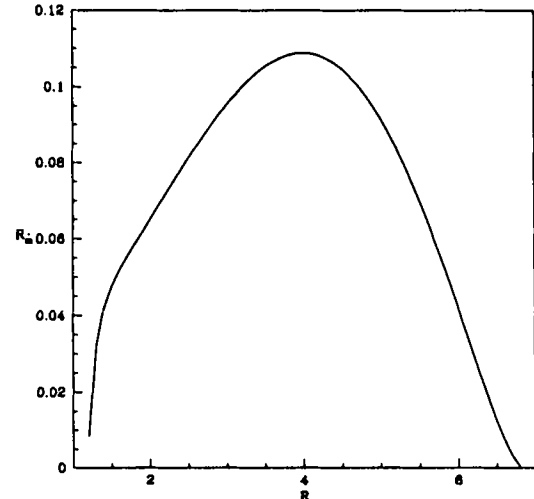


Fig. 3. Ratio of the outflow and the inflow rates as a function of the compression ratio of the inflow when the outflow is adiabatic. The general nature of the function remains the same as that of the isothermal outflow.

disk (of rate \dot{M}_{K}), sub-Keplerian halo matter (of rate \dot{M}_{h}) with lower viscosity flanks the Keplerian disk above and below (Fig. 4a). Since the inner boundary condition on the horizon forces the flow to be sub-Keplerian, irrespective of their origin (Chakrabarti 1990, 1996) matter mixes (at say, $r = r_{\text{tr}}$) from both the Keplerian and sub-Keplerian flows before entering a black hole to form a single component sub-Keplerian with an average energy and angular momentum of \mathcal{E} and λ respectively. The specific energy and angular momentum of the mixed flow is computed from:

$$\mathcal{E} = \frac{\dot{M}_{\text{K}}\mathcal{E}_{\text{K}} + \dot{M}_{\text{h}}\mathcal{E}_{\text{h}}}{\dot{M}_{\text{K}} + \dot{M}_{\text{h}}}, \quad (22)$$

and

$$\lambda = \frac{\dot{M}_{\text{K}}\lambda_{\text{K}} + \dot{M}_{\text{h}}\lambda_{\text{h}}}{\dot{M}_{\text{K}} + \dot{M}_{\text{h}}}. \quad (23)$$

Here, \mathcal{E}_{K} , \mathcal{E}_{h} , λ_{K} and λ_{h} are the specific energies and specific angular momentum of the Keplerian and the sub-Keplerian components at $r = r_{\text{tr}}$ respectively.

Figure 4a shows a schematic diagram of the cross-section of a two-component accretion flow. The transition radius ($r = r_{\text{tr}}$) where the Keplerian disk becomes sub-Keplerian, and the shock location $r = r_{\text{s}}$, are indicated. Figure 4b shows two solutions (marked I and II) of the equations governing a two-component flow (Chakrabarti 1996) where $\lambda_{\text{d}}/\lambda_{\text{K}}$ (Sub-Keplerian matter from the Keplerian disk) and $\lambda_{\text{h}}/\lambda_{\text{K}}$ (Sub-Keplerian halo) are plotted as a function of the logarithmic radial distance. Viscosities chosen for these two components are $\alpha = 0.04$ and $\alpha = 0.01$ respectively. For $r < r_{\text{tr}} = 45$ (lightly shaded region) the two sub-Keplerian flows mix to create a single component. For simplicity, we assume viscosity to be negligible in this region. Thus, the specific angular momentum and specific energy computed at

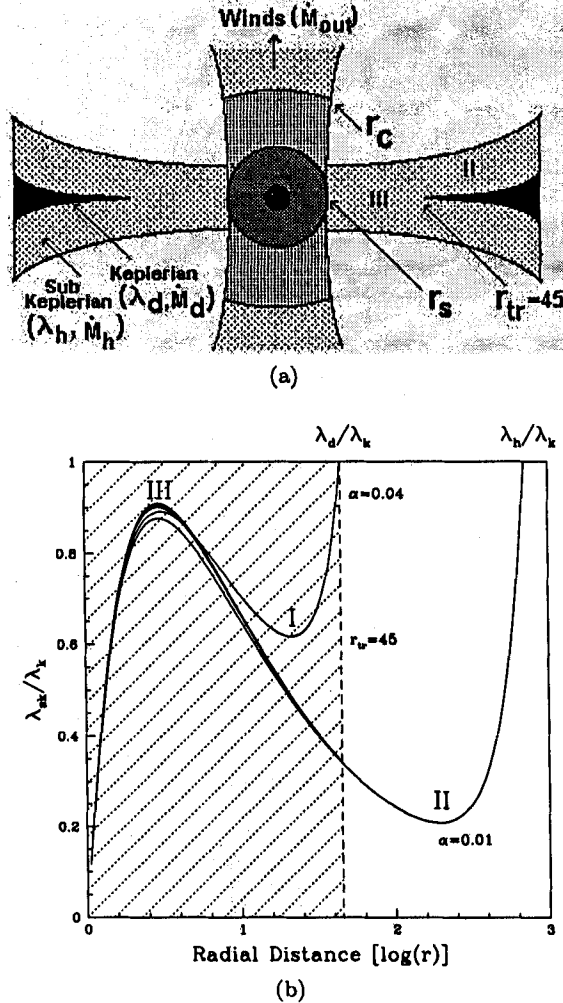


Fig. 4. a) Schematic diagram of the cross section of two-component accretion flow. See text for details; b) Solution of the two-component flow equations for two different viscosities. They are merged to form a single solution as depicted in Fig. 4a.

$r = r_{tr}$ from Eqs. (22) and (23) remain constant (λ) for $r < r_{tr}$. Dark solid curve (marked III) shows the angular momentum distribution λ/λ_K of all possible mixtures of the two components which allow shock formation. We chose a case where $M_d + M_h = 2.0M_{Edd}$ and vary the Keplerian component M_d where M_{Edd} is the Eddington accretion rate.

In Fig. 5, the computed outflow rates are shown when the half opening angle of the outflow is 10° . In this case, $\frac{\Theta_{out}}{\Theta_{in}} \sim \sqrt{\frac{n+1}{2n} \frac{\pi^2}{648a_* r_*^{1/2}}}$. The left axis shows the rate of outflow $\dot{m}_{out} = \dot{M}_{out}/\dot{M}_{Edd}$ as a function of the Keplerian disk rate (right panel) ($\dot{m}_d = \dot{M}_d/\dot{M}_{Edd}$) and the halo rate (upper panel) ($\dot{m}_h = \dot{M}_h/\dot{M}_{Edd}$). The lower axis gives the compression ratio at the shock. The most important conclusion that can be drawn here is that the

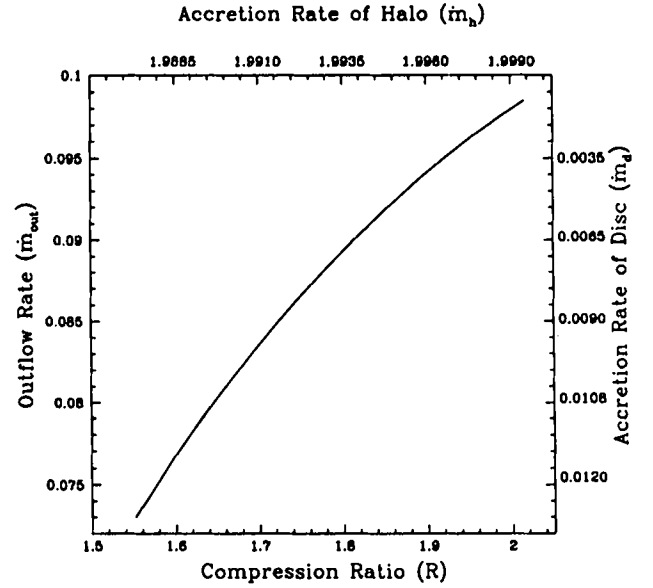


Fig. 5. Variation of outflow rates (left axis) with compression ratio at shocks (lower axis). The upper axis gives the variation of sub-Keplerian accretion rate and right axis gives the same for Keplerian accretion rate.

outflow rate steadily goes up as the Keplerian disk rate \dot{m}_d decreases and the spectrum goes to a harder state. When the Keplerian rate is higher, the compression ratio is lower and the outflow rate is also lower. This conclusion, drawn completely from dynamical considerations, is also found to be true from the spectral studies (CT95) where it was shown that the post-shock region cools down and the shock disappears ($R \rightarrow 1$). Our work therefore hints that the outflow would be negligible in softer states.

4. Discussion and concluding remarks

CT95 pointed out that the centrifugal pressure-supported boundary layer (CENBOL) of a black hole accretion flow is responsible for the spectral properties of a black hole candidate. In this Paper, we present analytical results to show that this CENBOL is also responsible for the production of the outflows, and the outflow rate is strongly dependent on the inflow parameters, such as specific energy and angular momentum. We showed that in general, the outflow rate is negligible when the shock is absent and very small when the shock is very strong. In intermediate strength, the outflow rate is the highest. As the specific angular momentum is increased, the outflow rate is also increased. This conclusion is valid when the flow is either isothermal or adiabatic.

We also demonstrated how a realistic two-component flow (TCAF) consisting of Keplerian and sub-Keplerian components produces a significant amount of outflow. Since matter close to a black hole is sub-Keplerian by nature, the two components must mix to form a single sub-Keplerian flow which has positive specific energy and almost constant specific angular momentum. We showed

that as the Keplerian rate of the disk is increased, the outflow rate is decreased as the shock compression ratio approaches unity. This conclusion, drawn from a dynamical point of view, is also corroborated by the spectral behavior as well – as the Keplerian rate is raised, the post-shock region is cooled due to inverse Comptonization and the shock disappears. This reduces the thermal pressure drive and the resulting outflow rate is reduced.

Acknowledgements. This work is partly supported by a project (Grant No. SP/S2/K-14/98) funded by Department of Science and Technology (DST), Govt. of India.

References

- Chakrabarti, S. K. 1986, ApJ, 303, 582
Chakrabarti, S. K. 1989, ApJ, 347, 365 (C89)
Chakrabarti, S. K. 1990, Theory of Transonic Astrophysical Flows (Singapore: World Sci.) (C90)
Chakrabarti, S. K., & Titarchuk, L. G. 1995, ApJ, 455, 623
Chakrabarti, S. K. 1996, ApJ, 464, 664
Chakrabarti, S. K. 1999, A&A, 351, 185 (Paper I)
Das, T. K., & Chakrabarti, S. K. 1999, Class Quant. Grav, 16, 3879
Das, S., Chattopadhyay, I., & Chakrabarti, S. K. 2001, ApJ, 557, 983
Ebisawa, K., Titarchuk, L. & Chakrabarti, S. K. 1996, PASJ, 48, 59
Miller, J. M., et al. 2001, ApJ, submitted [astro-ph/0107514]
Paczynski, B., & Wiita, P. J. 1980, A&A, 88, 23
Sakurai, T. 1985, Astron. Astrophys., 152, 121
Smith, D. M., Heindl, W. A., & Swank, J. H. 2001a, ApJ, submitted [astro-ph/0103304]
Smith, D. M., Heindl, W. A., Markwardt, C., & Swank, J. H. 2001b, ApJ, 554, L41
Tanaka, Y., & Lewin, W. H. G. 1985, in X-ray Binaries, ed. W. H. G. Lewin, J. van Paradijs, & E. P. I. van den Heuvel (Cambridge University Press), 166

Ejection of the inner accretion disk in GRS 1915+105: The magnetic rubber-band effect

A. Nandi¹, S. K. Chakrabarti^{1,2}, S. V. Vadawale³, and A. R. Rao³

¹ S.N. Bose National Center for Basic Sciences, Salt Lake, 700 098, Kolkata, India

² Centre for Space Physics, 114/v/1A Raja S.C. Mullick Rd., 700047, Kolkata, India

³ Tata Institute of Fundamental Research, Homi Bhabha Road, 400 005, Mumbai (Bombay), India

Received 19 April 2001 / Accepted 4 October 2001

Abstract. We examine theoretically the behaviour of the inner accretion disk in GRS 1915+105 when soft X-ray dips are present in the X-ray light curve. We assume the presence of a radial shock in the accretion disk, as in some of the Two Component Advective Flow (TCAF) solutions. We discuss the behaviour of the flux tubes inside a TCAF (which we name Magnetized TCAF or MTCAF model for brevity) and compare various competing forces on the flux tubes. In this MTCAF model, we find that the magnetic tension is the strongest force in a hot plasma of temperature $\gtrsim 10^{10}$ K and as a result, magnetic flux tubes entering in this region collapse catastrophically, thereby occasionally evacuating the inner disk. We postulate that this magnetic “rubber-band” effect induced evacuated disk matter produces the blobby components of outflows and IR/radio jets. We derive the size of the post-shock region by equating the time scale of the Quasi-Periodic Oscillations to the infall time of accreting matter in the post-shock region and found the shock location to be $\sim 45\text{--}66 r_g$. We calculate the transition radius r_{tr} , where the Keplerian disk deviates into a sub-Keplerian flow, to be $\sim 320 r_g$. Based on the derived X-ray spectral parameters, we calculate the mass of this region to be $\sim 10^{18}$ g. We conclude that during the X-ray dips the matter in the post-shock region, which manifests itself as the thermal-Compton component in the X-ray spectrum, is ejected, along with some sub-Keplerian matter in the pre-shock region.

Key words. accretion, accretion disks – black hole physics – stars: winds, outflows – stars: individual: GRS1915+105 – X-rays: stars

1. Introduction

GRS 1915+105 has proven to be an ideal source to study in detail many of the physical concepts regarding accretion onto black holes. Ever since its discovery (Castro-Tirado et al. 1992), it has been continuously bright in X-rays and it shows a variety of X-ray variability characteristics (Morgan et al. 1997; Munro et al. 1999; Yadav et al. 1999; Belloni et al. 2000). It has been monitored extensively in the radio band (Mirabel & Rodriguez 1994; Pooley & Fender 1997; Fender et al. 1999) and several episodes of high radio emissions, huge flares associated with superluminal motions, radio oscillations etc. are observed in this source. Several attempts have been made to associate the radio emission, presumably coming from jets, to the X-ray emission from the accretion disks (Fender et al. 1999; Naik et al. 2001; Naik & Rao 2001). The Spectral signature of winds from the Comptonising region has also been identified (Chakrabarti et al. 2001).

Chakrabarti & Manickam (2000, hereafter CM00) have applied the Two Component Advective Flow (TCAF) model of Chakrabarti & Titarchuk (1995) to explain various X-ray variability characteristics of GRS 1915+105. Recently there has been overwhelming evidence that the TCAF model is valid for many black hole candidates (Smith et al. 2001a; Smith et al. 2001b). CM00 invoked outflows from the inner accretion disk to explain a correlation between the QPO frequency and the duration of the burst-off states during a regular oscillations seen in the source. These outflows, however, are confined to the sonic sphere and fall back on the accretion disk after being cooled down by an inverse Compton effect. It was pointed out by Naik & Rao (2001) that the source does not show appreciable radio emission during such oscillations. A detailed inflow/outflow model has not been presented for this source to explain the radio emission, particularly to explain the superluminally moving radio blobs.

Recently Naik et al. (2001) have detected a series of soft X-ray dips during the declining phase of a huge radio flare and have postulated that such soft dips are responsible for the jet emission. Vadawale et al. (2001) made

Send offprint requests to: A. Nandi,
e-mail: anuj@bose.n.bose.res.in

a detailed study of X-ray dips observed during the radio flare using the Rossi X-ray Timing Experiment (RXTE) data and have presented evidence for the disappearance of the inner accretion disk during the dips. Since the disappearance of the inner disk is seen to be correlated with intense radio activity, the role of the magnetic field must be studied in order to understand the system completely. Rodriguez & Mirabel (1999) estimated the field in radio blobs to be around tens of mG at 500–1000 AU (in 1994 observation). Fender et al. (1997) requires the field to be around 8 G at around 1 AU (in their 1996 observations). From the similarity of ~ 30 min oscillations in IR and Radio, they concluded that the radio blobs are adiabatically expanding and are independently ejected from the disk every 30–40 min. If the trapped field inside a radio blob is of roughly $1/r$ (for toroidal field) then its interpolated value close to a black hole is around 10^7 G at around $10 r_g$ which is comparable to an equipartition value. Thus, one needs to correlate fields ejected from the disk with those observed inside the radio blobs. In this paper, we examine the mass ejection based on the TCAF model in presence of a magnetic field (we call this as Magnetized TCAF or MTCAF model) amplified due to strong shear at the transition radius of the Keplerian and a sub-Keplerian flow. In the next section, we discuss forces which govern the motions of the flux tubes and write equations of toroidal flux tubes inside an accretion disk with a constant angular momentum. We show that close to the black hole, where the flow could be very hot ($\gtrsim 10^{10}$ K) the flux tubes move at least with the Alfvén speed and may catastrophically collapse like a stretched rubber band. We conjecture that such rapid collapse would assist evacuation of matter from the disk and cause X-ray “dips” seen in the light curves. In Sect. 3 we estimate the mass of the ejecta which agrees with observations. Finally, in Sect. 4 we draw our conclusions.

2. The magnetized TCAF model for GRS 1915+105

Based on the global solutions of the most general advective accretion disk solution (Chakrabarti 1990, 1996a), Chakrabarti & Titarchuk (1995) presented a TCAF model of accretion onto black holes. According to this model, matter with high viscosity and angular momentum settles into the equatorial plane, while matter with lower viscosity and angular momentum surrounds the Keplerian disk. This sub-Keplerian component is likely to form a standing or an oscillating shock (Molteni et al. 1996; Ryu et al. 1997) front near the centrifugal barrier (few tens of Schwarzschild radii) depending on whether the Rankine-Hugoniot condition is satisfied or the cooling time in the post-shock region is comparable with the infall time. Soft photons from the Keplerian disk in the pre-shock flow are intercepted by the puffed up sub-Keplerian post-shock flow and are reprocessed due to inverse Comptonization. If the post-shock matter remains hot, the black hole exhibits a harder spectrum, while if the post-shock region is

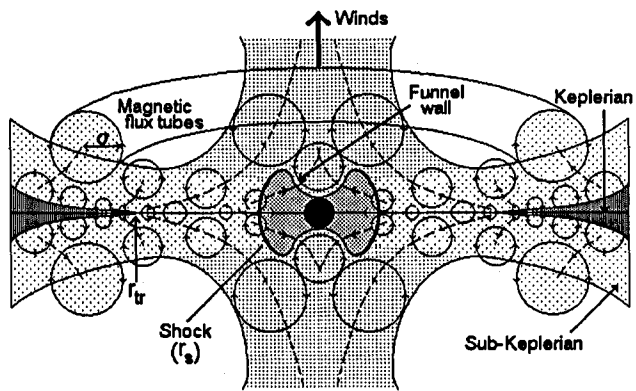


Fig. 1. A cartoon diagram of the accretion disk near a black hole which includes a shock (r_s), a sub-Keplerian and a Keplerian disk with a boundary at r_t . Stochastic magnetic fields are sheared and amplified as they leave a Keplerian disk. In a hot, sub-Keplerian flow, these toroidal flux tubes catastrophically collapse squirting matter along the axis, and thereby evacuating the disk and producing outflows. Dashed curves show typical trajectories (CD94).

cooled down by the soft photons, the black hole exhibits a soft spectrum. There could be a sub-Keplerian region just before the shock as well since with low viscosity and accretion rates a Keplerian disk recedes from a black hole and it is not necessary that the shocks form right at the region where a transition from Keplerian to sub-Keplerian flow takes place. Figure 1 schematically shows this behaviour of the two components.

The centrifugal pressure supported boundary layer (or, CENBOL for short) formed in a transonic, advective flow (Chakrabarti et al. 1996), has most of the features of a thick accretion disk although in advective disks, advection is included self-consistently and in thick disks advection is totally ignored. This is because at the CENBOL surface, matter undergoes a supersonic to sub-sonic transition and it moves very slowly in the radial direction. In some phases of accretion, matter can bring in a large stochastic magnetic field. The field is sheared due to strong azimuthal velocity and the toroidal field becomes very strong. These field lines will have very little matter within it and would likely be buoyant and emerge from various parts of the accretion disk. Figure 1 schematically shows this behaviour. Toroidal magnetic flux tubes released from the Keplerian disk are sheared, amplified and are advected in the sub-Keplerian flow. Due to the centrifugal barrier matter stays away from the axis. Thus a so-called funnel wall is created exactly as in a thick accretion disk (Paczynski & Wiita 1980). Chakrabarti & D’Silva (1994, hereafter CD94) computed the nature of their trajectories inside a thick accretion disk. They showed that in the event a strong flux tube enters a hot region with ion temperature $T_i \gtrsim 10^{10}$ K, the magnetic tension becomes the strongest force and the flux tube catastrophically collapses. Because of strong similarity of the thick accretion disk and an advective flow, especially inside the CENBOL, we believe that a similar

mechanism could be working and flux tube collapse would take place.

We shall consider the motion of the flux tubes on the equatorial plane of an accretion flow around a Schwarzschild black hole described by Paczyński-Wiita (1980) pseudo-Newtonian acceleration $g = -1/[2(x-1)^2]$. We use the geometric units. Masses are measured in units of the mass of the central black hole, M_{BH} ; distances from the axis (x) will be measured in units of the Schwarzschild radius $r_g = 2GM_{\text{BH}}/c^2$; and the time scales are measured in units of r_g/c . Inside the disk, we choose the polytropic equation of state, $P = K\rho^\gamma$, where K and γ are constants. The magnetic flux tubes brought in by advection are assumed to be sheared and *axisymmetric* toroidal flux tubes of random shape and size could be produced inside the flow. We however assume that the flux tubes are thin, i.e., the flux tube cross-sectional radius σ is smaller than the local pressure scale height of the disk. Close to a black hole, angular momentum of the flow remains constant (Chakrabarti 1996a) even in presence of moderate viscosity. Thus, we choose specific angular momentum λ in the sub-Keplerian region to be constant. The equations of motion for thin flux tubes have been given in CD94 and we do not repeat here. For the sake of completeness, we write down the radial equation only valid for the equatorial plane ($\theta = \pi/2$),

$$\ddot{x} + \frac{X}{(1+X)}[-x\dot{\phi}^2 - 2x\omega\dot{\phi}] = \frac{X}{(1+X)} \left\{ \frac{M_b}{X} [g - x\omega^2] - \frac{1}{m_i} \frac{\psi^2}{2\pi\sigma^2} - \frac{D_x}{\pi\sigma^2\rho_e} \right\}, \quad (1)$$

where $X = m_i/m_e$, $m_i = 2\pi^2\sigma^2x\rho_i$ and $m_e = 2\pi^2\sigma^2x\rho_e$ are the masses of the fluid inside and the fluid displaced by the flux tube respectively, ρ_i and ρ_e being the corresponding densities. Subscripts e and i indicate whether the relevant quantity is of the ambient (external) medium or within the flux tube (internal medium). $\psi = \pi\sigma^2B$, B being magnetic field of the tube and $\dot{\phi}$ is the intrinsic angular velocity of the flux tube inside the disk. The drag term is assumed to be similar to the drag experienced by a cylinder moving perpendicular to its axis in a fluid, and the drag per unit length in radial direction is given by,

$$D_x = -\frac{1}{2}C_D\rho_e\sigma(\dot{x} - u)^2 \quad (2)$$

where $C_D \sim 0.4$ (Goldstein 1938). The pre-shock, sub-Keplerian flow is assumed to have a radial velocity,

$$u \sim \beta/\sqrt{x-1} \quad (3a)$$

and the post-shock sub-Keplerian flow,

$$u \sim 1/R\sqrt{x-1}. \quad (3b)$$

Here, β is a factor by which sub-Keplerian matter slows down compared to a freely falling flow. $\beta \sim 1$ for very low angular momentum cool flow. R is the compression ratio of the shock by which matter is assumed to be slowed down inside the CENBOL.

From Eq. (1), we note that there are four forces in operation: (i) The second term inside the bracket of the left hand side is the Coriolis force $F_c = 2v_\phi\omega$, where $\omega = \lambda/x^2$ is the angular velocity of the flow. The Coriolis acceleration is given by (CD94),

$$a_C = \frac{\rho_i}{\rho_i + \rho_e} \frac{2\lambda^2}{x} \left[\frac{1}{x_0^2} - \frac{1}{x^2} \right]. \quad (4)$$

A flux tube brought from x_0 to x inside a flow of constant angular momentum would feel no Coriolis force if the motion is along the direction of constant angular velocity since $x_0 \sim x$ for rotating bodies. A magnetic flux tube with buoyancy factor $M_b (= \frac{\rho_e - \rho_i}{\rho_e}) = 1 - X$, will feel the (ii) Magnetic Buoyancy force (first term on the right hand side inside the curly bracket). The corresponding acceleration is (CD94):

$$a_{\text{MB}} = \frac{M_b}{1+X} \left[\frac{1}{2(x-1)^2} - \frac{\lambda^2}{x^3} \right]. \quad (5)$$

The tube will emerge out of the disk if a_{MB} dominates over a_C . The middle term on the right hand side of Eq. (1) is the (iii) force due to Magnetic Tension. The corresponding acceleration is a_T (CD94):

$$a_T = -\frac{1}{m_i + m_e} \frac{\Psi^2}{2\pi\sigma^2} = -\frac{B^2}{4\pi x(\rho_i + \rho_e)}. \quad (6)$$

The final and very important force is represented by the final term of Eq. (1). It is called the (iv) Drag Force exerted due to the motion of a rigid tube inside a flow. The corresponding acceleration is (CD94):

$$a_D = -\frac{C_D\rho_i\sigma(\dot{x} - u)^2}{2\pi\sigma^2(\rho_i + \rho_e)} \sim -\frac{C_D\rho_i u^2}{2\pi\sigma(\rho_i + \rho_e)}. \quad (7)$$

Here we used $\dot{x} \sim 0$ for computing the maximum value of the drag force.

Equating the acceleration due to buoyancy with that due to magnetic tension (Eq. (6)) on the equatorial plane, we get the critical temperature of the external gas as (CD94),

$$T_{p,0} = \frac{m_p c^2 [\lambda_K^2(x_0) - \lambda^2]}{4kx_0^2}, \quad (8)$$

above which the tension dominates over buoyancy and the flux tubes rush towards the funnel wall catastrophically. Here we used the mean electron number per ion to be $\mu = 1/2$ and k is the Boltzmann constant. Subscript 0 specifically indicates that the flux tube will behave like an over stretched rubber-band only after it crosses $x = x_0$, where $T > T_{p,0}$. Note that since we are dealing with a sub-Keplerian disk, $T_{p,0} > 0$ in the entire region of interest. For typical values $x_0 = 100$, $\lambda_0 = 1.8$, one obtains $T_{p,0} \sim 6 \times 10^9$ K. For an adiabatic disk, this assumption remains valid even when the flux tube collapses very rapidly since its internal temperature will increase adiabatically in the same way as in the external disk. For an efficiently cooled two-temperature flow, the above proton

temperature would correspond to an electron temperature of $T_e \sim \sqrt{m_e/m_p} T_p$. This is around 14 keV which is very reasonable for the temperature of the sub-Keplerian region. When the flux tubes fall radially, neither Coriolis force nor the drag term could be neglected. In fact, accelerated flux tubes would have high \dot{x} in the drag term as they move faster than the bulk radial motion. Meanwhile, assuming that internal mass of a flux tube is roughly constant, the cross-section $\sigma \sim 1/\sqrt{x}$ increases as the flux tube approaches the black hole. So, this will also increase the drag term. As a result, we expect that the flux tube would slow down somewhere close to the black hole and buoyancy would eject the flux tube out of the disk perpendicularly as shown in Fig. 1. Typical trajectories of the flux tubes, based on numerical integrations in CD94, are shown in Fig. 1.

The buoyancy timescale t_b is estimated from Eq. (5): $a_{MB} \sim h/t_b^2 = \frac{M_b}{(1+X)x^3} (\lambda_K^2 - \lambda^2)$, where $h \sim a_s x^{3/2}$ is the half thickness of the disk in vertical equilibrium at x and $a_s \sim x^{-1/2}$ is the speed of sound. Note that t_b is very large in a Keplerian disk ($\lambda_K \sim \lambda$). For a sub-Keplerian flow, $\lambda/\lambda_K \sim 0.4$ with $\lambda = 1.8$ at $x = 30$, $X \sim 0.1$, $M_b \sim 0.9$, $t_b \sim 240$.

Collapse time t_f of a flux tube is estimated in the following way: when tension is the most dominant force, the radial equation of the flux tube (Eq. (1)) is simplified to:

$$\ddot{x} + a_T = 0, \quad (9)$$

Putting $\ddot{x} \sim x/t_f^2$, we see that the velocity of collapse of the flux tube v_f is,

$$v_f \sim \left(\frac{B^2}{4\pi\rho_0} \right)^{1/2} \sim v_a \quad (10)$$

where v_a is the Alfvén velocity. Thus, flux tube collapses in Alfvén speed. Since $B \propto x^{-2}$, magnetic pressure is $\propto x^{-4}$, while the gas pressure $p_g \propto x^{-5/2}$, the ratio of magnetic to gas pressure $f \propto x^{-3/2}$, increasing with the decrease of x . As the flux tube leaves the Keplerian disk, large shear at the transition region and in the sub-Keplerian flow quickly intensifies the flux tube to $M_b \sim 1$ during infall. On the other hand, if $f \sim 1$ at $x \sim 300$ where the flow deviates from a Keplerian disk, $f \sim 30$ at $x = 30$, inside the CENBOL. The Alfvén speed $v_a \sim \left(\frac{B^2}{4\pi\rho_0} \right)^{1/2} \sim (f/\gamma)^{1/2} a_s \sim 5a_s$ where we used $\gamma = 4/3$. Since, inside a CENBOL, the velocity of matter v_m is highly sub-sonic, it is therefore high sub-Alfvénic: $v_m \ll v_a$. Thus, $v_f/v_m \gg 1$ and the flux tube collapses catastrophically. This justifies the conjecture made earlier that the rubber-band effect could evacuate the disk (Chakrabarti 1994, 1996b, 2000). For $a_s \sim x^{-1/2}$, $t_f \sim x^{3/2}/5 \sim 30$ at $x = 30$. Thus inside the CENBOL $t_b \gg t_f$.

So far, we have ignored many non-axisymmetric effects such as Parker instability (1979 and references therein) and shearing instability (e.g., Balbus & Hawley 1991). Foglizzo & Tagger (1995) treated this problem comprehensively in the context of a standard disk embedded in a large scale field. They found that (a) if the wave-length

is larger than the disk thickness then the flux tube is very unstable and buoyantly comes out of the disk and (b) instability is strongest if the field is weaker. According to Parker (1979), submerged field tubes may break up into filaments in timescales of around $3\Lambda/v_a$, where Λ is the scale height and the field is able to escape from the gas in timescales $t_P \sim \Lambda/v_a$. If $\Lambda \sim h \sim x$, which is especially true in CENBOL region, the time scale of the escape of the field may be comparable to the t_f as obtained above. As a result, the flux not only collapses catastrophically, but also escapes upwards following a curved trajectory as depicted in Fig. 1. In presence of a differential rotation, Balbus & Hawley (1991) suggested that even a small initially vertical field would be amplified to create all the components in the dynamical timescale $t_d \sim 1/\omega = x^2/\lambda \sim 50$ (at $x = 30$, $\lambda = 1.8$). Numerical simulation (Hawley et al. 1995) has verified this instability neglecting the tension effects. Even though the time scales of the collapse, the Parker instability and the shear instability are of the same order, we believe that the rubber-band effect would still be important for the destruction of the inner disk.

3. Estimation of mass of the post-shock region and the sub-Keplerian region

Vadawale et al. (2001) have shown that during the soft X-ray dips a thermal-Compton component in the X-ray spectrum gets suppressed. Several works in the literature talk about the disk-evacuation (e.g., Belloni et al. 1997; Feroci et al. 1999) in this context. We like to understand this using Two Component Advective Flow (TCAF) models of Chakrabarti & Titarchuk (1995) in presence of a Magnetic field (i.e., MTCAF model) and its time variability properties described in Molteni et al. (1996); Ryu et al. (1997) and Chakrabarti & Manickam (2000). The observation of possible disk-evacuation is clearly in line with the TCAF model and the shock oscillation model of the quasi-periodic oscillations (CM00; see also, Rao et al. 2000) which showed that the Comptonising post-shock region participates in oscillation. The sub-Keplerian region in the pre-shock flow does not emit much radiation and it is possible that some of this region may also be disrupted during the rapid collapse of the flux tube. Once we accept the destruction of the sub-Keplerian region by the magnetic rubber-band effect, we can compute the mass of this region in the following way:

The shock location is computed by equating the infall time from the shock with the time scale of QPO. This time scale t_{ff} can be written in the form (CM00):

$$t_{\text{ff}}^{-1} = \frac{1}{R} \frac{1}{r_s^\alpha} \frac{cv_0}{r_g}, \quad (11)$$

where, R is the compression ratio (see also, Eq. (3b)), r_s is the shock location, v_0 is a dimensionless constant. Here, $\alpha = 3/2$ for free-fall motion and $\alpha = 1$ for a flow of constant velocity cv_0/R in the post-shock region. Using this assumption, the shock location in the pre-dip and the post-dip flow (for parameters in these flow see,

Vadawale et al. 2001) are $\sim 45 r_g$ and $\sim 66 r_g$ respectively. CM00 proposes that a better fit in the correlation between the duration of the QPO and the frequency of QPO requires more or less constant velocity in the post-shock region with a rough velocity of $0.066c/R$. This produces the shock in the pre-dip and the post-dip flow at $79 r_g$ and $140 r_g$ respectively. Using the parameters of Vadawale et al. (2001), and the location of the shock as given above, the electron number density in the Comptonising region is found to be $n_e \sim 10^{17} \text{ cm}^{-3}$. The corresponding mass ($\frac{4}{3}\pi r_g^3 m_p n_e r_g^3$) of the region is $M_{\text{CENBOL}} \sim 2 - 3 \times 10^{18} \text{ g}$ depending on the model of the inflow. How much of this matter is squirted out of the disk along the axis? Again, in the absence of the size distribution of the flux tubes, the answer is difficult. However, because of centrifugal force, matter is unlikely to enter within the “funnel wall” (CD94) even after compression, sudden collapse of large flux tubes [$\sigma \sim h(r_g)$] would be expected to displace the whole CENBOL region parallel to the funnel wall. The outflow rate would be $\dot{M}_{\text{out}} \sim M_{\text{CENBOL}}/t_f$ which may be very large compared to the inflow rate for a short duration of t_f . If flux tubes are smaller in size, since the collapse velocity is much larger than the speed of sound, matter will still be displaced but would be refilled in free-fall time, unless there are many near-simultaneous flux collapse events.

If the magnetized sub-Keplerian disk is removed by imploding flux tubes as described in the earlier section, one requires to know the location of the inner edge of the Keplerian disk to estimate the complete mass involved. From the model fit (Vadawale et al. 2001), the Keplerian disk temperature turns out to be $T_K \sim 1.5 \text{ keV}$. With a hardening factor of around 1.7 (Shimura & Takahara 1995), the mass of the black hole as $10 M_\odot$ and Shakura-Sunyaev viscosity parameter $\alpha_{\text{SS}} = 0.01$, the above temperature corresponds to a transition radius at around $r_{\text{tr}} \sim 320 r_g$ (Shakura & Sunyaev 1973). Assuming density falling off as $\rho \sim \rho_0 (\frac{r_g}{x})^{3/2}$, the mass of the sub-Keplerian flow of size x_{tr} ($\int 4\pi x h(x) \rho dx$ with $h(x) \sim x$) is around 10^{20} g . These computations assume no pair production, i.e., there is exactly one electron for each proton in the Comptonising region.

Once the evacuation is complete, the disk is filled in quickly by sub-Keplerian matter in timescale of:

$$t_{\text{visc}} \sim \frac{1}{\alpha_{\text{SS}}} \left(\frac{h(x)}{x} \right)^{-2} \frac{x}{v_{\text{Kep}}} \\ = 192 \left(\frac{0.01}{\alpha_{\text{SS}}} \right) \left(\frac{0.03}{a_s} \right)^2 \left(\frac{x_{\text{tr}}}{300} \right)^{1/2} \frac{M_{\text{BH}}}{10 M_\odot} \text{ s.} \quad (12)$$

Here, $h(x) \sim a_s x^{3/2}$ (a_s is the speed of sound) is the local vertical height of the disk. The time scales seem to be reasonable, since the dips have been seen to be filled up in a matter of 150 to 200 s. It is to be noted that Dhawan et al. (2000) using disk-instability model of Belloni et al. (1997) obtained the missing inner disk region to be only 180 km. This distance is about $6 r_g$ and with $10^{18} \text{ g m s}^{-1}$ accretion rate which they employ, the mass of this region cannot be enough to create the 10^{23} g m blob (or, even 10^{18} g mini-blobs) observed by Mirabel & Rodríguez (1999). This is

particularly because the region $1-3 r_g$ is definitely supersonic and sub-Keplerian and therefore is of very little mass. We believe that the missing region should be much larger, possibly order of a $100 r_g$ or so.

4. Conclusion

In this paper, we have given a physical basis for a sudden mass ejection in GRS 1915+105. We showed that if matter brings in a particularly strong magnetic field, this would be sheared and amplified to a value much above the equipartition value before it can be expelled by buoyancy. Magnetic tension collapses these toroidal flux tubes at a highly supersonic speed, much faster than the flow velocity. This has the effect of displacing matter from the disk in transverse direction (much like a fast boat causing spillage on a shore) and depositing it to outflowing winds. From the observed fits of Vadawale et al. (2001) we estimated the electron number density and the mass of the post-shock region and the sub-Keplerian flow to be around 10^{18} g and 10^{20} g respectively. Our estimate of the post-shock mass is a factor of ten less than the mass estimate (10^{19} g) of “baby-jets” (Mirabel et al. 1998) associated with IR and radio flares and could therefore be due to ejection of some sub-Keplerian matter as well. These “baby-jets” are found to be associated with class β light curves which have soft X-ray dips. These dips are also seen in class θ light curves. During a major portion of the huge radio flares associated with superluminal blob emission a series of soft dips are present (Naik et al. 2001). Mirabel & Rodríguez (1999) have pointed out that in each epoch of this type of outflow, the mass condensation is around 10^{23} g . In order to achieve this, we require that matter is accumulated from disk evacuation at each “dip” and within each epoch, successive mini-blobs move faster than the earlier blob in order to “catch up”. This may indicate some other runaway process with a longer time scale of tens of days. Naik et al. (2001) have observed such X-ray dips at a rate of once in a few hundred seconds during the peak or the radio flare. If there are ~ 1000 evacuation events during an episode of superluminal blob ejection (in a few days), then total mass condensation would be 10^{23} g . Hence in order to explain the observation of Mirabel & Rodríguez (1999), one must require that in each epoch, matter is accumulated from at least a thousand evacuation events. Future observation would tell if such is the case.

It is to be noted that the mass of the condensation as estimated by Mirabel & Rodríguez (1999) is based on the presence of one electron per proton, i.e., no pair production is assumed. With a pair density, say, ten times larger, the estimated mass would be ten times less. However, at the same time, estimated mass of the disk would also be reduced by the same factor. Hence, the number of ejection events is not affected.

Acknowledgements. SKC and AN acknowledge receiving grants from DST project entitled Analytical and Numerical

Studies of Astrophysical Flows Around Compact Objects. The authors thank the referee for helpful comments.

References

- Balbus, S. A., & Hawley, J. F., 1991, *ApJ*, 376, 214
- Belloni, T., Mendez, M., King, A. R., van der Klis, M., & van Paradijs, J. 1997, *ApJ*, 479, L145
- Belloni, T., Klein-Wolt, M., Mendez, M., van der Klis, M., & van Paradijs, J. 2000, *A&A*, 355, 271
- Castro-Tirado, A. J., Brandt, S., & Lund, N. 1992, *IAU Circ.*, 5590
- Chakrabarti, S. K. 1990, *Theory of Transonic Astrophysical Flows* (World Scientific: Singapore)
- Chakrabarti, S. K. 1994, *Proc. of 17th Texas Symp.*, ed. H. Böhringer, E. Morfill, & J. Trümper (New York Academy of Sciences, New York), 546
- Chakrabarti, S. K. 1996a, *AJ*, 464, 664
- Chakrabarti, S. K. 1996b, *Phys. Rep.*, 266, 318
- Chakrabarti, S. K. 2000 *Class. Quant. Grav.*, 17, 2427
- Chakrabarti, S. K., & D'Silva, S. 1994, *ApJ*, 424, 138 (CD94)
- Chakrabarti, S. K., Titarchuk, L. G., Kazanas, D., & Ebisawa, K. 1996 *A&AS*, 120, 163
- Chakrabarti, S. K., Manickam, S., Nandi, A., & Rao, A. R. 2001 in *Proc. of the IXth Marcel Grossman meeting*, ed. R. Ruffini (World Scientific Press: Singapore), in press
- Chakrabarti, S. K., & Manickam, S. 2000, *ApJ*, 531, L41 (CM00)
- Chakrabarti, S. K., & Titarchuk, L. G. 1995, *ApJ*, 455, 623
- Dhawan, V., Mirabel, I. F., & Rodriguez, L. F. 2000, *ApJ*, 543, 373
- D'Silva, S., & Chakrabarti, S. K. 1994, *ApJ*, 424, 149
- Fender, R. P., Pooley, G., Brocksopp, C., & Newell, S. J. 1997, *MNRAS*, 290, L65
- Fender, R. P., Garrington, S. T., McKay, D. J., et al. 1999, *MNRAS*, 304, 865
- Feroci, M., Matt, G., Pooley, G., et al. 1999, *A&A*, 351, 985
- Goldstein, S. 1938, in *Modern Developments in Fluid Mechanics* (Oxford: Clarendon Press)
- Foglizzo, T., & Tagger, M. 1995, *A&A*, 301, 293
- Hawley, J. F., Gammie, C. F., & Balbus, S. A. 1995, *ApJ*, 440, 742
- Mirabel, I. F., & Rodriguez, L. F. 1994, *Nature*, 371, 46
- Mirabel, I. F., & Rodriguez, L. F. 1999, *ARA&A*, 37, 409
- Mirabel, I. F., Dhawan, V., Chaty, S., et al. 1998, *A&A*, 330, L9
- Molteni, D., Sponholz, H., & Chakrabarti, S. K. 1996, *ApJ*, 457, 805
- Morgan, E. H., Remillard, R. A., & Greiner, J. 1997, *ApJ*, 482, 993
- Muno, M. P., Morgan, E. H., & Remillard, R. A. 1999, *ApJ*, 527, 321
- Naik, S., Agrawal, P. C., Rao, A. R., Paul, B., et al. 2001, *ApJ*, 546, 1075
- Naik, S., & Rao, A. R. 2000, *A&A*, 362, 691
- Paczynski, B., & Wiita, P. J. 1980, *A&A*, 88, 23
- Parker, E. N. 1979, *Cosmical Magnetic Fields* (Clarendon press, Oxford)
- Pooley, G. G., & Fender, R. P. 1997, *MNRAS*, 292, 925
- Rao, A. R., Naik, S., Vadawale, S. V., & Chakrabarti, S. K. 2000, *A&A*, 360, L25
- Ryu, D., Chakrabarti, S. K., & Molteni, D. 1997, *ApJ*, 474, 378
- Shakura, N. I., & Sunyaev, R. A. 1973, *A&A*, 24, 337
- Shimura, T., & Takahara, F. 1995, *ApJ*, 445, 780
- Smith, D. M., Heindl, W. A., & Swank, J. H. 2001a, *ApJ*, submitted
- Smith, D. M., Heindl, W. A., Markwardt, C. B., & Swank, J. H. 2001b, *ApJ*, 554, 41
- Vadawale, S. V., Rao, A. R., Nandi, A., & Chakrabarti, S. K. 2001, *A&A*, 370, L17
- Yadav, J. S., Rao, A. R., Agrawal, P. C., et al. 1999, *ApJ*, 517, 935

ON THE EJECTION MECHANISM OF BULLETS IN SS 433

SANDIP K. CHAKRABARTI,^{1,2} P. GOLDONI,³ PAUL J. WIITA,⁴ A. NANDI,¹ AND S. DAS¹

Received 2002 July 4; accepted 2002 July 24; published 2002 August 2

ABSTRACT

We discuss plausible mechanisms to produce bulletlike ejecta from the precessing disk in the SS 433 system. We show that nonsteady shocks in the sub-Keplerian accretion flow can provide the basic timescale of the ejection interval while the magnetic rubber-band effect of the toroidal flux tubes in this disk can yield flaring events.

Subject headings: accretion, accretion disks — hydrodynamics — instabilities — shock waves — stars: individual (SS 433) — stars: mass loss

1. INTRODUCTION

SS 433 remains one of the most enigmatic objects in the sky. Even 25 years after its first appearance in the catalog of Stephanson & Sanduleak (1977), it is not clear whether the compact object is a black hole or a neutron star. However, there is ample evidence that the companion is an OB-type star with an orbital period of 13.1 days, which is losing mass at the rate of about $10^{-4} M_{\odot} \text{ yr}^{-1}$ (van den Heuvel 1981), corresponding to extremely super-Eddington accretion regardless of the mass of the compact object.

One of the most curious properties of the jets of SS 433, which first made their presence distinctly felt through the emission of variable H α lines, is that they are apparently ejected as bullets (e.g., Borisov & Fabrika 1987; Vermeulen et al. 1993; Paragi et al. 1999, 2002; Gies et al. 2002), with a surprisingly nearly constant radial velocity of about $0.26c$. The absence of a significant intrinsic rotational velocity (i.e., v_{rot}) component is clear from the fact that the kinematic model (e.g., Abell & Margon 1979), which assumes only radial injection, quite accurately explains the time variation of the red- and blueshifts of the H α emission from the jets with a period of 162 days, which is attributed to the precession of the accretion disk about the compact object. The radial velocity is less than the maximum allowed sound speed of $c/\sqrt{3}$, and thus hydrodynamic acceleration could, in principle, explain it. Therefore one may not require a magnetic or electrodynamic acceleration process (e.g., Belcher & MacGregor 1976; Lovelace 1976). However, the rather good collimation (Margon 1984; Paragi et al. 1999) supports the hypothesis that a substantial degree of confinement produced by toroidal flux tubes may be present. Gies et al. (2002) showed that the ratios of the H α emission equivalent widths from the approaching and receding jets as a function of precessional phase could be fitted nicely only if these emission components are bulletlike. Indeed, the recent *Chandra X-Ray Observatory* discovery of X-rays at a distance of about 10^{17} cm from the center may result from the collision of such bullets (S. Migliari, R. P. Fender, & M. R. Mendez 2002, in preparation).

SS 433 poses another interesting problem: it was pointed

out by Chakrabarti (1999) and Das & Chakrabarti (1999) that significant outflows are produced only when the accretion rate is such that the X-ray source is in a low/hard state, and all the observational indications in other microquasars also suggest that the jets are indeed produced in low/hard states (Corbel et al. 2001; Klein-Wolt et al. 2001). However, it is difficult to imagine how SS 433 manages to remain in the low/hard state with $10^{-4} M_{\odot} \text{ yr}^{-1}$ of wind matter ejected from its companion. The answer to this quandary probably lies in the recent results of Paragi et al. (1999) and Blundell et al. (2000), whose high-resolution radio maps show that there is a large region of roughly 50 AU in radius that is filled with enough gas and dust to obscure the accretion disk and the base of the jets. They also found an equatorial outflow. Gies et al. (2002) present additional evidence from observations of the “stationary” H α and He I lines for an extended “disk wind.” So it is distinctly possible that most of the matter from the donor is rejected either by centrifugal force (Chakrabarti 2002) or by radiation force far outside the central accretion disk, and thus the compact object receives only a few times the Eddington rate (\dot{M}_{Edd}) of its companion’s wind matter to accrete. This consideration finds further support from the fact that the kinematic luminosity of the jet itself is around 10^{39} ergs s^{-1} (Margon 1984), which corresponds to about 1 Eddington rate for a $10 M_{\odot}$ compact object.

In numerical simulations of supercritical winds by Eggum, Coroniti, & Katz (1985) designed to model SS 433, it was shown that only a fraction of a percent of the infalling matter is ejected from a radiation pressure–supported Keplerian disk, which indicates that the accretion rate must be at least $100\dot{M}_{\text{Edd}}$ if the accretion takes place through a Keplerian disk. On the other hand, numerical simulations of a sub-Keplerian disk by Molteni, Lanzafame, & Chakrabarti (1994) suggest that about 15%–20% of matter is ejected as an outflow, indicating that the accretion rate onto the compact object in SS 433 need be at most a few \dot{M}_{Edd} . Similar simulations with different parameters yield situations where no steady shocks can form, even though two saddle-type sonic points are present (Ryu, Chakrabarti, & Molteni 1997, hereafter RCM); under these conditions, large-scale shock oscillations produce intermittent outflows instead of continuous outflows. Since the compact object is a wind accretor, a low angular momentum, sub-Keplerian flow is the most likely description of the accretion flow. Indeed, the presence of sub-Keplerian flows in several other high-mass X-ray binaries has now been verified (Smith, Heindl, & Swank 2002).

In this Letter, we present a few scenarios leading to ejection of matter as bullets in SS 433. We discuss four possible ways

¹ S. N. Bose National Center for Basic Sciences, JD-Block, Salt Lake, Kolkata 700098, India; chakraba@bose.res.in, anuj@boson.bose.res.in, sbdas@bose.res.in.

² Also at Centre for Space Physics, P-61 Southend Gardens, Kolkata 700084, India.

³ Service d’Astrophysique, CEA/Saclay, 91191 Gif-sur-Yvette Cedex, France; paolo@discovery.saclay.cea.fr.

⁴ Department of Physics and Astronomy, Georgia State University, Atlanta, GA 30302; wiita@chem.gsu.edu

to create blobs of matter emerging from the disk and conclude that periodic ejection of the blobs by the large-scale oscillation of an accretion shock (something like a piston) may be the fundamental production mechanism of the “normal” bullets. The irregularly observed rapid flaring (Vermeulen et al. 1993) could be understood in terms of the catastrophic collapse of toroidal magnetic flux tubes, very similar to what has been argued to be occurring in GRS 1915+105 (Vadawale et al. 2001; Nandi et al. 2001). In the next section, we discuss these processes and their suitability or unsuitability for SS 433. In § 3, we present concluding remarks.

2. MECHANISMS TO PRODUCE BULLET-LIKE EJECTA FROM ACCRETION FLOWS

In both the works of Eggum et al. (1985) and Molteni et al. (1994), continuous ejection was reported when a radiation pressure-dominated Keplerian disk, or a sub-Keplerian disk capable of producing a steady shock, was considered. However, in SS 433 the basic ejection is bulletlike, and since the size of the X-ray-emitting region is smaller than $l_x \sim 10^{12}$ cm within which the material in the jets is already accelerated to $v_{\text{jet}} \sim 0.26c$ (Watson et al. 1986; Stewart et al. 1987), the bullets are not expected to be delayed by more than $l_x/v_{\text{jet}} \sim 100$ s. Indeed, recent *Rossi X-Ray Timing Experiment (RXTE)* observations of hard X-rays from SS 433 indicated variability on timescales of 50–1000 s (Safi-Harb & Kotani 2002), roughly corroborating this picture. In fact, a simultaneous measurement of a flare at 2 GHz in the radio (Kotani & Trushkin 2001) and in hard X-rays (Safi-Harb & Kotani 2002) indicated a strong anticorrelation of radio and X-ray fluxes, similar to what is observed in GRS 1915+105 (Mirabel & Rodriguez 1994). Moreover, the X-ray luminosity is very low ($\sim 10^{36}$ ergs s^{-1}) and is believed to come from the base of the jets (Watson et al. 1986). It is believed to have a thermal origin, and *EXOSAT* (Watson et al. 1986) and *Ginga* (Yuan et al. 1995) observations were adequately fitted with a thermal bremsstrahlung model with $kT \geq 30$ keV. The overall spectral shape suggests that the source has always been in a standard low/hard state, and so far no quasi-thermal emission expected from a “Keplerian disk” has been detected. From the interaction of the jet with the supernovae remnant W50, the lower limit of kinematic luminosity is found to be at least 10^{39} ergs s^{-1} (Biretta et al. 1983; Davidson & McCray 1980). This means that the mean mass outflow rate is around 10^{18} g s^{-1} , and if most of it is in the form of bullets ejected at 50–1000 s intervals, the mass accumulated in each bullet should be in the range of 10^{19} – 10^{21} g.

The above data imply that the essential features that one must explain when attempting to produce bullets out of the accretion disks are (a) the disk should be a sub-Keplerian flow, (b) the object (black hole or a neutron star) and its surroundings should be in a low/hard state, (c) bullets should be ejected in 50–1000 s timescales under normal circumstances, (d) the mass of each bullet should be around 10^{19} – 10^{21} g, and, finally, (e) there should be occasional flaring with an anticorrelation of radio and X-ray emission. We now discuss several scenarios and present what we believe to be the most probable picture of what is going on in SS 433. The four processes are schematically shown in Figures 1a–1d.

2.1. Cooling of the Jet Base by Comptonization and Separation of Blobs

It was shown by several numerical simulations that significant outflows are produced from regions very close to the

pressure-dominated region (Molteni et al. 1994, 2001). These jets are launched subsonically but quickly pass through the inner sonic point to become supersonic. In the subsonic region while the matter moves slowly, the density is high and the optical depth could be large enough ($\tau > 1$) to undergo Compton cooling (Fig. 1a) *provided there is a Keplerian disk underneath to supply soft photons*. A part of the outflow, which was subsonic previously, becomes supersonic because of this rapid cooling and separates from the base of the jet. This separation of blobs is expected to occur at the sonic surface r_s which is $\sim (2-3)r_c$, where r_c is the size of the centrifugal barrier (see Chakrabarti 1999)

This possibility, though attractive, and in fact likely to be a major mechanism for rapid state change in objects like GRS 1915+105 (Chakrabarti & Manickam 2000), is untenable in SS 433 because the latter is a wind accretor: thus no significant Keplerian disk is expected in this system to supply the soft photons, and indeed none has been detected so far (Watson et al. 1986; Yuan et al. 1995).

2.2. Resonance Oscillation of Accretion Shocks in the Presence of Bremsstrahlung Cooling

Numerical simulations of accretion flow show that in cases where the cooling timescale nearly matches the infall timescale, a shock forms, but it then starts oscillating and ejects matter quasi-periodically (Langer, Chanmugam, & Shaviv 1983; Molteni, Sponholz, & Chakrabarti 1996, hereafter MSC; see Fig. 1b). In order to have an oscillation period of around 50 s, the shock must be located at the large distance of $r_{s,\text{MSC}} \approx 6400r_g$ for a black hole of mass $M = 10 M_\odot$, where $r_g = 2GM/c^2$. The mass of the postshock region is computed by equating the bremsstrahlung (which we assume to be the major cooling mechanism) cooling time and the infall time in the postshock region (MSC):

$$T_{\text{MSC}} = \frac{\mathcal{E}}{\dot{E}} = \frac{r_{s,\text{MSC}}}{v_f} \approx \left(\frac{Rr_{s,\text{MSC}}}{r_g} \right)^{3/2} \frac{r_g}{c}, \quad (1)$$

where \mathcal{E} is the specific thermal energy, v_f is the infall velocity, and $R = (\gamma + 1)/(\gamma - 1) \approx 4-7$ (these limits are for a strong shock with $\gamma = 5/3$ and $\gamma = 4/3$, respectively) is the compression ratio at the shock. Assuming the gas density (n) and temperature (T) scale as $n \sim r^{-3/2}$ and $T \sim r^{-1}$, respectively, the mass of the sub-Keplerian region of $r < r_s$ turns out to be 7×10^{19} g (with $M = 10 M_\odot$, $\gamma = 5/3$). This is indeed of the same order as the mass of the bullets observed in SS 433. However, one has to have both the angular momentum and energy of the injected material comparable to the marginally bound values determined by the central object in order to achieve such an oscillation. On the other hand, if the mass expulsion from the system takes place at the similar radius of $r_{\text{ex}} \sim 10^4 r_g = 2 \times 10^9 M/M_\odot$ cm due to the centrifugal force, the specific angular momentum of the flow is approximately $[r_{\text{ex}}/(2r_g)]^{1/2} r_g c \sim 70 r_g c$, which is very large compared to the marginally bound value of $2r_g c$. So it is unlikely that this mechanism works in SS 433.

2.3. Nonsteady and Nonlinear Shock Oscillation

A standing shock can form in a sub-Keplerian flow only if there are two saddle-type sonic points and the Rankine-Hugoniot relation is satisfied at least at one point in between these two sonic points. However, Chakrabarti (1999) showed that there

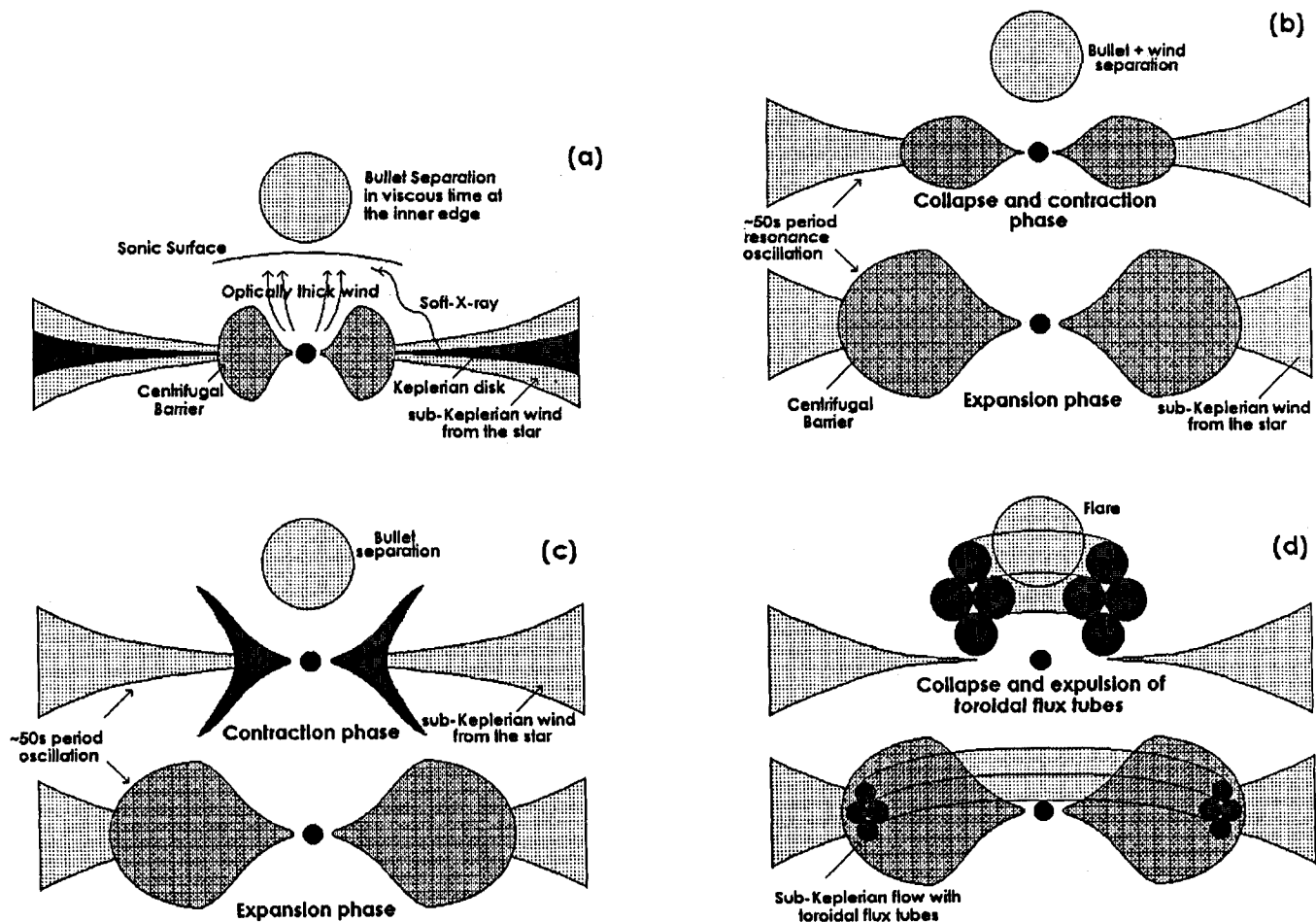


FIG. 1.—Four scenarios of bullet separation in SS 433 are schematically shown. (a) The base of the jet is cooled down by soft photons from a Keplerian disk and detaches when it becomes supersonic. (b) Resonance oscillation of the sub-Keplerian region due to the near matching of the infall time with the cooling time produces discrete ejecta during the phase when the centrifugal barrier contracts. (c) Nonsteady motion of the centrifugal barrier due to the inability of the flow to find a steady shock solution. (d) Magnetic tension from toroidal flux tubes (shown as shaded narrow tori) causes them to collapse catastrophically in a hot ambient medium in rapid succession, which evacuates the centrifugal barrier. The recurrence time of (a) is the viscous timescale in the inner part of the disk, ~ 10 s; (b–c) is ~ 50 s; and (d) is random and dictated by the enhanced magnetic activity.

saddle-type sonic points but the shock conditions are not satisfied. Even an initially supersonic accretion (such as the wind from the companion) can fall into this category.

What will happen to such a realistic flow, especially when the specific entropy at the inner sonic point is greater than that at the outer sonic point? RCM discovered that a flow injected with these parameters exhibits yet another type of shock oscillation (Fig. 1c). Here the shock searches for a stable location and oscillates without finding it. In the first half of the cycle, the shock recedes far away, the postshock region fills up, but the accretion is essentially completely blocked. In the second half of the cycle, the shock pushes the matter into the black hole, thereby evacuating the postshock region. In a realistic simulation, RCM find that while the ratio of actually accreted matter to the amount available from the companion, $R_{\text{al}} \equiv \dot{M}_{\text{acc}}/\dot{M}_{\text{inj}}$, would be around 0.2 during the first half-cycle, $R_{\text{al}} \sim 1.3$ in the second half-cycle. The outflow was also found to be very large. The timescale of oscillation was found to be $T_{\text{RCM}} \sim (4000\text{--}6000)r_g/c$ for a $r_s \approx 20r_g$ whose infall time is only about $T_{\text{MSC}} = (Rr_s/r_g)^{3/2}(r_g/c) \sim (350\text{--}400)r_g/c$. Thus, this type of oscillation takes about a factor of $R_T = T_{\text{RCM}}/T_{\text{MSC}} \sim 15$ times longer than the resonance oscillation discussed in § 2.2. For a 50 s oscillation, the location of the shock should

which gives $r_{\text{RCM}} \sim 450r_g$ for a $10 M_{\odot}$ black hole, a more physically reasonable value. Even though the size of the oscillating region goes down by a factor of 10 or so, compared with that involved in the resonance oscillation, the ejected mass need not go down (even for the same accretion rate as in the earlier case). This is because nearly all of the accretion flow is accumulated in half the cycle (~ 25 s in this case) before being ejected (see Fig. 2 of RCM).

Another advantage of this type of nonsteady shock oscillation is that it is driven by centrifugal force and not by thermal cooling. Hence the result is generally independent of the accretion rate. Thus, as long as the viscosity remains low, equivalent to having the Shakura-Sunyaev (1973) parameter $\alpha \leq \alpha_c \approx 0.015$ (Chakrabarti 1990), and \dot{M}_{inj} remains fairly constant, this oscillation, once established, could be sustained indefinitely.

2.4. Magnetic Rubber-Band Effect

In the event of increase in magnetic activity of the disk, as could happen for instance when the accretion disk bends toward the binary companion during its precessional motion, it is not unlikely that a strong magnetic field will be first intercepted

case the field will preferentially become toroidal due to shear in the rotating flow. Then, as has already been pointed out (Chakrabarti & D'Silva 1994; Nandi et al. 2001), the acceleration due to magnetic tension,

$$a_{\tau} = -\frac{B_{\phi}^2}{4\pi r(\rho_e + \rho_i)} \sim -\frac{B_{\phi}^2}{4\pi r\rho_e}, \quad (2)$$

would be the dominant force in the postshock region of the sub-Keplerian flow (Fig. 1d). Here r is the major radius of the toroidal flux tube and ρ_i and ρ_e are the densities of the medium internal and external to the flux tube, respectively. The last step in equation (2) is written because $\rho_i \ll \rho_e$ for a strong flux tube. Since $B_{\phi} \propto 1/r$ and $\rho_e \propto r^{-3/2}$, we get

$$a_{\tau} \propto r^{-3/2}, \quad (3)$$

thus increasing rapidly as the tube comes closer to the black hole, and even surpassing the magnetic buoyancy,

$$a_{\text{MB}} = \frac{1-X}{1+X} \left(\frac{\lambda_{\text{Kep}}^2 - \lambda^2}{r^3} \right) \approx \frac{\lambda_{\text{Kep}}^2 - \lambda^2}{r^3}, \quad (4)$$

where $X = \rho_i/\rho_e \rightarrow 0$ and λ_{Kep} and λ are, respectively, the specific angular momenta of a Keplerian disk and the disk under consideration. The accelerations in equations (3) and (4) do cross over, since at a location very close to a black hole, $\lambda \rightarrow \lambda_{\text{Kep}}$ for a sub-Keplerian flow.

The effect of magnetic tension is dramatic, and the inner part of the disk is evacuated in the Alfvén timescale: $r/v_{\lambda} \sim (r/a_{\tau})^{1/2} \lesssim 0.1$ s, for a $10 M_{\odot}$ black hole with a realistic Alfvén speed, $v_{\lambda} \approx 0.1c$ (Nandi et al. 2001). The enhanced plasma ejection along the axis presumably causes sporadic magnetic flare events that would be observable as radio outbursts, at the same time reducing the X-ray emission from the disk that forms the base of the jet. Recently, such effects may have been seen

(Safi-Harb & Kotani 2002) where simultaneous observations of 2 GHz radio and 2–20 keV X-ray fluxes from SS 433 have been made, and a clear dip in X-ray flux is seen at the same time a strong radio flare is observed. It is worth noting that similar anticorrelated variations are common during flares in GRS 1915+105 (Feroci et al. 1999; Naik et al. 2001), and we suggest that the flares in SS 433 originate in the same way.

3. CONCLUDING REMARKS

In this Letter, we have studied various competing processes for the creation of bullets which move ballistically in the jet of SS 433. We showed that blobs may be separated by (1) Comptonization, (2) shock oscillations due to resonance, (3) oscillations due to inherent unsteady accretion solutions, and (4) intense magnetic tension of the toroidal flux tubes. We reject the first possibility because it requires a large Keplerian disk, which is unlikely. We are unable to distinguish at this stage which type of shock oscillation is more capable of producing bullet formation in SS 433, but we prefer the third possibility owing to its impulsive and generic nature and smaller involved region. We believe that the fourth possibility of the inner disk evacuation should produce flaring events but will occur rather rarely, perhaps only once in a single precession period, when the magnetic field of the companion is preferentially tilted toward the accretion disk during precessional motion. This fourth mechanism gives rise to an anticorrelation between radio and X-rays, perhaps already observed in SS 433 (Safi-Harb & Kotani 2002).

S. K. C., A. N., and S. D. acknowledge a grant from the Department of Science and Technology, India, and financial support from CEA/Saclay, where part of this work was performed. P. J. W. is grateful for hospitality at the Department of Astrophysical Sciences, Princeton University, and for support from the Research Program Enhancement program at Georgia State University.

REFERENCES

- Abell, G. O., & Margon, B. 1979, *Nature*, 279, 701
 Belcher, J. W., & MacGregor, K. B. 1976, *ApJ*, 210, 498
 Biretta, J. A., Cohen, M. H., Unwin, S. C., & Pauliny-Toth, I. I. K., 1983, *Nature*, 306, 42
 Blundell, K. M., Mioduszewski, A. J., Muxlow, T. W. B., Podsiadlowski, P., & Rupen, M. P. 2001, *ApJ*, 562, L79
 Borisov, N. V., & Fabrika, S. N. 1987, *Soviet Astron. Lett.*, 13, 200
 Chakrabarti, S. K. 1990, *Theory of Transonic Astrophysical Flows* (Singapore: World Scientific)
 ———. 1999, *A&A*, 351, 185
 ———. 2002, in *IAU Colloq. 187, Exotic Stars as Challenges to Evolution*, ed. W. Vanhamme & C. Tout, in press
 Chakrabarti, S. K., & D'Silva, S. 1994, *ApJ*, 424, 138
 Chakrabarti, S. K., & Manickam, S. G. 2000, *ApJ*, 531, L41
 Corbel, S. et al. 2001, *ApJ*, 554, 43
 Das, T., & Chakrabarti, S. K. 1999, *Classical Quantum Gravity*, 16, 3879
 Davidson, K., & McCray, R. 1980, *ApJ*, 241, 1082
 Eggum, G. E., Coroniti, F. V., & Katz, J. I. 1985, *ApJ*, 298, L41
 Feroci, M., Matt, G., Pooley, G., Costa, E., Tavani, M., & Belloni, T. 1999, *A&A*, 351, 985
 Gies, D. R., McSwain, M. V., Riddle, R. L., Wang, Z., Wiita, P. J., & Wingert, D. W. 2002, *ApJ*, 566, 1069
 Klein-Wolt, M., Fender, R. P., Pooley, G. G., Belloni, T., Migliari, S., Morgan, E. H., & van der Klis, M. 2001, *Ap&SS Suppl.*, 276, 291
 Kotani, T., & Trushkin, S. 2001, *IAU Circ.* 7747
 Langer, S. H., Chanmugam, G., & Shaviv, G. 1982, *ApJ*, 258, 289
 Lovelace, R. V. E. 1976, *Nature*, 262, 649
 Margon, B. 1984, *ARA&A*, 22, 507
 Mirabel, I. F., & Rodriguez, L. F. 1994, *Nature*, 371, 46
 Molteni, D., Acharya, K., Kuznetsov, O., Bisikalo, D., & Chakrabarti, S. K. 2001, *ApJ*, 563, L57
 Molteni, D., Lanzafame, G., & Chakrabarti, S. K. 1994, *ApJ*, 425, 161
 Molteni, D., Sponholz, H., & Chakrabarti, S. K. 1996, *ApJ*, 457, 805 (MSC)
 Naik, S., Agrawal, P. C., Rao, A. R., Paul, B., Seetha, S., & Kasturirangan, K. 2001, *ApJ*, 546, 1075
 Nandi, A., Chakrabarti, S. K., Vadawale, S., & Rao, A. R. 2001, *A&A*, 380, 245
 Paragi, Z., Fejes, I., Vermeulen, R. C., Schilizzi, R. T., Spencer, R. E., & Stirling, A. M. 2002 in *Proc. 6th European VLBI Network Symposium*, ed. R. W. Porcas, A. P. Lobanov, & J. A. Zensus (Bonn: MPIfR), 263
 Paragi, Z., et al. 1999, *A&A*, 348, 910
 Ryu, D., Chakrabarti, S. K., & Molteni, D. 1997, *ApJ*, 474, 378 (RCM)
 Safi-Harb, S., & Kotani, T. 2002, in *Proc. 4th Microquasar Workshop*, ed. Ph. Dourouchaux, Y. Fuchs, & J. Rodriguez (Kolkata: CSP), in press
 Shakura, N. I., & Sunyaev, R. A. 1973, *A&A*, 24, 337
 Smith, D. M., Heindl, W. A., & Swank, J. H., 2002, *ApJ*, 569, 362
 Stephenson, C. B., & Sanduleak, N. 1977, *ApJS*, 33, 459
 Stewart, G. C., et al. 1987, *MNRAS*, 228, 293
 Vadawale, S. V., Rao, A. R., Nandi, A., & Chakrabarti, S. K. 2001, *A&A*, 370, L17
 van den Heuvel, E. P. J. 1981, *Vistas Astron.*, 25, 95
 Vermeulen, R. C., et al. 1993, *A&A*, 270, 189
 Watson, M. G., Stewart, G. C., Brinkmann, W., & King, A. R. 1986, *MNRAS*, 222, 261
 Yuan, W., Kawai, N., Brinkmann, W., & Matsuoka, M. 1995, *A&A*, 297, 451

SPECTRAL SIGNATURE OF MASS LOSS FROM (AND MASS GAIN BY) AN ACCRETION DISK AROUND A BLACK HOLE

SANDIP K. CHAKRABARTI,^{1,2} ANUJ NANDI,¹ S. G. MANICKAM,¹ S. MANDAL,² AND A. R. RAO³

Received 2002 July 26; accepted 2002 September 18; published 2002 September 27

ABSTRACT

Accretion and outflows are common in systems that include black holes. Assuming that outflows are primarily produced at the centrifugal pressure-supported boundary layer at the inner disk, the hard X-ray spectrum is softened in the presence of winds. Conversely, the spectrum would be hardened when mass gain takes place at the inner disk. We first demonstrate these changes in the spectrum from theoretical consideration. We then give examples of the spectra of a few black hole candidates that indicate that a significant mass loss or mass gain may be taking place in short timescales, causing changes in spectral slopes.

Subject headings: accretion, accretion disks — black hole physics — hydrodynamics —
ISM: jets and outflows — radiative transfer

1. INTRODUCTION

Chakrabarti & Titarchuk (1995, hereafter CT95) pointed out that in black hole accretion, both the Keplerian flow and the sub-Keplerian flow have very important roles to play. Recently, Smith, Heindl, & Swank (2002) have been able to verify that these two components are indeed present and in fact vary quite independently. The sub-Keplerian flow, which may arise out of wind accretion, can produce standing or oscillating shocks because of the centrifugal barrier, depending on its physical parameters. Chakrabarti (1999) computed the outflow rate in the presence of accretion shocks and showed that when shocks are absent or cooled down, the outflow rate is very low, and that when the shocks are of intermediate strength, the outflow rate is the highest. The variation of the outflow rate with spectral states has been observed (e.g., Dhawan, Mirabel, & Rodríguez 2000).

Recently, Chakrabarti & Manickam (2000, hereafter CM00) showed that when the accretion rate is high, the outflow up to the sonic point could be dense enough to cool down the base of the jet catastrophically, causing a quick-state transition. Is the change of the spectral slope due to wind activities detectable, and if so, has it been detected? In the present Letter, we answer these important questions. In the next section, we discuss how the spectral slope changes with mass loss or mass gain at the inner disk. Since the computation of the spectral slope is sensitive to the energy range of the fitted power law, a more robust measure of spectral variation is to compare the pivot point of the spectrum. In the presence of the softening of the hard state and/or the hardening of the soft state, the pivot energy will be shifted outward. In § 3, we show that the spectral hardening and softening can be observed. Finally, in § 4, we draw our conclusion. Our computation does not include magnetic effects.

2. THEORETICAL BACKGROUND

When matter enters into the horizon of a black hole, it is necessarily supersonic and thus sub-Keplerian; i.e., it must deviate from a Keplerian disk. The centrifugal barrier-dominated

boundary layer (CENBOL) of a black hole (CT95) is hot, and it is puffed up and intercepts soft photons from the pre-CENBOL Keplerian disk. Depending on whether the Keplerian disk rate or the sub-Keplerian halo accretion rate dominates, the emerging spectra may be softer or harder (CT95; Chakrabarti 1997). In “hard states,” soft photons are fewer and are unable to cool down the electrons in the CENBOL. In “soft states,” the supply of soft photons is profuse, and when the optical depth inside the CENBOL crosses unity ($\tau > 1$), the resulting spectrum is softened. The disk rate or the halo rate can vary locally and temporarily. For instance, when an outflow is formed from a centrifugal barrier, it reduces the number density of the electrons in the *post-shock* region, while the supply of soft photons in the preshock region remains the same. This will cause a “dynamic softening of state” (Chakrabarti 1998) very much like that found by Smith et al. (2002). Similarly, if the sonic sphere cools down and drops onto the inner disk, the density in the postshock region will go up, and the spectrum is expected to be hardened.

This CENBOL is also responsible for the outflows. Computation of the ratio of the outflow rate to the inflow rate as a function of the compression ratio R of matter showed that the presence or absence of outflows is directly related to the spectral states (Chakrabarti 1999). In a truly soft state, the shock is absent ($R \sim 1$), and no significant wind would be produced. In a hard state, the shock could be strong ($R \sim 5-7$). The outflow rate would be reduced, and a quasi-periodic oscillation (QPO) may exist because of the shock oscillation. For an intermediate shock (say, $R \sim 2.5-3$), the outflow rate is large, and the sonic surface in the outflow is close enough to be filled in quickly to create the burst-on/burst-off phenomenon and to form blobby jets. There is increasing evidence today (e.g., Junor, Biretta, & Livio 1999; Dhawan et al. 2000) that jets do emerge within tens to hundreds of Schwarzschild radii of a black hole for both quasars and microquasars.

Figures 1a and 1b give cartoon diagrams of the possible disk-wind connection. In the so-called burst-off states, outflows from the CENBOL fill in the sonic sphere gradually until it becomes optically thick (Fig. 1a). Most of the cooled-down matter falls back to the CENBOL and its vicinity, increasing the “local” accretion rate, which is subsequently drained out. This may correspond to the burst-on state (Fig. 1b). This picture receives support from the fact that in one of the most well-studied objects, GRS 1915+105, it has been observed that the burst-on duration (i.e., the duration of drainage) is comparable

¹ S. N. Bose National Centre for Basic Sciences, JD-Block, Salt Lake, Kolkata 700-098, India; chakraba@bose.res.in, anuj@bose.res.in, sivman@bose.res.in.

² Centre for Space Physics, P-61 Southend Gardens, Kolkata 700-084, India; space_phys@vsnl.com.

³ Tata Institute of Fundamental Research, Homi Bhabha Road, Colaba, Mumbai 400 005, India; arao@tifr.res.in

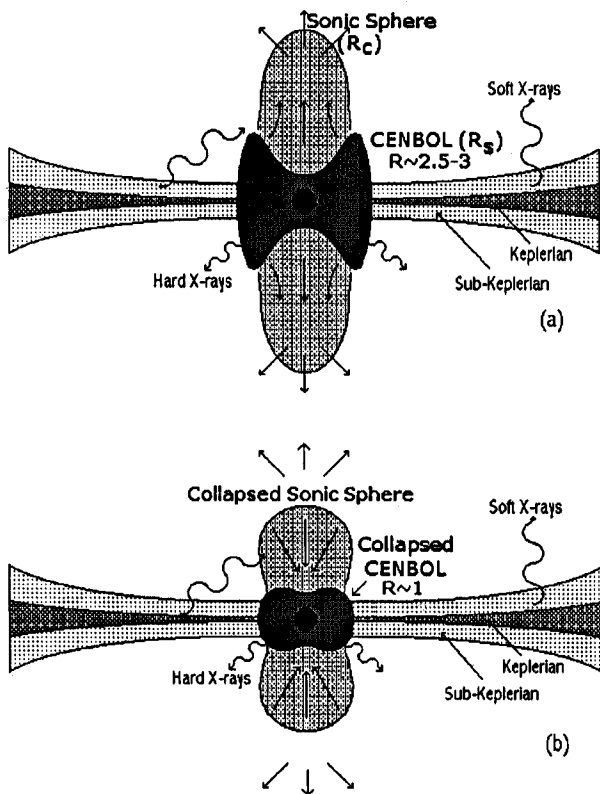


FIG. 1.—Cartoon diagrams of the accretion disk near a black hole that includes a boundary layer. Panel *a* shows the “burst-off” state where the outflow material fills up the region to the sonic point R_c . Panel *b* shows cases with prominent “burst-on” states where the material in the subsonic region cools and falls back on the CENBOL (see text) and takes time to drain.

to the duration of the *preceding burst-off* phase (i.e., the duration to fill in the sonic sphere; see Fig. 5 of Yadav et al. 1999) and not to the burst-off phase that immediately follows.

What could be the spectral signature of a CENBOL that is losing matter to hot winds or that is gaining matter from the cooler winds? The two-component advective flow model of CT95 and Chakrabarti (1997) has the answer. In Figure 2, we present two sets of calculated spectra. Disk accretion rates for the soft and the hard states are $0.1\dot{M}_{\text{Edd}}$ and $0.02\dot{M}_{\text{Edd}}$, respectively. The halo accretion rate is kept fixed at $0.2\dot{M}_{\text{Edd}}$, and the shock is located at $R_s = 6$ and $R_s = 40$, respectively, in high/soft and low/hard states (*dotted curves*). This is in line with the general conclusions that the inner edge moves during soft states. The solid curves are drawn to mimic the burst-off (mass-loss) and burst-on (mass-gain) state spectra. In these cases, the disk accretion rates are kept as before, but 20% of CENBOL matter is assumed to be lost in the wind in the burst-off state (Molteni, Lanzafame, & Chakrabarti 1994), and 10% (for illustration purpose) of matter in the outflow is assumed to be falling back on the halo in the burst-on state. Because of selective softening and hardening, the intersection (pivot) point is located at a higher energy.

3. OBSERVATIONAL SIGNATURES OF MASS LOSS/GAIN IN RXTE DATA

3.1. GRS 1915+105

The Rossi X-Ray Timing Explorer (RXTE) public archive

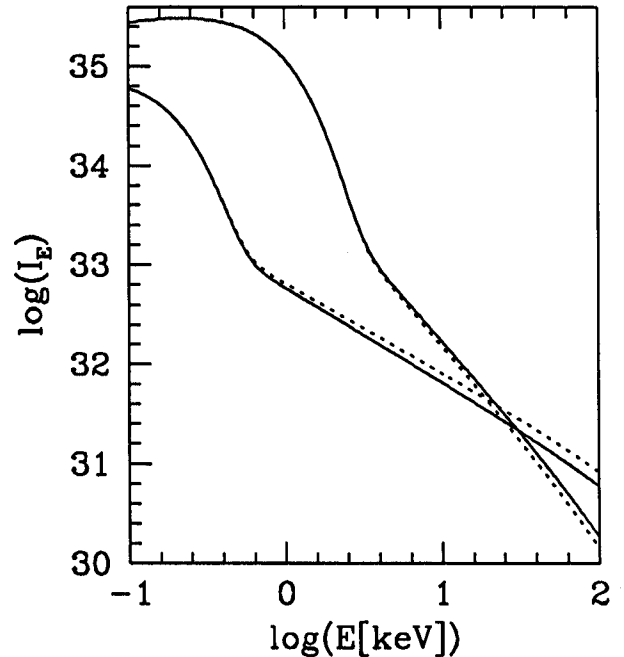


FIG. 2.—Typical nature of calculated spectra (uncorrected for absorption) for burst-off and burst-on states (*solid curves*) and low and high states (*dotted curves*). In the burst-off state, the spectrum appears to be softened with respect to low state, and in the burst-on state, the spectrum appears to be hardened with respect to the high state. As a result, the pivoting point shifts toward higher energy.

ing the RXTE Proportional Counter Array (PCA; see Jahoda et al. 1996 for a description of the PCA). The source was in a low state from 1996 December up to 1997 April. The spectral and temporal behavior during the low state was stable, characterized by a hard spectrum (with a power-law photon index of ~ 2 and the total flux in the power-law component being $\sim 80\%$) and 1–10 Hz QPOs (Trudolyubov, Churazov, & Gilfanov 1999; Munro, Morgan, & Remillard 1999). Since the source was in a similar state on several occasions (1996 July–August, 1997 October, and 1998 September–October), we treat this state as the low state of GRS 1915+105. The source reached a high state in 1997 August. We have selected one observation each from the low state (1997 March 26 with an identification [ID] number of 20402-01-21-00; Munro et al. 1999 and Trudolyubov et al. 1999) and the high state (1997 August 19 with a ID number of 20402-01-41-00; Munro et al. 1999) to quantify the spectral parameters. Spectra of these two states are shown in Figures 3*a*–3*c* and are marked.

During the transition between these two states, the source exhibited several types of bursting behavior. CM00 explained the burst-off/burst-on transitions in terms of the repeated filling of the sonic sphere of the outflow and its abrupt cooling due to inverse Comptonization. We present the spectral properties of the source during the irregular bursts (Yadav et al. 1999) observed on 1997 June 18 (ID 20402-01-33-00) in Figure 3*a*, on 1997 July 10 (ID 20402-01-36-00) in Figure 3*b*, and on 1997 July 12 (ID 20402-01-37-01) in Figure 3*c*.

We have used the standard procedures for data selection, background estimation, and response-matrix generation. The energy spectrum was fitted using the disk-blackbody and power-law model with absorption by intervening cold material parameterized as an equivalent hydrogen column density N_H kept fixed at $6 \times 10^{22} \text{ cm}^{-2}$. We have included a Gaussian line

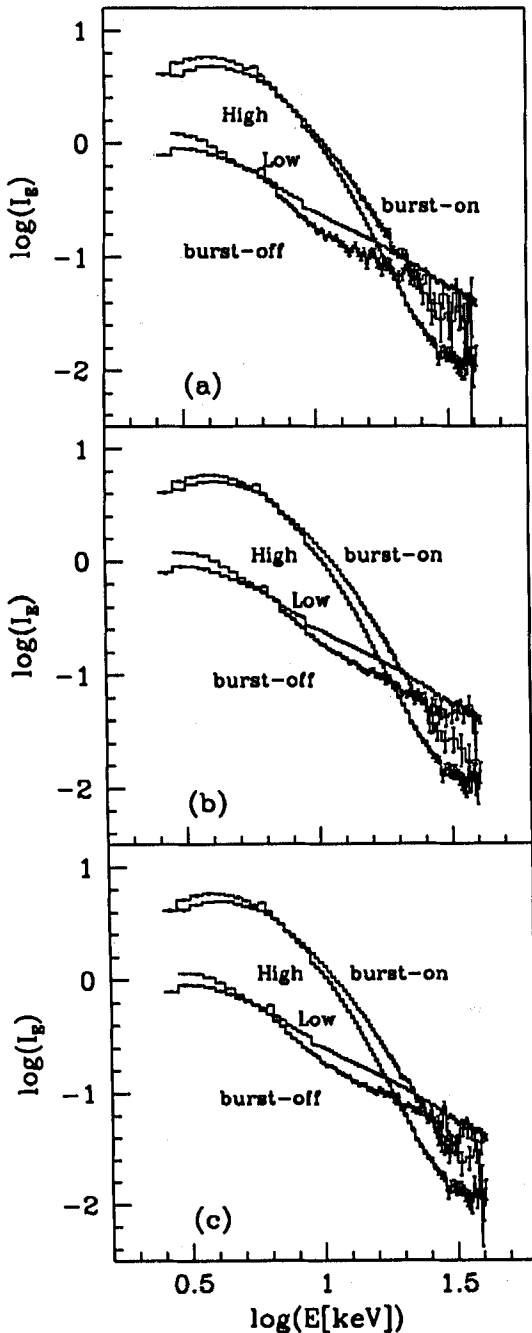


FIG. 3.—Unfolded *RXTE*-PCA spectra of GRS 1915+105 obtained during the low and high states compared with burst-on and burst-off spectra during the irregular bursts observed on (a) 1997 June 18, (b) 1997 July 10, and (c) 1997 July 12. The histogram shows the fitted model. During the burst-off/burst-on transition, the pivoting occurs at a higher energy.

due to iron. Systematic errors of 1%–2% have been added to the data. XSPEC version 10.0 has been used to fit the spectra.⁴

The resultant unfolded spectra for the two spectral states presented in Figures 3a–3c show that in the low state, the disk-blackbody component has a lower temperature ($kT_{in} = 0.60 \pm 0.05$ keV) and a larger inner-disk radius ($R_{in} = 115 \pm 2$ km) compared with the high state, which has an inner-disk temperature of 1.95 ± 0.01 keV and an inner-disk radius of 26 ± 1 km. The inner-disk parameters are calculated using a distance to the source of 10 kpc and an inclination to the disk

of 70° . The power-law index in the low state (2.40 ± 0.01) is much flatter than that seen in the high state (3.61 ± 0.02). The quoted errors are for nominal 90% confidence levels obtained by the condition of $\chi^2_{min} + 2.7$. The disk-blackbody component has a 3–26 keV flux of less than 10% of the total flux in the low state, which increase to greater than 65%. The two spectra intersect at around 17 keV. Since the PCA generally shows a steeper spectrum because of uncertainties in the response matrix, the results presented here highlight the broad changes in the spectral states.

The corresponding unfolded spectra during the irregular burst of 1997 June 18 presented in Figure 3a show that the burst-off state has spectral parameters similar to that of the low state ($kT_{in} = 0.76$ keV, index = 2.76) and that the burst-on state spectrum resembles that of the high state ($kT_{in} = 2.2$ keV, index = 3.1). It is clear that the spectrum of the burst-off state is softer than that of the low state and that the spectrum of the burst-on state is harder than that of the high/soft state. As a result, the energy at which the two spectra pivot is much higher (~ 26 keV). The same behavior is also seen in Figures 3b and 3c, where the IDs used were 20402-01-36-00 and 20402-01-37-01. The low and high states have been kept as above. The intersection in all these cases during the burst-on/burst-off transition is around 25 keV, far above the low/high intersection.

Recently, Dhawan et al. (2000) pointed out a direct correlation between the All-Sky Monitor X-ray data from *RXTE* and IR/radio observations. The radio activity at around 500 AU made on 1997 October 31 would be perturbed by the CENBOL activity of around 1997 October 28.5 if perturbation propagates with 0.98c. Unfortunately, no PCA data are available for October 28 or 29. Figure 4 shows the spectral properties on 1997 October 30 (ID 20402-01-52-02). To compare with the high/low spectrum, we chose the low-state observation closest to this day, namely, 1997 October 25 (ID 20402-01-52-00), and we chose the same high state as mentioned above. The spectral slopes of the high, low, on, and off states are 3.61 ± 0.02 , 2.76 ± 0.018 , 3.34 ± 0.021 , and 2.85 ± 0.013 , respectively. This again shows the softening of the hard state and the hardening of the soft state. The intersection of the spectra of low and high states is at around 14 keV, whereas the intersection of the burst-on and burst-off states is at around 17 keV. Thus, the effect of winds could be significant here as well.

3.2. GRO 1655–40

GRO 1655–40 does not exhibit the burst-off/burst-on transition as does GRS 1915+105, but a state transition has been observed (Sobczak et al. 1999; Remillard et al. 1999). The count rate has a systematic drop that signifies that there is a steady decrease in the accretion rate. A method similar to that presented above was used to analyze the data. A Gaussian emission line is included as before in the spectral fitting since there is an excess in 6.0–7.0 keV. The hydrogen column density was fixed at 0.89×10^{22} cm⁻² (Zhang et al. 1997). We use (1) 20402-02-02-00 (1997 March 5), (2) 20402-02-24-00 (1997 August 3), (3) 20402-02-25-00 (1997 August 14), and (4) 20402-02-26-00 (1997 August 18) to represent the high/soft state, the intermediate soft state just before state transition (very similar to the mass-gain/burst-on state), the intermediate hard state (similar to the mass-loss/burst-off state), and a true hard state, respectively. From theoretical consideration (Fig. 2), one should expect case 2 to have harder spectra compared with case 1, and case 3 to have a softer spectra compared with case 4. Figure 5a compares the spectra of cases 1 and 2 and Fig.

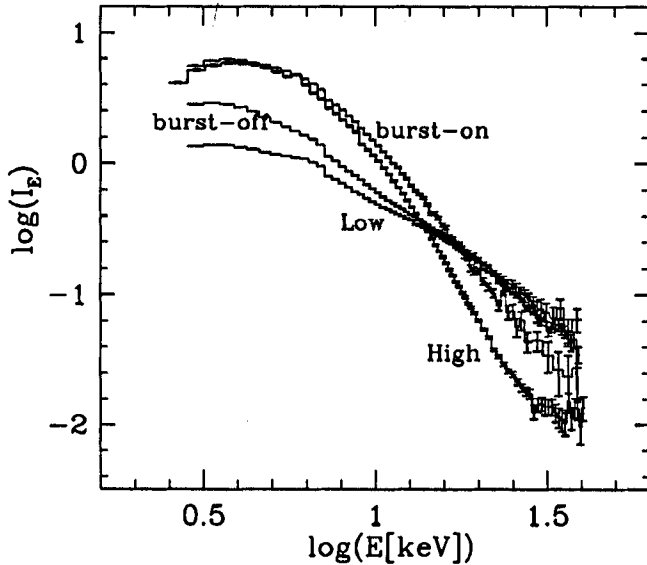


FIG. 4.—Same as in Fig. 3, except that the observation ID of the burst-on/burst-off and low states are chosen close to 1997 October 31 when IR/radio flares were observed (Dhawan et al. 2000). The spectral slope variations are seen on this day also.

indices (α) are written within parentheses. Note that the soft state is hardened (Fig. 5a) and that the hard state is softened (Fig. 5b). We purposely did not superpose these two plots since the net accretion rate steadily decreases. There is no evidence of a QPO in both soft states (Fig. 5a), while the QPO is strong in case 3 at 1.4 and 6.4 Hz, and the QPO is weak in case 4 at 0.2 and 0.8 Hz. The QPO disappears completely in the hard state after this date. If the oscillation of shocks corresponds to QPOs (Molteni, Sponholz, & Chakrabarti 1996; CM00) and if shocks also produce outflows (Chakrabarti 1999), then it is clear that a strong shock (and therefore outflow) is present in case 3, that there is a weak shock very far out (since $\nu_{\text{QPO}} \propto R_s^{3/2}$, where R_s is the shock location; see CM00) in case 4, and that the shock disappears for the time being after this date.

4. DISCUSSION AND CONCLUSIONS

A comparison of the two spectral states in Figures 3a–3c and in Figure 4 shows that in GRS 1915+105 during the bursting phase, the low-energy component (≤ 5 keV) remains essentially the same as found during the extended low and high states of the source. The major change is above ~ 10 keV where the hard component of the low state softens to form a burst-off state and where the soft component of the high state hardens

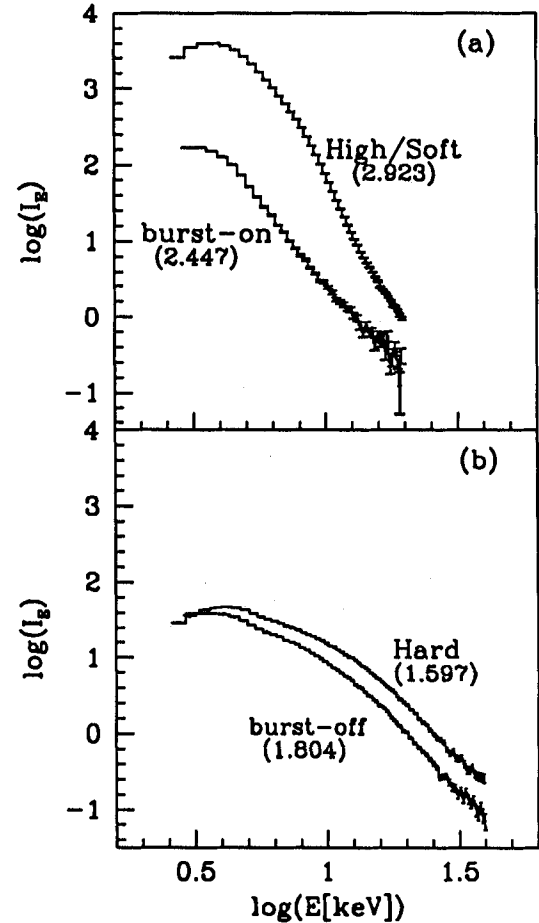


FIG. 5.—Same as in Fig. 3, except that the observations are for GRO 1655–40 before and after the soft/hard state transition. In panel a, The high/soft and burst-on states in panel a and the burst-off and hard states in panel b are compared. Spectral indices are marked in parentheses. Hardening of the soft state (a) and softening of the hard state (b) could be observed.

to form a burst-on state. The same conclusion is true in GRO 1655–40 also. Spectral variabilities in active galactic nuclei have recently been reported (Maraschi 2002; Papadakis et al. 2002), and these may also signify some mass-gain/loss activity at the inner edge of the disk.

S. K. C. and S. G. M. acknowledge the support of the Indian Space Research Organization for the RESPOND project. A. N. acknowledges DST project grant SP/S2/K-14/98 for funding his research at SBNBCBS.

REFERENCES

- Chakrabarti, S. K. 1997, *ApJ*, 484, 313
 ———. 1998, *Indian J. Phys.*, 72B(6), 565
 ———. 1999, *A&A*, 351, 185
 Chakrabarti, S. K., & Manickam, S. G. 2000, *ApJ*, 531, L41 (CM00)
 Chakrabarti, S. K., & Titarchuk, L. G. 1995, *ApJ*, 455, 623 (CT95)
 Dhawan, V., Mirabel, I. F., & Rodríguez, L. F. 2000, *ApJ*, 543, 373
 Jahoda, K., Swank, J. H., Giles, A. B., Stark, M. J., Strohmayer, T., Zhang, W., & Morgan, E. H. 1996, *Proc. SPIE*, 2808, 59
 Junor, W., Biretta, J. A., & Livio, M. 1999, *Nature*, 401, 891
 Maraschi, L. 2002, in *Active Galactic Nuclei: From Central Engine to Host Galaxy*, ed. S. Collin, F. Combes, & I. Shlosman (San Francisco: ASP), 36
 Molteni, D., Lanzafame, G., & Chakrabarti, S. K. 1994, *ApJ*, 425, 161
 Molteni, D., Sponholz, H., & Chakrabarti, S. K. 1996, *ApJ*, 457, 805
 Muno, M. P., Morgan, E. H., & Remillard, R. A. 1999, *ApJ*, 527, 321
 Papadakis, I. E., Petrucci, P. O., Maraschi, L., McHardy, I. M., Uttley, P., & Haardt, F. 2002, *ApJ*, 573, 92
 Remillard, R. A., Morgan, E. H., McClintock, J. E., Bailyn, C. D., & Orosz, J. A. 1999, *ApJ*, 522, 397
 Smith, D. M., Heindl, W. A., & Swank, J. H. 2002, *ApJ*, 569, 362
 Sobczak, G. J., McClintock, J. E., Remillard, R. A., Bailyn, C. D., & Orosz, J. A. 1999, *ApJ*, 520, 776
 Trudolyubov, S. P., Churazov, E. M., & Gilfanov, M. R. 1999, *Astron. Lett.*, 25, 718
 Yadav, J. S., Rao, A. R., Agrawal, P. C., Paul, B., Seetha, S., & Kasturirangan, K. 1999, *ApJ*, 517, 935
 Zhang, S. N., et al. 1997, *ApJ*, 479, 381

POSSIBLE PHOTOMETRIC EVIDENCE OF EJECTION OF BULLET-LIKE FEATURES IN THE RELATIVISTIC JET SOURCE SS 433

SANDIP K. CHAKRABARTI,^{1,2} S. PAL,² A. NANDI,¹ B. G. ANANDARAO,³ AND SOUMEN MONDAL³

Received 2003 February 6; accepted 2003 August 12; published 2003 August 22

ABSTRACT

SS 433 is well known for its precessing twin jets having optical bullets inferred through *spectroscopic* observation of $H\alpha$ lines. Recently, Chakrabarti et al. described processes that may be operating in the accretion disk of SS 433 to produce these bullets. In a recent multiwavelength campaign, we find a sharp rise in intensity in timescales of a few minutes in X-ray, IR, and radio waves through *photometric* studies. We interpret them to be possible evidence of ejection of bullet-like features from accretion disks.

Subject headings: methods: data analysis — radio continuum: stars — stars: individual (SS 433) — stars: mass loss — techniques: spectroscopic — X-rays: stars

1. INTRODUCTION

SS 433 is a well-studied bright emission line compact system that is ejecting matter in symmetrically opposite directions at a speed of $v_{\text{jet}} \sim 0.26c$. It has a mass-losing ($\dot{M} \sim 10^{-4} M_{\odot} \text{ yr}^{-1}$) companion orbiting in 13.1 days. The jets are precessing in 162.15 days around the symmetry axis. The velocity is remarkably constant to within a percent or so (Margon 1984; Gies et al. 2002). As a result of the remarkable constancy in the precession timescales and the velocity, the instantaneous locations of the red- and blueshifted $H\alpha$ lines are well predicted by the so-called kinematic model (Abell & Margon 1979), and the compilation of 20 years of timing properties (Eikenberry et al. 2001) suggests that the kinematic model can explain the general variation of the red- and blueshifts very well.

A very exciting observation, made within years of the discovery of SS 433, suggests that the passage of the jets is not continuous but as if through successive and discrete bullet-like entities, at least in the optical region (Grandi 1981; Brown et al. 1991). The $H\alpha$ lines were seen to brighten up and fade away without changing their red-/blueshifts, indicating that the brightened bullets are radially ejected and do not have any rotational velocity component. Since the bullets of energy $\sim 10^{35}$ ergs do not change their speed for a considerable time (~ 1 – 2 days), Chakrabarti et al. (2002) postulated that they must be ejected from the accretion disk itself. They presented a mechanism to produce quasi-regular bullets. Using the results of numerical simulations involving oscillation of shocks in accretion disks, they concluded that in normal circumstances, a 50–1000 s interval is expected between the bullet ejection. These bullets would be ejected from the X-ray-emitting region and propagate through the optical, IR ($\sim 10^{13}$ – 10^{14} cm), and finally to the radio-emitting region at $\geq 10^{15}$ cm (roughly the distance covered in a day with $v \sim v_{\text{jet}}$) or so. Thus, if the object is in a low or quiescence state, each individual bullet flaring and dying away in a few minutes timescale should be observable not only in optical wavelengths (Grandi 1981; Margon 1984; Brown, Cassinelli, & Collins 1991; Gies et al. 2002) but also in all the wavelengths, including X-ray, IR, and radio-emitting regions. So far, no such observations of individual bullets have been

reported in the literature, and it was necessary to make a multi-wavelength observation at relatively quieter states.

In this Letter, we present some results of our multiwavelength studies. From the long-term analysis of radio flares (Bonsignori-Facondi et al. 1986; Vermeulen et al. 1993), it is known that between big flares that occupy $\sim 20\%$ of the time, the object may go to a very quiescence state. So, it is likely that one could “catch” these bullets in action, provided that observations are carried with very short time resolution. Our multiwavelength observations lasted from 2002 September 25 to October 6, with X-ray, IR, optical, and radio observations made simultaneously on 2002 September 27. Here, we report only X-ray, IR, and radio observations of 2002 September 27 and 29. Optical studies required longer integration times, and these results along with other days of observations are reported elsewhere (S. K. Chakrabarti et al. 2003, in preparation).

Our main results indicate that there are considerable variations in the timescale of minutes in all the wavelengths. These may be called microflares. When the Fourier transform is made, some excess power is observed in the 2–8 minute timescale (often beyond 3σ level). The X-ray count rate was found to increase by 15%–20% within a minute. Since the emitting regions of X-ray, IR, and radio are not well known with absolute certainty, while duration of the flares lasts less than a few minutes, we could not prove beyond doubt that there are indeed correlations among the microflares observed in these wavelengths. However, variabilities that we find are not the flicker type or shot-noise type, in the sense that the power density spectrum (PDS) is not of $1/f$ type and the duration is not very short (i.e., less than 1 s). We therefore believe that we may have found evidence of bullet ejection through these observations in other wavelengths.

2. OBSERVATIONS AND DATA REDUCTION

Radio observation was carried out with the Giant Meter Radio Telescope (GMRT) at 1280 MHz (bandwidth 16 MHz), which has 30 antennas each 45 m in diameter spread over a 25 km region (Swarup et al. 1991) near Pune, India, along a roughly Y-shaped array. The data are binned at every 16 s. On 2002 September 27 and 29, the number of antennas working was 28 and 13, respectively. The AIPS package was used to reduce the data. Bad data were flagged using tasks UVFLG and TVFLG, and the standard deviation at each time bin using the UVPLT package was computed. On September 27, 3C 48 and 3C 286 were used as the flux calibrator while on September

¹ S. N. Bose National Center for Basic Sciences, JD-Block, Salt Lake, Kolkata 700098, India.

² Centre for Space Physics, P-61 Southend Gardens, Kolkata 700084, India.

³ Physical Research Laboratory, Navarangapura, Ahmedabad 380009, India; chakraba@bose.res.in, space_phys@vsnl.com, anuj@bose.res.in, anand@prl.ernet.in, soumen@prl.ernet.in

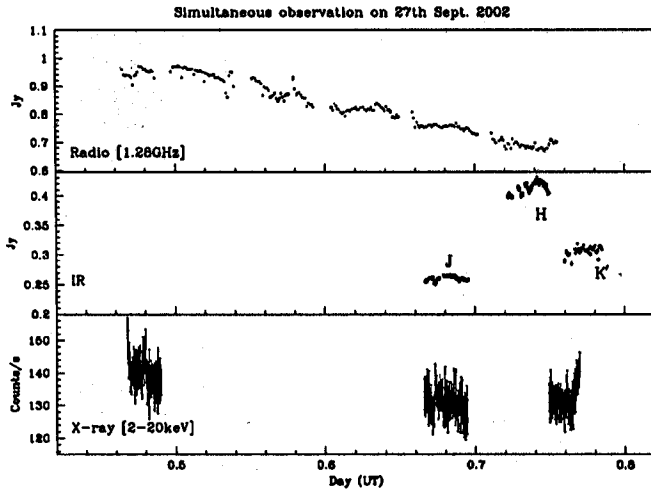


FIG. 1.—Multiwavelength observation of short time variability in SS 433 by radio (top), IR (middle), and X-ray (bottom) on 2002 September 27. The observations were made at the GMRT, Pune, at 1.28 GHz (radio), 1.2 m Mt. Abu infrared telescope at *J*, *H*, and *K'* bands, and the *RXTE* satellite (2–20 keV), respectively.

29, only 3C 48 was used. Generally, the observation condition was very stable.

The IR observation was made using the Physical Research Laboratory 1.2 m Mt. Abu infrared telescope equipped with the Near-Infrared Camera and Multi-Object Spectrometer (NICMOS), having a 256×256 HgCdTe detector array cooled to 77 K. The filters used were standard *J* ($\lambda = 1.25 \mu\text{m}$, $\Delta\lambda = 0.30 \mu\text{m}$), *H* ($\lambda = 1.65 \mu\text{m}$, $\Delta\lambda = 0.29 \mu\text{m}$), and *K'* ($\lambda = 2.12 \mu\text{m}$, $\Delta\lambda = 0.36 \mu\text{m}$) bands. The observational data on September 27 for the *J* and *H* bands are binned at every 10 s, while that of the *K'* band is binned every 20 s. The data reduction was performed using the IRAF software package. All the object frames were debiased, sky-subtracted, and flat-fielded using normalized dome flats. The sky frame was created by the usual practice of median combining of five position-dithered images in which the source was within the NICMOS field of $2' \times 2'$. At each dithered position, 10 frames were taken with each integration time of 10 s. The nearby IR-bright standard star GL 748 (Elias et al. 1982) was used as the calibrator, and it was observed for at least 15 minutes at each filter band. We measured the stellar magnitudes using the aperture photometry task (APPHOT) in IRAF. Our derived mean *JHK'* magnitudes on September 27 are 9.47 ± 0.02 , 8.48 ± 0.02 , and 8.32 ± 0.02 , respectively, and the corresponding mean flux densities are 0.261 ± 0.002 , 0.413 ± 0.003 , and 0.305 ± 0.003 , respectively. The magnitudes are converted to flux density (in units of janskys) using the zero-magnitude flux scale of Bessell, Castelli, & Plez (1998). To estimate reddening, we assumed visual extinction $A_v = 8.0$ (Gies et al. 2002). Using the relation given in Bessell et al. (1998), the *JHK'* extinctions were found to be $A_J = 2.32$, $A_H = 1.84$, and $A_{K'} = 0.88$. The dereddened flux in *JHK'* is 2.24, 2.21, and 1.67 Jy, respectively. The differential magnitudes are determined using the two brightest stars (std1: *J* = 12.1, *H* = 10.6 mag; std2: *J* = 12.5, *H* = 11.1 mag) in the same frame of the object. The error in individual flux density measurement is the usual propagation error of the observed photometric magnitude. Photometric errors ϵ are calculated for the individual frame of every star, and for the subtracted differential magnitude the final error was

calculated as $(\epsilon_1^2 + \epsilon_2^2)^{1/2}$, where ϵ_1 and ϵ_2 are the error bars of the individual stars.

The X-ray observation was carried out using the Proportional Counter Array (PCA) on board the *Rossini X-Ray Timing Explorer (RXTE)* satellite. The data reduction and analysis was performed using software (LHEASOFT) FTOOLS version 5.1 and XSPEC version 11.1. We extract light curves from the *RXTE/PCA* Science Data of GoodXenon mode. We combine the two event analyzers of 2 s readout time to reduce the Good Xenon data using the perl script MAKE_SE. Once the MAKE_SE script was run on the Good_Xenon_1 and Good_Xenon_2 pairs, the resulting file was reduced as Event files using SEEXTRACT script to extract light curves. Good time intervals were selected to exclude the occultations by the Earth and South Atlantic Anomaly passage and also to ensure the stable pointing. We also extracted energy spectra from PCA Standard2 data in the energy range 2.5–20.0 keV (out of five Proportional Counter Units [PCUs], only data from 0, 2, and 3 PCUs are added together). For each spectrum, we subtracted the background data that are generated using PCABACKEST version 4.0. PCA detector response matrices are created using PCARSP version 7.10.

3. RESULTS ON SHORT-TIMESCALE VARIABILITIES

The observational result of 2002 September 27 is shown in Figure 1 with UT (day) along the X-axis. The top and middle panels show the radio and IR fluxes (uncorrected for reddening) in units of janskys, and the bottom panel shows X-ray counts per second in 2–20 keV. Typical error bars of the mean flux measurements (standard deviation in each time bin for radio and IR and squared root of counts per bin size for X-ray), which are included in the figure, are as follows: in radio ~ 1 mJy, in IR 0.5 mJy, and in X-ray ~ 3 counts s^{-1} . These observations correspond to an average flux of 10^{-14} , 5×10^{-10} , and 10^{-10} ergs $\text{cm}^{-2} \text{s}^{-1}$, respectively. In other words, assuming isotropic emission, at a distance of 3 kpc for the source the average radio, IR, and X-ray luminosities are 1.1×10^{30} , 5.5×10^{34} , and 10^{35} ergs s^{-1} , respectively. Observations in radio and IR were carried out during 2002 September 25–30, and no signature of any persistent “flare” was observed. The radio data clearly showed a tendency to go down from 1.0 to 0.7 Jy, reaching about 0.3 Jy on September 28/29, while the X-ray data showed a tendency to rise toward the end of the observation of September 27. The IR data in each band remained virtually constant. The *H*-band result was found to be higher compared to the *J*- and *K*-band results during September 25–29. A similar result of turnaround at about $4 \mu\text{m}$ was reported earlier by Fuchs (2003). This turnover could be possibly due to free-free emission in the optically thin limit. A detailed discussion will be presented elsewhere (S. K. Chakrabarti et al. 2003, in preparation).

In Figure 2, we present the same light curves as in Figure 1 but plotted around the “local” mean, i.e., mean values taken in each “spell” of observation. We note that there are significant variations in a matter of minutes in observations at all the wavelengths. From eye-estimate, we see the variability time-scale to be $T_{\text{var}} \sim 2$ –8 minutes. The error bars include errors in individual measurements plus the standard deviation of the flux variation in the light curve. To impress that the variability is real, we show in Figure 3 the differential flux density variation of IR observations in the *J* and *H* bands during 2002 September 27 using differential photometry. The error bars

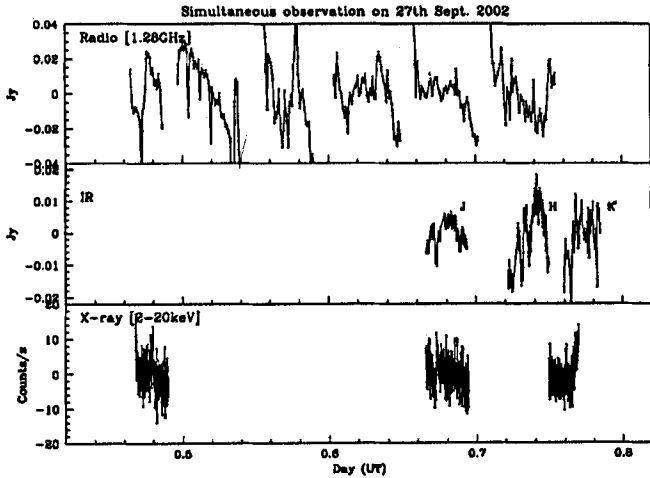


FIG. 2.—Observations in Fig. 1 are plotted around the mean taken in each spell of observation. Considerable variations at a timescale of a few minutes are observed.

are also shown. The 1σ error bar ($J = 0.00035$ Jy, $H = 0.00085$ Jy) of the differential flux variation between SS 433 and std1 for the whole light curve is a factor of 3.5 and 2.5 in the J and H band, respectively, in comparison to that between two standards ($J = 0.0001$ Jy, $H = 0.00035$ Jy). The 1σ for the light curve is more than a factor of 5σ of single point measurement error. Thus, the variation in the IR light curves of SS 433 is likely to be intrinsic, and the analysis shows above 2σ level variability in both bands.

Could these variations be due to individual bullets? In order to be specific, we present in Figure 4a one microflare-like event in radio from the data collected on 2002 September 29, when radio intensity was further down ~ 0.3 Jy so that the microflares could be prominently seen. Here 0 s corresponds to 15 hr 35 minutes UT. We observe brightening in the source from 0.35 to 0.8 Jy in ~ 75 s, which faded away in another ~ 75 s. That is, the intensity became more than doubled in ~ 1 minute. Similarly, in Figure 4b, where we presented a microflare from the second

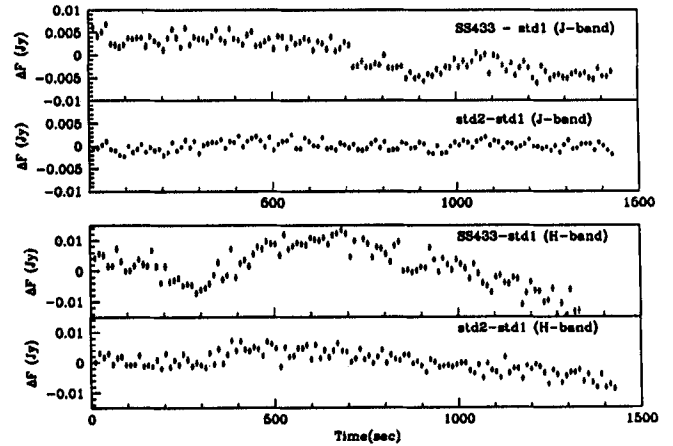


FIG. 3.—Differential photometry of SS 433 with respect to the two brightest standard stars (std1 and std2) in the same frame of the object is plotted. Different curves are marked on the top right corner in each panel. The X-axis of the graph is the relative time of measurements in seconds. The error bar for each individual differential measurement is also shown. Differential flux variation of SS 433 is above the 2σ level in comparison with that of standards.

(central) spell of X-ray data of 2002 September 27 (Figs. 1 and 2), we also observe significant brightening and fading in ~ 100 s. Here 0 s corresponds to 16 hr 5 minutes UT. The count rate went up more than 15% or so in about a minute. The energy contained in the radio microflare, integrated over their lifetime, is about $I\nu\tau 4\pi D^2 10^{-23} = 1.1 \times 10^{33}$ ergs (here, $I \sim 0.8$ is the intensity in janskys, $\nu = 1.28 \times 10^9$ Hz is the frequency of observation, $\tau \sim 100$ s is the rise time of the bullet, and $D = 9 \times 10^{21}$ cm is the distance of SS 433). Similarly, the energy contained in the X-ray microflare is about $\frac{1}{2}\tau(N_{\gamma, \max} - \bar{N}_{\gamma})E_{\gamma} 4\pi D^2/A_{\text{PCA}} = 2.7 \times 10^{35}$ ergs (here, $\tau \sim 100$ s is the rise time of the flare, $N_{\gamma, \max}$ is the maximum photon count rate, \bar{N}_{γ} is the average photon number, E_{γ} is the average photon energy, and A_{PCA} is the area of the PCA detectors). The spectroscopic study yields an average flux of 2.41×10^{-10} ergs cm^{-2} s^{-1} . With an estimated duration of 100 s and about 15% energy going to the microflare (Fig. 4b), one obtains the microflare energy to be 4.1×10^{35} ergs, in general

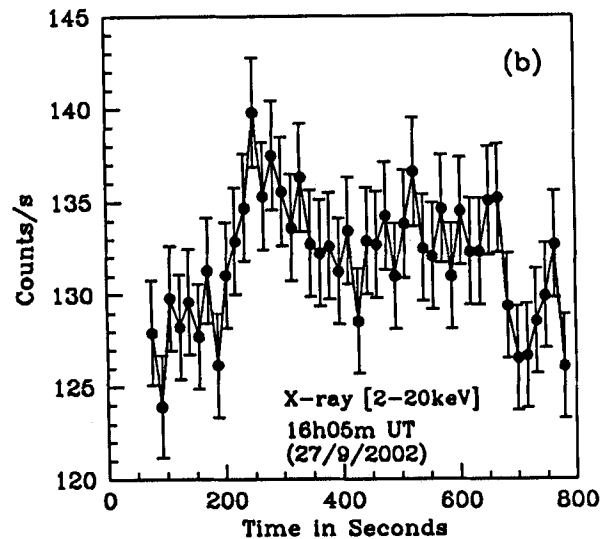
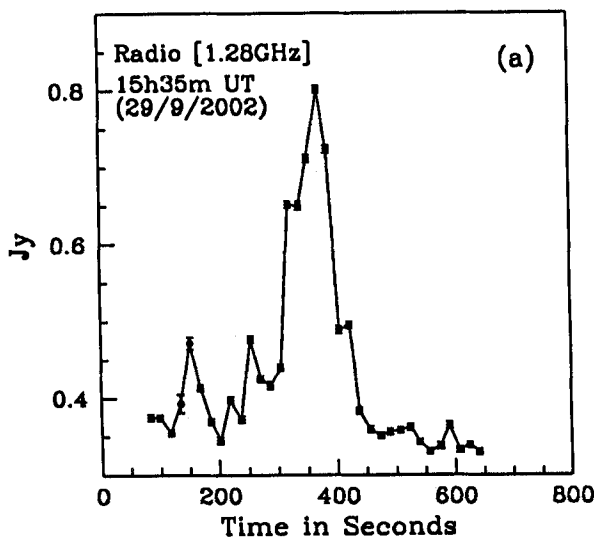


FIG. 4.—Individual flares in very short timescales are caught. (a) A radio flare lasting 2.5 minutes (observed on 2002 September 29) and (b) an X-ray flare (observed on 2002 September 27) lasting for about 3.5 minutes. Each bin size is 16 s.

agreement with the result obtained from photometric study. Since the radio luminosity is very small, even when integrated over a 0.1–10 GHz radio band (with a spectral index of ~ -0.5 ; Vermeulen et al. 1993), we find that almost all the injected energy at the X-ray band is lost on the way during its passage of ~ 1 –2 days.

Although the variations that we find are not periodic (strictly speaking, they are not expected to be periodic, either), the PDS does show considerable power in frequencies ~ 0.002 – 0.008 Hz. Deviation of the PDS from a power-law background proportional to $\nu^{-\alpha}$ (e.g., Mineshige, Ouchi, & Nishimori 1994) in all three bands gives an estimate of excess power at low frequencies. We fit $\alpha = 1.8$ for X-ray power, 1.9 for IR power, and 1.6 for radio power in the PDS. X-ray power shows excess at ~ 0.003 Hz (greater than 2.7σ), i.e., at $T_{\text{var},x} \sim 5.5$ minutes and at 0.0077 Hz (greater than 1.4σ), i.e., at $T_{\text{var},x} \sim 2.1$ minutes. IR power shows excess at 0.0022 Hz (greater than 4σ), i.e., $T_{\text{var},ir} \sim 7.7$ minutes. Radio PDS shows excess at ~ 0.0023 Hz (greater than 3.2σ), i.e., at $T_{\text{var},r} \sim 7.2$ minutes and at ~ 0.003 Hz (greater than 1.6σ), i.e., at $T_{\text{var},r} \sim 5.5$ minutes, respectively. Here 1σ error in residual power is the standard deviation computed separately for each PDS after subtracting the power-law background $\nu^{-\alpha}$. Because the peaks in PDS are often marginally significant, we do not claim that we see quasi-periodic oscillations that are observed in numerous black hole and neutron star candidates.

In order to establish that the features that we observe are really due to “bullets” emitting at different wave bands, one should find correlations among them or try to “follow” them from one band to the other. Unfortunately, cross-correlation among our observations did not yield sharp peaks, partly because the observations were of short duration. The main problem is that the locations of the IR/radio-emitting regions themselves are very uncertain. Also, the average duration of an “event” (~ 1 minute) and average interval of the events (2–8 minutes) are very short compared to the travel time of the bullets to IR ($\sim 10^4$ s) or radio ($\sim 10^5$ s) regions. However, we can exclude that the variabilities are due to “fluctuations” at the inner regions of the accretion disk—the typical timescale of such variabilities (say, at $r \sim 3r_g$, where $r_g = 2GM/c^2$, M , G , and c being the mass of the black hole, G being the gravitational constant, and c being the velocity of light) of an $M = 10 M_\odot$ object would be $\sim 2\pi r/c \sim 20GM/c^3 \sim 10^{-3}$ s, i.e., of much shorter duration than what we see. Similarly, if it were due to random or flicker noise, we should have seen $1/f^\alpha$ ($\alpha \sim 1$) dependence of the PDS. However, the best fit of PDS is $\alpha \sim 1.6$ – 1.8 instead. Thus, the origin of these features must be different and could be due to bullet-like ejections from the disk.

In the spectrum, we find two strong Fe line features in all three spells of X-ray observation. The best fit was found to be

the thermal bremsstrahlung model with two Fe lines ($kT \sim 18$ keV) having a reduced χ^2 of around 1.2 in each case. We failed to fit with a model having a blackbody emission component. Thus, no evidence for a Keplerian disk was found. The average flux was found to be 2.3×10^{-10} ergs cm^{-2} s^{-1} . This corresponds to a luminosity of 2.5×10^{36} ergs s^{-1} . Since a bullet has about 10%–15% of the total count (Fig. 4b), each bullet will have an energy of around 2.5×10^{35} ergs s^{-1} .

4. CONCLUDING REMARKS

In this Letter, we presented results of our multiwavelength observations that were saved at short time intervals. From the analysis of the observations of radio, IR, and X-ray in the quiescence state, we conclude that we may be observing ejection events of bullet-like features from the accretion disk in timescales of ~ 2 –8 minutes. Identification of small microflare events with those of bullet ejection is derived from the timescales of variabilities, which are roughly the same in all these wavelengths. We find their presence in X-ray ($\leq 10^{11}$ – 10^{12} cm), IR ($\leq 10^{13}$ – 10^{14} cm), and radio ($\leq 10^{15}$ cm) emission regions. Vermeulen et al. (1993) found evidence for optical bullets with a lifetime of 1–2 days. This is perhaps due to the propagation of a burst of indistinguishable bullets and not due to a single one. We identified microflare-like features in all these observations that may be signatures of the bullets. The count rate of X-rays was seen to increase 15%–20% in a matter of a minute. One way to actually identify each bullet could have been to follow them from the X-ray region outward. This will require very careful time delay measurements, since the distances of emission regions are not very accurately known to follow a feature of a duration of a minute. We exclude the possibility that what we saw was flicker noise, since neither the duration nor the PDS properties match with those of flicker noise. One could have perhaps distinguished the energetic bullets by observing polarization properties of the radio emissions during the short-lived flares, but unfortunately, because of technical reasons, this observation could not be carried out. We plan to do such an observation in the near future.

S. K. C. thanks J. Swank of NASA/GSFC and Professor A. P. Rao of GMRT/NCRA for giving us time in *RXTE* and GMRT for observations. He also thanks J. Kodilkar of GMRT/NCRA for his assistance in analyzing the radio data. This work is supported in part by a CSIR fellowship (S. P.) and a DST project (S. K. C. and A. N.). The authors thank the unknown referee for suggestions leading to considerable improvement of the observational aspects.

REFERENCES

- Abell, G. O., & Margon, B. 1979, *Nature*, 279, 701
 Bessell, M. S., Castelli, F., & Plez, B. 1998, *A&A*, 333, 231
 Bonsignori-Facondi, S. R., Padrielli, L., Montebugnoli, S., & Barbieri, R. 1986, *A&A*, 166, 157
 Brown, J. C., Cassinelli, J. P., & Collins, G. W., II. 1991, *ApJ*, 378, 307
 Chakrabarti, S. K., Goldoni, P., Wiita, P. J., Nandi, A., & Das, S. 2002, *ApJ*, 576, L45
 Eikenberry, S. S., et al. 2001, *ApJ*, 561, 1027
 Elias, J. H., Frogel, J. A., Matthews, K., & Neugebauer, G. 1982, *AJ*, 87, 1029
 Fuchs, Y. 2003, in *New Views on Microquasars*, ed. P. Durouchoux, Y. Fuchs, & J. Rodriguez (Kolkata: CSP), 269
 Gies, D. R., McSwain, M. V., Riddle, R. L., Wang, Z., Wiita, P. J., & Wingert, D. W. 2002, *ApJ*, 566, 1069
 Grandi, S. 1981, *Vistas Astron.*, 25, 7
 Margon, B. 1984, *ARA&A*, 22, 507
 Mineshige, S., Ouchi, N. B., & Nishimori, H. 1994, *PASJ*, 46, 97
 Vermeulen, R. C., et al. 1993, *A&A*, 270, 189
 Swarup, G., et al. 1991, *Curr. Sci.*, 60, 95

EVIDENCE OF CLASS TRANSITIONS IN GRS 1915+105 FROM INDIAN X-RAY ASTRONOMY EXPERIMENT DATA

SANDIP K. CHAKRABARTI,^{1,2} A. NANDI,¹ ASIT CHOUDHURY,³ AND UTPAL CHATTERJEE³

Received 2003 December 18; accepted 2004 January 29

ABSTRACT

GRS 1915+105 shows at least 12 distinct classes of light curves. By analyzing the data obtained from the Indian X-ray Astronomy Experiment (IXAE) instrument on board the *IRS-P3* satellite, we show that on several days, transitions between one class to another were observed. On these days, the so-called κ class went to ρ class and the χ class went to ρ class. In the frequency-time plane, such transitions exhibited change in quasi-periodic oscillation (QPO) frequency. We could detect that low-frequency QPOs occurred in anticipation of a class transition several hundred minutes before the actual transition.

Subject headings: black hole physics — stars: individual (GRS 1915+105) — X-rays: stars

1. INTRODUCTION

GRS 1915+105 has been studied quite extensively for almost 10 years (see Castro-Tirado et al. 1994 and Mirabel & Rodríguez 1994 for early papers), and yet it continues to reveal new physical insights into the phenomenon of black hole accretion. This enigmatic X-ray transient source exhibits at least 12 classes of light curves, if not more (Belloni et al. 2000). These 12 types have been designated as χ , α , ν , β , λ , κ , ρ , μ , θ , δ , γ , and ϕ , and are based on the nature of the hardness ratios exhibited in the light curve. In some classes (e.g., χ) only hard X-rays are seen, in some other classes (e.g., ϕ) only soft X-rays are seen, while in the majority (such as κ , λ , and ρ) photons come in the so-called “burst-on” and “burst-off” states, which are similar to quick transitions between soft and hard states. Subsequently Nandi, Manickam, & Chakrabarti (2000) rearranged these classes in a pattern more easily understandable by advective disk models (see also Naik, Rao, & Chakrabarti 2002). While the *Rossi X-Ray Timing Explorer (RXTE)* satellite has observed this object about a thousand times, it has not been able to pinpoint exactly how and when a class transition actually takes place.

In the present paper, we show that observations by the Proportional Counters (PPCs) of the Indian X-ray Astronomy Experiment (IXAE) instrument on board the *IRS-P3* satellite have revealed such class transitions several times. While the time-resolution and the number of energy bins of the IXAE instrument are low, the observations nevertheless are good enough to identify the classes and the transitions. Here we report two such class transitions from the archived data of IXAE. We also show that the source probably had “premonition” about the class transition about a few hundred seconds prior to the observation, as is evidenced by the presence of a drift in low-frequency quasi-periodic oscillations (LFQPO) in the power density spectrum (PDS). We observed light curves of “unknown” class just before the transition. We compare our results with *RXTE* observations in nearby times. We present

two transitions: one is a $\kappa \rightarrow \rho$ transition on 1997 June 22, and the other is a $\chi \rightarrow \rho$ transition on 1997 June 25. On both days, we find evidence of the LFQPO in the pre- and post-transition classes.

While the exact cause of the class transition is not yet known, it has been pointed out by Nandi et al. (2000) that it may be due to the variation in accretion rates in both the Keplerian and sub-Keplerian components. They actually rearranged the 12 classes of Belloni et al. (2000) into four major classes, hard, soft, semisoft, and intermediate, and showed that the class transitions could be understood by slow variation of the accretion rate of the sub-Keplerian component. Chakrabarti & Manickam (2000), while explaining the correlation between the duration and QPO frequency in burst-off states of κ and λ classes, pointed out that the real cause of QPO is most probably the oscillations of the standing shocks. Furthermore, the transition between the burst-off and burst-on states inside a class is most probably due to the cooling of the outflowing wind by soft photons from the accretion disk. As a result, two QPO frequencies are expected in classes that have burst-on and burst-off states. The one at a high frequency (around 1–20 Hz or so) would be due to the shock oscillation, while the one at low frequency (say around 0.01–0.02 Hz) would be due to the quasi-periodic cooling of the outflows. If this is correct, then it is possible that the basic nature of the quasi-periodic cooling of the outflow could continue to take place during a class transition, while the shock itself could be weakened. This would mean that the LFQPOs could persist across class transitions. In § 2, we present results of our analysis and show that this is indeed the case.

In § 2, we also report the observations and show that such transitions actually took place on the same day in the data set from a single orbit. We perform fast Fourier transforms (FFT) at various times of observation and plot time-frequency diagrams for observations in each orbit. We also compare our results with those of *RXTE* (which missed the transitions) on the same date. Finally in § 3, we draw our conclusions.

2. OBSERVATIONAL RESULTS AND DATA ANALYSIS

IXAE, which was launched from Sriharikota Range on 1996 March 21, carried out observations until the year 2000. It was flown on the Indian satellite *IRS-P3* and had three

¹ S. N. Bose National Centre for Basic Sciences, JD-Block, Salt Lake, Calcutta 700098, India; chakraba@bose.res.in, anuj@bose.res.in.

² Centre for Space Physics, Chalanika 43, Garia Station Road, Calcutta 700084, India; space_phys@vsnl.com.

³ Centre for Space Physics-Malda Branch, Atul Market, Malda 732101, India; space_phys@vsnl.com.

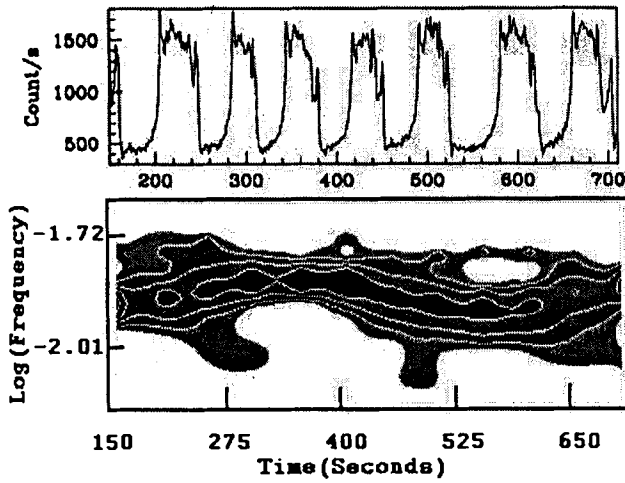


FIG. 1a

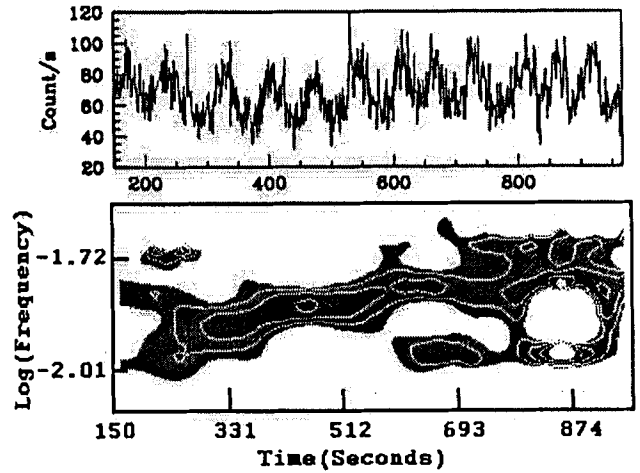


FIG. 1b

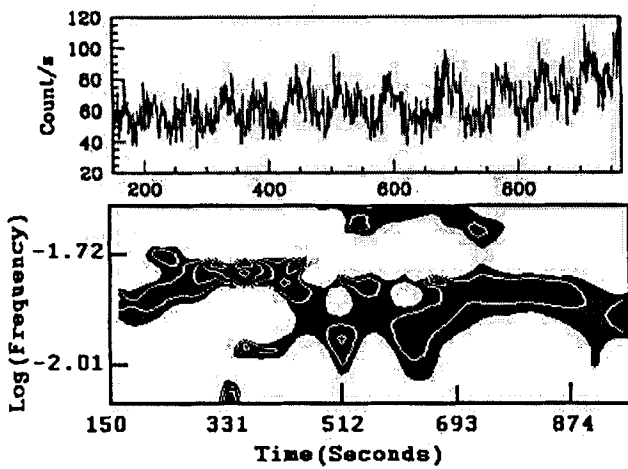


FIG. 1c

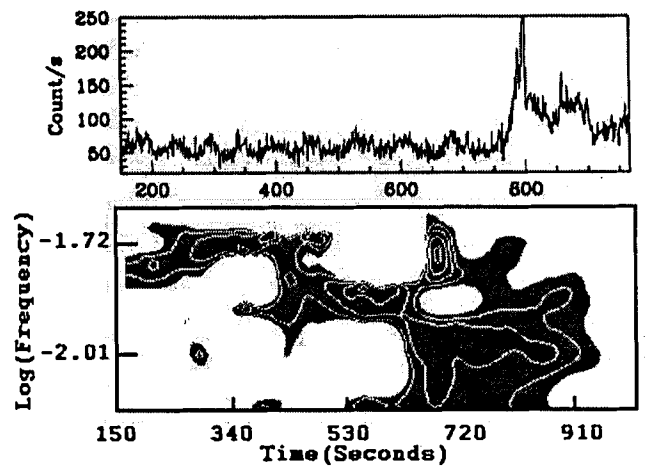


FIG. 1d

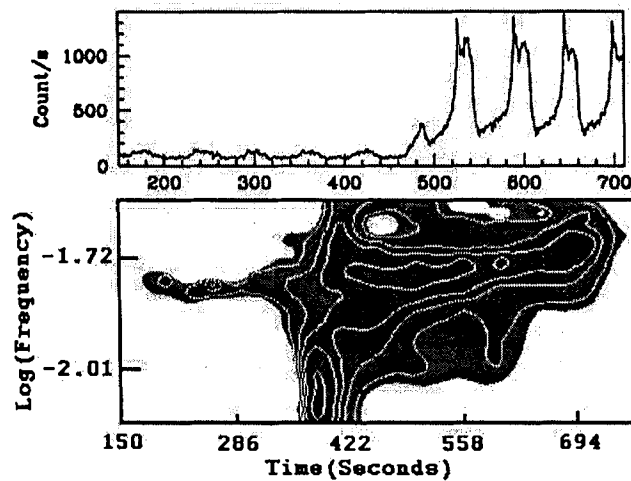


FIG. 1e

FIG. 1.—(a–e): Light curves (*top*) and time-frequency plots (*bottom*) of GRS 1915+105, as observed by IXAE in five successive orbits on 1997 June 22. In (a) the light curve is of κ class, while in (b), (c), and part of (d), the light curve is of unknown class. In (d), a failed attempt for transition was made where a “spike” is seen (as is evidenced from the disparate PDS in the pre- and post-transition period). In (e), a real transition to ρ class is seen. This is also reflected in the time-frequency plot.

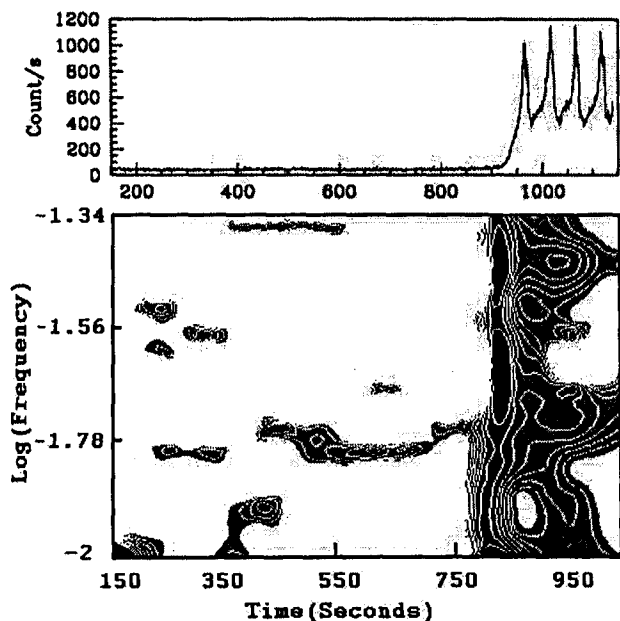


FIG. 2.—Light curves (*top*) and time-frequency plots (*bottom*) of GRS 1915+105 as observed by IXAE on 1997 June 25. The upper panel shows the transition from χ to ρ class. The lower panel shows the characteristic noise in the PDS at the transition.

identical PPCs (Agrawal 1998). Each counter was filled with a gas mixture of 90% argon and 10% methane at a pressure of 800 torr with a total effective area of 1200 cm². The operating energy range was between 2 and 18 keV, with an average detection efficiency of 60% at 6 keV. The counts are saved in the archive in two channels, 2–6 and 6–18 keV. Although the time resolution could be 0.1 s in Medium mode, because of restrictions in data storage onboard, usually observations were carried out in 1 s resolution to have data for five consecutive orbits per day. This is a great advantage that allowed us to observe class transitions at the cost of missing the fast variability behavior for which *RXTE* is undoubtedly the champion.

In Figures 1a–1e, we show the light curves (*top*) and time-frequency diagrams (*bottom*) obtained in five successive orbits on 1997 June 22. The light curves were obtained by adding counts from all three PPCs from both energy channels, 2–6 and 6–18 keV. The bottom panels were obtained by FFT of the photon counts in 6–18 keV. While in Figure 1a, the first orbit is class κ , in Figure 1e, it is class ρ . In between, the light curves do not appear to belong to any known class. The data have been analyzed using the FTOOLS and XSPEC packages from NASA. Since the time resolution of the observation is only 1 s, we are unable to identify the high-frequency QPOs in the IXAE data. However, the LFQPOs in burst-on/burst-off sources have been detected. For each panel of Figure 1, we divide the data into segments of 306 s and stagger each segment by 51 s. For each segment of 306 s, we take the FFT and place the PDS at its mean time. Finally, we plot contours of constant normalized power P as a function of the frequency and time of observation in each lower panel of Figure 1.

The times of observations have been taken from Table 1 of Yadav et al. (1999). There is an error of 1 day in the Date column in this table, which we have corrected. The observation started at 12:12:24, but Figure 1a starts at 12:14:57, 153 s

later, because of our choice of segment size. The observation ended at 19:20:50, while Figure 1e ends at 19:18:17, 153 s earlier. There is no available record of the exact beginning and end times of each gap between orbits. Two successive data sets are separated by ~ 83 minutes. Thus, the exact time of the observation cannot be given within 2–3 minutes of accuracy. Only the duration is known with certainty. However, this does not affect our conclusions.

The contours in the lower panel of Figure 1a are drawn for normalized power $P = 2.0, 2.3, 2.6, 2.9, 3.2, 3.5,$ and 3.8 (highest power has the darkest shade), clearly indicating an LFQPO frequency, ν , oscillating between $\log(\nu) = -1.896$ and -1.824 . In Figure 1b, contours are drawn for $P = 1.7, 2.0, 2.3, 2.6,$ and 2.9 . We note that in this unknown class, the LFQPO frequency monotonically drifts from $\log(\nu) = -1.937$ to -1.793 . In Figure 1c, the contours are drawn for $P = 1.7, 2.0, 2.3, 2.6,$ and 2.9 . The drift of LFQPO frequency undergoes large amplitude fluctuations, with a high reaching up to $\log(\nu) \sim -1.73$. In Figure 1d, which was drawn with contours of $P = 1.7, 2.0, 2.3, 2.6, 2.9,$ and 3.2 , the first failed attempt of the class transition is seen around 750 s after the beginning of the observation, where a large spike is seen in the light curve. The completely different PDSs in the pre- and post-transition region produce a “mixed” PDS in the transition region, causing large-scale noise of duration ~ 300 s, the size of our segments over which FFTs were taken. In the results from the final orbit, in Figure 1e, the contours are drawn for $P = 1.7, 2.0, 2.5, 2.8, 3.1,$ and 3.5 . Besides the noise generated by the transition region, it is clear that the LFQPO frequency at $\log(\nu) \sim -1.75$ in the pretransition unknown class continues to drift toward a higher value [$\log(\nu) \sim -1.664$] as the light curve enters into the well-known ρ class. Indeed, only 7 minutes after this IXAE observation ends, *RXTE* observed GRS 1915+105 for 1 hr (ObsID: 20402-01-34-01)

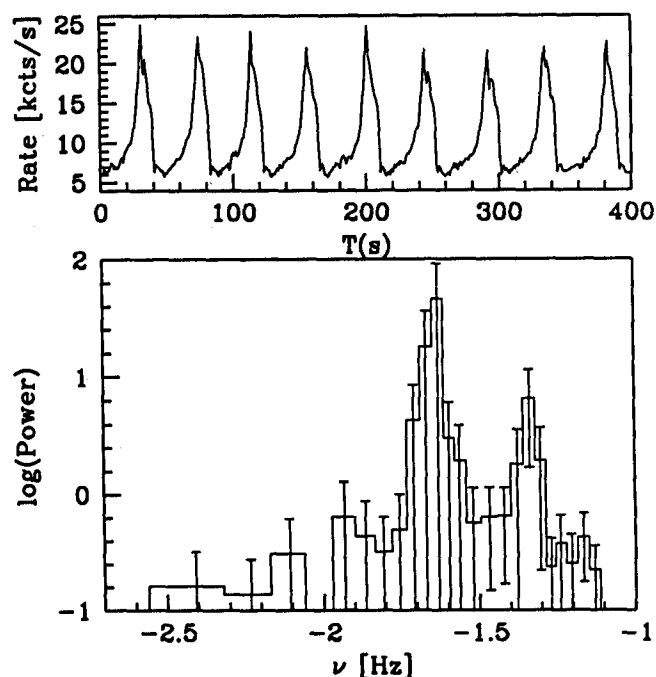


FIG. 3.—*RXTE* observation of GRS 1915+105 a half-hour after the IXAE observation as presented in Fig. 2. The upper panel shows that the light curve is still in ρ class. The PDS in the lower panel shows that the low frequency QPO is also close to where IXAE found it.

between 19:27:28 and 20:27:04 and found it in the ρ class with the same characteristics. There was an observation by *RXTE* on 1996 June 18 (ObsID: 20402-01-33-00), and the class observed was κ , the same as the pretransition class in the IXAE observation on 1997 June 22 (Fig. 1a).

In Figure 2, we show another class transition on 1997 June 25. On this day, observations were also carried out for five successive orbits. The first orbital observation begins at 11:12:15 and the fifth observation ends at 18:18:52, with gaps between the data of two successive orbits ~ 83 minutes as before. We show only the results of the fourth orbit, when the actual transition took place. The light curve (*top*) clearly shows a transition from χ to ρ class. The time-frequency plot after FFT of 306 s segments staggered by 51 s, shows (*bottom*) the familiar noise in the PDS of duration ~ 300 s. The class transition itself took place at around $T \sim 950$ s. The contours are drawn for $P = 0.3, 0.6, 0.9, 1.2, 1.5, 1.8, 2.1,$ and 2.4 . It is very clear that even from ~ 400 s after the observation starts, the system started showing a LFQPO with frequency $\log(\nu) \sim -1.78$, while after transition, the LFQPO drifts toward $\log(\nu) \sim -1.70$. The first harmonics can also be observed at around $\log(\nu) \sim -1.4$. Assuming the gaps between the orbits are of exactly equal duration, we estimate that this orbital observation ended at $\sim 16:36:58$.

In this case *RXTE* has also observed GRS 1915+105 a few minutes after this observation, from 17:05:20 to 17:15:04 for a period of 10 minutes (ObsID: 20402-01-34-00). Figure 3 shows the light curve and the PDS. The nature of the light curve matches the IXAE observation, and the PDS shows a clear peak at $\log(\nu) \sim -1.63$ with the first harmonics. It

appears that the LFQPO frequency drifted a bit in the intervening half-hour.

3. CONCLUDING REMARKS

In this paper, we have presented evidence of the direct transition of GRS 1915+105 from one class of light curve to another. Three such occasions have been found in data obtained by IXAE on 1997 June 22 and 25. We find that every time such a transition takes place, the PDSs in the pre- and post-transition look very different, the intervening period is characterized by noise (induced because of mixing of these two types of PDS results), and in all the cases, the LFQPO frequency continues through the transition. On June 22, we found that an unknown class was sandwiched by the κ and ρ class and a "failed" attempt was made for a class transition about 90 minutes prior to the actual transition. In both the dates, we verified that our results are consistent with *RXTE* observations. Indeed, *RXTE* also observed on several occasions the χ state followed by the ρ state (e.g., ObsIDs 20402-01-27-01 and 20402-01-27-02, and 20402-01-29-00 and 20402-01-30-00; Belloni et al. 2000), as in our observation on 1997 June 22, although the exact transition time was not detected by *RXTE*. We observed several similar class transitions in IXAE data from 2000, details of which will be presented elsewhere.

This work is supported in part from a DST project (A. N.) and an ISRO project (S. K. C.). A. C. and U. C. thank Achintya Chatterjee for discussions. The authors thank P. C. Agrawal of TIFR for making the IXAE data available to us.

REFERENCES

- Agrawal, P. C. 1998, in *High Energy Astronomy and Astrophysics*, ed. P. C. Agrawal & P. R. Vishwanath (Hyderabad: University Press), 408
 Belloni, T., Wolt, M.-K., Méndez, M., van der Klis, M., & van Paradijs, J. 2000, *A&A*, 355, 271
 Castro-Tirado, A. J., Brandt, S., Lund, N., Lapshov, I., Sunyaev, R. A., Shlyapnikov, A. A., Guziy, S., & Pavlenko, E. P. 1994, *ApJS*, 92, 469
 Chakrabarti, S. K., & Manickam, S. G. 2000, *ApJ*, 531, L41
 Mirabel, I. F., & Rodríguez, L. F. 1994, *Nature*, 371, 46
 Naik, S., Rao, A. R., & Chakrabarti, S. K. 2002, *J. Astrophys. Astron.*, 23, 213
 Nandi, A., Manickam, S. G., & Chakrabarti, S. K. 2000, *Indian J. Phys.*, 74B, 331
 Yadav, J. S., Rao, A. R., Agrawal, P. C., Paul, B., Seetha, S., & Kasturirangan, K. 1999, *ApJ*, 517, 935

X-ray Observation of SS 433 with RXTE

A. Nandi¹, Sandip K. Chakrabarti^{1,2}, Tomaso Belloni³ and P. Goldoni⁴

¹*S.N. Bose National Center for Basic Sciences,*

JD-Block, Salt Lake, Kolkata, 700098, India

²*Centre for Space Physics, Chalanika 43, Garia Station Rd., 700084, India*

³*INAF-Osservatorio Astronomico di Brera, Merate, Italy*

⁴*CEA Saclay, Service D' Astrophysique, France*

3 December 2004

ABSTRACT

Apart from regular monitoring by ASM, the compact object SS 433 was observed with RXTE several times last two/three years. We present the first analysis of these observations. We also include the results of the recent exciting TOO campaign made during donor inferior (orbital phase $\phi = 0$) and superior ($\phi = 0.5$) conjunctions which took place on Oct. 2nd, 2003, and on March 13th, 2004 respectively, when the jet itself was directly pointing towards us (i.e., precessional phase $\psi \sim 0$). Generally, we found that two distinct lines fit the spectra taken on all these days. We present some of the light-curves and the X-ray spectra, and show that the Doppler shifts of the emitted lines roughly match those predicted by the kinematic model for the jets. We find that the line with a higher energy can be best identified with a FeXXVI Ly- α transition while the line with lower energy can be identified with a FeXXV ($1s2p - 1s^2$) transition. We observe that the X-ray flux on March 13th, 2004 (when the base of the jet is exposed) is more than twice compared to that on Oct. 2nd, 2003 (when the base is covered by the companion). We find the flux to continue to remain high at least till another orbital period. We believe that this is because SS 433 was undergoing a weak flaring activity during the recent observation. ASM light curve showed the presence of many stronger flares in the past and the folded ASM light curve indicated possible presence of a periodic flare of ~ 50 d duration occurring after every 368days.

1 INTRODUCTION

The galactic micro-quasar SS 433 is an enigmatic X-ray binary system, ejecting material in the form of bipolar jets with almost constant velocity ($v \sim 0.26c$) (Margon 1984; Gies et al. 2002). Even after 25 years of its discovery, it is not clear whether the compact object is a neutron star or a black hole. The nature of the companion is also not known with certainty. Recently, Gies et al. (2002) pointed out from their UV spectroscopic study of the mass donor star of SS 433 that the nature of the companion is probably an evolved A-type star with a black hole as the primary. The disk, along with the jet which is along the instantaneous normal to it, itself precesses with a 162.15 day periodicity. The binary has a 13.1 day periodicity (Margon 1984). There are observational supports in optical as well as in radio/IR/X-rays (Borisov & Fabrika, 1987; Vermeulen et al. 1993ab; Chakrabarti et al. 2002, 2003; Migliari, Fender and Méndez, 2002) support that the jets are ejected in a bullet-like fashion, i.e., as blobs ejected along the instantaneous axis of the disk having only the *radial velocity component*. The red/blue shifts of the lines emitted from these jets are described very accurately by the so-called kinematic model of Abell & Margon (1979). These blobs in Radio/X-ray are seen within a few arcseconds from the core, although radio emissions and X-rays are also present much farther out, in the scale of half a degree (e.g., Margon, 1984; Migliari, Fender & Mendéz, 2002).

Although extensive optical and radio monitoring of the source has provided the basic parameters to describe the disk-jet system, there are very few observation in X-rays. In X-rays, SS 433 is a relatively weak source and is not generally observable in hard X-rays beyond ~ 30 keV. Previous observations by EXOSAT, Ginga, ASCA confirmed the existence of the Doppler-shifted X-ray emission lines (Watson et al. 1986; Yuan et al. 1995; Kotani et al. 1994). The shifting of the Fe-line was found to be consistent with the predictions of the kinematic model. This therefore indicated that the X-ray emitting material is physically associated with the jets. Recently, the Chandra observation of SS 433 spectrum (Marshall et al. 2002, Namiki et al. 2003) shows very much complex behaviour with a large number of blue and red shifted lines. Kinematic model was also established, but higher velocity was required for the line emitting gases. Iron line emission from the extended region of the jet has also been observed by Chandra (Migliari, Fender and Méndez, 2002).

In the present paper, we report results obtained using the RXTE satellite, compiling archival data as well as TOO data triggered by us. Most importantly, for the first time, the

spectrum obtained during (a) the *inferior conjunction* (when the central compact object and the base of the jet is blocked exactly by the companion; i.e., the orbital phase $\phi = 0$) and at the same time, when the precessional phase, ψ was also 0 and (b) the *superior conjunction* (when the companion is hidden by the disk and the jet is completely exposed to us, i.e., the orbital phase $\phi = 0.5$) and at the same time, when the precessional phase, ψ was also 0 are presented and analyzed. In these special days, the jet was directly pointing towards us emitting lines with the highest possible line shifts. These data were obtained on Oct. 2nd, 2003 and on Mar. 13th, 2004. Because of lower energy resolution of RXTE/PCA instrument ($< 18\%$ at 6keV), it is not often easy to identify the exact source of the lines and line flux would also be inaccurate due to blending with other lines. Fortunately comparing results with the earlier observations by ASCA (Kotani et al. 1996) and Chandra (Marshall et al. 2002, Namiki et al. 2003) the identification became easier.

In the next section, we present the Tables containing a log of observations analysed by us and the results of our analysis. We also present the light curves of some of these observations. In Section 3, we present fits of the spectrum obtained by us at three epochs, including the ones at the inferior and the superior conjunctions. We also show how the line energy (including red/blue shifts) match with the shifts predicted from the kinematic model. In Section 4, we discuss the possibility of regular X-ray flares in this system by comparing RXTE/ASM results. Finally, in Section 5, we draw our conclusions.

2 OBSERVATIONS

SS 433 was pointed at several times by Proportional Counter Array (PCA) detectors on board RXTE satellite. The PCA contains five (0 ... 4) Proportional Counter Units (PCUs). We concentrate on observations taken since November, 2001. In order to avoid biasing the analysis, we selected only those observations which were taken by the same units of PCA detector, namely, 2 & 3. We made the analysis by adding data from these two PCUs together. A log of these observations is given in Table 1. The first Column gives the log of observation and the second column gives the date and time when the observation begins (in MJD) along with the RXTE Observation ID. To calculate the precessional phase (ψ) and orbital phase (ϕ), at the beginning time of these observations, we adopt the following ephemeris (Goranskii et al. 1998): HJD 2451458.12 + 162.15E for ψ and HJD 2450023.62 + 13.0821E for ϕ . These are given in Column 3. Observations I (made on Oct. 2nd, 2003) and observation K (made

on Mar. 13th, 2004) had $\phi \sim 0.0$ and $\phi \sim 0.5$ respectively both having $\psi \sim 0$. TOO observations G-L were triggered at our request. A recent TOO data (Observation M made on 25th of March, 2004) is also included. We also re-analysed the archival data of Nov. 2001. The spectra were fitted with a thermal bremsstrahlung (TB) and iron line(s) and the temperature is given in Column 4 (See next section for details of the fitting procedure.) The total integrated flux of X-rays in 3 – 25keV range in units of $10^{-10}\text{ergs cm}^{-2} \text{sec}^{-1}$ is presented in Column 5. During the recent superior conjunction when the jet was exposed to us (March 13th, 2004), the net flux was found to be more than twice as high compared to that in the inferior conjunction (Oct. 2nd, 2003). The net flux remained high for at least another orbital period indicating that SS 433 may be undergoing a weak flaring activity.

One can compare the X-ray flux by RXTE observations with earlier results of EXOSAT (Watson et al. 1986) and Chandra (Namiki et al. 2003). For instance, in the same unit as in Table 1, at $\psi \sim 0$, the 2-6keV flux of EXOSAT was 1.5 while our fluxes vary from 1.07 – 1.6 depending on ϕ in the same range of 2-6keV. Chandra, on the other hand, found the total integrated flux in 1-10keV at $\psi \sim 0.4$ to be 0.9. We did not make any observation at this phase, and our result at phase $\psi \sim 0$ in 3 – 9keV is 1.6 – 3. Thus the fluxes measured by RXTE are comparable to previous measurements, although an actual comparison requires observation to be carried out at the same precessional and orbital phases as well.

According to the kinematic model (Abell & Margon, 1979; Margon 1984), the red/blue shifts z of the emitted line are computed from:

$$1 + z = \gamma(1 \pm v_j \sin\theta \sin i \cos\psi \pm v_j \cos\theta \cos i), \quad (1)$$

where, v_j (taken here to be 0.2602, see, Gies et al. 2002) is the proper velocity of the line emission in units of velocity of light c from the jet matter, $i = 78^\circ.83$ is the angle that the normal to the disk subtends with the line of sight, $\theta = 19^\circ.85$ is the angle subtended by the jet with the disk-normal, ψ is the precession phase taken from Table 1. In this convention, a negative z corresponds to blue-shifts and a positive z corresponds to red-shifts. Note that we use the definition of ψ such that $\psi = 0$ when the shifts of the blue and red-jets are maximally different as in Margon (1984). In Table 2, we presented these values in Column 2. The significance of the Columns 3-10 will be discussed in the next Section.

Figure 1 shows background-subtracted light curves for the observations G, H, I, K and L (marked). The error-bars obtained from $\text{counts}^{1/2}/\text{binsize}$ are included. We extracted the light curves both from the GoodXenon and Standard2 mode data. The binsize was chosen

Table 1. RXTE Observation log^a

Obs. log	MJD(UT)	ψ	kT_b	Flux ^b
	(Date) ObsID	ϕ	(keV)	
A	52222(07:10:27) (09th Nov'01)	0.716	23.02	2.824
	60058-01-01-00	0.106	+1.19 -1.10	
B	52224(06:47:29) (11th Nov'01)	0.728	27.03	2.966
	60058-01-03-00	0.257	+1.85 -1.56	
C	52227(06:11:11) (14th Nov'01)	0.747	26.91	3.436
	60058-01-06-00	0.485	+1.62 -1.41	
D	52228(06:00:16) (15th Nov'01)	0.753	24.01	3.480
	60058-01-07-00	0.561	+1.45 -1.19	
E	52234(08:03:15) (21st Nov'01)	0.790	25.93	2.786
	60058-01-12-00	0.025	+7.53 -4.44	
F	52235(07:54:37) ^c (22nd Nov'01)	0.796	27.63	3.547
	60058-01-13-00	0.102	+1.83 -1.54	
G	52545(16:57:34) (27th Sep'02)	0.705	13.92	2.375
	70416-01-01-01	0.747	+0.57 -0.71	
H	52914(16:41:24) (01st Oct'03)	0.981	17.23	3.183
	80429-01-01-00	0.956	+0.71 -0.66	
I	52914(05:20:00) ^d (02nd Oct'03)	0.984	17.50	2.993
	80429-01-01-01	0.997	+0.91 -0.81	
J	53077(18:55:12) (12th Mar'04)	0.986	51.35	7.557
	90401-01-01-01	0.423	+5.00 -3.18	
K	53078(18:33:04) ^e (13th Mar'04)	0.992	44.93	6.912
	90401-01-01-00	0.498	+2.60 -2.19	
L	53079(18:12:00) (14th Mar'04)	0.998	40.10	6.778
	90401-01-01-02	0.574	+1.99 -1.72	
M	53089(01:51:28) (25th Mar'04)	0.062	46.41	7.592
	90401-01-02-01	0.363	+4.17 -3.40	

a) Error bars in temperature are at 90% confidence level; b) Flux is in the range (3 – 25keV) in units of 10^{-10} ergs cm^{-2} sec^{-1} ; c) Massive radio flare observed (Safi-Harb & Kotani, 2003); d) TOO observation at $\psi \sim 0$ and $\phi \sim 0$; e) TOO observation at $\psi \sim 0$ and $\phi \sim 0.5$

to be 16s. The panel of Observation G was already presented in Chakrabarti et al. (2003), where, the multi-wavelength campaign was reported. It was especially mentioned that this observation showed a very rapid change in counts (around 15%) in a matter of minutes. The panels of Observations H and I show the light curves of Oct. 1st, 2003 and Oct. 2nd 2003 respectively, the second observation being at the donor inferior conjunction. While these light curves also show similar rapid variation, there appears to be an overall modulation of X-ray counts. At least 25% of the flux modulation occurs in 6-7 minutes timescale. Given

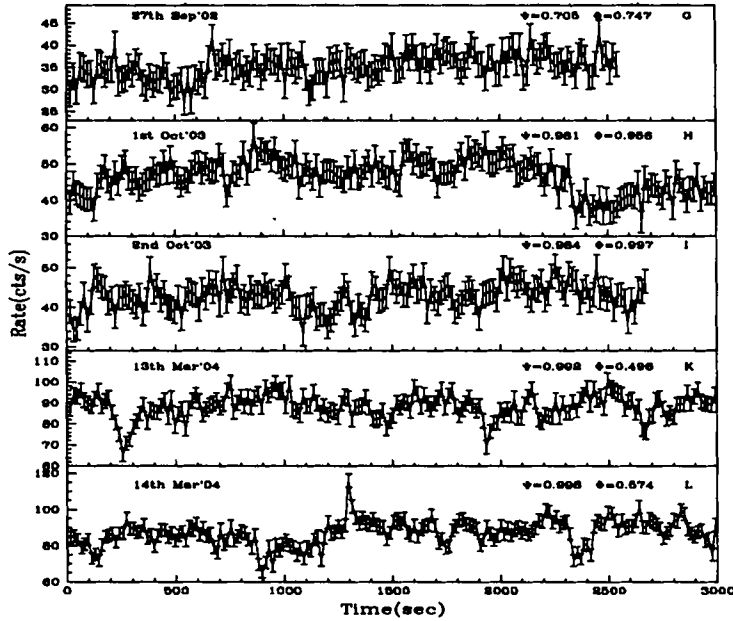


Fig. 1: X-ray light curves (background subtracted) of SS433 extracted from **Standard2** data for observations G , H , I, K and L (marked). Along X-axis is time (in seconds) and along Y-axis is the count rate.

that the companion star is directly blocking the base of the jet, and the X-rays received may be passing through the star's atmosphere this could even be due to some kind of oscillation in the atmosphere of the star. By analysing both the GoodXenon and Standard2 mode data, we could not detect any quasi-periodicity in the power density spectra (PDS). The panel of Observation K shows the light curve of March the 13th, 2004 when the companion was right behind the disk. The jet pointing towards the observer had the highest blue-shift and the base of the jet was totally exposed. The X-ray flux was more than twice as high compared to average flux of past observations. The X-ray count was also much higher on this date and a variation of $\sim 30\%$ was observed in a matter of few minutes. Similar result persisted on the next day (Observation L of 14th of March, 2004; see, Fig. 1) when short time-scale variability was more prominent. In fact, the X-ray flux remained high even after one orbital period (Observation M).

In the next section, we analyze line emissions from the RXTE observations listed in Table 1.

Table 2. Results^a of RXTE observations of SS 433

Obs. log	z_{blue} z_{red}	χ^2_1 (χ^2 /dof)	χ^2_2 (χ^2 /dof)	P_{F-stat}	E_{obs} (keV)	σ_{line} (keV)	F_{line}^b ($\times 10^{-3}$)	z FeXXVI	z FeXXV
A	0.005 0.066	0.742 (35.6/48)	0.633 (28.5/45)	1.7×10^{-2} (2.1 σ)	$6.822^{+0.038}_{-0.039}$ -	$0.692^{+0.054}_{-0.053}$ -	$2.536^{+0.144}_{-0.135}$ -	$0.020^{+0.005}_{-0.005}$ -	-0.021 -
B	-0.001 0.073	0.966 (46.4/48)	0.682 (31.4/46)	4.9×10^{-4} (2.8 σ)	$6.905^{+0.138}_{-0.153}$ $6.819^{+0.002}_{-0.001}$	$1.050^{+0.209}_{-0.169}$ 0.309 ± 0.0	$2.026^{+0.269}_{-0.271}$ $0.808^{+0.330}_{-0.460}$	$0.009^{+0.019}_{-0.021}$ 0.021	-0.033 $-0.020^{+0.0003}_{-0.0002}$
C	-0.012 0.083	1.261 (60.5/48)	0.775 (35.6/46)	5.1×10^{-6} (3.5 σ)	$6.976^{+0.081}_{-0.088}$ $6.891^{+0.004}_{-0.099}$	0.125 ± 0.0 $1.159^{+0.132}_{-0.114}$	$0.613^{+0.164}_{-0.176}$ $3.216^{+0.262}_{-0.246}$	$-0.002^{+0.012}_{-0.013}$ 0.011	-0.044 $-0.031^{+0.012}_{-0.015}$
D	-0.015 0.087	1.819 (87.3/48)	1.265 (58.2/46)	3.6×10^{-4} (2.9 σ)	$6.986^{+0.067}_{-0.074}$ $6.837^{+0.128}_{-0.170}$	0.246 ± 0.0 $1.209^{+0.198}_{-0.160}$	$0.894^{+0.184}_{-0.213}$ $2.632^{+0.305}_{-0.271}$	$-0.003^{+0.009}_{-0.011}$ 0.018	-0.045 $-0.023^{+0.019}_{-0.025}$
E ^c	-0.036 0.107	1.373 (65.9/48)	1.027 (47.2/46)	1.7×10^{-3} (2.6 σ)	$7.281^{+0.136}_{-0.154}$ -	$1.227^{+0.184}_{-0.171}$ -	$3.212^{+0.745}_{-0.595}$ -	$-0.045^{+0.019}_{-0.022}$ -	-0.089 -
F ^d	-0.039 0.111	1.011 (48.5/48)	0.745 (34.3/46)	3.3×10^{-4} (2.9 σ)	$6.950^{+0.092}_{-0.104}$ $6.876^{+0.119}_{-0.147}$	0.257 ± 0.0 $1.128^{+0.206}_{-0.168}$	$0.708^{+0.198}_{-0.264}$ $2.403^{+0.290}_{-0.268}$	$0.002^{+0.013}_{-0.015}$ 0.013	-0.039 $-0.029^{+0.018}_{-0.022}$
G	0.011 0.060	1.202 (54/45)	0.831 (35.7/43)	1.4×10^{-4} (3.0 σ)	$7.012^{+0.106}_{-0.105}$ $6.802^{+0.104}_{-0.125}$	$0.939^{+0.140}_{-0.118}$ 0.125 ± 0.0	$2.059^{+0.113}_{-0.228}$ $0.518^{+0.163}_{-0.181}$	$-0.007^{+0.015}_{-0.015}$ 0.023	-0.049 $-0.018^{+0.075}_{-0.018}$
H	-0.102 0.173	1.596 (76.6/48)	0.789 (36.3/46)	2.0×10^{-7} (3.9 σ)	$7.722^{+0.099}_{-0.108}$ $5.359^{+0.186}_{-0.212}$	$1.191^{+0.107}_{-0.099}$ 0.544 ± 0.0	$2.747^{+0.259}_{-0.227}$ $0.647^{+0.135}_{-0.164}$	$-0.108^{+0.014}_{-0.015}$ 0.230	-0.155 $0.198^{+0.028}_{-0.032}$
I ^e	-0.103 0.174	1.691 (81.2/48)	0.845 (38.9/46)	1.9×10^{-7} (4.0 σ)	$7.731^{+0.115}_{-0.129}$ $5.221^{+0.238}_{-0.262}$	$1.181^{+0.128}_{-0.119}$ 0.615 ± 0.0	$2.594^{+0.308}_{-0.266}$ $0.748^{+0.166}_{-0.173}$	$-0.110^{+0.016}_{-0.018}$ 0.250	-0.157 $0.219^{+0.035}_{-0.039}$
J	-0.103 0.174	3.768 (180.9/48)	1.693 (76/45)	1.5×10^{-8} (4.3 σ)	$7.693^{+0.085}_{-0.070}$ $5.333^{+0.146}_{-0.146}$	$1.073^{+0.065}_{-0.069}$ $0.567^{+0.211}_{-0.167}$	$6.149^{+0.367}_{-0.388}$ $1.487^{+0.556}_{-0.376}$	$-0.104^{+0.012}_{-0.010}$ 0.234	-0.151 $0.202^{+0.022}_{-0.022}$
K ^f	-0.103 0.174	3.570 (171.4/48)	1.628 (73.3/45)	2.1×10^{-8} (4.2 σ)	$7.587^{+0.054}_{-0.032}$ $5.323^{+0.132}_{-0.141}$	$1.011^{+0.056}_{-0.055}$ $0.495^{+0.148}_{-0.132}$	$5.731^{+0.282}_{-0.284}$ $1.103^{+0.305}_{-0.244}$	$-0.089^{+0.008}_{-0.005}$ 0.236	-0.135 $0.204^{+0.020}_{-0.021}$
L	-0.103 0.175	3.176 (152.5/48)	1.597 (72.9/45)	1.8×10^{-7} (4.0 σ)	$7.523^{+0.065}_{-0.058}$ $5.352^{+0.136}_{-0.069}$	$1.031^{+0.061}_{-0.061}$ $0.462^{+0.148}_{-0.154}$	$5.804^{+0.293}_{-0.322}$ $1.010^{+0.336}_{-0.247}$	$-0.080^{+0.009}_{-0.008}$ 0.231	-0.126 $0.199^{+0.020}_{-0.010}$
M	-0.096 0.168	1.454 (69.8/48)	0.845 (38/45)	4.4×10^{-6} (3.5 σ)	$7.570^{+0.114}_{-0.099}$ $5.453^{+0.209}_{-0.207}$	$1.014^{+0.104}_{-0.104}$ $0.439^{+0.234}_{-0.237}$	$6.202^{+0.569}_{-0.591}$ $1.204^{+0.589}_{-0.446}$	$-0.087^{+0.016}_{-0.014}$ 0.217	-0.132 $0.184^{+0.031}_{-0.031}$

a) Error bars are at 90% confidence level; b) Total photons $\text{cm}^{-2} \text{sec}^{-1}$ in the line; c) the fitting of the lower energy component was uncertain; d) Massive radio flare observed (Safi-Harb & Kotani, 2003); e) TOO observation at $\psi \sim 0$ and $\phi \sim 0$; f) TOO observation at $\psi \sim 0$ and $\phi \sim 0.5$

3 SPECTRAL FITS OF RXTE OBSERVATIONS

Recently, Marshall et al. (2002), using Chandra observation, pointed out that the lines emitted do show blue- and red-shifted components. Migliari et al. (2002) reported Chandra observation of iron lines emitted from extended regions of the jets. However, similar observations from RXTE have not been reported so far.

The data reduction and analysis was performed with the software HEASOFT 5.1 consisting of FTOOLS 5.1 and XSPEC 11.1. We extracted energy spectra from PCA Standard-2 data. For each spectrum, we have followed the standard procedures to generate the background spectra and PCA detector response matrices. We performed fitting the spectra simultaneously with different combination of models such as TB, line contribution, disk-blackbody

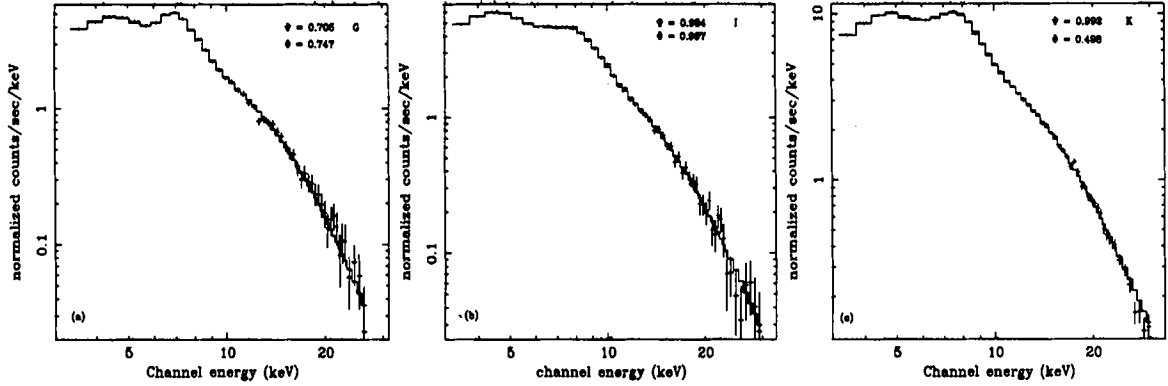


Fig. 2a-c: Raw X-ray spectra with the folded model of SS 433 on (a) obs. G on 27th September 2002, (b) obs. I on 2nd of October, 2003 (inferior conjunction) and (c) obs. K on 13th of March, 2004 (superior conjunction). Along the X-axis is energy (in keV) and along Y-axis is the normalized photon counts ($\text{sec}^{-1}\text{keV}^{-1}$). Precessional (ψ) and orbital (ϕ) phases are marked.

spectrum and the power-law spectrum modified by interstellar absorption (WABS model, Morrison & McCammon, 1983).

During fitting, we find that the so-called ‘traditional model’ are best fitted with a minimum reduced χ^2 value. We find good fitting while keeping the hydrogen column density fixed at $2.4 \times 10^{22}\text{cm}^{-3}$ except on Oct. 1st-2nd, 2003, when $1.6 \times 10^{22}\text{cm}^{-3}$ was needed. We did not set any systematic error. We also found that reduced χ^2 is smaller if two lines are included instead of a single line. We have included in the Table 2 the normal χ^2 values and the degrees of freedom (dof) as well as the reduced χ^2 when one (denoted by χ_1^2 in Column 3) or two (denoted by χ_2^2 in Column 4) lines are fitted. We find that χ_2^2 is always smaller than χ_1^2 .

In Fig. 2(a-c), we present raw spectra of the observations G, I, and K showing a distinct bump at around 6 – 7keV indicating the presence of Fe lines. On them, we superpose our folded spectra. While in (a), the precession/orbital phases were generic (see Table 1), in (b), the phases were very close to zero when the companion blocked the central compact object and in (c), the precession phase is close to zero but the orbital phase is close to 0.5.

For all observation, for the best fitting, two additional line features were tried out on the top of TB fit. In Fig. 3(a-c), we present the unfolded spectra of the same observations, i.e., G (Fig. 3a), I (Fig. 3b) and K (Fig. 3c) respectively with different model components. The requirement of two line fitting in the spectrum is tested using the F-statistics with the *ftest* task within XSPEC. P_{F-stat} is the F-statistic probability for the addition of the 2nd Gaussian line to the same model with a single line. This is given in Column 5 of Table 2. The significance is given under this P value and is denoted in parenthesis. Based on the

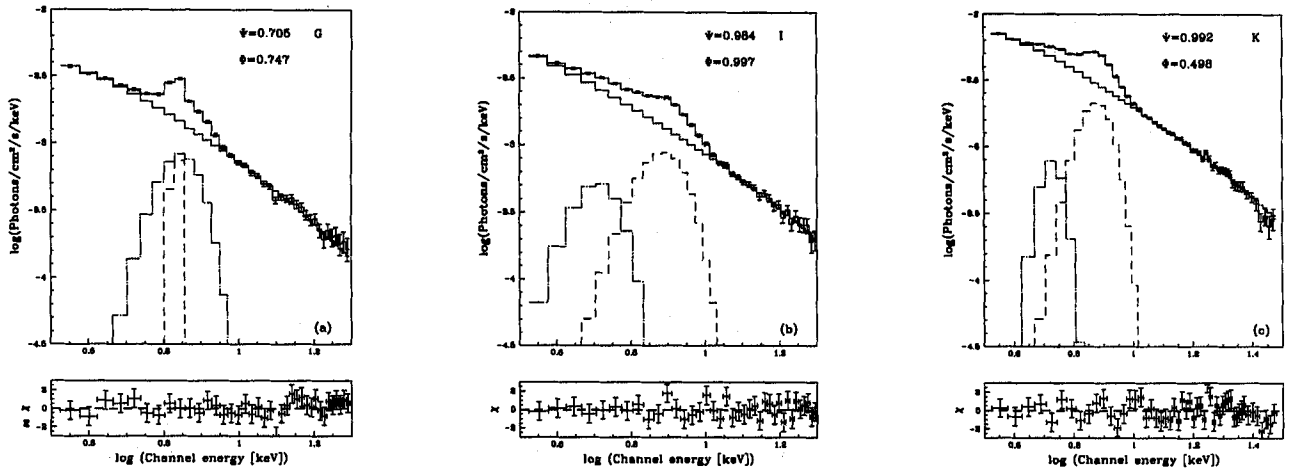


Fig. 3a-c: Unfolded X-ray spectrum of SS 433 with different model components for the same observations presented in Figs. 2(a-c). The model components are: thermal bremsstrahlung (solid histogram) and two Fe lines (dashed and long dash-dotted curves). In lower panels, residuals have also been shown.

significance value we find that all the observations favour the two-line model except Obs. A and Obs. E as these fits are significant only at 2.1σ and 2.6σ levels respectively. Indeed, we observe that on MJD 52234 (Observation E), the X-ray flux is very low. Given that it takes about a day for the jet to arrive from the X-ray emitting region to the radio emitting region, it is possible that the massive radio flare on MJD 52335 (Observation F. See, Safi-Harb & Kotani 2003) actually was ejected on the previous day. Similar behaviour of anti-correlation between Radio and X-ray fluxes has been reported by Mirabel & Rodriguez (1999). During the final fit of the observations B, C, D, F and G, we froze the narrower line width. In our fit, there was no signature of any soft-X-ray bump characteristics of a Keplerian disk. As has been pointed out earlier (Chakrabarti et al. 2002), there is evidence that the flow is actually from a wind accretion and thus possibly sub-Keplerian. This is also required for the production of the observed jets (Chakrabarti 1999). The line energies (in keV) we obtained are given in Column 6. The residuals given in the lower panels of Figs. 3(a-c) indicate that the fits are satisfactory. Note that in Observations J-K-L, there are significant contributions from high energy ($\sim 30\text{keV}$) photons and the flux is also much higher (see, Table 1). This behaviour persisted even after one orbital period (Observation M). Columns 7 and 8 give the line width (keV) and line strength (in units of photons $\text{cm}^{-2} \text{s}^{-1}$) respectively for each line. It has been noted earlier (Kotani et al. 1996, Marshall et al. 2002, Namiki et al. 2003) from the ASCA and Chandra observations that the FeXXV lines are on an average 2-3 times (or more) stronger compared to FeXXVI lines. In our RXTE observations C, D and F (when

$\psi \sim 0.7$), we find roughly a similar result when we identify both the lines to come from the approaching jet components. However, in observations B and G, where the lines were similarly identified as above, the FeXXV line is found to be weaker compared to the FeXXVI line. In observations H-M the jets are pointing towards the observer ($\psi \sim 0$) and we find that two lines are roughly agreeing with the prediction of the kinematic model provided the line with higher energy (brighter component) is identified with FeXXVI of the approaching jet and the lower energy (dimmer component) is identified with FeXXV of the receding jet. In Observation E, we could fit with only one line, possibly because of certain disturbances of the inner disk and the jet one day ahead of the massive radio flare reported by Safi-Harb & Kotani (2003).

It is pertinent to ask whether one could have fitted the spectra with one Fe line and multiple TB components instead of the way we fitted so far (single TB with two Fe lines). We have tried this for the thin Fe line occurring at low energy and found that the fit is deteriorated. For instance, for Observation K, we replaced the Fe line of 5.323keV by the TB of plasma electron temperature 0.5keV and 0.8keV respectively (These temperatures were chosen in a way that the low energy cut-off is at around 6 keV.) and we found the reduced χ^2 to be 3.586 and 3.862 respectively. However, with two Fe lines, the reduced χ^2 is 1.628 (see, Table 2). We therefore do not find evidence for multi-temperature bremsstrahlung components in our analysis.

In Fig. 4(a-b), we drew contour plots of $\Delta\chi^2$ for Obs. C in the (a) line width (σ) vs. line energy (E_{obs}) plane and (b) line width (σ) vs. line flux (F_{line}) plane to show the correlations. Similarly, in Fig. 5(a-b), we drew the contour plots of $\Delta\chi^2$ for Obs. K in the line width (σ) vs. line energy (E_{obs}) plane for the (a) broad line and (b) narrow line. The contours are of 68%, 90% and 99% confidence level. It can be seen that the lines are resolved at the 90% confidence level.

While comparing with the absolute line strength with previous observations, we note that Chandra (Marshall et al. 2002) obtained a red-jet FeXXV line ($1s2p - 1s^2$) flux of ~ 0.13 in the same unit chosen in Table 2, while we obtained the value of ~ 1.2 (Observation M), both observations being at a similar precessional phase of $\psi \sim 0.06$ if the same ephemeris (Goranskii et al. 1998) were used. This high value may be because (a) the SS 433 was intrinsically brighter in X-ray in our observation and (b) blending of lines which RXTE was unable to resolve especially there could be always a significant contribution from the neutral

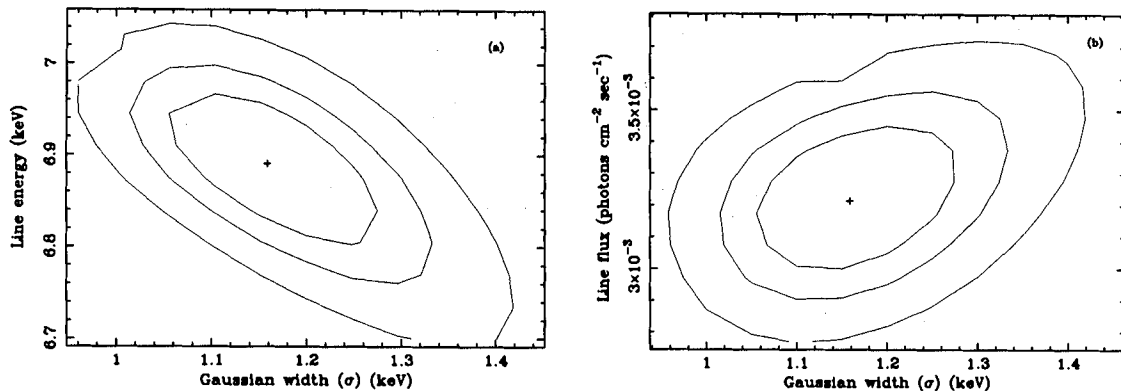


Fig. 4a-b: Two parameter confidence region of the broad FeXXV (a) line energy vs. Gaussian width and (b) line flux vs. Gaussian width from spectral fitting to the RXTE/PCA data of Obs. C. Contours correspond to 68%, 90% and 99% confidence.

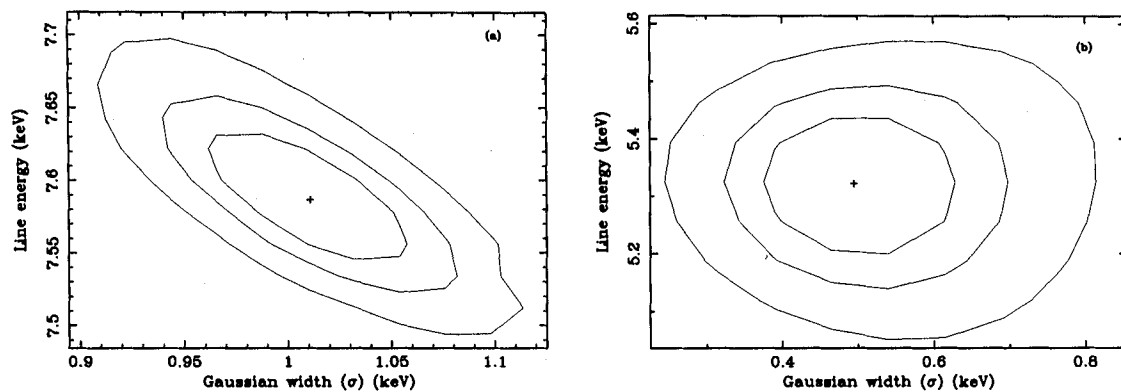


Fig. 5a-b: Two parameter confidence region of the (a) broad FeXXVI line energy vs. Gaussian width and (b) narrow FeXXV line energy vs. Gaussian width from the spectral fitting to the RXTE/PCA data of Obs. K. Contours correspond to 68%, 90% and 99% confidence.

Fe line emitted from regions at rest in the observed frame (Kotani et al. 1996, Marshall et al. 2002).

In Columns 9-10 we present the computed red- and blue-shift factors (z) of the observed lines, had their origins been the FeXXVI ($\text{Ly } \alpha$ transition at 6.965 keV) or the FeXXV line ($1s2p - 1s^2$ transition at 6.684 keV), respectively. In bold faced letters we have highlighted the probable identification of the lines. Generally speaking, the line with higher energy could be identified with the blue-shifted FeXXVI line quite satisfactorily (Fig. 6a). However, the line with lower energy could be fitted with red-shifted FeXXV lines when $\psi \sim 0$ and with blue-shifted FeXXV line elsewhere (Fig. 6b). The error-bars (at 90% confidence level) drawn in Fig. 6(a-b) are given in Table 2. The data has been folded with 162.15d periodicity for

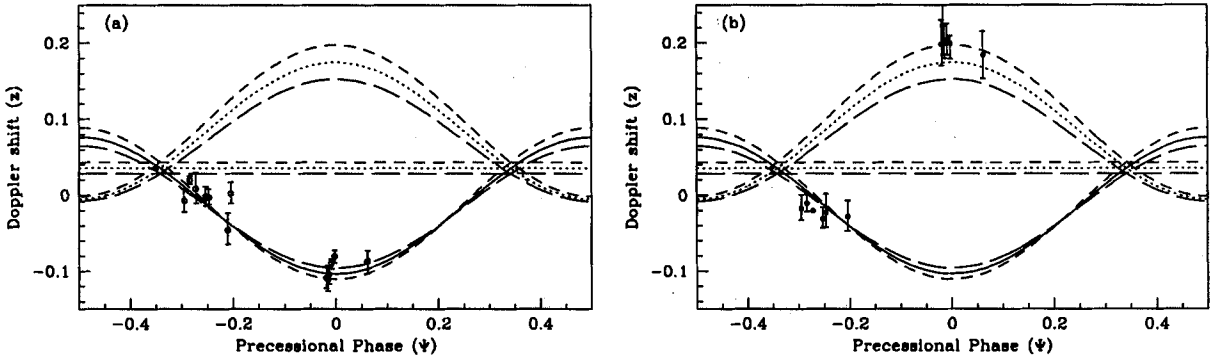


Fig. 6a-b: Observed Doppler shifts (y-axis) of (a) FeXXVI and (b) FeXXV lines from the approaching (solid curve) and receding (dotted curve) jets super-imposed on the prediction from the kinematic model with standard parameters (see text) as a function of the precessional phase ψ . Also shown in short-dashed and long-dashed curves the shifts obtained by respectively reducing and enhancing the jet velocity by ten percent. The horizontal curves represent intrinsic red-shifts for the corresponding jet velocities. See text for detailed criteria used in line-identifications. All the observations were plotted against the same precessional phase for clarity of the plot of the lines.

convenience. Superimposed are the solid and dotted curves representing the Doppler shifts (Eq. 1) of the jet component pointing towards us and the component pointing away from us respectively. Though the poor resolution in RXTE/PCA detector may be the main cause of the deviation of the fitted shifts from that of the kinematic model, one can assume that the lines energies are correct in order to estimate the possible variation of jet velocity, if any, which may be responsible for this deviation, when other system parameters are kept unchanged. We plot the short and long-dashed curves in Figs. 6(a-b) for $v_j = 0.286$ and $v_j = 0.234$ respectively which are 10% away from the velocity $v_j = 0.2602$ of the standard model. The horizontal lines correspond to the intrinsic red-shifts for these velocities. Since at $\psi \sim 0$, the blue jet seems to have a large scattering of velocity, while the red jet seems to have a higher velocity, we could not conclude with certainty if the jets have truly different velocity than that of the standard kinematic model (e.g., Eikenberry et al. 2001), even though there are reports (e.g., Marshall et al. 2002) that the jet velocity could be higher close to the compact object.

We also examined if the lines could be fitted with NiXXVII ($1s2p - 1s^2$ transition at 7.788 keV). However, except for the lower energy component of observation F, none seems to be satisfactory. It may be noted that near $\psi \sim 0$, RXTE observation showed the evidence of both the components of the jet which has not been reported before.

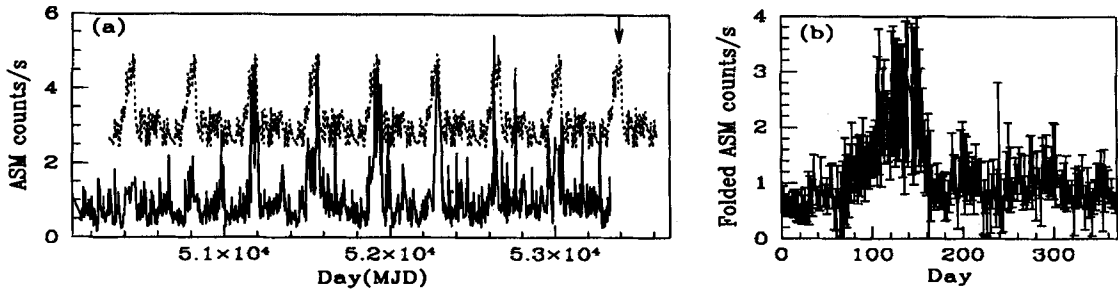


Fig. 7a-b: (a) ASM counts/s of SS 433 since 7th Jan. 1996 till Nov. 26th, 2004. For clarity, we plotted only those points when the count over the background rate is positive. We superpose (with a shift of 2/s along y-axis) the mean light-curve when folded around 368 days to show the periodic nature of a strong flare which repeats after every 368 days interval. We predict the next flare to peak around Jan. 22nd, 2005 which is denoted by an arrow. (b) Average ASM light curve obtained by folding around 368 days showing the presence of the strong flare.

4 X-RAY FLARES IN SS 433?

During the recent TOO campaign of 12-14th March, 2004, the X-ray flux is found to be very high. This may indicate that SS 433 was undergoing some kind of weak X-ray ‘flare’. In fact a cursory look at the entire ASM rate profile since 7th Jan. 1996 till Nov. 26th, 2004 (Fig. 7a) where we plotted (solid) only those points when the count over the background rate is positive, shows that there had been a few occurrences of flaring activities in the past. One spike on MJD 52086 was removed as it had a very unusual count (11.5/s). In Fig. 7b, we folded the ASM light curve around 368 days of interval and taken the mean count along with standard deviation as the error bars to indicate that there are indeed some indication of periodicity. This mean is plotted as dashed curve in Fig. 7a, just to show that the periodicity is real. While there are at least two other weaker peaks with this periodicity, they do not appear to be significant. By an arrow we indicated the next time when the flares in SS 433 is expected. From the width ~ 50 d of the stronger flare (with the average count rate larger than 2/s), we predict that the next strong flare should occur during Dec. 21st, 2004 till Feb. 8th, 2005, with the highest peak on Jan. 22nd, 2005.

5 CONCLUSION

In the present paper, we analyzed a set of RXTE observations of SS 433 some of which were triggered by us. We presented the results of opportune moments at inferior ($\phi \sim 0$) and superior ($\phi \sim 0.5$) conjunctions when the jets had the highest possible Doppler shifts ($\psi \sim 0$; Observations I and K respectively). We observed a considerable change in the

emitted flux. In particular, we observed a very high flux (more than twice the average flux seen in other days) in Observations J,K, L and M, the last one being taken one orbital period later than the previous one. We did not find any evidence of any short time-scale quasi-periodicity in the PCA light curves except perhaps a modulation at around 25% level in time-scales of a few minutes, especially when the companion blocked the base of the jet. It may be due to the oscillation of the atmosphere of the companion. During the superior conjunction the source was highly variable in a very short time-scale < 100 s. The spectra were best fitted with a model consisting of thermal bremsstrahlung component and emission lines. No signature of any Keplerian disk was found, possibly because of the obscuration of the inner part by matter gathered from the mass-loss of the companion. We generally found that two lines were required to fit the spectrum. The higher energy lines were generally identified with blue-shifted FeXXVI. The lower energy lines were generally identified with FeXXV blue-shifted or red-shifted depending on the precessional phases.

Since RXTE/PCA detectors have poor energy resolution ($< 18\%$ at 6keV) compared to ASCA and Chandra, we could not be sure if the deviation of the Doppler-shifts from the value predicted by the kinematic model is solely due to deviation from the standard jet-parameters, i.e., the velocity and orientation angles. It is possible that the jet velocity may be different (as inferred by Marshall et al. 2002 using Chandra observation) or there could be some effects due to the nodding motion which we did not include in our fitting. Furthermore, the neutral Fe line at $z = 0$ can also contribute to the flux (Kotani et al. 1996, Marshall et al. 2002) We observed that on Oct. 2nd, 2003, the X-ray flux is lower (less than 10%) compared to that observed on Oct. 1st, 2003, only twelve hours earlier. This could be an indication that the X-ray source is progressively blocked by the companion at the conjunction is reached. Similarly, on March 13th, 2004 (Observation K) the exposed jet was more than twice as bright and this trend continued even after one orbital period (Observation M). These may also indicate that the base of the jet is perhaps the major source of X-rays in SS 433.

From the ASM data we identified some flaring phenomena in SS 433, the first report of its kind. From the folded ASM light curve we find an indication that a strong and a long duration (~ 50 d) X-ray flare of a periodicity of 368d may be present. If correct, this time-scale will be yet another puzzle which must be explained in order to have a complete understanding of SS 433. We predict that the next flare will take place during Dec. 21st, 2004 till Feb. 8th, 2005.

ACKNOWLEDGMENTS

We thank Jean Swank for giving us adequate RXTE time and an anonymous referee for suggesting several improvements in data analysis. The research of AN is partly supported by DST grant No. Grant No. SP/S2/K-15/2001.

REFERENCES

- Abell, G. O., & Margon, B. 1979, *Nature*, 279, 701
- Borisov, N. V., & Fabrika, S. N. 1987, *Soviet Ast. Lett.*, 13, 200
- Chakrabarti, S. K., 1999, *A&A*, 351, 185
- Chakrabarti, S. K., Goldoni, P., Wiita, P.J., Nandi, A., Das, S. 2002, *ApJ*, 576, L45
- Chakrabarti, S. K., Pal, S., Nandi, A., Ananda Rao, B. G. & Mandal, S. 2003, *ApJ*, 595, L45
- Eikenberry, S. S. et al. 2001, *ApJ*, 561, 1027
- Gies, D. R., McSwain, M. V., Riddle, R. L., Wang, Z., Wiita, P. J., & Wingert, D. W. 2002, *ApJ*, 566, 1069
- Goranskii, V. P., Esipov, V. F., & Cherepashchuk, A. M. 1998, *Astron. Rep.*, 42, 209
- Kotani, T., Kawai, N., Aoki, T. et al. 1994, *PASJ*, 46, L147
- Kotani, T., Kawai, N., Matsuoka, M. & Brinkman, W. 1996, *PASJ*, 48, 619
- Namiki, M., Kawai, N., Kotani, T. & Makishima, K. 2003, *PASJ*, 55, 281
- Margon, B. 1984, *ARA&A*, 22, 507
- Marshall, H. L., Canizares, C.R. & Schulz, N.S. 2002, *ApJ*, 564, 941
- Migliari, S., Fender, R. & Méndez, M. 2002, *Sci.* 297, 1673
- Mirabel, I. F. & Rodríguez, L. F., 1999, *ARA&A*, 37, 409
- Morrison, R. & McCammon, D., 1983, *ApJ*, 270, 119
- Safi-Harb, S. & Kotani, T., 2003, in *New Views of Microquasars*, P. Durouchaux, Y. Fuchs, J. Rodríguez (Eds.), 279 (Centre for Space Physics: Kolkata)
- Vermeulen, R. C. et al. 1993a, *A&A*, 270, 177
- Vermeulen, R. C. et al. 1993b, *A&A*, 270, 204
- Watson, M. G., Stewart, G. C., Brinkmann, W., King, A. R. 1986, *MNRAS*, 222, 261
- Yuan, W., Kawai, N., Brinkmann, W., Matsuoka, M. 1995, *A&A*, 297, 451

Class transitions and two component accretion flow in GRS 1915+105

S. K. Chakrabarti^{1,2}, A. Nandi¹, A. K. Chatterjee³, A. K. Choudhury³, and U. Chatterjee³

¹ S. N. Bose National Centre for Basic Sciences, Salt Lake, Kolkata 700098, India
e-mail: chakraba@bosc.bose.res.in

² Centre for Space Physics, Chalantika 43, Garia Station Rd., Kolkata, 700084, India

³ Centre for Space Physics (Malda Branch), Atul Market, Malda 732101, India
e-mail: chakraba@bose.res.in; space_phys@vsnl.com

Received 14 July 2004 / Accepted 14 October 2004

Abstract. The light curve of the galactic micro-quasar GRS 1915+105 changes in at least thirteen different ways which are called classes. We present examples of the transitions from one class to another as observed by the IXAE instrument aboard the Indian Satellite IRS-P3. We find that the transitions are associated with changes in photon counts over a time-scale of only a few hours and they take place through unknown classes. Assuming that the transitions are caused by variation of the accretion rates, this implies that a significant fraction of the matter must be nearly freely falling in order to have such dramatic changes in such a short time.

Key words. black hole physics – X-rays: binaries – radiation mechanisms: general – X-rays: individuals: GRS 1915+105

1. Introduction

GRS 1915+105 is well known for its diversity of light curves (e.g. Morgan et al. 1997; Belloni et al. 2000). RXTE has pointed at it numerous times and yet the light curve has remained largely unpredictable. Belloni et al. (2000), in a model independent way, classified most of the light curves into twelve classes which are designated as χ , α , ν , β , λ , κ , ρ , μ , θ , δ , γ and ϕ . Naik et al. (2002a) showed that there is another independent class called ω . Although the light curve was observed to change from one class to another, the actual transition was never reported and therefore, the actual physical process which triggers a specific class transition has never been investigated.

It was predicted in several earlier papers using the advective flow paradigm (Chakrabarti & Nandi 2000; Nandi et al. 2000; Chakrabarti et al. 2002) that variation of the Keplerian and the sub-Keplerian accretion rates might cause class transitions. It was pointed out that there are actually five fundamental states differing only by Keplerian and sub-Keplerian accretion rates. Ways in which the transition occurs between these states decide which class would be seen. It was also pointed out that the outflows play a major role in class transitions, since they interact with the soft photons and affect the spectral slopes as well. Recently, Chakrabarti et al. (2004) presented two examples of class transitions from IXAE observations and concluded that a class transition always take place through some unknown class. In many of the classes that GRS 1915+105 exhibits, one could see the presence of Quasi-Periodic Oscillations (QPOs). Very recently, using extensive time-dependent numerical sim-

ulation of accretion flows that include cooling effects, it has been shown (Chakrabarti et al. 2004) that the so-called advective disk paradigm is capable of explaining QPOs very naturally. The prime cause of the quasi periodic oscillations (QPOs) of X-rays from compact objects is found to be quasi-coherent shock oscillations. The post-shock region (i.e., the so-called CENTrifugal pressure supported BOUNDary Layer, or CENBOL) outside a black hole horizon acts as the Compton cloud by intercepting soft photons from a Keplerian disk and reprocessing them to high energies. Along with the shock oscillations, the size of the CENBOL changes and therefore the number of intercepted soft photons oscillates, causing the observed QPO. Power density spectra of these ‘simulated’ light curves directly show how QPOs occur at or near break frequency – a well-known observed phenomenon. The frequency of oscillation is thought to be related to the inverse of the in-fall time-scale (Molteni et al. 1996) and as such should increase with the increase of the sub-Keplerian accretion rate undergoing the shock transition as the cooling rate is increased. This general behaviour has also been observed (Remillard et al. 1999).

In this paper, we present a large number of examples of the “rare” class transitions, all of them being from the Indian satellite data, and analyze what happens during such a transition. In particular, we follow the light-curve, the power density spectra and the photon spectra throughout the transition. We found that: (a) A class transition is invariably accompanied by a significant variation of the average X-ray photon count

Table 1. Class transitions of GRS 1915+105 reported in this paper.

FIGURE	Satellite	Date Time (UT)	Orbit No. obs. ID	Class transition
1.	IXAE	22th June, 1997	1, 3, 5	$\kappa \rightarrow \rho$
		12:12 ^a		
2.	IXAE	25th June, 1997	3, 4, 5	"χ" → ρ
		11:12 ^a		
3.	IXAE	08th June, 1999	2, 3	"χ" → θ
		11:02 ^a		
3.	RXTE	08th June, 1999	40702-01-03-00	"χ" → θ
		13:52		
5.	IXAE	25th June, 2000	2, 3	"ρ" → α
		14:07 ^b		

a) Observation time at the beginning of the first orbit; b) Observation time at the beginning of the second orbit.

rate, indicating that either the Keplerian disk rate, or the sub-Keplerian flow rate or both may be changing; (b) In between two known classes, a class of unknown type appears for hundreds of minutes; and (c) During a transition, the photon index becomes noisy until the flows settles into a new class indicating the presence of turbulent behaviour during transition. At the same time, we also study the behaviour of QPOs and show how the frequency is changed consistently with the accretion rates as inferred from the spectra. In the next Section, we present the observational results on class transition. Based on the new inputs from the observational results, in Sect. 3, we discuss what the nature of the accretion flows might be. We find that in order to enable class transition in a few hours, a significant fraction of the flow must be nearly freely falling, i.e., sub-Keplerian. Finally, in Sect. 4, we draw our conclusions.

2. Observation of class transitions

The results we discuss in this section were obtained by the Pointed Proportional Counters (PPCs) in the IXAE instrument aboard the Indian Satellite IRS-P3 (Agrawal 1998) which functioned during 1996–2000. The operating energy range is between 2 and 18 keV. The counts are saved in the archive only in two channels – one is 2–6 keV and the other is 6–18 keV. The time resolution in Medium mode could be 0.1 s but normally the time resolution was set to be 1 s. As a result of the presence of only two energy channels, only two points could be obtained in the spectrum and a so-called "mean photon index" (MPI) s_ϕ can be calculated after each second. Similarly, 0.1 s time resolution in the Medium mode restricts the observation of QPOs up to 5 Hz only, while the 1 s resolution restricts the reporting of QPOs up to 0.5 Hz only. Nevertheless, the light curves are clear enough and the identification of the specific class can be done without ambiguity (e.g., Naik et al. 2001 2002ab; Paul et al. 2001). It is to be noted that (a) the counts in the high energy bin could be very low and the s_ϕ suffers from low number statistics; and (b) the slope itself is known to vary in the 2–18 keV range, especially, the spectrum

becomes harder above 10–12 keV in the hard state. An assumption of a constant slope s_ϕ will thus be erroneous. Therefore, while s_ϕ gives an indication of how the slope changes (as a colour–colour diagram) its absolute value should be treated with caution.

Before we present the IXAE observations, it is useful to give a brief description of the QPOs which are so far observed in GRS 1915+105. Broadly speaking, this can be subdivided into four classes: (i) low frequency QPO (LFQPO) in the range ~ 0.001 – 0.02 Hz; (ii) break frequency (BF) or intermediate frequency QPO (IFQPO) in the range ~ 0.1 – 0.3 Hz; (iii) high frequency QPO (HFQPO) in the range ~ 1 – 10 Hz; and (iv) the very high frequency QPO (VHFQPO) around 67 Hz.

In Table 1, we present the log of the observations we report in this paper which showed class transitions. The first column refers to the figure where the results are shown. The second column refers to the name of the Satellite. The third column shows the date of observation and the time when the observation started. The fourth column gives the orbit numbers (or, the Obs. ID in case of RXTE) plotted in the figure. Typically, the time interval between two successive orbits is around 80 min. The fifth column gives the exact nature of class transition. Since during transition, a given class is not found to be "canonical" as defined by Belloni et al. (2000), we have put the class-names inside quotation marks.

In Figs. 1a–c, we present the light curves (2–18 keV) of the June 22nd, 1997 observation in the upper panel and the mean photon index (MPI) in the lower panels. The MPI s_ϕ is obtained using the definition:

$$s_\phi = -\frac{\log(N_{6-18}/E_2) - \log(N_{2-6}/E_1)}{\log(E_2) - \log(E_1)}, \quad (1)$$

where N_{2-6} and N_{6-18} are the photon count rate from the top layer of the PPC and E_1 and E_2 are the mean energies in each channel. Thus, $E_1 = 4$ keV and $E_2 = 12$ keV respectively. We have thus normalized the count rate per keV and then obtained the slope in the log-log plot since we expect a power-law slope in the 4–12 keV range. The panel 1a is in the so-called

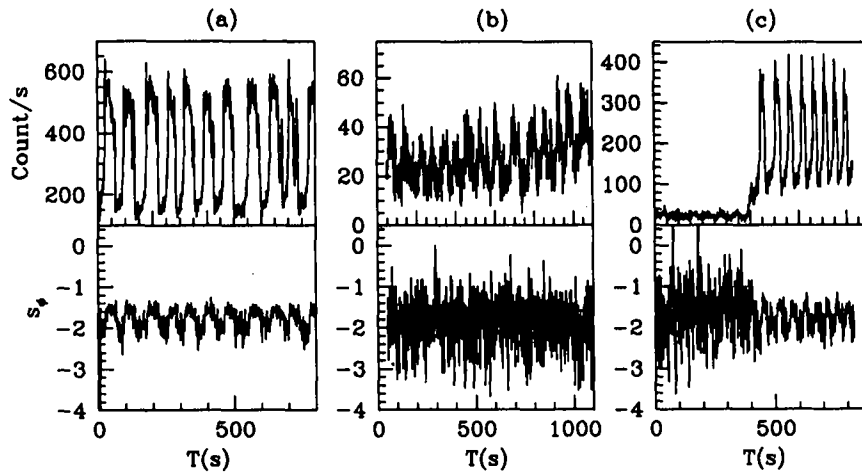


Fig. 1. 2–18 keV light curves as observed by IXAE (*upper panel*) and the mean photon spectral index s_ϕ (*lower panel*) in 1st, 3rd and 5th orbits of June 22nd, 1997 (see, Table 1). GRS1915+105 was **a)** in the κ class; **b)** in an unknown class; and **c)** went to the ρ class on that day. Lower panels show how s_ϕ distinctly change. Specifically it is noisy during the transition.

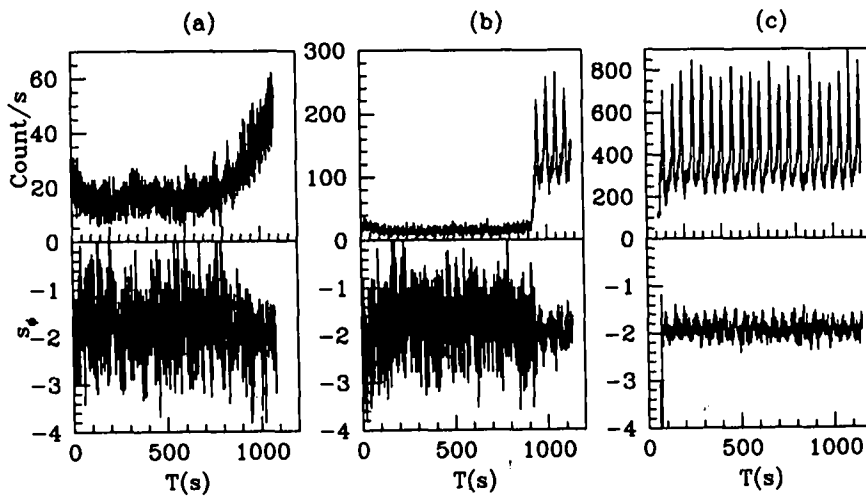


Fig. 2. Class transition of GRS 1915+105 as observed by IXAE on the 25th of June, 1997 in three successive orbits (See, Table 1). It was **a)** in an unknown class similar to χ ; **b)** in transition to ρ -type class with very low count rate; and **c)** in ρ class after stabilization in that class. In the lower panels are s_ϕ showing noisy behaviour during transition before settling down in **c)**.

k class (Belloni et al. 2000). The panel 1b is in a unknown class and the panel 1c clearly shows the transition from the unknown class to the so-called ρ class. The panels are separated by about three hours.

In the lower panels, the s_ϕ oscillates between ~ 2.4 to ~ 1.4 in Fig. 1a very systematically. In Figs. 1b and c, the unknown class produced very noisy photon spectral slope variation. As soon as the ρ class is achieved after one “semi- ρ ” oscillation, noise in s_ϕ is reduced dramatically.

The IXAE observation of the 23rd, 24th and 25th of June, 1997 showed that the system was still in ρ class after the transition on 22nd of June, 1997. Subsequently, on 25th June, 1997 there was another transition to χ and it returned back to ρ . It remained in ρ class on the 26th of June before returning to κ on the 27th. Thus $\kappa \rightarrow$ (unknown) $\rightarrow \rho \rightarrow$ (unknown) $\rho \rightarrow$ (unknown) $\rightarrow \kappa$ transitions took place in a matter of five days.

The exact time and duration of the last transition mentioned above could not be seen because of the lack of observation.

In Figs. 2a–c the observation of IXAE on 25th of June, 1997 is presented. The panels are separated by about one and a half hours. Here too, the upper and lower panels represent variation of photon count rates and s_ϕ respectively. In Fig. 2a, the GRS 1915+105 is in the so-called χ -like class, though the photon count rate showed considerable variations, not characteristic of χ . Correspondingly, the average spectra also softened as is suggested by the gradual decrease in s_ϕ . In Fig. 2b, this trend continued until a “semi- ρ ” class was achieved and the noise in the photon spectra went down. In Fig. 2c, after one full orbit, the count rate went up further by about a factor of four and a steady ρ state was achieved. The average (photon) spectral index s_ϕ was ~ 1.75 in Fig. 2a, but it became ~ 1.9 in Fig. 1c, indicating general softening.

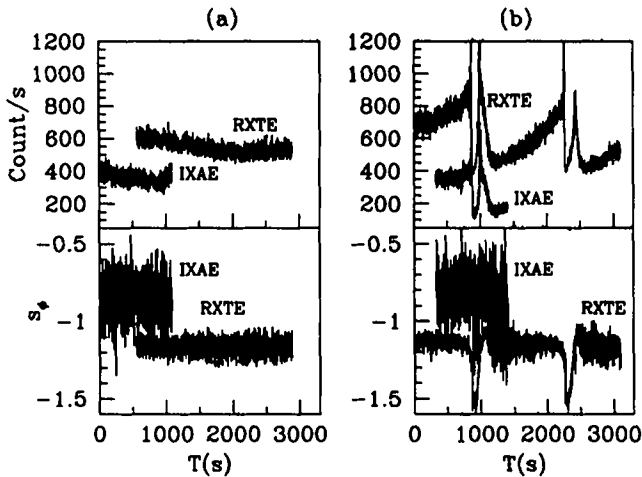


Fig. 3. Class transition as seen from IXAE and RXTE observations on the 8th of June, 1999 in two successive orbits (marked). RXTE photon count rates are divided by 50 and shifted upward by 200/s for comparison. In (a), for a period of about 3000 s, there was no significant variation in light curve or spectral index. The object was in a class similar to χ but the count rates were a factor of 10–20 times higher. There is a gap of 44 min in the two RXTE data presented in (a) and (b). In (b), the object is distinctly in the θ class. RXTE data is less noisy than the IXAE data because of higher counts. It was binned in 2–6 and 6–15 keV before computing s_ϕ so that comparison with IXAE could be made.

In Figs. 3a–b we show the light curve and s_ϕ from IXAE data obtained on the 8th of June, 1999. The two panels are from two successive orbits ~ 80 min apart. In Fig. 3a, the count rate was very high compared to what is expected from a typical χ state although the power density spectrum (PDS) is typical of that of the χ class. A QPO at 4.7 Hz is present. The s_ϕ is 0.85 which is harder than what is observed in Fig. 2. When combined with RXTE data of that date (Fig. 3a), one finds that for a long time (~ 3000 s) there was no signature of any “dip” which is the characteristic of the θ class. Hence, this must be in an unknown class, more close to χ than any other. RXTE also observed this object on the 7th of June, 1999 and found the object to be in the χ class. In Fig. 3b, the light curve in the next orbit of IXAE shows evidence of the so-called θ class. Interestingly, the spectra gradually “hardened” to $s_\phi \sim 0.6$ just before the “dip”. The spectra characteristically softened in the “dip” region with $s_\phi \sim 1.4$ as the inner edge of the disk disappeared. This class transition is confirmed in the data of RXTE also shown in Fig. 3b. The lower panels showed that the spectral slopes obtained for RXTE data calculated in a similar way to s_ϕ was calculated (Eq. (1)). Here, the photons were first binned in 2–6 keV and 6–15 keV (In epoch 4 of RXTE, the science data is available in a maximum of 35 channels. Thus the energy channel width could not be made identical to 6–18 keV as in IXAE) before computing s_ϕ from

$$s_\phi = -\frac{\log(N_{6-15}/E_2) - \log(N_{2-6}/E_1)}{\log(E_3) - \log(E_1)}, \quad (2)$$

where $E_1 = 4$ keV, $E_2 = 9$ keV and $E_3 = 10.5$ keV. Note that there is a large difference between the mean spectral slopes cal-

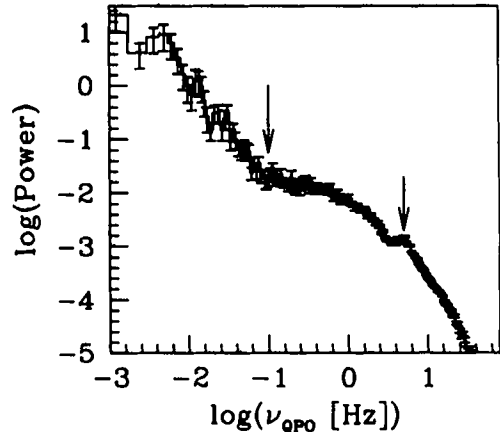


Fig. 4. The power density spectrum of the RXTE light curve in (b). The signature of 0.1 Hz break and a kink (weak and broad QPO) at around 5.4 Hz are typical of a θ class. These, along with softening of the spectrum at the dips (prominent in both the data) indicating that a class transition has indeed taken place.

culated from IXAE and RXTE data. The main reasons appear to be (a) by decreasing E_2 from 18 keV in IXAE to 15 keV the value of s_ϕ is increased by ~ 15 per cent. (b) usually the spectrum in the low state (as in between the “dips” in the θ class) has a harder tail for energy above 12 keV. Thus decreasing the bin-size limit from 18 keV, to 15 keV decreases the photon counts in harder parts of the spectrum. These two combined effects cause the mean spectrum of RXTE to be softer. Its lower noise is clearly due to its very high count rates (about 50 times higher than IXAE) for its higher effective surface area (6500 cm² as opposed to 400 cm² for one of the detectors of IXAE) and its usage of xenon as opposed to a mixture of 90 per cent argon and 10 per cent methane.

To show that the class in Fig. 3b is indeed that of the θ class, we plot in Fig. 4 the power density spectra. This showed a characteristic break at $BF \sim 0.1$ Hz and the HFQPO at 5.4 Hz with a broad “Q” weak QPO at the break frequency. The PDS of the light curve (Fig. 3a) in the previous orbit is χ -like and it does not show any LFQPO, BF/IFQPO or VHFQPO.

In Figs. 5a–b, we show another example of a class transition in which the light curve in the “ ρ ” class (Fig. 5a) goes over to the so-called α class (Fig. 5b). This is from the IXAE observation on the 25th of June, 2000. The count rate in this “ ρ ” class was much higher than that seen in Figs. 1 and 2 and the photon spectral index in the lower panel also showed that the spectra are harder (average $s_\phi \sim 0.65$ as compared to ~ 1.8 in Fig. 1 and ~ 1.9 in Fig. 2.). So, it could be an intermediate class. In the alpha class s_ϕ became noisy and the transition is clearly obvious. This “ α ” lasted for a short time, since observations from 18th June, 2000 to 25th June, 2000 as reported in Naik et al. (2002b) always showed a ρ class with gradually increasing burst recurring time-scale. On the 25th, this trend reversed after this “ α ” class and from the 26th the recurred time again went up. So the system might have experience perturbations for only a short time.

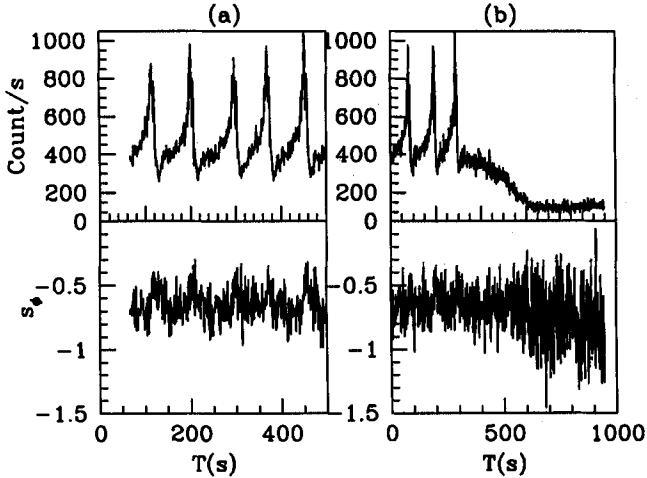


Fig. 5. Two successive orbital IXAE data showing a class transition on the 25th of June, 2000. In **a**), the class is similar to ρ but the count rate is higher and the recurring time-scale between bursts is large (~ 100 s). In **a**), the spectral index is less noisy but in the beginning of **b**) it becomes very noisy though superficially it is still in “ ρ ” class. After transition it went to the so-called α class and s_ϕ becomes very noisy.

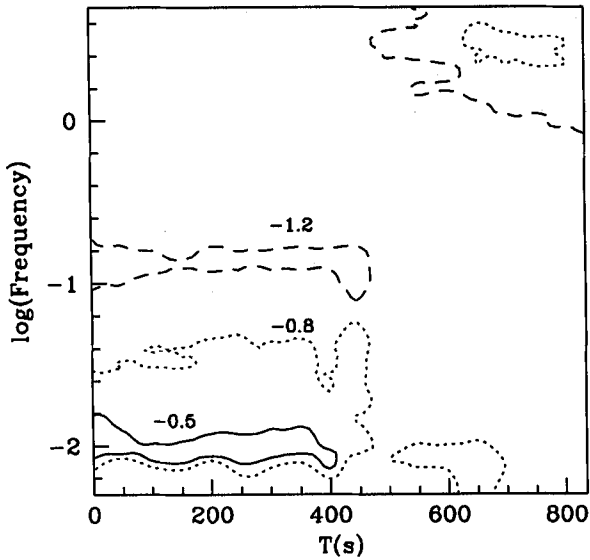


Fig. 6. Time dependence of the power density spectrum for the medium mode (0.1 s time resolution) IXAE observations presented in Fig. 5b. Along X-axis is the time after the observation started. The contours of constant power (in logarithmic scale) are plotted (marked on the contours). A strong peak at $\log(\nu_{\text{QPO}}) \sim -2$ in the first half signifies the Low Frequency QPO (LFQPO) in the ρ state and another weak peak at ~ 0.1 Hz (break frequency, see text) is also present. After the transition, the peak occurs at ~ 2.5 Hz.

The change of class is also reflected in Fig. 6 where the time dependence of the power density spectra (PDS) is plotted. Along the Y-axis, the frequency (ν) of the PDS is presented. The power (P) itself is marked on the contours plotted: solid curve, dotted curve and dashed curves are for $\log(P) = -0.5$, -0.8 and -1.2 respectively. Note that the highest power remains at around $\log(\nu) \sim -2$ in the ρ state. A weaker peak

occurs at around $\log(\nu) = -0.85$. However, after the transition, the dominant frequency seems to be at around $\log(\nu) \sim 0.4$ which corresponds to $\nu \sim 2.5$ Hz.

3. Possible nature of the accretion flow emerging from class transitions

The first and the most important point to note is the variation in the count rate in the pre-transition period and the duration of a transition. The variation in the count rate points to the variation in the accretion rate while the duration gives an indication of the infall time. Details of the possible nature of the flow geometry during transition will be discussed elsewhere (Nandi et al. in preparation). Given that there is a gap of more or less 80 min in between two successive observations of IXAE, the duration T_d could be at the most ~ 3 – 5 h i.e., $10\,000$ – $20\,000$ s. This is short even for a free falling gas from the outer edge of the disk located at $r_d \sim 1.5 \times 10^6 r_g$, where $r_g = 2 GM/c^2$ is the Schwarzschild radius of the central black hole of mass $M \sim 14 \pm 4 M_\odot$ (Greiner et al. 2001) since this is around

$$T_{\text{infall}} \sim r_d^{3/2} (r_g/c) \sim \left(\frac{r_d}{1.5 \times 10^6} \right)^3 / 2 \left(\frac{M}{14 M_\odot} \right) \text{ s} \\ \sim 2.6 \times 10^5 \text{ s.} \quad (3)$$

The viscous time for a Keplerian disk of similar size must be at least ten to a hundred times larger, i.e., few $\times 10^6$ s for any reasonable viscosity. This indicates that if the transition takes place in $\sim 10^4$ s, the accretion flow must be nearly freely falling, i.e., sub-Keplerian, and must originate from intermediate distances, rather than from the outer edge, i.e., out of a Keplerian disk through energy deposition or otherwise. This flow is neither a static corona, nor a flow which is radiatively less efficient. Smith et al. (2001, 2002) indeed found observational signatures of the nearly free-falling matter in several black hole candidates which causes dynamical spectral state changes. We thus believe that the variation of the rate of the sub-Keplerian matter may be responsible for the class transitions we presented here.

4. Concluding remarks

In this paper, we presented several examples of variability class transitions in GRS 1915+105 as observed by the Indian X-Ray Astronomy Experiment (IXAE) aboard the Indian Satellite IRS-P3. We also presented one example from RXTE. We showed that while the signature of a class transition in the light curve may be abrupt, the process itself is gradual over a period of about 3–5 h during which the light curve passes through unknown classes. During the transition, the photon count rates change significantly which indicates changes in the accretion rates. In a model-independent way, we argue that probably only the rate of the sub-Keplerian flow changes since the duration of transition is $\sim 2 \times 10^4$ s, much shorter than the viscous time by factor of ten to hundred. During the transitions, the photon count rates were found to be abnormal and were rapidly changing. For instance in Fig. 3a, the X-ray count rate was seen to vary by more than 25% in a matter of a few minutes in the unknown class. These are indications that nearly freely

falling (i.e., a low angular momentum) sub-Keplerian flow may present in the accretion flow of GRS 1915+105, supporting earlier conclusions of Smith et al. (2001, 2002) in the context of several other black hole candidates.

Acknowledgements. This work is supported in part by Grant No. SP/S2/K-15/2001 of Department of Science and Technology, Govt. of India. The authors thank Prof. P. C. Agrawal for allowing the IXAE data to be placed in the ISRO-sponsored Databank at Centre for Space Physics which were analysed in this paper.

References

- Agrawal, P. C. 1998, in *Perspective in High Energy Astronomy and Astrophysics*, ed. P. C. Agrawal, & P. R. Vishwanath (Hyderabad: University Press), 408
- Belloni, T., Klein-Wolt, M., Méndez, M., van der Klis, M., & van Paradijs 2000, *A&A*, 355, 271
- Chakrabarti, S. K., Acharyya, K., & Molteni, D. 2004, *A&A*, 421, 1
- Chakrabarti, S. K., Manickam, S. G., Nandi, A., & Rao, A. R. 2002, *Proc. Ninth Marcel Grossman Meeting General Relativity and Gravitation*, ed. V. Gurzadyan, R. T. Jentzen, & R. Ruffini, 2279
- Chakrabarti, S. K., & Nandi, A. 2000, *Ind. J. Phys.*, 75B, 1 [arXiv:astro-ph/0012526]
- Chakrabarti, S. K., Nandi, A., Choudhury, A., & Chatterjee, U. 2004, *ApJ*, 607, 406
- Chakrabarti, S. K., & Titarchuk, L. G. 1995, *ApJ*, 455, 623
- Greiner, J., Cuby, J. G., & McCaughrean, M. J. 2001, *Nature*, 417, 522
- Molteni, D., Sponholz, H., & Chakrabarti, S. K. 1996, *ApJ*, 457, 805
- Morgan, E. H., Remillard, R. A., & Greiner, J. 1997, *ApJ*, 482, 993
- Naik, S., Rao, A. R., & Chakrabarti, S. K. 2002a, *A&A*, 23, 213
- Naik, S., Agrawal, P. C., Rao, A. R., et al. 2001, *ApJ*, 546, 1075
- Naik, S., Agrawal, P. C., Rao, A. R., & Paul, B. 2002b, *MNRAS*, 330, 487
- Nandi, A., Manickam, S. G., & Chakrabarti, S. K. 2000, *Ind. J. Phys.*, 74B(5), 331 [arXiv:astro-ph/0012523]
- Paul, B., Agrawal, P. C., Mukerjee, K., et al. 2001, *A&A*, 370, 529
- Remillard, R., Morgan, E. H., McClintock, J. E., Bailyn, C. D., & Orosz, J. A. 1999, *ApJ*, 522, 397
- Smith, D. M., Heindl, W. A., Markwardt, C. B., & Swank, J. H. 2001, *ApJ*, 554, 41
- Smith, D. M., Heindl, W. A., & Swank, J. H. 2002, *ApJ*, 569, 362.

SS 433: Results of a Recent Multi-wavelength Campaign

Sandip K. Chakrabarti^{1,2}, B.G. Anandarao³, S. Pal², Soumen Mondal³, A. Nandi¹, A. Bhattacharyya², Samir Mandal², Ram Sagar⁴, J. C. Pandey⁴, A. Pati⁵ and S.K. Saha⁵

¹*S.N. Bose National Center for Basic Sciences, JD-Block, Salt Lake, Kolkata, 700098, India*

²*Centre for Space Physics, Chalantika 43, Garia Station Rd., Kolkata, 700084, India*

³*Physical Research Laboratory, Navarangapura, Ahmedabad, 380009, India*

⁴*ARIES, Manora Peak, Nainital, 263129, India*

⁵*Indian Institute of Astrophysics, Bangalore 560034, India*

e-mail: chakraba@bose.res.in, anand@prl.ernet.in, space-phys@vsnl.com, soumen@prl.ernet.in, anuj@bose.res.in,

sagar@upso.ernet.in, jeewan@upso.ernet.in, pati@iiap.res.in, sks@iiap.res.in

6 January 2005

ABSTRACT

We conducted a multi-wavelength campaign in September–October, 2002, to observe SS 433. We used 45 meter sized 30 dishes of Giant Meter Radio Telescope (GMRT) for radio observation, 1.2 meter Physical Research Laboratory Infra-red telescope at Mt Abu for IR, 1 meter Telescope at the State Observatory, Nainital for Optical photometry, 2.3 meter optical telescope at the Vainu Bappu observatory for spectrum and Rossi X-ray Timing Explorer (RXTE) Target of Opportunity (TOO) observation for X-ray observations. We find sharp variations in intensity in time-scales of a few minutes in X-rays, IR and radio wavelengths. Differential photometry at the IR observation clearly indicated significant intrinsic variations in short time scales of minutes throughout the campaign. Combining results of these wavelengths, we find a signature of delay of about two days between IR and Radio. The X-ray spectrum yielded double Fe line profiles which corresponded to red and blue components of the relativistic jet. We also present the broadband spectrum averaged over the campaign duration.

1 INTRODUCTION

The enigmatic compact star SS 433 is an well studied bright emission line object which is known to have a companion with an orbital period of 13.1d, a large disk and two highly collimated relativistic jets moving at $v \sim 0.26c$. Disk axis makes an angle of $\sim 78^\circ$ with the line of sight, while the jet precesses with the axis at an angle of $\sim 19^\circ$ (Margon, 1984) with a periodicity of about 162.15d. Several observations have been carried out over the last three decades, and yet, the object alluded a proper identification. Most recent estimates (Hillwig et al, 2004) suggest that the central object could be a low mass black hole ($2.9 \pm 0.7M_\odot$) with a high mass ($10.9 \pm 3.1M_\odot$) companion.

So far, there has been a few multi-wavelength campaign in SS 433 (e.g., Neizvestnyj, Pustilnik & Efrenov, 1980; Ciatti et al. 1981; Seaquist et al. 1982; Vermeulen et al. 1989; Band & Gordon 1989; and Kotani et al. 1999). However, these are confined to two or three wavelengths. The aim of our campaign was (a) to carry out observations in as many wavelengths as possible, (b) to detect the nature of the short time-scale variabilities in all the wavelengths, (c) to obtain a broad band spectrum of this enigmatic system in order to model the emission processes in future. We carried out the campaign in Radio (1.28 GHz), in IR (J, H, and K' bands), in optical (B and V bands) and in X-ray (3-30 keV) wavelengths in September-October, 2002, when the jet is more or less normal to the line of sight and the X-ray intensity is statistically in its minimum. Given that the jet is produced out of matter ejected from the accretion disk, one would expect that small variabilities, if present, would exist in all the wavelengths and one would hope to correlate these variabilities in order to 'follow' individual flares or knots as they propagate through the jets. We did observe such variabilities in time scales of few minutes, though, given that quite 'unknown' time delays are present between X-rays and Optical, IR or radio emitting regions, we found it difficult to correlate these variabilities. However, we did find a lag of two days between overall variation of intensities in IR and Radio wavelengths. Our radio observation was carried out during 26th September to 6th of October, 2002. The IR observations were made during 25th to 29th of September, 2002. The optical photometry was made during 27th September to 3rd October, 2002, while X-ray observation was taken only on the 27th of September, 2002. Optical spectra were taken on the 27th and 28th of September, 2002. A brief report on the variabilities in radio, IR and X-rays, observed on the 27th of September, 2002 has already been published in Chakrabarti et al. (2003).

In the following Sections, we present the results of our multi-wavelength campaign. In §2, we briefly describe the observations and the data reduction. In §3, we present our results including the lightcurve and the broadband spectrum. Finally, in §4, we draw conclusions.

Our major results are as follows: (a) The short time-scale variations are present (2 – 8 minutes) on all the days in all the wavelengths. We present differential photometry results in IR for all the days. (b) The optical and X-ray spectra contain the blue and red-shifted lines which are compatible with the kinematic model (Abell & Margon, 1979). (c) For the first time, we obtained the broadband spectrum over ten decades of frequency range based on contemporaneous data. Observations in X-rays and radio waves at regular intervals are in progress and we plan to present results over longer time scales in future.

2 OBSERVATIONS AND DATA REDUCTION

Table 1 gives a log of our observations during the campaign and brief remarks on each observation. Column 1 gives Modified Julian Day (MJD) and the date of observation, Column 2 gives the wave band, Column 3 gives the telescope used and its location. For the Giant Meter Radio Telescope (GMRT), we also give the number of antennas working during the observation in squared brackets. Column 4 gives the duration of the observations in seconds.

Radio observations were carried out with the GMRT which has 30 antennas each of 45m in diameter in a Y-shaped array with the longest baseline interferometry over 25km region (Swarup et al. 1991) near Pune, India along roughly Y shaped array. The observations were carried out at 1.280 GHz (bandwidth 16 MHz) during Sept. 26th, 2002 to Oct. 1st, 2002 and at 610 MHz (bandwidth 16 MHz) during 2nd-6th October, 2002. However, results of 3rd-4th October were full of scintillations. The data was binned at every 16 seconds. AIPS package was used to reduce the data. Bad data was flagged using tasks UVFLG and TVFLG and the standard deviation at each time bin using UVPLT package was computed. Generally, 3C48 and 3C286 were used as the flux calibrators whenever available.

Infrared observation was made using the Physical Research Laboratory (PRL) 1.2m Mt. Abu infrared telescope equipped with Near-Infrared Camera and Spectrograph (NICMOS) having 256×256 HgCdTe detector array cooled to the liquid nitrogen temperature 77K. One pixel corresponds to 0.47 arcsec on the sky, giving a field of view of 2×2 arcmin². The filters used were standard J ($\lambda=1.25 \mu\text{m}$, $\Delta\lambda= 0.30 \mu\text{m}$), H ($\lambda=1.65 \mu\text{m}$, $\Delta\lambda= 0.29 \mu\text{m}$) and K' ($\lambda=2.12 \mu\text{m}$, $\Delta\lambda= 0.36 \mu\text{m}$) bands. Short exposures were taken in immediate

Table 1. Observation log of SS 433

MJD (Date)	Wave Band	Telescope (Location)	Duration (s)
52542 (25/9/02)	J	PRL(Mt. Abu)	1480
	H	PRL(Mt. Abu)	1720
	K'	PRL(Mt. Abu)	740
52543 (26/9/02)	1.28 GHz	GMRT(Pune) [20] ^{a)}	2160
	J	PRL(Mt. Abu)	3640
52544(27/9/02)	1.28 GHz	GMRT(Pune) [28]	21600
	J	PRL(Mt. Abu)	2500
	H	PRL(Mt. Abu)	2390
	K'	PRL(Mt. Abu)	2180
	B	State Obs.(Nainital)	1320
	Optical	VBT (Kavalur)	2400
	spectroscopy 3-30 keV	VBT (Kavalur) RXTE	2400 5696
52545(28/9/02)	1.28 GHz	GMRT(Pune) [24]	960
	B	State Obs. (Nainital)	4860
	Optical	VBT (Kavalur)	3900
	spectroscopy	VBT (Kavalur)	3900
52546(29/9/02)	1.28 GHz	GMRT(Pune) [13]	840
	J	PRL(Mt. Abu)	1160
	H	PRL(Mt. Abu)	780
	K'	PRL(Mt. Abu)	475
52547(30/9/02)	1.28 GHz	GMRT(Pune) [26]	3777
52548(1/10/02)	1.28 GHz	GMRT(Pune) [28]	3777
52550(3/10/02)	B	State Obs. (Nainital)	120
	V	State Obs. (Nainital)	120
52552(5/10/02)	610 MHz	GMRT(Pune) [29]	1130
52553(6/10/02)	610 MHz	GMRT(Pune) [10]	2850

a) The number of antennas working during the observation.

succession in the three bands. Single-frame exposure time during whole observations in the J and H filters were 10 seconds. Observations in K' filter were taken with 2 sec exposure and 5 successive frames were binned to obtain 10 sec for a better signal to noise ratio. On the 26th of Sept. only J band observation could be made before clouds covered the sky. At each dithered position ten frames were taken with each integration time of 10 seconds. The nearby infrared bright standard star GL748 (Elias et al. 1982) were used as the flux calibrator and it was observed for 50 frames with exposure time of 10 sec were observed in each filter during each night.

Data reduction of JHK' images were performed in a standard way using the DAOPHOT task of IRAF package. All the objects and standard star frames were de-biased, sky-subtracted and flat fielded. The sky frames were created by usual practice of median combining of at least five position-dithered images where the source was kept within the field of NICMOS of $2' \times 2'$. At each dithered position at least 10 frames of 10 sec exposure were taken for J and H bands while 20 frames of 2 sec exposure were taken for K' band. The zero point of the instrument was taken from the standard star observations. We measured the stellar

magnitudes using the aperture photometry task (APPHOT) in IRAF. Our derived mean JHK' magnitudes on Sept. 25th, 27th and 29th are 9.51 ± 0.04 , 8.48 ± 0.03 and 8.49 ± 0.08 ; 9.47 ± 0.02 , 8.48 ± 0.02 and 8.32 ± 0.02 ; 9.51 ± 0.01 , 8.49 ± 0.04 and 8.38 ± 0.03 respectively. On the 26th of September J magnitude was 9.52 ± 0.02 . The magnitudes are converted to flux density (Jansky) using the zero-magnitude flux scale of Bessell, Castelli & Plez (1998) for plotting purpose. The differential magnitudes are determined using two brightest stars in the same frame of the object. The error in individual flux density measurement is the usual propagation error of the observed photometric magnitude. Photometric errors ϵ are calculated for individual frame of every star and for the subtracted differential magnitude the final error was calculated as $\sqrt{\epsilon_1^2 + \epsilon_2^2}$, where ϵ_1 and ϵ_2 are the error-bars of the individual stars.

The optical photometry was carried out at the State Observatory (currently known as ARIES), Nainital, India using its 1m reflector. The photometric observations in Johnson B and V bands were carried out using a CCD camera at f/13 Cassegrain focus of the telescope. The CCD system consists of $24 \times 24 \mu^2$ size pixel, having 2048×2048 pixels. To improve the signal-to-noise ratio the observations have been taken in a binning mode of 2×2 pixel², where each super pixel corresponds to 0.72×0.72 arcsec². The CCD covers a field of view of $\sim 13 \times 13$ arcminute². Multiple CCD frames were taken with the exposure time of 120 secs. A number of bias and twilight flat field frames were also taken during the observing run. The frames were cleaned employing the IRAF/MIDAS software. The magnitude of the star is determined by using the DAOPHOT. The value of atmospheric extinction in B pass band is 0.26 during the observation and this was taken into account. Due to scattered clouds, only a few exposures could be made on the 27th of September, 2002 and only one exposure on each of the B and V bands could be made on the 3rd of October, 2002. Several exposures were taken on the 28th of September, 2002.

The optical spectroscopic study of SS 433 was carried out with the 2.3 meter Vainu Bappu Telescope (VBT) at the Vainu Bappu Observatory (VBO), Kavalur, India. CCD images were obtained during the period of 27th - 28th September'02. Detailed description of the telescope characteristics and observation techniques are given in Prabhu et al. (1995). The source was pointed at for a maximum exposure time of 20 min with the source positioned at the center of the CCD frame. The data was analysed with PC-IRAF 2.12.1-EXPORT version. The spectrum processing comprised of several subroutines which were performed in pipe-line. These include (a) making the MASTERBIAS using all the bias files supplied

with the data with *median combine* option, (b) making the MASTERFLAT using all flat files supplied with data with *median combine* option, (c) checking one of the flat files to get range of useful data, (d) using *CCDPROC* on all the science and science calibration files to correct for BIAS, FLAT fielding, trimming out of noise, (e) removal of cosmic rays using *cosmicrays* utility, (f) aperture synthesis of science data after checking dispersion axis and matching with *apall* parameters, (g) using *apall* for science calibration file with reference to the science data to calibrate with the proper science data, (h) calibration of spectrum lines in calibration data, (i) wavelength calibration (non-linear) of science data file using science calibrator file using *dispcor* (j) continuum calibration of wavelength calibrated science data. Since we did not have a standard spectrum (due to bad weather), we could not perform absolute flux calibration and so we had to rely on the simple continuum calibrated data. Iron and Neon lines were used to calibrate lines.

X-ray observation was carried out using the Proportional Counter Array (PCA) aboard RXTE satellite. The data reduction and analysis was performed using software (LHEASOFT) FTOOLS 5.1 and XSPEC 11.1. We extract light curves from the RXTE/PCA Science Data of GoodXenon mode. We combine the two event analyzers (EAs) of 2s readout time to reduce the Good Xenon data using the perl script *make_se*. Once *make_se* script was run on the Good_Xenon_1 and Good_Xenon_2 pairs, the resulting file was reduced as Event files using *seextrct* script to extract light curves. Good time intervals were selected to exclude the occultations by the earth and South Atlantic Anomaly (SAA) passage and also to ensure the stable pointing. We also extracted energy spectra with an integration time of 16s from PCA Standard2 data in the energy range 3 - 30 keV (out of the five PCUs only data from No. 2 and No. 3 PCUs are added together). For each spectrum, we subtracted the background data that are generated using PCABACKEST v4.0. PCA detector response matrices are created using PCARSP v7.10. We perform fits to the energy spectra in the energy range 3-27 keV with the so-called ‘traditional model’ for SS 433, consisting of the super-position of thermal bremsstrahlung and Gaussian lines due to the emission from the iron atoms, modified by the interstellar absorption.

3 RESULTS AND DISCUSSIONS

Before we present the results of our campaign, we would like to give an overview of the long term behaviour of SS 433 in X-rays (Nandi et al. 2004). Figure 1 shows the average RXTE

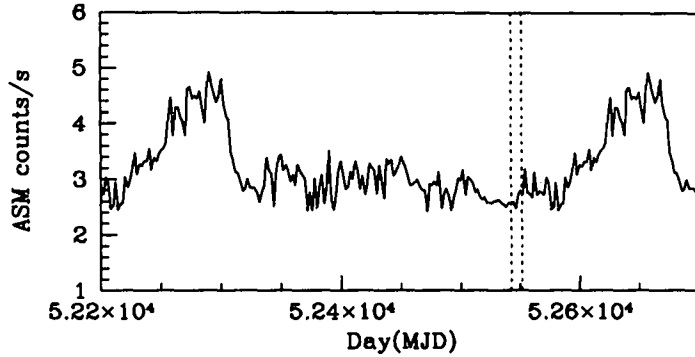


Fig. 1: The average All Sky Monitor (ASM) light curve of SS 433 as taken by RXTE satellite. The dotted vertical lines show the days of the present campaign, indicating that the object was expected to be X-ray quite.

All Sky Monitor (ASM) data. The complete set of ASM data since 1996 till date have been averaged after folding it around 368 days. This shows clear periodicity which is shown in Fig. 1. This ‘flaring’ is probably due to special alignment of SS 433 with the sun as seen by ASM. The vertical dashed lines represent the duration of our campaign. Thus our campaign took place in a time-frame away from such confusing region where X-ray was generally weak. Because of this we expected that even small variations in intensities would be detectable. In Chakrabarti et al. (2003) such short time variations have been reported.

In Fig. 2a, we present the images of SS 433 obtained by our Radio observation at 1.28GHz on the 1st of October, 2002. The contours are drawn at intervals of 0.055Jy. The beam size is shown as a circle in the lower left. In Fig. 2b, the image of SS 433 on the 27th of Sept. 2002, along with the those of the two standard stars in J band are shown. The magnitudes of the standard stars are also given.

Figure 3 shows the results of our multi-wavelength observation of SS 433 at 1.28 GHz (triangles) band and at 610 MHz (filled hexagons) in radio, at J (crosses), H (filled boxes), K' (filled pentagons) bands in IR, B (filled circles) and V (open circle) bands in optical, and 3 – 25 keV (open squares) in X-ray during the campaign. There seems to be a minimum in IR data on \sim MJD 52544.674 (see, Fig. 5 below) while the radio shows minimum at \sim MJD 52546.7, almost two days later. If the IR data could be taken as the pre-cursor of the radio data, one would infer that IR was also in a state of minimum intensity during the campaign. However, it is to be noted that this IR intensity is the sum of the components coming

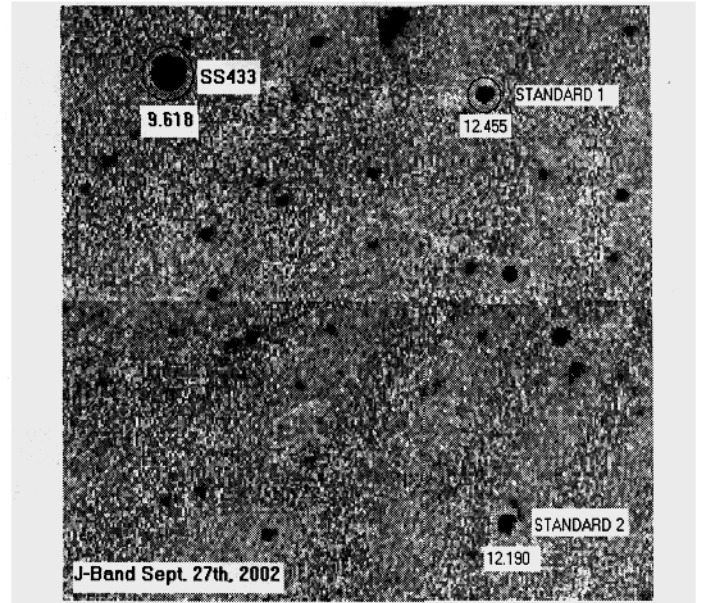
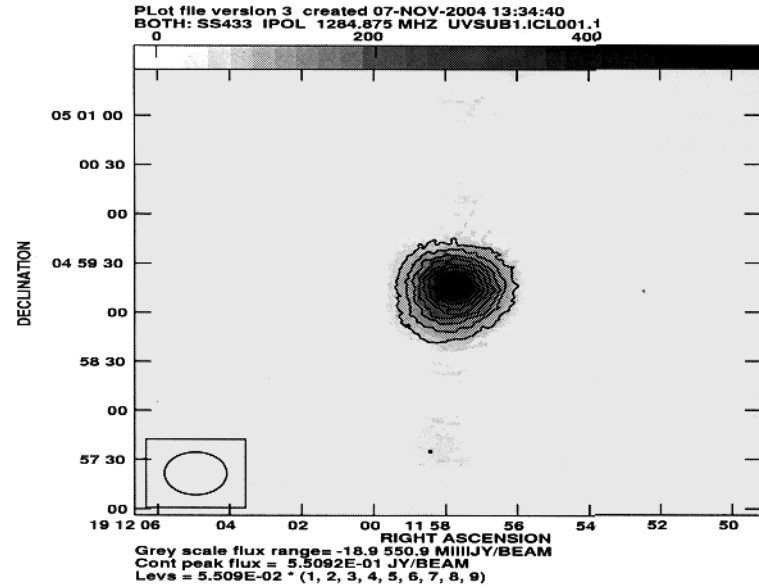


Fig. 2(a-b): (a) Radio and (b) IR images of SS 433. This radio image taken on 1st of October, 2002 is at 1.28 GHz. The peak flux is ~ 0.55 Jy/beam. The size of the beam is given in the lower left. The contours are at intervals of ~ 0.055 Jy. The IR image taken on the 27th of Sept. 2002 is in the J band. The standard stars (1 and 2) referred in the text are also shown. The magnitudes are given as well.

from the companion and the jet. From the IR observation of Kodaira, Nakada & Backman (1985), one notices that at the precessional and orbital phases of SS 433 corresponding to our campaign, the relative K magnitude was expected to remain almost constant ($\sim 0 \pm 0.05$), while in our observation we find it to be highly variable (~ 0.225) which suggests that there are intrinsic variation in IR band which may have been reflected in the Radio band two days later. The H-band result was found to be higher compared to the J and K' band results during the whole period. A similar result of turn-around at about 4 micron was reported earlier by Fuchs (2003). This turn over could be possibly due to free-free emission in optically thin limit. Absorption in the J band by the surrounding matter or the jets may also be a possibility.

In Fig. 4 we present the multi-wavelength lightcurves in radio (1.28GHz), in J,H, and K' bands, in B band and in X-rays (3-30 keV). The mean radio flux was seen to gradually go down while behaviours in other wavebands were not so straight forward. For instance, the flux in H band was found to be the higher compared to J or K' . This was not clearly understood, while a monotonic behaviour was expected. As we mentioned above, extra emission at H band is possible due to bremsstrahlung.

In Fig. 5 we present the entire IR observations taken during the campaign. The flux was clearly diminishing during 25th to 27th and it started rising again on the 28th. The minimum is at around MJD 52544.674. The data is clearly variable in a few minutes time scale. This

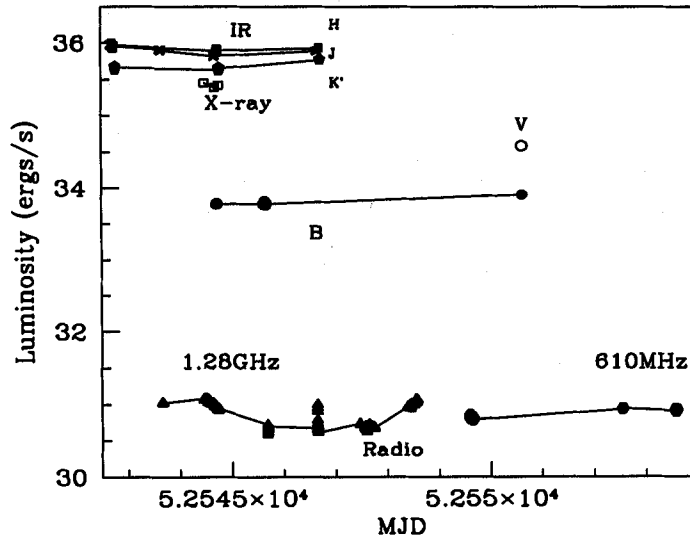


Fig. 3: Multi-wavelength observation of SS 433 at 1.28 GHz (triangles) band and at 610 MHz (filled hexagons) in radio, at J (crosses), H (filled boxes), K' (filled pentagons) bands in IR, B (filled circles) and V (open circle) bands in optical, and 3 – 25 keV (open squares) in X-ray during the campaign. There seems to be a lag of minimum intensity region in radio (MJD 52545.5 to MJD 52547.5) with respect to the Infra-red minimum region (\sim MJD 52544-52545) by about 1.7 days.

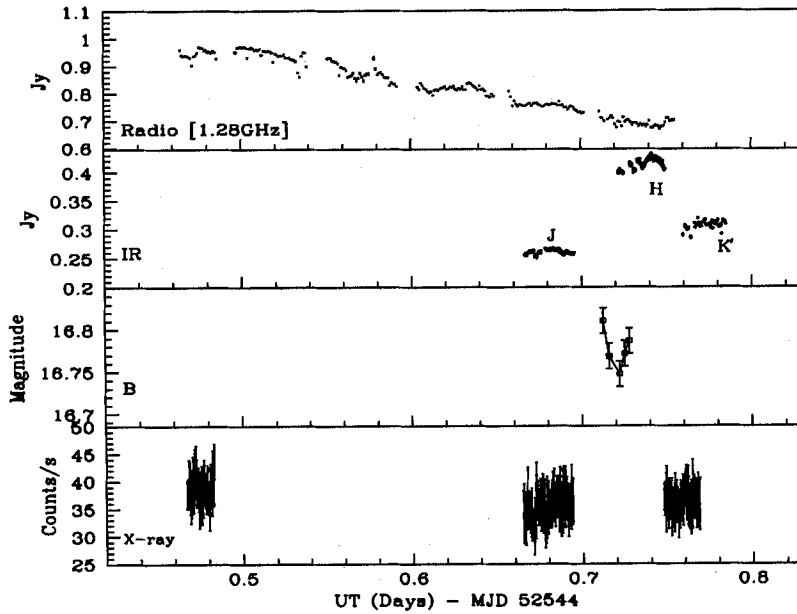


Fig. 4: Light curves of SS 433 on the 27th of September, 2002, as obtained by our multi-wavelength campaign at different wavelengths. Upper panel: Radio observation at 1.28 GHz at GMRT, Pune. Second panel: IR observation at J, H and K' bands at Mt. Abu. Third panel: B band observation at the State Observatory, Nainital and the Bottom panel: Background subtracted X-ray count rates by RXTE satellite.

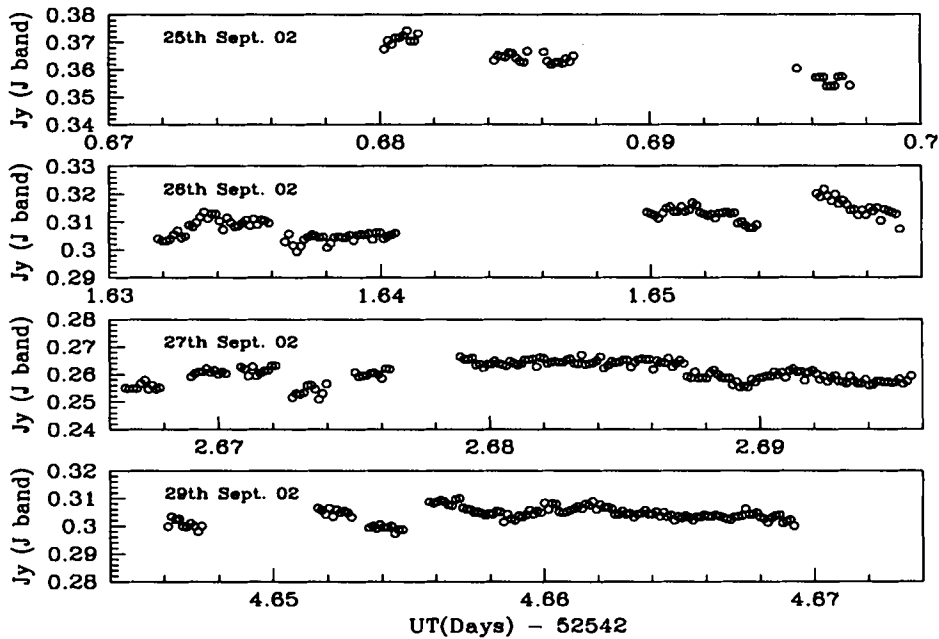


Fig. 5: Light curves in J band as a function of the UT (Days). Considerable variations could be seen in all the days. The size of the error-bars are well below the size of the circles. The intensity seems to be minimum (around 0.25Jy) on MJD 52544.674.

could be seen more clearly in the differential photometry results in the IR observations. In Figs. 6(a-b) this is presented. In Figs. 6a (upper panel) the results in J band are presented, while in Fig. 6b (lower panel) the results in H band are presented. In each panel, the upper box shows the difference between SS 433 and the Standard 1 star while in the lower box, the difference between the two standard stars have been plotted. The error-bars are also shown. In general, the upper boxes show at least twice more variation than the lower boxes. The 1σ error-bar ($J=0.00035$ Jy, $H=0.00085$ Jy) of the differential flux variation between SS 433 and std1 for the whole light curve is a factor of 3.5 and 2.5 in the J-band and H-band respectively in comparison to that between two standards ($J=0.0001$ Jy, $H=0.00035$ Jy). The 1σ for the light curve is more than a factor of 5σ of single point measurement error. Thus, the variation in the IR light curves of SS 433 is likely to be intrinsic and the analysis shows above 2σ level variability in the both bands. Short time-scale variation on the order of ten minutes have also been reported by Kodaira & Lenzen (1983).

Since the optical results depended heavily on the local sky conditions, the data acquisition was not uninterrupted. Indeed, although two observatories, one in southern part of India (VBT, Kavalur) and the other in the northern part of India (ARIES, Nainital) were chosen, both observations were affected by the late monsoon activities. Table 1 showed the duration

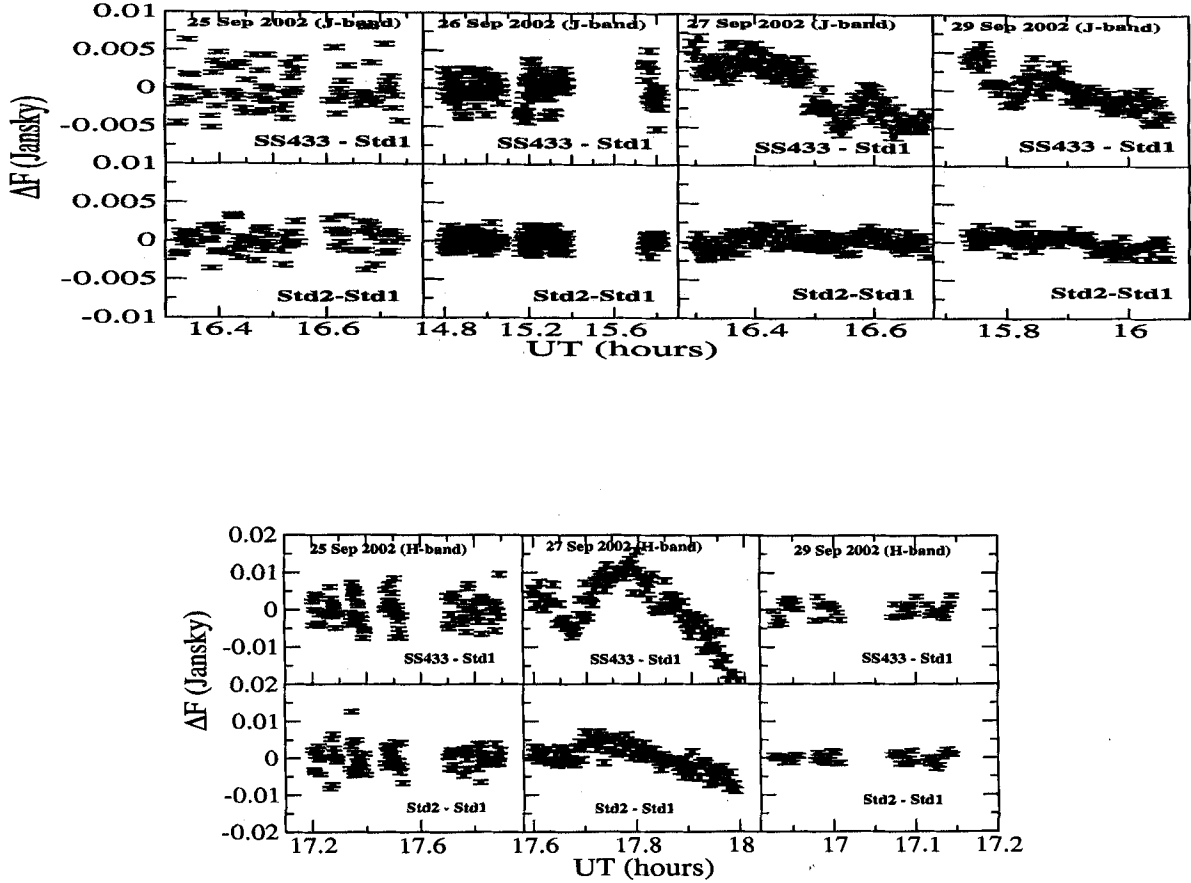


Fig. 6(a-b): Differential photometry of SS 433 in IR with respect to a standard star (std1) in the same frame of the object are plotted against the universal time on various days of the campaign in the upper panels. Also shown in lower panels are the differences of intensities ΔF (Jansky) of one standard star (std1) to the other (std2). The upper plots are for the data for the J band and in the lower plots are the data for the H band. Differential flux variation of SS 433 is above 2σ level in comparison to that of the standard stars.

of the data acquisition and the exposure time taken. In Figs. 7(a-b) we present the spectrum of SS 433 taken at VBT. Fig. 7a shows the raw spectrum, while Fig. 7b shows the spectrum on the 27th of Sept. 2002 corrected as described in Sec. 2. In Fig. 8a, the wavelength calibrated spectrum is shown and major lines were identified. On this date, both the jets were showing redshifts. The shifted line wavelengths match with what is expected from the kinematic model of Abell and Margon (1979) within the instrument resolution of 5\AA . For instance, at 13:49 UT, on 27th of Sept. 2002, the expected red shifts were 0.05901 and 0.01234 respectively and the $H_{\alpha-}$ and $H_{\alpha+}$ lines were expected at 6950\AA and 6644\AA respectively. Our observed lines were at 6961\AA and 6642\AA respectively. The spectra on the 28th of September, 2002, presented in Fig. 8b, had two bright lines (marked by ‘U’ on the figure) at 7029\AA and 6481\AA respectively apart from the usual lines. The red/blue shifted H_{α}

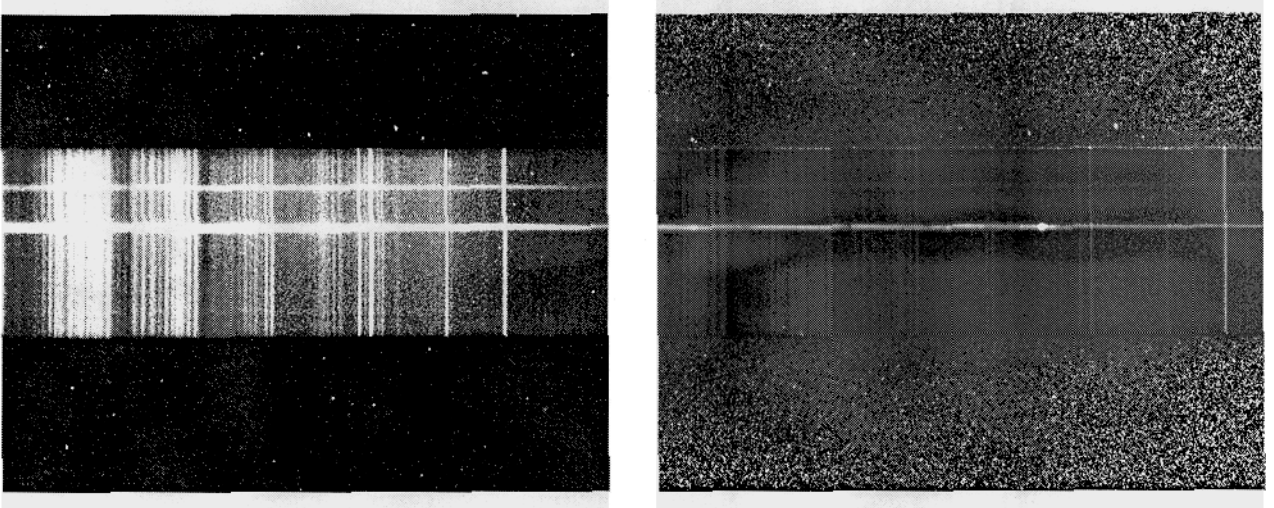


Fig. 7(a-b): a) The raw and (b) the corrected spectrum of SS 433 taken at the 2.3m Vainu Bappu Telescope. See text for detailed procedure.

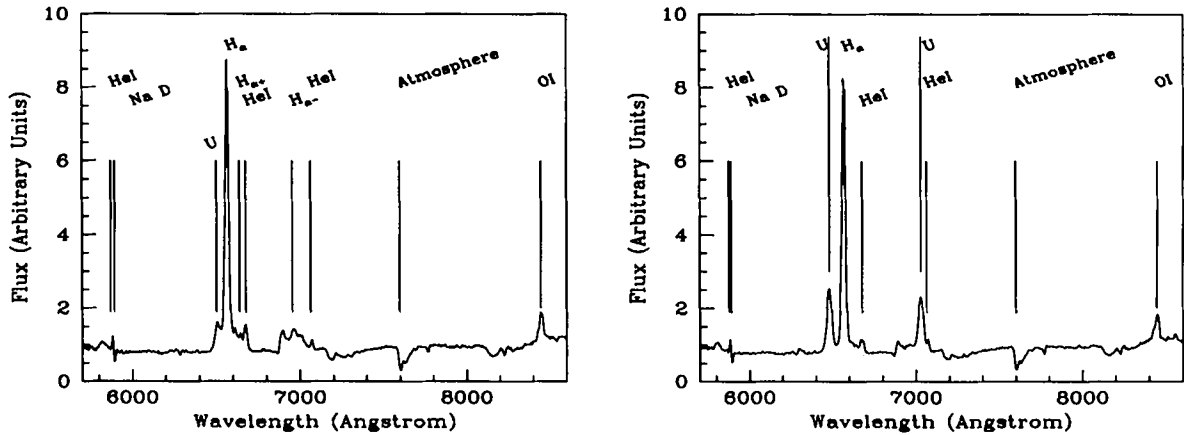


Fig. 8(a-b): The calibrated, continuum subtracted, optical spectrum of SS 433 on the (a) 27th and (b) 28th of September, 2002. In (a) the H_{α} line, blue and red shifted H_{α} lines (denoted by $H_{\alpha+}$ and $H_{\alpha-}$ respectively), HeI lines, OI line, atmospheric and sodium absorption lines are identified. The Doppler shifted H_{α} lines are exactly where they are expected from kinematic model of Abell and Margon (1979) within the instrumental resolution of 5 Å. In (b) we also see two bright lines, marked by ‘U’ at 7029.07Å and 6481.09Å respectively.

lines had very low intensity, indicating the decaying phase of the so-called optical bullets (Margon 1984; Vermeulen et al. 1993). On the 28th, the spectrum was taken 6 times, and in all the spectra these two unidentified lines were seen. The origins of the brighter ‘U’-marked lines are not totally clear as they are not close to the expected $H_{\alpha}\pm$ lines expected on that day. On the 27th of September, 2002, there was an un-identified line on the blue-ward side of the H_{α} line at 6503Å as well. This is also marked as ‘U’ in Fig. 8a. These could be from the accretion streams or from the winds from the companion itself. If correct, and are identified as the blue and red-shifted lines of the H_{α} line from the companion, then,

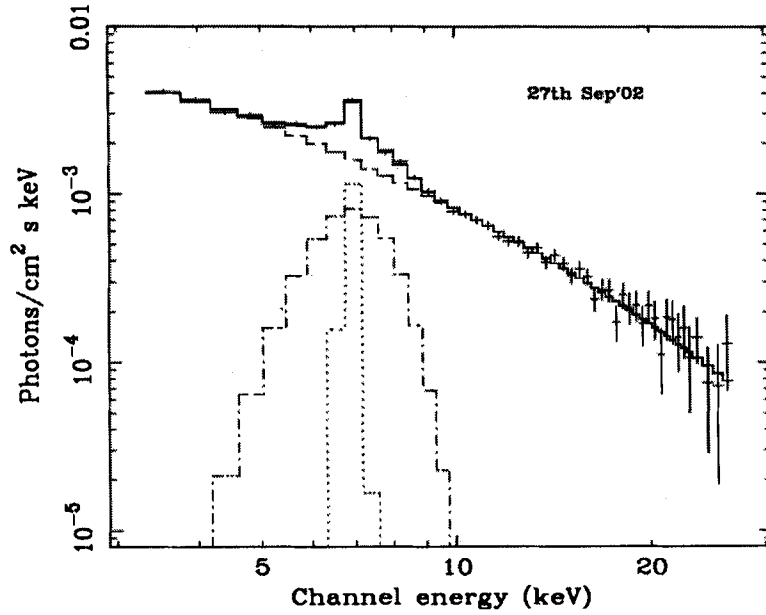


Fig. 9: The X-ray spectrum of the first spell of the RXTE observation of the 27th of Sept., 2002. The spectrum was fitted with a bremsstrahlung and two iron lines showed with dotted and dot dashed curves.

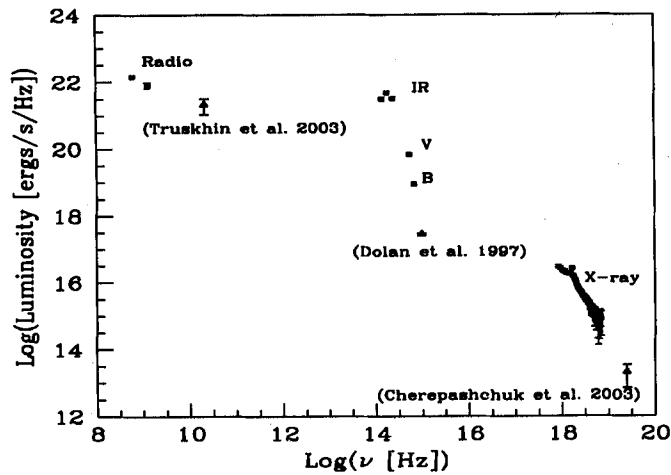


Fig. 10: The multi-wavelength spectrum of SS 433 as obtained by our campaign. Here, average luminosity (open boxes) over our available data has been plotted and the wavebands are marked. For comparison, we included three points, marked by open triangles with error bars, from literature (marked) which are not contemporaneous with our observation.

the projected velocity components long the line of sight required to produce these lines would be $21,300 \text{ km s}^{-1}$ (away from the observer) and 3748 km s^{-1} (towards the observer) respectively. Abnormal activities in the jets may not be ruled out either, in which case the asymmetry of the red and blue-shifts would be due to probable intrinsic red-shifts of the

relativistic system. Unfortunately the spectrum on the 30th of September, 2002 could not be used, as there was focusing error in the telescope.

The three spells of X-ray data (see, Fig. 4, bottom panel) were analyzed separately. We found that generally speaking, two line model with a thermal bremsstrahlung is necessary for statistically and physically acceptable fit to the X-ray spectra. However, the significance depends on the duration of observation. In Fig. 9, we present the X-ray spectrum of the first spell of our RXTE observation. The single line fit to the spectra yields $\chi^2/\nu = 44.94/45$ (ν is degrees of freedom) whereas the double line fit gives more acceptable value with $\chi^2/\nu = 34.84/43$. The requirement of the 2nd line in the spectrum is tested from the *ftest task* within XSPEC and found that the fit is significant at (2.4σ) level. The best fitted two lines found at energies 6.966 keV and 6.898 keV correspond to the Doppler-shifted values of $z = -0.00014$ (FeXXVI) and $z = -0.032$ (FeXXV) or $+0.0096$ (FeXXVI) respectively. Therefore, both the lines that we have identified are coming from the blue-jet of SS 433. The observed flux is 2.6524×10^{-10} ergs cm^{-2} sec^{-1} in the energy range 3-25 keV with the bremsstrahlung temperature at 15.77 keV. We failed to fit with a model having a blackbody emission component. Thus, no evidence for a Keplerian disk was found. Similarly, the single line fit to the spectra of the second spell yields a $\chi^2/\nu = 54/45$ whereas a double line fit gives more acceptable value with $\chi^2/\nu = 35.7/43$. The requirement of the 2nd line in the spectrum is tested and found that the fit is significant at (3σ) level. The best fitted two lines found at energies 7.012 keV and 6.802 keV which correspond to the Doppler-shifted values of $z = -0.007$ (FeXXVI) and $z = -0.018$ (FeXXV) respectively. Here too, both the lines are from the blue-jet of SS 433. The observed flux is 2.375×10^{-10} ergs cm^{-2} sec^{-1} in the energy range 3 – 25 keV with the bremsstrahlung temperature at 13.92 keV.

Figure 10 gives the broadband spectrum of SS 433 that we obtained using our multi-wavelength campaign. Campaign average data has been used for simplicity. In radio, results of 610 MHz and 1.28 GHz data have been put, while in infra-red, the results of I,J, K' bands have been put. We included V and B band observations which clearly show heavy extinction and the luminosity drops dramatically. X-ray spectrum in 3 – 27 keV is also shown. To compare with the results of others, we have included three observations at wavelengths which were not covered during our campaign (triangles). Thus, 21.7GHz observation of Trushkin et al (2003), ultra-violet observation of Dolan et al. (1997) and gamma-ray observation of Cherepashchuk et al. (2003) have been included. These three points were not contempo-

aneous to our campaign, but yet, they generally fall at reasonable values in the overall spectrum.

4 CONCLUDING REMARKS

In this paper, we have presented results of a recent multi-wavelength campaign on SS 433 carried out during 25th September, 2002 till 6th of October, 2002 using radio, IR, optical and X-ray instruments. Average ASM result indicated that the campaign was conducted when X-ray intensity was generally low which we also verify from our observations. We found that there is a tendency for the radio intensity variation to lag the IR variation by about two days. The broadband spectrum clearly showed evidence of very high extinction in optical region, possibly due to large scale obscuration of the central object by matter coming from the companion wind (Paragi et al. 1999). The X-ray data could be fitted with two Fe lines, both of which appear to be coming from the blue-shifted jet, i.e., the jet pointing towards us. We also find very small time-scale (few minutes) variations in all the wavelengths which could be suggestive of small bullets propagating from the base of the jet on the accretion disk to the radio regions as originally suggested in earlier communications (Chakrabarti 2002, 2003). The differential photometry in IR gives very clear indications that these short time scale variations were intrinsic to the jet. In optical spectra we observed that the blue- and red-shifted H_{α} lines to appear at the same location on the 27th of Sept. 2002 – on the 28th the intensities of these lines were very low possibly because the so-called optical bullet emission was on the decaying phase. We also see two bright, unidentified lines in all the frames taken on the 28th Sept. which could be due to sudden winds in the companion. Our optical and X-ray spectra indicated that the kinematic model generally gives the correct description even today.

SS 433 has always been a puzzle and it is still so even after 25 years of its discovery. The mass estimate of the recent observation (Hillwig et al. 2004) is an indication that the central compact object could be a small mass black hole. Given that in the last decade fresh understanding about the accretion processes onto black holes have emerged, it may be necessary to look into this system with a fresh look. Our result gives some idea about the physical processes that is going on near the compact object (a) The X-ray spectrum does not show any indication of a Keplerian disk. Thus the flow may be totally sub-Keplerian or advective (Chakrabarti, 1990), as is expected if the accretion is from winds. (b) Broadband

spectrum indicated heavy extinction in the optical/UV region. This is expected from the matter that is accumulated around the system (Paragi et al, 1999). (c) Short-time scale variations may indicate ejection of bullet-like entities, which could be formed due to shock oscillations in the advective flows (Chakrabarti et al. 2002). (d) There is a general indication that the radio intensity follows the IR by about two days. This could not be rigorously confirmed as the coverages in the campaign were not very high. If correct, and if we assume that the same matter generally propagates from the IR jet to radio jet, this would indicate that the radio emission takes place only about 6.73×10^{14} cm away from IR emitters. This seems to be quite reasonable. In fact, while comparing the results of Kodaira, Nakada & Backman (1985) with our observation, we conclude that there are intrinsic variation in IR band which may have been reflected in the Radio band two days later.

According to Brinkmann et al. (1991), the length of the X-ray jet is smaller than $\sim 10^{11}$ cm. Marshall et al (2002), further quantified this limit at $2 \times 10^{10-11}$ cm. In our analysis, we find the temperature of X-ray emitting region to be $kT \sim 15$ keV which, using the model of Kotani et al. (1996), correspond to even smaller distance of $\sim 10^{10}$ cm. While analysing RXTE data of SS 433 for over two years, Nandi et al. (2004) found the temperature to be even higher. Therefore, the X-ray emission must be from a region much closer to the compact object. On the other hand, IR emission of the jet may be emitted some where around 10^{12-13} cm (Fuchs 2003). Thus, the time lag between X-rays and IR should be at most a few hundreds of seconds. Lack of continuous X-ray observation during our campaign does not allow us to make definite comment on whether this lag was observed or not.

SKC thanks Dr. J. Swank of NASA/GSFC for giving us TOO time in RXTE. We thank the staff of the GMRT who have made these observations possible. GMRT is run by the National Centre for Radio Astrophysics of the Tata Institute of Fundamental Research. This work is supported in part by CSIR fellowship (SP) and a DST project (SKC and AN). and the team of GMRT/NCRA for giving

REFERENCES

- Abell, G. O., & Margon, B. 1979, *Nature*, 279, 701
 Band, D. L. & Gordon, M. A., 1989, *ApJ*, 338, 945
 Bessell, M.S., Castelli, F. & Plez, B., 1998, *A&A*, 333, 231
 Brinkmann, W., Kawai, N., Matsuoka, M., Fink, H. H., 1991, *A&A*, 241, 112
 Chakrabarti, S.K., 1990, *Theory of Transonic Astrophysical Flows*, World Scientific Co. (Singapore)
 Chakrabarti, S.K., Goldoni, P., Wiita, P.J., Nandi, A. & S. Das, 2002, *ApJ*, 576, L45

- Chakrabarti, S.K., Pal, S., Nandi, A., Anandarao, B.G. & S. Mondal, 2003, *ApJ*, 595, L45
- Cherepashchuk, A. M. et al. 2003, *A&A*, 411, 441
- Ciatti, F. et al. 1981, *A&A*, 95, 177
- Dolan, J. F. et al. 1997, *A&A*, 327, 648
- Elias, J.H., Frogel, J.A., Matthews, K. & Neugebauer, G. 1982, *AJ*, 87, 1029
- Fuchs, Y. 2003, Ph.D. Thesis, SACLAY, France
- Hillwig, T. C. et al. 2004, *ApJ*, 615, 422
- Kodaira, K. & Lenzen, R., 1983, *A&A*, 126, 440
- Kodaira, K., Nakada, Y. & Backman, D. E., 1985, *ApJ*, 296, 232
- Kotani, T. et al. 1999, *Astronomische Nachrichten (AN)*, 320 335
- Kotani, T., Kawai, N., Matsuoka, M. & Brinkmann, W. 1996, *PASJ*, 48, 619
- Margon, B. 1984, *ARA&A*, 22, 507
- Marshall, H.L., Canizares, C.R. & Schulz, N.S. 2002, *ApJ*, 564, 941
- Nandi, A., Chakrabarti, S. K., Belloni, T. & Goldoni, P., 2004, *MNRAS* (submitted) (astro-ph/0409662)
- Neizvestnyj, S. I., Pustilnik, S. A. & Efremov, V. G., 1980, *Sov. Astron. Lett.*, 6, 368
- Paragi, Z. et al. 1999, 348, 910
- Prabhu, T. et al. 1995, *A&A*, 295, 403
- Sequist, E. R., Gilmore, W. S., Johnston, K. J. & Grindlay, J. E., 1982, *ApJ*, 260, 220
- Swarup, G. et al. 1991, *Curr. Sci.* 60, 95
- Trushkin, S. A., Bursov, N. N. & Smirnova, J. V., 2003, in *New Views of Microquasars*, P. Durouchaux, Y. Fuchs, J. Rodriguez (Eds.), 283 (Centre for Space Physics: Kolkata)
- Vermeulen, R. C., 1989, *Multi-wavelength studies of SS 433*, Ph.D. Thesis (Leiden: Rijksuniversiteit)
- Vermeulen, R. C., et al. 1993, *A&A*, 270, 189